Distribution Agreement

In presenting this thesis or dissertation as a partial fulfillment of the requirements for an advanced degree from Emory University, I hereby grant to Emory University and its agents the non-exclusive license to archive, make accessible, and display my thesis or dissertation in whole or in part in all forms of media, now or hereafter known, including display on the world wide web. I understand that I may select some access restrictions as part of the online submission of this thesis or dissertation. I retain all ownership rights to the copyright of the thesis or dissertation. I also retain the right to use in future works (such as articles or books) all or part of this thesis or dissertation.

Signature:

_____ _____

Rebecca S. Dillard Date

Structural Studies of Host-Microbe Interactions

By

Rebecca S. Dillard
Doctor of Philosophy

Graduate Division of Biological and Biomedical Sciences
Microbiology and Molecular Genetics

Elizabeth R. Wright, Ph.D.
Advisor

Graeme L. Conn, Ph.D.
Committee Member

Joanna B. Goldberg, Ph.D.
Committee Member

Charles P. Moran, Jr., Ph.D.
Committee Member

Philip N. Rather, Ph.D.
Committee Member

Accepted:

Lisa A. Tedesco, Ph.D.
Dean of the James T. Laney School of Graduate Studies

Date

Structural Studies of Host-Microbe Interactions

By

Rebecca S. Dillard

B.S., The University of Alabama, 2011

Advisor:

Elizabeth R. Wright, Ph.D.

An abstract of

A dissertation submitted to the

Faculty of the James T. Laney School of Graduate Studies of Emory University

in partial fulfillment of the requirements for the degree of

Doctor of Philosophy

in

Graduate Division of Biological and Biomedical Sciences

Microbiology and Molecular Genetics

2018

Abstract

Structural Studies of Host-Microbe Interactions

By Rebecca S. Dillard

Recent advances in cryo-electron microscopy (cryo-EM) have drastically improved our ability to study the interactions between viruses and their hosts. The development of direct electron detectors has substantially improved image quality, and new techniques such as cryo-correlative light and electron microscopy (cryo-CLEM) are allowing us to understand more intricate systems. We have used cryo-EM to investigate host-microbe interactions at many stages of the viral replication cycle, including entry and assembly, and to provide insights into structural aspects of the host.

Identifying regions of interest in the transmission electron microscope can be challenging. We have shown that the use of native immunolabeling is therefore extremely helpful in order to study cellular and viral surface proteins in eukaryotic systems. This technique cannot be used, however, to mark internal components, which require alternative labeling strategies. We developed a workflow for correlated cryo-fluorescence light microscopy and cryo-EM (cryo-CLEM) of fluorescently tagged virus-infected or transfected mammalian cells. Cryo-CLEM combines the spatiotemporal information provided by fluorescence microscopy imaging with structural information from cryo-EM. These studies have provided insights into the assembly and morphology of respiratory syncytial virus (RSV) and entry and fusion events of human immunodeficiency virus type I (HIV-1).

We used cryo-ET along with several functional assays to study bacteriophage interactions in prokaryotic systems. We found that *Vibrio cholerae* outer membrane vesicles (OMVs) act as a defense mechanism to protect *V. cholerae* against bacteriophage infection in a dose- and receptor-dependent manner, suggesting that OMVs are an important consideration for the use of phage therapy. In *Caulobacter crescentus*, we found that that type IVc pilus retraction is required for bacteriophage ϕCbK attachment, and that proper assembly of the flagellum, cell motility, and ϕCbK adsorption depend on multiple flagellins.

In summary, we have used cryo-EM to provide information about both eukaryotic and prokaryotic virus interactions with their hosts, allowing us to examine RSV assembly, HIV-1 entry, and bacteriophage interactions with *V. cholerae* OMVs, *C. crescentus* pili, and *C. crescentus* flagella. Our studies illustrate that cryo-EM is a valuable technique for investigating host-microbe interactions.

Structural Studies of Host-Microbe Interactions

By

Rebecca S. Dillard

B.S., The University of Alabama, 2011

Advisor:

Elizabeth R. Wright, Ph.D.

A dissertation submitted to the

Faculty of the James T. Laney School of Graduate Studies of Emory University

in partial fulfillment of the requirements for the degree of

Doctor of Philosophy

in

Graduate Division of Biological and Biomedical Sciences

Microbiology and Molecular Genetics

2018

Acknowledgements

I would like to express my deep appreciation to my advisor, Dr. Elizabeth R. Wright, for her patience and guidance and for providing endless opportunities to me; to my committee members, Dr. Graeme L. Conn, Dr. Joanna B. Goldberg, Dr. Charles P. Moran, and Dr. Philip N. Rather, who each supported me in considerable ways; and to Dr. Wah Chiu, Htet A. Khant, and Caroline J. Fu for introducing me to cryo-EM.

I would like to recognize past and present Wright Lab members, Dr. Ricardo C. Guerrero Ferrerira, Dr. Gabriella Kiss, Dr. Leon G. De Masi, Dr. Joshua D. Strauss, Dr. Cheri M. Hampton, Dr. Kristen M. Lamb, Dr. Max Housman, Dr. Conrad W. Shebelut, Raven Shah, Rachel E. Storms, Fredrick Leon, Deanna Altomara, Mengtian Jin, Somnath Ganapa, Dylan Price-Wittenauer, and particularly Zunlong Ke, for their collegiality and contributions to my scientific growth.

Thank you to our collaborators, Dr. Andrew Camilli, Dr. Tamara Reyes-Robles, Dr. Yves V. Brun, Courtney K. Ellison, Dr. Patrick H. Viollier, Dr. Gaël Panis, and Dr. Phillip D. Aldridge, and to the Robert P. Apkarian Integrated Electron Microscopy Core staff, Hong Yi, Jeannette V. Taylor, and Arthur L. McCanna.

I acknowledge the Department of Pediatrics Division of Infectious Diseases faculty members and researchers, the MMG faculty, and all of the MMG students, particularly Kelsie Brooks, Jessica Coates, Emily Crispell, Hannah Ratner, and Emily Woods.

I'm grateful for the Cold Spring Harbor Advanced Bacterial Genetics 2016 instructors and students, who were truly inspirational.

Thank you to Dr. Jaap Brink, Aaron Graham, Dr. Sohei Motoki of JEOL USA, Inc; Dr. Benjamin Bammes and Dr. Michael Spilman of Direct Electron, LP; and everyone at Leica Microsystems for technical support; to Shenita Bryant, Emily Morran, Karen Pierce, Deirdre Russell,

Rosa White, and Rebecca Masel for administrative support; and to Ryan Wilkins, Jon Lauer, Islam Abd Elhai, and John Lucy for personal support.

Finally, I would like to thank my family. Thank you to my grandmother and grandma, who were so proud of me; to my sister, Natalie, brother-in-law, Joshua, nephews, Jack and Lukas, and niece, Helena, for encouraging me; and to my parents, for everything.

Table of Contents

Figures and Tables

Chapter 1

Chapter 2

Chapter 3

Chapter 4

Chapter 5

Chapter 6

Appendix A

Appendix B

Appendix C

Appendix D

Chapter 1: Introduction

Cryo-EM portions adapted from:

Biological applications at the cutting edge of cryo-electron microscopy

Rebecca S. Dillard[1], Cheri M. Hampton[1], Joshua D. Strauss[1], Zunlong Ke[1,2], Deanna Altomara[1], Ricardo C. Guerrero-Ferreira[1], Gabriella Kiss[1], and Elizabeth R. Wright[1,3]

[1]Division of Pediatric Infectious Diseases, Emory University School of Medicine, Children's Healthcare of Atlanta, Atlanta, GA

[2]School of Biology, Georgia Institute of Technology, Atlanta, GA

[3]Robert P. Apkarian Integrated Electron Microscopy Core, Emory University, Atlanta, GA

Submitted to *Microscopy and Microanalysis*

CRYO-ELECTRON MICROSCOPY

Cryo-electron microscopy (cryo-EM) technologies were pioneered in order to retain specimen hydration and reduce electron-beam damage to the specimen during direct imaging and electron diffraction in the transmission electron microscope (TEM) [1]. Initial work focused on catalase crystals preserved in a thin film of vitreous ice [1]. Subsequently, suspensions of viruses and other samples were vitrified and imaged, functionally extending cryo-EM to structural investigations of broad ranges of targets [2-5]. Most aqueous samples are prepared for cryo-EM or cryo-electron tomography (cryo-ET) by first applying a small aliquot of a suspension to an EM grid, blotting the grid to near dryness, and then rapidly plunge freezing it in liquid ethane or liquid propane cooled to cryogenic temperatures. This method effectively preserves the biological sample in a thin layer of vitreous, non-crystalline ice in a near native state [4, 6]. Continued developments to specimen preservation equipment and methods by research groups and EM manufacturers have improved the quality and reproducibility of the cryo-EM grids prepared.

The cryo-preserved specimens are then loaded into grid-holders, e.g. cryo-holders, which maintain the specimen at close to liquid nitrogen temperatures in order to minimize the de-vitrification or warming of the specimen. There have been many improvements made to these holders since their introduction in the late 1970s. Many of the cryo-holders available may be used for standard side-entry microscopes. In order to facilitate the preservation of specimen integrity, instrument automation, and the demands of high-throughput data collection, starting in the early 2000s, EM companies began to design and produce instruments with 'multi-specimen' cartridge-style systems in which three to twelve individual specimens can be loaded into the column of the microscope. Simultaneously, improvements to overall microscope stability, the use of field emission electron sources, computer control, and the automation of standard functions enabled the beginning of the

'resolution revolution in cryo-EM' [7] by facilitating the acquisition of high quality EM data both on film and CCD cameras via automated routines [8, 9].

Recent advances in sample preparation, imaging, and data processing have led to a dramatic expansion of cryo-EM in structural biology [10, 11]. The workflow for structure determination by cryo-EM is outlined in Figure 1. Sample optimization is followed by a freezing step, either the vitrification of a thin film sample on a grid (plunge freezing) or of a sample volume using pressure (high pressure freezing (HPF) or self-pressurized rapid freezing (SPRF)). The sample may be further processed by thinning (cryo-focused ion beam milling (cryo-FIB) or cryo-sectioning) or examined by cryo-correlative light and electron microscopy (cryo-CLEM) before TEM imaging and image processing. We discuss some of the recent advancements at various steps of this workflow, which we have used to improve imaging of biological specimens. These include the use of new substrates and methods for sample preparation, phase plates and direct electron detectors for cryo-EM image acquisition, and the application of cryo-CLEM, which combines spatiotemporal information about the sample from fluorescence light microscopy with structural information from cryo-EM. There have, of course, been many other developments in techniques and data processing that are described elsewhere [12-16].

Substrates and Specimen Preparation

One of the essential components of high-quality, high-resolution cryo-EM is reproducible and robust sample preparation. Cryo-EM samples are typically applied to an EM grid consisting of an amorphous carbon film supported by a metal mesh. The grid is then blotted to remove excess liquid and plunge-frozen in a liquid cryogen ("plunge freezing" in Figure 1). This process preserves the close-to-native-state structure of the hydrated specimen, but can be low throughput and

unpredictable in terms of ice thickness and particle distribution. Additionally, it has been shown that irradiation in the electron microscope leads to deformation of amorphous carbon, causing sample movement and therefore blurred images [17-19]. Recently, several new sample purification methods, substrates, and grid preparation systems have been developed to optimize performance during imaging.

Cryo-EM single particle reconstructions are based on averaging projections of thousands of identical particles in random orientations [10, 15, 20, 21]. Homogeneity of the sample is therefore extremely important although such purification can be challenging. GraFix is a sample purification method developed for reducing heterogeneity during cryo-EM sample preparation. The particles undergo a weak chemical fixation during density gradient centrifugation to provide conformational stability and purify the sample, leading to a more homogenous population [22, 23].

Another concern is preferred orientations of the particles on the grid. Because the sample is confined to a thin layer of vitreous ice, it can interact with both the grid support and the air-water interface, potentially leading to a bias in binding and therefore nonisotropic sampling of particle orientations [23]. The use of continuous carbon support films to improve particle distribution may be used to provide particular particle orientations, but it may also lead to even more significant orientation problems [24]. Self-assembled monolayers [25], poly-L-lysine [26], and detergents [27, 28], have all been used to reduce preferred orientation, but tend to be sample specific [29]. The GraFix process has the additional advantage of disrupting particle aggregation and reducing preferred orientations by altering the charge distribution of the particles during the chemical fixation step [23]. The preferred orientation problem may also be more widely addressed at the imaging level, by tilting the specimen during data collection [29].

Single particle cryo-EM of membrane proteins tends to be challenging because the proteins must be extracted from the membrane and solubilized in detergents, which may affect protein structure and function and reduce image contrast [30-32]. Amphipathic polymers called amphipols are a potential alternative to detergents. These are milder surfactants used to non-covalently bind the transmembrane portion of the protein, improving membrane protein solubility without affecting contrast in the images. Amphipols have been used in the determination of several membrane protein structures [33-39]. Another method of preparing membrane proteins for cryo-EM is the use of lipid nanodiscs [40-47]. Nanodiscs consist of scaffold proteins surrounding a small lipid bilayer in which the protein of interest is reconstituted. This maintains a near native environment for the protein and provides additional particle size, although heterogeneity of the nanodisc may be a concern [31, 32].

Affinity grids are a new substrate designed to selectively adsorb particles on the EM grid by applying specific affinity between substrate and sample, allowing purification steps to be combined with grid preparation. The grid has a lipid monolayer containing Ni-NTA lipids that can recruit His-tagged proteins from cell extracts, reducing the required amount of protein and time for purification [48]. Our lab has utilized affinity grids with His-tagged Protein A and anti-Env polyclonal antibody to study HIV CD84 virus-like particles (VLPs), resulting in less background and better control of particle density, as shown in Figure 2 [49]. Further developments of the affinity grid include the use of a NTA-PEG based coating, which combines the anti-fouling properties of brush conformation methoxypolyethylene glycol with NTA ligands on flexible PEG spacers to prevent preferred orientation of the bound His-tagged proteins [50]. Another example is a functionalized carbon film with covalently bound Ni-NTA, Protein G, or oligonucleotides to selectively recruit macromolecular complexes [51]. In a simplified affinity grid method called cryo-Solid Phase Immune Electron Microscopy (SPIEM), antibodies or Protein A are applied directly to grids, eliminating the need to

first apply a lipid monolayer [52, 53].

The use of the affinity capture system with silicon nitride (SiN) membrane support films has also shown promising improvements for sample preparation. The hydrophobicity of SiN supports interactions with the lipid tails of the Ni-NTA lipid monolayer, allowing for effective sample capture on the grid. Additionally, the membranes are flat, durable, and can be consistently manufactured, addressing the delicate and inconsistent nature of amorphous carbon supports [54]. Affinity grids combine purification steps with grid preparation, significantly reducing the time required to produce samples for cryo-EM imaging, and can be used for structure determination at high resolution. Yu *et al.* have recently used the method to determine the structure of a low concentration virus at 2.6 Å resolution [55].

New electron microscopy grids and substrates have allowed great improvements for cryo-EM imaging. Traditional lacey, Quantifoil (Quantifoil Micro Tools), or C-flat (Protochips) EM grids are made of a metal scaffold (e.g., copper, nickel, or gold) and an amorphous carbon support. Irradiation of amorphous carbon in the electron microscope causes it to bend, however, leading to movement of the sample, often referred to as beam-induced motion, and therefore blurry images. Since the linear thermal expansion coefficient is much lower for carbon than for the metal support, the carbon film may also pucker at cryo temperatures [56]. This can lead to poor imaging and the loss of information at high spatial frequencies. Several alternative substrates have been developed to address these deformations. Titanium-silicon metal glass films, a nanocrystalline silicon carbide substrate called Cryomesh (ProtoChips Inc), and hydrogen plasma treated graphene all decrease beam-induced motion, but do not completely eliminate it [57-59]. Ultrastable gold substrates, which consist of a gold foil across a gold mesh grid, are one of the most promising solutions. By using the

same material for the support and grid, differential thermal contraction, and therefore puckering, during cooling is prevented and the high conductivity of gold nearly eliminates beam-induced motion, significantly improving image quality [19, 60, 61].

3D-DNA origami sample supports aim to address many of the current concerns for grid preparation. The sample particles are bound within a hollow support made up of double stranded DNA helices. This helps to control particle orientation, protects particles from the force of blotting with filter paper and from the air-liquid interface, and improves ice thickness consistency. The method was shown to be successful for the DNA binding protein p53, but will require more rigidity to precisely control particle orientation and will need to expand to be more widely applicable to various types of samples [62].

Protein scaffolds are also being used to determine the structures of monomeric proteins that would otherwise be too small for cryo-EM. Coscia *et al.* have designed a self-assembled symmetric protein scaffold with a small protein genetically fused, producing a large, rigid, and symmetric particle that is more amenable to cryo-EM, and solved the structure at subnanometer resolution [63]. Liu *et al.* have achieved near atomic resolution of a small protein called DARPin, which is rigidly fused to a self-assembled symmetric protein cage through terminal helices. The amino acid sequence of DARPin can be altered to tightly bind other small proteins, making it widely applicable [64].

Cryo-EM grid ice should ideally be only slightly thicker than the sample. Excess ice thickness should be avoided because it allows the particles within an image to be at different focal heights and contributes to noise in the images [65]. Conventional blotting with filter paper often leads to inconsistent ice thickness and sample degradation due to the blotting force and it exposes the

particles to an air-water interface of the sample. To address these problems, a "self-blotting" grid has been developed to generate reproducibly thin films of ice without the use of a filter paper blotting step [66, 67]. An ammonium persulfate and sodium hydroxide solution is applied to copper grids, supporting the growth of $Cu(OH)_2$ nanowires on the copper grid bars. The nanowires draw up excess liquid when the sample is applied to the grid, resulting in a thinly spread film of liquid on the grid that is then plunge frozen without the requirement of a blotting step. The self-blotting grids are used in conjunction with a newly designed freezing apparatus called the Spotiton [68, 69]. This device uses a piezo controlled electric inkjet dispense head to deposit small volumes of sample at defined locations on the grid, which is then plunge frozen. Use of the self-blotting grid with the Spotiton results in thin films of uniform ice and the process is almost entirely automated, increasing the reproducibility and throughput of cryo-EM grid preparation [66-69].

Another blotless freezing system called the cryoWriter allows real-time monitoring of the water thickness prior to vitrification [70]. A microcapillary is used to deposit a small sample volume (3 – 20 nanoliters) onto the grid. Depending on the volume applied, excess sample can either be recovered using the microcapillary or allowed to evaporate. The sample film is evaluated using a laser beam and photodetector and once the appropriate thickness is reached, the grid is plunge frozen. This system prevents the potentially damaging effects of filter paper blotting and uses significantly smaller volumes, allowing the investigation of lowly abundant samples.

Methods for time resolved imaging to capture transient states of biological molecules by mixing reaction components immediately prior to blotting have also seen recent improvements. This was initially achieved by applying one reaction component to the EM grid in the conventional pipetting and blotting manner to achieve a thin film, then spraying another component onto the film and

rapidly freezing [71-76]. The reaction only proceeds where the components mix, however, potentially leading to heterogeneity in the sample across the grid. This problem was addressed by coupling a micromixer with a microsprayer, allowing external homogenous mixing of the reactants before spraying onto an EM grid and plunge freezing [77-79]. While this method allows the capture of dynamic processes for cryo-EM imaging, variability in ice thickness and coverage of the grid limits the regions suitable for data collection. The more recent development by Feng *et al.* of a polydimethylsiloxane (PDMS)-based microsprayer allows the control of ice thickness through sprayer pressure and distance from the grid and has the potential to provide time-resolved sample preparation by mixing reactants in a channel for specified amounts of time [80].

Direct Electron Detectors

Low electron doses are necessary for the imaging of biological specimens in order to limit radiation damage of the sample. Cryo-EM images are therefore inherently noisy. Additionally, beam-induced motion of the sample leads to blurriness in the images. Both of these issues have been significantly improved by the development of direct electron detectors.

Several types of sensors may be used for the detection of electrons and the performance of the detector is extremely important for achieving high quality data. Detectors can be described by the detective quantum efficiency (DQE), a measure of signal produced from the sample and noise contributed to the image by the detector. A detector that contributes no noise to the image would have a DQE of 1.

Photographic film has historically been used to record cryo-EM images due to its large imaging area and high resolution. Its DQE is ~0.3-0.35 at half Nyquist frequency [81, 82]. The use of film can be

labor intensive and time consuming, however, as it requires development and scanning to a digital format [13, 24, 83]. Charge coupled device (CCD) cameras provide a much more automated mode of imaging, allowing for images to be immediately evaluated and for large datasets to be collected quickly. As the electrons hit the CCD, a scintillator is used to induce the emission of photons. The photons are converted to electrical signals and an electrical charge accumulates that can be read and digitized to form the image [24, 84, 85]. The scintillator of a CCD camera produces electron and photon scattering, however, contributing additional noise to the images and leading to a DQE of ~0.07-0.1 at half Nyquist frequency, significantly inferior to that of photographic film [81, 82].

Direct detection devices (DDDs) allow electrons to be recorded directly on a sensor, rather than through a scintillator. This, along with back-thinning, which decreases backscattering of electrons, results in a considerable reduction of noise in the image compared to the noise from electron and photon scattering generated in the scintillator and fiber optics of a CCD [86]. There are several types of DDDs that can be operated in various modes. In integration mode, charge is collected in each pixel, then integrated and read out. The DQE at half Nyquist in integration mode is ~0.4-0.6 [81]. In counting mode, the signal from each electron event is recorded and weighted the same, which reduces read noise and variability in electron signal. Operating in counting mode while using a high frame rate allows even higher DQEs to be achievable [87, 88]. Some cameras may additionally be operated in what is called "super-resolution" mode, in which the electron events are sublocalized within the pixel, surpassing the Nyquist frequency limit [87-89].

Another advantage of DDDs is the ability to fractionate the electron dose of an exposure over multiple frames by using a high frame rate. This allows the optimal use of electron dose in the image because one can compensate for the loss of high spatial frequency information as the dose

accumulates. Frames can then be aligned before summing to correct for beam-induced motion and specimen drift in the image [90]. The effects of motion correction can be seen in the image of coliphage BA14 shown in Figure 3. The image was acquired at 12 frames per second with an exposure time of 5 seconds and then summed (Figure 3A) or motion-corrected using scripts from Direct Electron, LP and summed (Figure 3B). Blurring is significantly reduced by motion correction as shown in the images and power spectra. The ability to combine a high DQE with automation and the implementation of dose compensation and motion correction have led to a dramatic increase in the quality of cryo-EM data and the number of near-atomic to atomic resolution structures being determined [38, 91-96].

Despite the improvements in DQE and signal-to-noise ratio provided by direct electron detectors, low contrast in cryo-EM images can still be problematic, particularly for small samples. Additional contrast enhancement, such as through the use of energy filters or phase plates, can be particularly useful in these cases.

Phase Plates

The contrast of unstained biological materials is inherently weak under low-electron dose cryo-EM imaging conditions. Contrast can be improved by defocusing of the objective lens, although this results in a reduction of the high spatial frequency components of the image, or with the use of an energy filter, which removes inelastically scattered electrons thereby improving the signal-to-noise ratio [97, 98]. Another strategy for addressing low contrast in cryo-EM images is the use of phase plates. The Wright lab is currently implementing two types of phase plates, the thin carbon-film Zernike-style phase plate and the hole-free carbon-film phase plate (HFPP), or Volta phase plate (VPP).

Zernike phase contrast (ZPC) cryo-EM uses a thin carbon film with a small hole produced by a focused ion beam (FIB) placed in the back focal plane [99-102]. Unscattered electrons pass through the hole while the scattered electrons go through the carbon film, shifting the phase of the unscattered electrons relative to the scattered electrons by $\pi/2$. This changes the contrast transfer function (CTF) from a sine function to a cosine function [103] and significantly improves the contrast at low spatial frequencies. The images are acquired in focus, eliminating the loss in resolution due to defocusing. The higher contrast provided by phase plates improves image alignment, making it possible for fewer particles to be averaged to produce high resolution structures by single particle analysis [99], and providing excellent results for cryo-ET [100, 104-107]. The use of ZPC cryo-EM can be challenging, however, due to a short lifespan, charging, difficulty keeping the phase plate aligned, and fringing artifacts in the images [108-113]. Figure 4 illustrates the contrast provided by the Zernike-style phase plate in a tomogram of a *Caulobacter crescentus* cell infected with bacteriophage ϕCbK, as well as the fringing artifacts.

HFPP (or VPP) cryo-EM uses a homogenous carbon film in the back focal plane. Local charges are induced on the film to generate an electric potential and create the phase shift for increased contrast [114]. This form of phase plate has been shown to be more stable for data collection and does not introduce strong fringing artifacts [99, 108, 109, 114-116]. It has recently been used to resolve extraordinary *in situ* detail via cryo-ET [117-122] and to solve several high-resolution structures via single particle analysis [116, 123-125]. More recently, however, it has been possible to implement a slight defocus with this style of phase plate due to improvements in reconstruction software [126]. This lessens the requirement for accuracy in focusing thus increasing the ease of use and the speed of data collection [125, 127, 128]. Processing of defocused VPP data has been shown to be more robust than that of conventional cryo-EM or in-focus VPP data, providing better reconstructions

using fewer particles [129]. In Figure 5, we show 2D projection images of reovirus serotype 1 Lang (T1L) particles collected using HFPP and a slight defocus. The increased contrast allows the viral attachment fibers and released genome to be clearly resolved, without extreme fringing artifacts.

Correlative Light And Electron Microscopy

Correlative Light and Electron Microscopy (CLEM or cryo-CLEM) is a technique that combines the spatiotemporal physiological information gained from fluorescence microscopy with the ever-higher resolution of structures from cryo-EM. The technique was developed in response to the absence of methods to unobtrusively label internal cell contents for cryo-EM. The fluorescence imaging can be done live or following vitrification of the cells to capture structures in their near-native state ("LM imaging" and "cryo-CLEM imaging", respectively, in Figure 1) [130]. This is made possible by the introduction of cryo-cooled stages for the inverted or upright light microscope as well as the integrated light and electron microscope [131-134]. Several advantages of cryo-fluorescence microscopy (cryo-fLM) include the absence of morphology-altering fixation, longer fluorophor lifespan [133, 135, 136], as well as a large field of view [137, 138]. This allows regions of interest to be identified quickly without subjecting the sample to a lengthy screening process in the electron microscope, therefore preventing unnecessary irradiation of the sample prior to imaging. Relocating the region of interest in the electron microscope is facilitated by the use of special finder-style EM grids or commercially available fiducials such as FluoSpheres or TetraSpeck beads (100-200 nm) that are both fluorescent and electron dense [139, 140]. Marker-free alignment methods are also possible, as demonstrated by Anderson *et al.*, in which the centers of the holes in the sample support are used for localization [141].

Samples must be relatively thin in order to be penetrable by the electron beam (less than 1 μm) [142], but must be even thinner for reliable 3D tomographic reconstruction (~250 nm). This is ideal for cryo-CLEM imaging of viruses [140], bacterial cells [143, 144], or the thinnest regions of mammalian cells [134, 139, 145, 146]. Additional techniques, such as FIB milling to produce thin lamella [121, 147-152], or cryo-ultramicrotomy (CEMOVIS) [142, 153-155], however, are required to access the interior of vitrified mammalian cells.

CLEM has been used to visualize the process of virus entry and exit from mammalian cells with great success. Using live-cell fluorescent imaging, cryo-fLM, and cryo-ET, Jun *et al.* has directly observed pseudotyped HIV-1 virions with GFP-tagged HIV-1 Vpr interacting with HeLa cells at different time points after infection [156]. Ibiricu *et al.* used live-cell fluorescence microscopy followed by cryo-ET to identify time points and location of GFP-labeled herpes simplex virus undergoing axonal transport in primary neurons cultured directly on TEM grids [157]. To visualize virus after release, Strauss *et al.* used CLEM procedures to determine the arrangement of mCherry-Gag labeled HIV-1 particles anchored to cell plasma membranes via EGFP-tagged tetherin, a host cellular restriction factor that inhibits enveloped virus release, which can be seen in Figure 6 [158]. Hampton *et al.* further investigated these tethered particles using cryo-CLEM, as shown in Figure 7 [159].

The latest improvements address many of the challenges associated with cryo-CLEM, such as contamination from atmospheric moisture during grid transfer steps, maintaining proper cryogenic temperatures during cryo-fLM imaging, and accurately correlating cryo-fLM and cryo-EM data. Schorb *et al.* have developed a system that optimizes grid transfer, stage stability, microscope optics, and software, establishing a comprehensive cryo-CLEM workflow [160]. Another system by Li *et al.*

uses a high-vacuum chamber on the fluorescent microscope stage, decreasing contamination of the sample and allowing the objective lens to remain at room temperature. It has additionally been adapted to use a cryo-EM holder, reducing the number of grid transfer steps [161]. Future developments in CLEM will expand the use of cryo-super-resolution microscopy to localize specific proteins, further bridging the gap in resolution between light and electron microscopy [162-166].

The following sections will discuss the systems that we have investigated using cryo-EM and cryo-ET methods. These include the assembly and morphology of respiratory syncytial virus (RSV), fusion, entry, and tethering of human immunodeficiency virus type I (HIV-1), *Vibrio cholerae* outer membrane vesicles as a defense mechanism against bacteriophage infection, and the use of pilus retraction and multiple flagellins by bacteriophage ϕCbK to infect *Caulobacter crescentus*.

RESPIRATORY SYNCYTIAL VIRUS

Respiratory syncytial virus (RSV) is an enveloped, single stranded, negative sense RNA virus of the *Pneumoviridae* family within the order Mononegavirales [167]. It is the leading cause of lower respiratory disease in infants and poses a high risk for morbidity and mortality in immunocompromised adults [168, 169]. The monoclonal antibody Palivizumab is the only available prophylaxis, but it is expensive and only administered to high-risk infants [168]. There are many vaccines currently in development, although this process has proven to be challenging and many aspects of the virus remain poorly understood [170-177].

RSV Genome and Structure

The RSV genome encodes nine structural proteins: the glycoproteins G (attachment), F (fusion), and SH (small hydrophobic, unknown function) which project from the viral membrane; M (matrix)

which lines the inner layer of the viral membrane and is important for viral filament formation; N (nucleocapsid protein), which binds the RNA and provides resistance to RNases; P (phosphoprotein), which serves as a chaperone for N protein; M2-1, an antitermination factor and linker between the ribonucleoprotein (RNP) complex and M [178, 179]; L, the large polymerase subunit [180]; and M2-2 which regulates the switch between RNA transcription and replication [181-183]. There are additionally two nonstructural proteins, NS1 and NS2, which are involved in type I interferon suppression in the host [184, 185].

RSV Assembly

RSV viral filaments form at the cell surface enveloped in a lipid bilayer derived from the host cell membrane [186]. The glycoproteins are translated then trafficked to the cell surface through the secretory pathway, while other structural proteins are translated in the cytoplasm [187]. New genomic RNA is produced in inclusion bodies associated with M and L proteins within the cytoplasm [179, 188]. Several host cellular factors, including actin and microtubules, cellular trafficking pathways, plasma membrane microdomains, and the small GTPase RhoA, are also involved in the assembly process [189-196]. Many of the mechanisms of RSV assembly remain unclear, however, such the recruitment order of structural proteins to the plasma membrane. These areas are ideal for investigation using cryo-EM and cryo-CLEM techniques, as demonstrated in Chapter 2.

HUMAN IMMUNODEFICIENCY VIRUS TYPE I

In Chapter 2, we also used cryo-CLEM to investigate human immunodeficiency virus type I (HIV-1) entry and tethering processes. HIV-1 is an enveloped, single stranded, positive-sense RNA virus of the Lentivirus genus within the *Retroviridae* family. Upon entry into the host cell, it is reverse

transcribed into double-stranded DNA that can then integrate into the host cell genome. It may become latent or be transcribed to continue the replication cycle. HIV-1 infects human immune cells and long-term replication of the virus leads to the onset of immunodeficiency and eventually acquired immunodeficiency syndrome (AIDS) [197]. With over a million people newly infected each year, a vaccine is a major priority [198, 199].

HIV-1 Genome and Structure

The HIV-1 genome includes 9 genes that encode for structural, regulatory, and accessory proteins. The major structural proteins are transcribed from three genes as polyproteins: gag, which codes for the structural proteins of the viral core (matrix, MA, capsid, CA, nucleocapsid protein, NC, and P6); pol, which codes for enzymes required for viral replication (reverse transcriptase, RT, integrase, IN, RNase H, and protease, PR); and env, which codes for the viral envelope glycoprotein gp160. gp160 is cleaved by the host protease furin to produce the surface glycoprotein gp120, which binds receptors on the host cell, and gp41, a transmembrane protein that aids in cell attachment and fusion [200, 201]. The tat and rev genes encode regulatory proteins involved in reverse transcription and the synthesis of viral proteins, respectively [202]. The accessory proteins are encoded by vpr, vif, nef, pu, and tev. Vpr is involved in nuclear import of pre-initiation complexes (PICs) for integration of the viral genome into the host cell genome and arresting the host cell cycle, Vif is required for infectivity of specific cell types, Nef contributes to cell apoptosis and infectivity, Vpu releases virions from the cells after assembly, and Tev functions similarly to Rev [202-204]. The mature virion is a spherical particle enveloped in a host cell derived lipid bilayer with Env exposed on the outer surface and a conical nucleocapsid (core) encasing two copies of the RNA genome, PR, RT, IN, Vpu, Vif, Vpr, and Nef within [203, 205].

HIV-1 Entry

Binding of the host cell receptor by Env is followed by internalization of HIV-1 particles into endosomes [206]. The viral membrane must then fuse with the endosome in order to release viral components into the cell [207]. HIV-1 fusion is mediated by Env. Cleavage of gp160 frees the N-terminal of gp41 to serves as a fusion peptide that inserts into the host membrane [208]. When the conical core is released, it must disassemble, or uncoat. This process is important for regulating reverse transcription and PIC nuclear import, as is its timing [209-212]. Time-resolved fluorescence imaging has provided spatio-temporal information about uncoating, but higher resolution information is needed for a more complete understanding [213].

Tetherin Restriction of HIV-1

Tetherin (BST-2) is a host cell restriction factor that binds a wide range of enveloped viruses by inserting into the viral membrane to retain them at the cell surface [214, 215]. It is a type II integral membrane protein composed of a short cytoplasmic tail, a transmembrane domain, a coiled-coil ectodomain, and a GPI anchor [216, 217]. It functions as a coiled-coil dimer that requires one of three conserved cysteine residues and membrane insertion of both the transmembrane domain and GPI anchor [218, 219]. Visualization of tethers by cryo-ET reveals virions linked in linear and branched chains and supports a model in which the coiled-coil ectodomains are perpendicular the host and viral membranes [158]. The HIV-1 accessory protein Vpu can counteract tetherin-mediated restriction of viral particles by surface downregulation and degradation [215, 220]. In Chapter 2, we sought to visualize tetherin-mediated restriction of HIV-1 virus-like particles using cryo-CLEM in order to correlate the presence of tetherin via fluorescence light microscopy with the densities linking the particles observed by cryo-EM.

BACTERIOPHAGES

Bacteriophages, or phages, are viruses that infect bacteria. The majority of phage genomes are double-stranded DNA, while there are single-stranded DNA, single-stranded RNA, and very rarely, double-stranded RNA phages. 96% of phages are tailed, with the rest being cubic, filamentous, or pleomorphic. The tailed phages all have double-stranded DNA genomes and icosahedral or elongated capsids and are divided into three families: *Myoviridae*, *Siphoviridae*, and *Podoviridae*. The *Myoviridae* tend to be the largest and their tails consist of a neck, a contractile sheath, and a central tube. The *Siphoviridae* are the most numerous and their tails are noncontractile flexible or rigid tubes. The *Podoviridae* have short, noncontractile tails. Filamentous phages are also divided into three families: *Inoviridae*, *Lipothrixviridae*, and *Rudiviridae*. The *Inoviridae* have single-stranded DNA genomes and using a "rolling-circle" replication cycle with a double-stranded DNA intermediate. Some are able to integrate this intermediate into the host cell genome. These phages assemble and release without killing the host cell. The *Lipothrixviridae* have double-stranded DNA genomes, form long rods with a lipoprotein envelope, and inhabit hot springs. The *Rudiviridae* also have double-stranded DNA genomes and inhabit hot springs, but they form straight rods without an envelope. The cubic phages are made up of seven families of all four types of genomes: *Microviridae*, *Corticoviridae*, *Tectiviridae*, *SH1*, *STIV*, *Lenviviridae*, and *Cystoviridae*. The pleomorphic phages are also made up of seven families that all have double-stranded DNA genomes: *Plasmaviridae*, *Fuselloviridae*, *Salterprovirus*, *Guttaviridae*, *Ampullaviridae*, *Bicaudaviridae*, and *Globuloviridae* [221].

Bacteriophage Adsorption and Receptors

Phage infection is a multistep sequential process consisting of: adsorption to the host cell surface, penetration of the cell and genome entry, synthesis of phage components, virion assembly, lysis of the host cell, and release of progeny phages. The adsorption step is critical for determining the

specificity of the phage for the host cell, which depends on the cell surface receptor, and can be divided into reversible and irreversible steps [222]. Since phages lack specific motility structures, adsorption relies on random collisions with the bacterial cell [223]. The rate of adsorption is therefore affected by the concentration of phages and cells, as well as pH, temperature, ions, and the host cell physiology and culture conditions [224-227]. Many cell surface structures serve as phage receptors, including proteins, such as surface layers or outer membrane porins, LPS, capsule, flagella, and pili [228, 229].

LPS is divided into two types, rough and smooth. Rough LPS consists of a Lipid A membrane anchor and an oligosaccharide core. Smooth LPS additionally has an O-antigen made up of polymeric carbohydrates that is linked to Lipid A by the oligosaccharide core [230]. The use of rough LPS as a receptor would generally allow a broader phage host range because the O-antigen is highly variable and therefore requires higher specificity.

Bacterial capsules are substances, commonly polysaccharides or proteins, released by bacteria that extend from the cell [231]. Some phages bind the bacterial cell capsule in a reversible manner with cell wall components necessary for irreversible binding. The initial binding to the capsule is often associated with enzymatic cleavage of the polysaccharide to reach the cell wall [232-239].

When using flagella as a receptor, head or tail fibers of the phage will often bind the flagellum reversibly, translocate to the cell surface, and then bind irreversibly to a cell surface receptor [107, 240-242]. Alternatively, some phages bind the flagellum at the phage head/tail connection site [243].

Several phages initially adsorb to bacterial pili, with some binding along the entire filament [244-250], and others binding the terminal region of the filament only and reaching the cell surface via pilus retraction [223, 251-255].

Bacteriophage Genome Ejection

Two main mechanisms of double-stranded DNA phage genome ejection have been proposed based on the diameter of the channel through which the genome will be transported into the cell [256]. The osmotic pressure within growing bacterial cells must exceed the osmotic pressure of the environment in order for the cells to grow [257], and the osmotic pressure of the cytoplasm is further exceeded by the internal pressure of a phage capsid, which is particularly high due to the dehydrated state of the packaged DNA [258]. When the diameter of the channel through which the phage genome enters the cell exceeds the diameter of the double-stranded DNA helix, the difference in osmotic pressure between the cell and the environment leads to an influx of water through the capsid, aiding in phage genome ejection into the cell [259-261]. This is not possible, however, when the channel is only large enough to allow the passage of the double-stranded DNA. Enzymes would then be used to catalyze the transfer of the genome into the cell, as is the case for phages such as T7 and N4 [262-265]. Other phages use a related process in which the first part of the genome is ejected by the internal pressure of the phage capsid, and then early proteins are synthesized and used to pull the rest of the genome [266-269].

Bacteriophage Therapy

Therapeutic treatment of humans using phages was first attempted soon after the discovery of phages. Although the results were promising, inconsistency and inadequate controls were criticized and interest waned as antibiotics became more widespread [270, 271]. In recent years, the

development of multi-drug resistance in many bacterial pathogens has led to renewed interest in phage therapy [272].

There are several advantages of phage therapy over the use of antibiotics. The isolation of phages is generally simple, quick, and relatively inexpensive and bacterial resistance to phages develops much more slowly than antibiotic resistance [273]. Phages maintain infectivity even in harsh environments and continue replicating until their host population has significantly decreased [274]. Most phages are highly specific, so they do not infect eukaryotic cells and could be chosen not to infect the human microbiota [273].

Phage therapy also poses significant challenges. Intracellular pathogens are likely inaccessible and although phages don't infect eukaryotic cells, the immune system may recognize them as foreign antigens and produce neutralizing antibodies [272]. Phages are also capable of acquiring genetic material via horizontal gene transfer [275], which could allow the transduction of virulence or antibiotic resistance genes to the bacterial host [276]. This could be avoided by selecting phages that are unable to package bacterial DNA [277], but it could also be exploited to transfer lethal or antibiotic susceptibility genes [278]. Another concern is the development of bacterial resistance to the phage through CRISPR-Cas systems or altered receptors [279]. One method to combat the development of resistance is to use phage cocktails composed of multiple phages [280].

Despite these challenges, the use of phages as a therapeutic, or combining phage therapy with antibiotics, shows promise as an alternative to antibiotics alone [281].

VIBRIO CHOLERAE

In Chapter 3, we investigate *Vibrio cholerae* outer membrane vesicles as a defense mechanism against bacteriophage infection. Cholera is a water-borne diarrheal disease that is caused by the Gram-negative bacterium *V. cholerae* [282]. Disease is caused by one of two serogroups of *V. cholerae*, O1 or O139, which are distinguished by the composition and structure of their lipopolysaccharide (LPS) [283-286], and follows a seasonal pattern that corresponds with changes in climate in endemic regions [287-294]. Serotype O1 is further divided into two biotypes, classical and El Tor, by physiological characteristics such as antibiotic resistance and hemolysin activity [295], which also differ in severity of disease [296]. There have been seven recorded cholera pandemics with O1 El Tor dominating the current pandemic [283, 297] along with periodic emergence of O139 [298]. It is transmitted by the fecal-oral route and colonizes the small bowel after ingestion, where its virulence factors are induced [299-301]. Several factors have been identified as important for colonization, including LPS [302, 303], outer membrane porins [304], toxin-coregulated pili (TCP) [305, 306], and flagella [307].

V. cholerae Virulence Factors

The main virulence factors are cholera toxin (CT), the toxin-coregulated pilus (TCP), and the flagellum. CT is responsible for the profuse rice-water diarrhea [296], which leads to severe dehydration and death within hours if left untreated [308]. CT is composed of one A and five B subunits, which are encoded on an operon of the prophage form of the filamentous CTXϕ [309]. The subunits are synthesized in the cytosol and translocated to the periplasm via the Sec pathway. Here they are folded to form CT, which crosses the outer membrane (OM) via a type two secretion system [310]. The B subunit binds intestinal epithelial cell receptors and CT enters the host cell by endocytosis [311]. The TCP is a type IV pilus that functions in adherence and is required for

colonization [300, 306, 312]. It is encoded by a large cluster of genes known as the *V. cholerae* pathogenicity island [313]. *V. cholerae* cells assemble a single polar, sheathed flagellum that is driven by the sodium motive force [314] and motility has been linked to regulation of virulence gene expression [315-319].

V. cholerae Outer Membrane Vesicles

Outer membrane vesicles (OMVs), which are released from the OM of many Gram-negative bacteria [320-327], including *V. cholerae* [328, 329], have been shown to transport virulence factors, adhere to and enter into host cells, and modulate immune responses [330, 331]. OMVs generally reflect the composition of the OM from which they are derived, although some proteins may be enriched or excluded, suggesting specificity in sorting [320, 332-334]. CT, cytolysin, and the protease PrtV have all associate with and are delivered by *V. cholerae* OMVs to host cells [335-337]. Immunization with *V. cholerae* OMVs has been shown to provide protection in mice [338], implicating OMVs as a potential vaccine candidate. The OMVs can also be loaded with foreign proteins that are secreted into the cytoplasm, so they could potentially be used to deliver antigens [339-341].

CAULOBACTER CRESCENTUS

Chapters 4 and 5 describe the interactions between the bacteriophage ϕCbK with *Caulobacter crescentus* pili and flagella. *C. crescentus* is a non-pathogenic, Gram-negative oligotrophic bacterium that lives in aquatic environments [342]. It divides asymmetrically after a progression of morphological changes, producing a stalked cell and a swarmer cell [343]. The sessile stalked cell inherits a polar stalk with an adhesive holdfast at the tip [342]. It remains anchored after cell division and is replication competent [344]. The motile, quiescent swarmer cell inherits a single polar flagellum and

expresses polar pili [250, 345-347]. Swarmer cells can only enter S phase after transitioning to stalked cells [344]. At this transition, the flagellum is released and the pili are lost [345-347]. These morphological changes require precise spatial and temporal control, coordinated by three core transcriptional regulators, CtrA, DnaA, and GcrA [348-351].

TYPE IV PILI

Type IV pili (T4P) are surface appendages that are often important for bacterial pathogens to cause disease [352]. T4P form filaments of oligomerized pilin subunits up to several micrometers long. They play roles in adherence to surfaces and host cells, biofilm formation, bacteriophage and DNA uptake, and twitching motility [353, 354]. T4P were initially classified based on their major pilin and gene organization into two subgroups, T4aP and T4bP [355]. Recent phylogenetic analysis has revealed a distinct T4cP subgroup that had previously been included in the T4bP. The T4cP are more similar to the type IV secretion system and archaellum than to T4aP or T4bP. While T4aP and some T4bP have retraction ATPases, most of the T4bP and the T4cP do not, although they have been shown to be capable of retraction [356].

Type IV Pilus Assembly and Structure

Precursor pilins are inserted into the inner membrane by the Sec machinery and are processed by a prepilin peptidase [357, 358]. Mature pilins are taken from the inner membrane and incorporated into the base of an assembling pilus. An outer membrane secretin forms a pore through which the pilus filament can extend and retract [359-361] and an inner membrane platform associates with cytoplasmic ATPases for assembly and disassembly [362, 363]. Structures of the pilus assembly machinery of two T4aP systems have been solved at low resolution using cryo-electron tomography

and sub-tomogram averaging [364, 365]. Structural information about the T4bP and T4cP is currently lacking.

C. crescentus Pili

C. crescentus swarmer cells express type IV pili at the flagellated swarmer pole. Pili are assembled later than flagella and are lost at the swarmer to stalked cell transition [345, 346]. Transcription of *pilA*, the gene encoding the pilin that composes the pilus filament, is regulated by CtrA, linking pilus biogenesis to the cell cycle [250]. Six adjacent genes required for pilus biogenesis, *cpaA-F*, were identified by Skerker *et al.* using resistance to the pilus specific phage ϕCbK as a genetic tool [250]. *cpaA* encodes a prepilin peptidase; *cpaB*, *cpaC*, and *cpaD* encode the outer membrane pilus secretion channel; and *cpaE* and *cpaF* encode pilus assembly ATPases [250, 366]. Eight additional genes encoding pilus secretion components were identified by Christen *et al.*, by examining genes conferring susceptibility to ϕCbK using Tn-Seq [366].

BACTERIAL FLAGELLA

Bacterial flagella are large macromolecular machines used for motility by many bacteria [367]. This includes both swimming in liquid environments and swarming across solid surfaces. Flagella also play roles in adhesion [368-370], biofilm formation [371, 372], and sensing of environmental conditions [373]. The flagellum is composed of three main structures: the basal body, hook, and filament [374]. The basal body at the base of the flagellum is a motor driven by the proton motive force, or sodium motive force in some bacteria. It consists of a rotor that is connected to the hook and filament and a non-rotating stator within the bacterial membrane that converts the energy required to power rotation. The hook serves as a universal joint connecting the basal body to the filament, which acts as the propeller [375].

The basal body in Gram-negative bacteria consists of five oligomeric rings (C, cytoplasmic, M-S, cytoplasmic membrane, P, peptidoglycan, and L, outer membrane) connected by a rod [367]. The rotor extends into the cytoplasm of the cell forming the C-ring, which includes switch proteins that allow rotation to be immediately reversed in response to the environment [375]. The stator is composed of two proteins, MotA and MotB, which form a proton or sodium ion channel. The flow of ions generates the proton motive force or sodium motive force and determines the speed of flagellar rotation.

The filament is a hollow tube formed by up to 30,000 subunits of flagellin [376]. Unfolded flagellins are transported through the lumen of the filament for assembly at the distal end with the length of the filament likely determined by diffusion of the flagellin subunits [377]. The flagellin subunit generally consists of four domains: D0-D3. D0 and D1 form the core of the filament, while D2 and D3 are surface exposed. The flagellar filament is made up of a number of protofilaments formed by flagellin subunits. The protofilaments can be in left-handed (L) or right-handed (R) states. Because the L-form protofilament has a slightly larger subunit spacing, a mix of L and R-state protofilaments leads to curvature of the flagellar filament, allowing it to generate thrust upon rotation.

Multi-flagellin Flagella

Almost half of the annotated flagellar systems encode for multiple flagellins, ranging from two to fifteen [378]. *Salmonella enterica* serovar Typhimurium expresses two phase variable flagellins with only one present in the flagellum at a time [379, 380]. Other bacteria, such as *Bdellovibrio bacteriovorus [381], Caulobacter crescentus [382], Helicobacter pylori [383], Sinorhizobium melioloti, and Vibrio* spp. [384], use all encoded flagellins simultaneously. The genes for each species encode flagellins with molecular weights within a few kilodaltons of each other and there is always a level of redundancy [378].

C. crescentus Flagella

Flagellum biogenesis is described in terms of hierarchical classes of genes. In *C. crescentus*, this hierarchy consists of four classes: class I (early genes), CtrA and the sigma factor RpoD (σ^{73}); class II (middle genes), the earliest flagellar genes and the transcription factors RpoN (σ^{54}) and FlbD; class III (late genes), late flagellar genes; and class IV, the flagellins [385]. The genes must be expressed in order, with expression depending on transcription factors produced by the previous class and checkpoints ensuring assembly of the proper components [386-391]. In *C. crescentus*, class III gene expression requires the completion of the MS ring-switch assembly and expression of class IV flagellin genes requires completion of the basal body-hook structure [392, 393]. Class IV flagellin genes are also subject to post-transcriptional regulation .

The *C. crescentus* flagellum is composed of six flagellins, FljJ (29 kDa), FljK (25 kDa), FljL (27 kDa), FljM (25 kDa), FljN (25 kDa), and FljO (25 kDa) [382], with the flagellins genes found in two clusters, α and β [382]. The α-cluster genes are *fljJ*, *fljK*, and *fljL* and their transcription depends on the flagellar-dependent activation of σ^{54} [348]. The β-cluster genes are *fljM*, *fljN*, and *fljO* and their transcription is under CtrA and σ^{73} control. The expression of the β-flagellin genes therefore does not rely on the flagellar hierarchy [378].

Some structural aspects of the *C. crescentus* flagellar filament have been studied and suggest structural requirements for multiple flagellins. FljJ has been shown to form the first 60 nm of the flagellar filament, FljL forms the next 1-2 μm with increasing amounts of the 25 kDa flagellins incorporated at the distal end, and the rest of the filament is composed of the 25 kDa flagellins alone [394]. No single flagellin is required for filament formation and mutants expressing single flagellins are all

capable of forming flagella except for FljJ alone [378, 395]. Deletion of one or more flagellins often leads to reductions in filament length and swimming speed [378].

CONCLUSIONS

The following chapters will describe the use of cryo-electron microscopy techniques to investigate the interactions between various viruses and their hosts. Chapter 2 examines the assembly of respiratory syncytial virus and HIV-1 from mammalian cells using CLEM. The use of *Vibrio cholerae* OMVs as a decoy for phage infection is described in Chapter 3. The interactions between the bacteriophage ϕCbK and *C. crescentus* pili are investigated in Chapter 4. Additionally, Chapter 5 covers the role of multiple flagellins in *C. crescentus* in the context of ϕCbK adsorption and flagellar structure. Finally, the contributions and future directions of this work and the outlook for cryo-EM as a tool to study host-microbe interactions are discussed.

REFERENCES

1. Taylor, K. A. and Glaeser, R. M. Electron diffraction of frozen, hydrated protein crystals. *Science*, 1974. **186**(4168): p. 1036-7.
2. Dubochet, J., McDowall, A. W., Menge, B., Schmid, E. N., and Lickfeld, K. G. Electron microscopy of frozen-hydrated bacteria. *J Bacteriol*, 1983. **155**(1): p. 381-390.
3. McDowall, A. W., Chang, J. J., Freeman, R., Lepault, J., Walter, C. A., and Dubochet, J. Electron microscopy of frozen hydrated sections of vitreous ice and vitrified biological samples. *J Microsc*, 1983. **131**(Pt 1): p. 1-9.
4. Lepault, J., Booy, F. P., and Dubochet, J. Electron microscopy of frozen biological suspensions. *J Microsc*, 1983. **129**(Pt 1): p. 89-102.
5. Adrian, M., Dubochet, J., Lepault, J., and McDowall, A. W. Cryo-electron microscopy of viruses. *Nature*, 1984. **308**(5954): p. 32-36.
6. Dubochet, J., Adrian, M., Chang, J. J., Homo, J. C., Lepault, J., McDowall, A. W., and Schultz, P. Cryo-electron microscopy of vitrified specimens. *Q Rev Biophys*, 1988. **21**(2): p. 129-228.
7. Kuhlbrandt, W. Biochemistry. The resolution revolution. *Science*, 2014. **343**(6178): p. 1443-4.
8. Hewat, E. A. and Neumann, E. Characterization of the performance of a 200-kV field emission gun for cryo-electron microscopy of biological molecules. *J Struct Biol*, 2002. **139**(1): p. 60-4.
9. Stagg, S. M., Lander, G. C., Pulokas, J., Fellmann, D., Cheng, A., Quispe, J. D., Mallick, S. P., Avila, R. M., Carragher, B., and Potter, C. S. Automated cryoEM data acquisition and analysis of 284742 particles of GroEL. *J Struct Biol*, 2006. **155**(3): p. 470-81.
10. Cheng, Y., Grigorieff, N., Penczek, P. A., and Walz, T. A primer to single-particle cryo-electron microscopy. *Cell*, 2015. **161**(3): p. 438-449.

11. Nogales, E. The development of cryo-EM into a mainstream structural biology technique. *Nat Methods*, 2015. **13**: p. 24.

12. Bai, X.-c., McMullan, G., and Scheres, S. H. W. How cryo-EM is revolutionizing structural biology. *Trends Biochem Sci*, 2015. **40**(1): p. 49-57.

13. Binshtein, E. and Ohi, M. D. Cryo-electron microscopy and the amazing race to atomic resolution. *Biochemistry*, 2015. **54**(20): p. 3133-41.

14. Fernandez-Leiro, R. and Scheres, S. H. W. Unravelling biological macromolecules with cryo-electron microscopy. *Nature*, 2016. **537**: p. 339.

15. Frank, J. Advances in the field of single-particle cryo-electron microscopy over the last decade. *Nat Protoc*, 2017. **12**: p. 209.

16. Murata, K. and Wolf, M. Cryo-electron microscopy for structural analysis of dynamic biological macromolecules. *Biochim Biophys Acta, Gen Subj*, 2018. **1862**(2): p. 324-334.

17. Brilot, A. F., Chen, J. Z., Cheng, A., Pan, J., Harrison, S. C., Potter, C. S., Carragher, B., Henderson, R., and Grigorieff, N. Beam-induced motion of vitrified specimen on holey carbon film. *J Struct Biol*, 2012. **177**(3): p. 630-637.

18. Glaeser, R. M., McMullan, G., Faruqi, A. R., and Henderson, R. Images of paraffin monolayer crystals with perfect contrast: Minimization of beam-induced specimen motion. *Ultramicroscopy*, 2011. **111**(2): p. 90-100.

19. Russo, C. J. and Passmore, L. A. Ultrastable gold substrates: Properties of a support for high-resolution electron cryomicroscopy of biological specimens. *J Struct Biol*, 2016. **193**(1): p. 33-44.

20. Guo, F. and Jiang, W. Single particle cryo-electron microscopy and 3-D reconstruction of viruses. *Methods Mol Biol*, 2014. **1117**: p. 401-443.

21. Doerr, A. Single-particle cryo-electron microscopy. *Nat Methods*, 2015. **13**: p. 23.

22. Kastner, B., Fischer, N., Golas, M. M., Sander, B., Dube, P., Boehringer, D., Hartmuth, K., Deckert, J., Hauer, F., Wolf, E., Uchtenhagen, H., Urlaub, H., Herzog, F., Peters, J. M., Poerschke, D., Luhrmann, R., and Stark, H. GraFix: Sample preparation for single-particle electron cryomicroscopy. *Nat Methods*, 2008. **5**(1): p. 53-5.

23. Stark, H. Grafix: Stabilization of fragile macromolecular complexes for single particle cryo-EM. *Methods Enzymol*, 2010. **481**: p. 109-26.

24. Thompson, R. F., Walker, M., Siebert, C. A., Muench, S. P., and Ranson, N. A. An introduction to sample preparation and imaging by cryo-electron microscopy for structural biology. *Methods*, 2016. **100**: p. 3-15.

25. Meyerson, J. R., Rao, P., Kumar, J., Chittori, S., Banerjee, S., Pierson, J., Mayer, M. L., and Subramaniam, S. Self-assembled monolayers improve protein distribution on holey carbon cryo-EM supports. *Sci Rep*, 2014. **4**: p. 7084.

26. Chowdhury, S., Ketcham, S. A., Schroer, T. A., and Lander, G. C. Structural organization of the dynein-dynactin complex bound to microtubules. *Nat Struct Mol Biol*, 2015. **22**(4): p. 345-347.

27. Zhang, J., Ma, B., DiMaio, F., Douglas, N. R., Joachimiak, L. A., Baker, D., Frydman, J., Levitt, M., and Chiu, W. Cryo-EM structure of a group II chaperonin in the prehydrolysis ATP-bound state leading to lid closure. *Structure*, 2011. **19**(5): p. 633-639.

28. Lyumkis, D., Julien, J. P., de Val, N., Cupo, A., Potter, C. S., Klasse, P. J., Burton, D. R., Sanders, R. W., Moore, J. P., Carragher, B., Wilson, I. A., and Ward, A. B. Cryo-EM structure of a fully glycosylated soluble cleaved HIV-1 envelope trimer. *Science*, 2013. **342**(6165): p. 1484-90.

29. Tan, Y. Z., Baldwin, P. R., Davis, J. H., Williamson, J. R., Potter, C. S., Carragher, B., and Lyumkis, D. Addressing preferred specimen orientation in single-particle cryo-EM through tilting. *Nat Methods*, 2017. **14**(8): p. 793-796.

30. Linke, D. Detergents: An overview. *Methods Enzymol*, 2009. **463**: p. 603-17.

31. Baker, M. R., Fan, G., and Serysheva, I. I. Single-particle cryo-EM of the ryanodine receptor channel in an aqueous environment. *Eur J Transl Myol*, 2015. **25**(1): p. 35-48.

32. Efremov, R. G., Gatsogiannis, C., and Raunser, S., Chapter One - Lipid nanodiscs as a tool for high-resolution structure determination of membrane proteins by single-particle cryo-EM, in *Methods Enzymol*, C. Ziegler, Editor. 2017, Academic Press. p. 1-30.

33. Flötenmeyer, M., Weiss, H., Tribet, C., Popot, J.-L., and Leonard, K. The use of amphipathic polymers for cryo electron microscopy of NADH:ubiquinone oxidoreductase (Complex I). *J Microsc*, 2007. **227**(3): p. 229-235.

34. Althoff, T., Mills, D. J., Popot, J.-L., and Kühlbrandt, W. Arrangement of electron transport chain components in bovine mitochondrial supercomplex $I_1III_2IV_1$. *EMBO J*, 2011. **30**(22): p. 4652-4664.

35. Cvetkov, T. L., Huynh, K. W., Cohen, M. R., and Moiseenkova-Bell, V. Y. Molecular architecture and subunit organization of TRPA1 ion channel revealed by electron microscopy. *J Biol Chem*, 2011. **286**(44): p. 38168-38176.

36. Cao, E., Liao, M., Cheng, Y., and Julius, D. TRPV1 structures in distinct conformations reveal mechanisms of activation. *Nature*, 2013. **504**(7478): p. 113-118.

37. Liao, M., Cao, E., Julius, D., and Cheng, Y. Structure of the TRPV1 ion channel determined by electron cryo-microscopy. *Nature*, 2013. **504**(7478): p. 107-12.

38. Lu, P., Bai, X. C., Ma, D., Xie, T., Yan, C., Sun, L., Yang, G., Zhao, Y., Zhou, R., Scheres, S. H., and Shi, Y. Three-dimensional structure of human gamma-secretase. *Nature*, 2014. **512**(7513): p. 166-70.

39. Wilkes, M., Madej, M. G., Kreuter, L., Rhinow, D., Heinz, V., De Sanctis, S., Ruppel, S., Richter, R. M., Joos, F., Grieben, M., Pike, A. C. W., Huiskonen, J. T., Carpenter, E. P., Kühlbrandt, W., Witzgall, R., and Ziegler, C. Molecular insights into lipid-assisted Ca^{2+} regulation of the TRP channel Polycystin-2. *Nat Struct Mol Biol*, 2017. **24**: p. 123.

40. Frauenfeld, J., Gumbart, J., van der Sluis, E. O., Funes, S., Gartmann, M., Beatrix, B., Mielke, T., Berninghausen, O., Becker, T., Schulten, K., and Beckmann, R. Cryo-EM structure of the ribosome–secye complex in the membrane environment. *Nat Struct Mol Biol*, 2011. **18**(5): p. 614-621.

41. Efremov, R. G., Leitner, A., Aebersold, R., and Raunser, S. Architecture and conformational switch mechanism of the ryanodine receptor. *Nature*, 2015. **517**: p. 39.

42. Gao, Y., Cao, E., Julius, D., and Cheng, Y. TRPV1 structures in nanodiscs reveal mechanisms of ligand and lipid action. *Nature*, 2016. **534**: p. 347.

43. Frauenfeld, J., Löving, R., Armache, J.-P., Sonnen, A., Guettou, F., Moberg, P., Zhu, L., Jegerschöld, C., Flayhan, A., Briggs, J. A. G., Garoff, H., Löw, C., Cheng, Y., and Nordlund, P. A novel lipoprotein nanoparticle system for membrane proteins. *Nat Methods*, 2016. **13**(4): p. 345-351.

44. Gatsogiannis, C., Merino, F., Prumbaum, D., Roderer, D., Leidreiter, F., Meusch, D., and Raunser, S. Membrane insertion of a Tc toxin in near-atomic detail. *Nat Struct Mol Biol*, 2016. **23**: p. 884.

45. Shen, P. S., Yang, X., DeCaen, P. G., Liu, X., Bulkley, D., Clapham, D. E., and Cao, E. The structure of the polycystic kidney disease channel PKD2 in lipid nanodiscs. *Cell*, 2016. **167**(3): p. 763-773.e11.

46. Matthies, D., Dalmas, O., Borgnia, M. J., Dominik, P. K., Merk, A., Rao, P., Reddy, B. G., Islam, S., Bartesaghi, A., Perozo, E., and Subramaniam, S. Cryo-EM structures of the magnesium channel cora reveal symmetry break upon gating. *Cell*, 2016. **164**(4): p. 747-756.

47. Jin, P., Bulkley, D., Guo, Y., Zhang, W., Guo, Z., Huynh, W., Wu, S., Meltzer, S., Cheng, T., Jan, L. Y., Jan, Y.-N., and Cheng, Y. Cryo-EM structure of the mechanotransduction channel NOMPC. *Nature*, 2017. **547**(7661): p. 118-122.

48. Kelly, D. F., Abeyrathne, P. D., Dukovski, D., and Walz, T. The affinity grid: A pre-fabricated EM grid for monolayer purification. *J Mol Biol*, 2008. **382**(2): p. 423-33.

49. Kiss, G., Chen, X., Brindley, M. A., Campbell, P., Afonso, C. L., Ke, Z., Holl, J. M., Guerrero-Ferreira, R. C., Byrd-Leotis, L. A., Steel, J., Steinhauer, D. A., Plemper, R. K., Kelly, D. F., Spearman, P. W., and Wright, E. R. Capturing enveloped viruses on affinity grids for downstream cryo-electron microscopy applications. *Microsc Microanal*, 2014. **20**(1): p. 164-74.

50. Benjamin, C. J., Wright, K. J., Hyun, S. H., Krynski, K., Yu, G., Bajaj, R., Guo, F., Stauffacher, C. V., Jiang, W., and Thompson, D. H. Nonfouling NTA-PEG-based TEM grid coatings for selective capture of histidine-tagged protein targets from cell lysates. *Langmuir*, 2016. **32**(2): p. 551-9.

51. Llaguno, M. C., Xu, H., Shi, L., Huang, N., Zhang, H., Liu, Q., and Jiang, Q. X. Chemically functionalized carbon films for single molecule imaging. *J Struct Biol*, 2014. **185**(3): p. 405-17.

52. Yu, G., Vago, F., Zhang, D., Snyder, J. E., Yan, R., Zhang, C., Benjamin, C., Jiang, X., Kuhn, R. J., Serwer, P., Thompson, D. H., and Jiang, W. Single-step antibody-based affinity cryo-

electron microscopy for imaging and structural analysis of macromolecular assemblies. *J Struct Biol*, 2014. **187**(1): p. 1-9.

53. Yu, G., Li, K., and Jiang, W. Antibody-based affinity cryo-EM grid. *Methods*, 2016. **100**: p. 16-24.

54. Tanner, J. R. D., A.C.; Dukes, M.J.; Melanson, L.A.; McDonald, S.M.; Kelly, D.F. Cryo-SiN - an alternative substrate to visualize active viral assemblies. *J Analyt Molecul Tech*, 2013. **1**(1): p. 6.

55. Yu, G., Li, K., Huang, P., Jiang, X., and Jiang, W. Antibody-based affinity cryoelectron microscopy at 2.6-Å resolution. *Structure*, 2016. **24**(11): p. 1984-1990.

56. Booy, F. P. and Pawley, J. B. Cryo-crinkling: What happens to carbon films on copper grids at low temperature. *Ultramicroscopy*, 1993. **48**(3): p. 273-80.

57. Rhinow, D. and Kuhlbrandt, W. Electron cryo-microscopy of biological specimens on conductive titanium-silicon metal glass films. *Ultramicroscopy*, 2008. **108**(7): p. 698-705.

58. Yoshioka, C., Carragher, B., and Potter, C. S. Cryomesh: A new substrate for cryo-electron microscopy. *Microsc Microanal*, 2010. **16**(1): p. 43-53.

59. Russo, C. J. and Passmore, L. A. Controlling protein adsorption on graphene for cryo-EM using low-energy hydrogen plasmas. *Nat Methods*, 2014. **11**(6): p. 649-52.

60. Russo, C. J. and Passmore, L. A. Electron microscopy: Ultrastable gold substrates for electron cryomicroscopy. *Science*, 2014. **346**(6215): p. 1377-80.

61. Russo, C. J. and Passmore, L. A. Progress towards an optimal specimen support for electron cryomicroscopy. *Curr Opin Struct Biol*, 2016. **37**: p. 81-9.

62. Martin, T. G., Bharat, T. A., Joerger, A. C., Bai, X. C., Praetorius, F., Fersht, A. R., Dietz, H., and Scheres, S. H. Design of a molecular support for cryo-EM structure determination. *Proc Natl Acad Sci U S A*, 2016. **113**(47): p. E7456-e7463.

63. Coscia, F., Estrozi, L. F., Hans, F., Malet, H., Noirclerc-Savoye, M., Schoehn, G., and Petosa, C. Fusion to a homo-oligomeric scaffold allows cryo-EM analysis of a small protein. *Sci Rep*, 2016. **6**: p. 30909.

64. Liu, Y., Gonen, S., Gonen, T., and Yeates, T. Near-atomic cryo-EM imaging of a small protein displayed on a designed scaffolding system. *bioRxiv*, 2017.

65. Glaeser, R. M., Han, B. G., Csencsits, R., Killilea, A., Pulk, A., and Cate, J. H. Factors that influence the formation and stability of thin, cryo-EM specimens. *Biophys J*, 2016. **110**(4): p. 749-55.

66. Razinkov, I., Dandey, V., Wei, H., Zhang, Z., Melnekoff, D., Rice, W. J., Wigge, C., Potter, C. S., and Carragher, B. A new method for vitrifying samples for cryoEM. *J Struct Biol*, 2016. **195**(2): p. 190-198.

67. Wei, H., Dandey, V. P., Zhang, Z., Raczkowski, A., Rice, W. J., Carragher, B., and Potter, C. S. Optimizing "self-wicking" nanowire grids. *J Struct Biol*, 2018.

68. Jain, T., Sheehan, P., Crum, J., Carragher, B., and Potter, C. S. Spotiton: A prototype for an integrated inkjet dispense and vitrification system for cryo-TEM. *J Struct Biol*, 2012. **179**(1): p. 68-75.

69. Dandey, V. P., Wei, H., Zhang, Z., Tan, Y. Z., Acharya, P., Eng, E. T., Rice, W. J., Kahn, P. A., Potter, C. S., and Carragher, B. Spotiton: New features and applications. *J Struct Biol*, 2018.

70. Arnold, S. A., Albiez, S., Bieri, A., Syntychaki, A., Adaixo, R., McLeod, R. A., Goldie, K. N., Stahlberg, H., and Braun, T. Blotting-free and lossless cryo-electron microscopy grid preparation from nanoliter-sized protein samples and single-cell extracts. *J Struct Biol*, 2017. **197**(3): p. 220-226.

71. Berriman, J. A. and Rosenthal, P. B. Paraxial charge compensator for electron cryomicroscopy. *Ultramicroscopy*, 2012. **116**: p. 106-14.

72. Berriman, J. and Unwin, N. Analysis of transient structures by cryo-microscopy combined with rapid mixing of spray droplets. *Ultramicroscopy*, 1994. **56**(4): p. 241-52.

73. Unwin, N. and Fujiyoshi, Y. Gating movement of acetylcholine receptor caught by plunge-freezing. *J Mol Biol*, 2012. **422**(5): p. 617-34.

74. Unwin, N. Acetylcholine receptor channel imaged in the open state. *Nature*, 1995. **373**(6509): p. 37-43.

75. Walker, M., Zhang, X.-Z., Jiang, W., Trinick, J., and White, H. D. Observation of transient disorder during myosin subfragment-1 binding to actin by stopped-flow fluorescence and millisecond time resolution electron cryomicroscopy: Evidence that the start of the crossbridge power stroke in muscle has variable geometry. *Proc Natl Acad Sci U S A*, 1999. **96**(2): p. 465-470.

76. Walker, M., Trinick, J., and White, H. Millisecond time resolution electron cryo-microscopy of the M-ATP transient kinetic state of the acto-myosin atpase. *Biophys J*, 1995. **68**(4 Suppl): p. 87S-91S.

77. Shaikh, T. R., Yassin, A. S., Lu, Z., Barnard, D., Meng, X., Lu, T. M., Wagenknecht, T., and Agrawal, R. K. Initial bridges between two ribosomal subunits are formed within 9.4 milliseconds, as studied by time-resolved cryo-EM. *Proc Natl Acad Sci U S A*, 2014. **111**(27): p. 9822-7.

78. Lu, Z., Shaikh, T. R., Barnard, D., Meng, X., Mohamed, H., Yassin, A., Mannella, C. A., Agrawal, R. K., Lu, T. M., and Wagenknecht, T. Monolithic microfluidic mixing-spraying devices for time-resolved cryo-electron microscopy. *J Struct Biol*, 2009. **168**(3): p. 388-95.

79. Lu, Z., Barnard, D., Shaikh, T. R., Meng, X., Mannella, C. A., Yassin, A., Agrawal, R., Wagenknecht, T., and Lu, T. M. Gas-assisted annular microsprayer for sample preparation for time-resolved cryo-electron microscopy. *J Micromech Microeng*, 2014. **24**(11): p. 115001.

80. Feng, X., Fu, Z., Kaledhonkar, S., Jia, Y., Shah, B., Jin, A., Liu, Z., Sun, M., Chen, B., Grassucci, R. A., Ren, Y., Jiang, H., Frank, J., and Lin, Q. A fast and effective microfluidic spraying-plunging method for high-resolution single-particle cryo-EM. *Structure*, 2017. **25**(4): p. 663-670.e3.

81. McMullan, G., Faruqi, A. R., and Henderson, R. Direct electron detectors. *Methods Enzymol*, 2016. **579**: p. 1-17.

82. McMullan, G., Chen, S., Henderson, R., and Faruqi, A. R. Detective quantum efficiency of electron area detectors in electron microscopy. *Ultramicroscopy*, 2009. **109**(9): p. 1126-43.

83. Faruqi, A. R. and Henderson, R. Electronic detectors for electron microscopy. *Curr Opin Struct Biol*, 2007. **17**(5): p. 549-55.

84. Faruqi, A. R. Design principles and applications of a cooled CCD camera for electron microscopy. *Adv Exp Med Biol*, 1998. **453**: p. 63-72.

85. Sander, B., Golas, M. M., and Stark, H. Advantages of CCD detectors for de novo three-dimensional structure determination in single-particle electron microscopy. *J Struct Biol*, 2005. **151**(1): p. 92-105.

86. McMullan, G., Faruqi, A. R., Henderson, R., Guerrini, N., Turchetta, R., Jacobs, A., and van Hoften, G. Experimental observation of the improvement in MTF from backthinning a cmos direct electron detector. *Ultramicroscopy*, 2009. **109**(9-3): p. 1144-1147.

87. Li, X., Zheng, S. Q., Egami, K., Agard, D. A., and Cheng, Y. Influence of electron dose rate on electron counting images recorded with the K2 camera. *J Struct Biol*, 2013. **184**(2): p. 251-60.

88. Li, X., Mooney, P., Zheng, S., Booth, C. R., Braunfeld, M. B., Gubbens, S., Agard, D. A., and Cheng, Y. Electron counting and beam-induced motion correction enable near-atomic-resolution single-particle cryo-EM. *Nat Methods*, 2013. **10**(6): p. 584-90.

89. Chiu, P.-L., Li, X., Li, Z., Beckett, B., Brilot, A. F., Grigorieff, N., Agard, D. A., Cheng, Y., and Walz, T. Evaluation of super-resolution performance of the K2 electron-counting camera using 2D crystals of aquaporin-0. *J Struct Biol*, 2015. **192**(2): p. 163-173.

90. McMullan, G., Faruqi, A. R., Clare, D., and Henderson, R. Comparison of optimal performance at 300keV of three direct electron detectors for use in low dose electron microscopy. *Ultramicroscopy*, 2014. **147**: p. 156-63.

91. Voorhees, R. M., Fernandez, I. S., Scheres, S. H., and Hegde, R. S. Structure of the mammalian ribosome-Sec61 complex to 3.4 Å resolution. *Cell*, 2014. **157**(7): p. 1632-43.

92. Hesketh, E. L., Meshcheriakova, Y., Dent, K. C., Saxena, P., Thompson, R. F., Cockburn, J. J., Lomonossoff, G. P., and Ranson, N. A. Mechanisms of assembly and genome packaging in an RNA virus revealed by high-resolution cryo-EM. *Nat Commun*, 2015. **6**: p. 10113.

93. Parent, K. N., Tang, J., Cardone, G., Gilcrease, E. B., Janssen, M. E., Olson, N. H., Casjens, S. R., and Baker, T. S. Three-dimensional reconstructions of the bacteriophage CUS-3 virion reveal a conserved coat protein I-domain but a distinct tailspike receptor-binding domain. *Virology*, 2014. **464-465**: p. 55-66.

94. von der Ecken, J., Muller, M., Lehman, W., Manstein, D. J., Penczek, P. A., and Raunser, S. Structure of the F-actin-tropomyosin complex. *Nature*, 2015. **519**(7541): p. 114-7.

95. Bartesaghi, A., Merk, A., Banerjee, S., Matthies, D., Wu, X., Milne, J. L., and Subramaniam, S. 2.2 Å resolution cryo-EM structure of beta-galactosidase in complex with a cell-permeant inhibitor. *Science*, 2015. **348**(6239): p. 1147-51.

96. Merk, A., Bartesaghi, A., Banerjee, S., Falconieri, V., Rao, P., Davis, M. I., Pragani, R., Boxer, M. B., Earl, L. A., Milne, J. L. S., and Subramaniam, S. Breaking cryo-EM resolution barriers to facilitate drug discovery. *Cell*, 2016. **165**(7): p. 1698-1707.

97. Langmore, J. P. and Smith, M. F. Quantitative energy-filtered electron microscopy of biological molecules in ice. *Ultramicroscopy*, 1992. **46**(1-4): p. 349-73.

98. Schroder, R. R. Zero-loss energy-filtered imaging of frozen-hydrated proteins: Model calculations and implications for future developments. *J Microsc*, 1992. **166**(Pt 3): p. 389-400.

99. Danev, R. and Nagayama, K. Single particle analysis based on Zernike phase contrast transmission electron microscopy. *J Struct Biol*, 2008. **161**(2): p. 211-8.

100. Murata, K., Liu, X., Danev, R., Jakana, J., Schmid, M. F., King, J., Nagayama, K., and Chiu, W. Zernike phase contrast cryo-electron microscopy and tomography for structure determination at nanometer and subnanometer resolutions. *Structure*, 2010. **18**(8): p. 903-12.

101. Schroder, R. R. Advances in electron microscopy: A qualitative view of instrumentation development for macromolecular imaging and tomography. *Arch Biochem Biophys*, 2015. **581**: p. 25-38.

102. Nagayama, K. and Danev, R. Phase contrast electron microscopy: Development of thin-film phase plates and biological applications. *Philos Trans R Soc B Biol Sci*, 2008. **363**(1500): p. 2153-2162.

103. Nagayama, K., Phase contrast enhancement with phase plates in electron microscopy, in *Adv Imaging Electron Phys*. 2005, Elsevier. p. 69-146.

104. Dai, W., Fu, C., Raytcheva, D., Flanagan, J., Khant, H. A., Liu, X., Rochat, R. H., Haase-Pettingell, C., Piret, J., Ludtke, S. J., Nagayama, K., Schmid, M. F., King, J. A., and Chiu, W. Visualizing virus assembly intermediates inside marine cyanobacteria. *Nature*, 2013. **502**(7473): p. 707-710.

105. Danev, R., Kanamaru, S., Marko, M., and Nagayama, K. Zernike phase contrast cryo-electron tomography. *J Struct Biol*, 2010. **171**(2): p. 174-181.

106. Fukuda, Y. and Nagayama, K. Zernike phase contrast cryo-electron tomography of whole mounted frozen cells. *J Struct Biol*, 2012. **177**(2): p. 484-489.

107. Guerrero-Ferreira, R. C., Viollier, P. H., Ely, B., Poindexter, J. S., Georgieva, M., Jensen, G. J., and Wright, E. R. Alternative mechanism for bacteriophage adsorption to the motile bacterium *Caulobacter crescentus*. *Proc Natl Acad Sci U S A*, 2011. **108**(24): p. 9963.

108. Danev, R. and Nagayama, K. Transmission electron microscopy with Zernike phase plate. *Ultramicroscopy*, 2001. **88**(4): p. 243-52.

109. Danev, R. and Nagayama, K. Optimizing the phase shift and the cut-on periodicity of phase plates for TEM. *Ultramicroscopy*, 2011. **111**(8): p. 1305-15.

110. Nagayama, K. Another 60 years in electron microscopy: Development of phase-plate electron microscopy and biological applications. *J Electron Microsc*, 2011. **60**(Suppl 1): p. S43-S62.

111. Danev, R. and Nagayama, K. Phase plates for transmission electron microscopy. *Methods Enzymol*, 2010. **481**: p. 343-69.

112. Danev, R., Glaeser, R. M., and Nagayama, K. Practical factors affecting the performance of a thin-film phase plate for transmission electron microscopy. *Ultramicroscopy*, 2009. **109**(4): p. 312-325.

113. Fukuda, Y., Fukazawa, Y., Danev, R., Shigemoto, R., and Nagayama, K. Tuning of the Zernike phase-plate for visualization of detailed ultrastructure in complex biological specimens. *J Struct Biol*, 2009. **168**(3): p. 476-484.

114. Danev, R., Buijsse, B., Khoshouei, M., Plitzko, J. M., and Baumeister, W. Volta potential phase plate for in-focus phase contrast transmission electron microscopy. *Proc Natl Acad Sci U S A*, 2014. **111**(44): p. 15635-40.

115. Danev, R. and Baumeister, W. Cryo-EM single particle analysis with the Volta phase plate. *eLife*, 2016. **5**.

116. Khoshouei, M., Radjainia, M., Phillips, A. J., Gerrard, J. A., Mitra, A. K., Plitzko, J. M., Baumeister, W., and Danev, R. Volta phase plate cryo-EM of the small protein complex Prx3. *Nat Commun*, 2016. **7**: p. 10534.

117. Asano, S., Fukuda, Y., Beck, F., Aufderheide, A., Forster, F., Danev, R., and Baumeister, W. Proteasomes. A molecular census of 26S proteasomes in intact neurons. *Science*, 2015. **347**(6220): p. 439-42.

118. Chlanda, P., Mekhedov, E., Waters, H., Schwartz, C. L., Fischer, E. R., Ryham, R. J., Cohen, F. S., Blank, P. S., and Zimmerberg, J. The hemifusion structure induced by influenza virus haemagglutinin is determined by physical properties of the target membranes. *Nat Microbiol*, 2016. **1**(6): p. 16050.

119. Fukuda, Y., Laugks, U., Lucic, V., Baumeister, W., and Danev, R. Electron cryotomography of vitrified cells with a Volta phase plate. *J Struct Biol*, 2015. **190**(2): p. 143-54.

120. Khoshouei, M., Pfeffer, S., Baumeister, W., Forster, F., and Danev, R. Subtomogram analysis using the Volta phase plate. *J Struct Biol*, 2017. **197**(2): p. 94-101.

121. Mahamid, J., Pfeffer, S., Schaffer, M., Villa, E., Danev, R., Cuellar, L. K., Forster, F., Hyman, A. A., Plitzko, J. M., and Baumeister, W. Visualizing the molecular sociology at the HeLa cell nuclear periphery. *Science*, 2016. **351**(6276): p. 969-72.

122. Sharp, T. H., Koster, A. J., and Gros, P. Heterogeneous MAC initiator and pore structures in a lipid bilayer by phase-plate cryo-electron tomography. *Cell Rep*, 2016. **15**(1): p. 1-8.

123. Danev, R. and Baumeister, W. Expanding the boundaries of cryo-EM with phase plates. *Curr Opin Struct Biol*, 2017. **46**: p. 87-94.

124. Chua, E. Y., Vogirala, V. K., Inian, O., Wong, A. S., Nordenskiold, L., Plitzko, J. M., Danev, R., and Sandin, S. 3.9 Å structure of the nucleosome core particle determined by phase-plate cryo-em. *Nucleic Acids Res*, 2016. **44**(17): p. 8013-9.

125. Khoshouei, M., Radjainia, M., Baumeister, W., and Danev, R. Cryo-EM structure of haemoglobin at 3.2 Å determined with the Volta phase plate. *Nat Commun*, 2017. **8**: p. 16099.

126. Rohou, A. and Grigorieff, N. Ctffind4: Fast and accurate defocus estimation from electron micrographs. *J Struct Biol*, 2015. **192**(2): p. 216-21.

127. Danev, R., Tegunov, D., and Baumeister, W. Using the Volta phase plate with defocus for cryo-EM single particle analysis. *eLife*, 2017. **6**.

128. Liang, Y. L., Khoshouei, M., Radjainia, M., Zhang, Y., Glukhova, A., Tarrasch, J., Thal, D. M., Furness, S. G. B., Christopoulos, G., Coudrat, T., Danev, R., Baumeister, W., Miller, L. J., Christopoulos, A., Kobilka, B. K., Wootten, D., Skiniotis, G., and Sexton, P. M. Phase-plate cryo-EM structure of a class B GPCR-G-protein complex. *Nature*, 2017. **546**(7656): p. 118-123.

129. von Loeffelholz, O., Papai, G., Danev, R., Myasnikov, A. G., Natchiar, S. K., Hazemann, I., Menetret, J. F., and Klaholz, B. P. Volta phase plate data collection facilitates image processing and cryo-EM structure determination. *J Struct Biol*, 2018.

130. Briegel, A., Chen, S., Koster, A. J., Plitzko, J. M., Schwartz, C. L., and Jensen, G. J., Chapter Thirteen - Correlated Light and Electron Cryo-microscopy, in *Methods Enzymol*, G.J. Jensen, Editor. 2010, Academic Press. p. 317-341.

131. Agronskaia, A. V., Valentijn, J. A., van Driel, L. F., Schneijdenberg, C. T., Humbel, B. M., van Bergen en Henegouwen, P. M., Verkleij, A. J., Koster, A. J., and Gerritsen, H. C.

Integrated fluorescence and transmission electron microscopy. *J Struct Biol*, 2008. **164**(2): p. 183-9.

132. Sartori, A., Gatz, R., Beck, F., Rigort, A., Baumeister, W., and Plitzko, J. M. Correlative microscopy: Bridging the gap between fluorescence light microscopy and cryo-electron tomography. *J Struct Biol*, 2007. **160**(2): p. 135-45.

133. Schwartz, C. L., Sarbash, V. I., Ataullakhanov, F. I., McIntosh, J. R., and Nicastro, D. Cryo-fluorescence microscopy facilitates correlations between light and cryo-electron microscopy and reduces the rate of photobleaching. *J Microsc*, 2007. **227**(2): p. 98-109.

134. van Driel, L. F., Valentijn, J. A., Valentijn, K. M., Koning, R. I., and Koster, A. J. Tools for correlative cryo-fluorescence microscopy and cryo-electron tomography applied to whole mitochondria in human endothelial cells. *Eur J Cell Biol*, 2009. **88**(11): p. 669-84.

135. Moerner, W. E. and Orrit, M. Illuminating single molecules in condensed matter. *Science*, 1999. **283**(5408): p. 1670-1676.

136. Le Gros, M. A., McDermott, G., Uchida, M., Knoechel, C. G., and Larabell, C. A. High-aperture cryogenic light microscopy. *J Microsc*, 2009. **235**(1): p. 1-8.

137. Rigort, A., Villa, E., Bäuerlein, F. J. B., Engel, B. D., and Plitzko, J. M., Chapter Fourteen - Integrative Approaches for Cellular Cryo-electron Tomography: Correlative Imaging and Focused Ion Beam Micromachining, in *Methods Cell Biol*, T. Müller-Reichert and P. Verkade, Editors. 2012, Academic Press. p. 259-281.

138. Bykov, Y. S., Cortese, M., Briggs, J. A. G., and Bartenschlager, R. Correlative light and electron microscopy methods for the study of virus–cell interactions. *FEBS Lett*, 2016. **590**(13): p. 1877-1895.

139. Schellenberger, P., Kaufmann, R., Siebert, C. A., Hagen, C., Wodrich, H., and Grunewald, K. High-precision correlative fluorescence and electron cryo microscopy using two independent alignment markers. *Ultramicroscopy*, 2014. **143**: p. 41-51.

140. Schorb, M. and Briggs, J. A. Correlated cryo-fluorescence and cryo-electron microscopy with high spatial precision and improved sensitivity. *Ultramicroscopy*, 2014. **143**: p. 24-32.

141. Anderson, K. L., Page, C., Swift, M. F., Hanein, D., and Volkmann, N. Marker-free method for accurate alignment between correlated light, cryo-light, and electron cryo-microscopy data using sample support features. *J Struct Biol*, 2018. **201**(1): p. 46-51.

142. Al-Amoudi, A., Chang, J. J., Leforestier, A., McDowall, A., Salamin, L. M., Norlen, L. P., Richter, K., Blanc, N. S., Studer, D., and Dubochet, J. Cryo-electron microscopy of vitreous sections. *EMBO J*, 2004. **23**(18): p. 3583-8.

143. Koning, R. I., Celler, K., Willemse, J., Bos, E., van Wezel, G. P., and Koster, A. J., Chapter Ten - Correlative Cryo-fluorescence Light Microscopy and Cryo-electron Tomography of *Streptomyces*, in *Methods Cell Biol*, T. Müller-Reichert and P. Verkade, Editors. 2014, Academic Press. p. 217-239.

144. Daley, D. O., Skoglund, U., and Söderström, B. FtsZ does not initiate membrane constriction at the onset of division. *Sci Rep*, 2016. **6**: p. 33138.

145. Zhang, P. Correlative cryo-electron tomography and optical microscopy of cells. *Curr Opin Struct Biol*, 2013. **23**(5): p. 10.1016/j.sbi.2013.07.017.

146. Carter, S. D., Mageswaran, S. K., Farino, Z. J., Mamede, J. I., Oikonomou, C. M., Hope, T. J., Freyberg, Z., and Jensen, G. J. Distinguishing signal from autofluorescence in cryogenic correlated light and electron microscopy of mammalian cells. *J Struct Biol*, 2018. **201**(1): p. 15-25.

147. Rigort, A., Bauerlein, F. J., Leis, A., Gruska, M., Hoffmann, C., Laugks, T., Bohm, U., Eibauer, M., Gnaegi, H., Baumeister, W., and Plitzko, J. M. Micromachining tools and correlative approaches for cellular cryo-electron tomography. *J Struct Biol*, 2010. **172**(2): p. 169-79.

148. Heymann, J. A., Hayles, M., Gestmann, I., Giannuzzi, L. A., Lich, B., and Subramaniam, S. Site-specific 3D imaging of cells and tissues with a dual beam microscope. *J Struct Biol*, 2006. **155**(1): p. 63-73.

149. Marko, M., Hsieh, C., Schalek, R., Frank, J., and Mannella, C. Focused-ion-beam thinning of frozen-hydrated biological specimens for cryo-electron microscopy. *Nat Methods*, 2007. **4**(3): p. 215-7.

150. Chaikeeratisak, V., Nguyen, K., Khanna, K., Brilot, A. F., Erb, M. L., Coker, J. K., Vavilina, A., Newton, G. L., Buschauer, R., Pogliano, K., Villa, E., Agard, D. A., and Pogliano, J. Assembly of a nucleus-like structure during viral replication in bacteria. *Science*, 2017. **355**(6321): p. 194-197.

151. Mahamid, J., Schampers, R., Persoon, H., Hyman, A. A., Baumeister, W., and Plitzko, J. M. A focused ion beam milling and lift-out approach for site-specific preparation of frozen-hydrated lamellas from multicellular organisms. *J Struct Biol*, 2015. **192**(2): p. 262-9.

152. Arnold, J., Mahamid, J., Lucic, V., de Marco, A., Fernandez, J.-J., Laugks, T., Mayer, T., Hyman, Anthony A., Baumeister, W., and Plitzko, Jürgen M. Site-specific cryo-focused ion beam sample preparation guided by 3D correlative microscopy. *Biophys J*, 2016. **110**(4): p. 860-869.

153. Kolovou, A., Schorb, M., Tarafder, A., Sachse, C., Schwab, Y., and Santarella-Mellwig, R. A new method for cryo-sectioning cell monolayers using a correlative workflow. *Methods Cell Biol*, 2017. **140**: p. 85-103.

154. Chlanda, P. and Sachse, M. Cryo-electron microscopy of vitreous sections. *Methods Mol Biol*, 2014. **1117**: p. 193-214.

155. Bouchet-Marquis, C. and Fakan, S. Cryoelectron microscopy of vitreous sections: A step further towards the native state. *Methods Mol Biol*, 2009. **464**: p. 425-39.

156. Jun, S., Ke, D., Debiec, K., Zhao, G., Meng, X., Ambrose, Z., Gibson, G. A., Watkins, S. C., and Zhang, P. Direct visualization of HIV-1 with correlative live-cell microscopy and cryo-electron tomography. *Structure*, 2011. **19**(11): p. 1573-1581.

157. Ibiricu, I., Huiskonen, J. T., Dohner, K., Bradke, F., Sodeik, B., and Grunewald, K. Cryo electron tomography of herpes simplex virus during axonal transport and secondary envelopment in primary neurons. *PLoS Pathog*, 2011. **7**(12): p. e1002406.

158. Strauss, J. D., Hammonds, J. E., Yi, H., Ding, L., Spearman, P., and Wright, E. R. Three-dimensional structural characterization of HIV-1 tethered to human cells. *J Virol*, 2016. **90**(3): p. 1507-1521.

159. Hampton, C. M., Strauss, J. D., Ke, Z., Dillard, R. S., Hammonds, J. E., Alonas, E., Desai, T. M., Marin, M., Storms, R. E., Leon, F., Melikyan, G. B., Santangelo, P. J., Spearman, P. W., and Wright, E. R. Correlated fluorescence microscopy and cryo-electron tomography of virus-infected or transfected mammalian cells. *Nat Protoc*, 2017. **12**(1): p. 150-167.

160. Schorb, M., Gaechter, L., Avinoam, O., Sieckmann, F., Clarke, M., Bebeacua, C., Bykov, Y. S., Sonnen, A. F. P., Lihl, R., and Briggs, J. A. G. New hardware and workflows for semi-automated correlative cryo-fluorescence and cryo-electron microscopy/tomography. *J Struct Biol*, 2017. **197**(2): p. 83-93.

161. Li, S., Ji, G., Shi, Y., Klausen, L. H., Niu, T., Wang, S., Huang, X., Ding, W., Zhang, X., Dong, M., Xu, W., and Sun, F. High-vacuum optical platform for cryo-CLEM (HOPE): A

new solution for non-integrated multiscale correlative light and electron microscopy. *J Struct Biol*, 2018. **201**(1): p. 63-75.

162. Wolf, S. G., Mutsafi, Y., Horowitz, B., Elbaum, M., and Fass, D. Cryo-STEM tomography provides morphological and chemical characterization of precipitated calcium-phosphate clusters sequestered in mitochondria of intact vitrified fibroblasts. *Biophys J*, 2016. **110**(3): p. 23a.

163. Kaufmann, R., Schellenberger, P., Seiradake, E., Dobbie, I. M., Jones, E. Y., Davis, I., Hagen, C., and Grünewald, K. Super-resolution microscopy using standard fluorescent proteins in intact cells under cryo-conditions. *Nano Lett*, 2014. **14**(7): p. 4171-4175.

164. Chang, Y.-W., Chen, S., Tocheva, E. I., Treuner-Lange, A., Löbach, S., Søgaard-Andersen, L., and Jensen, G. J. Correlated cryogenic photoactivated localization microscopy and cryo-electron tomography. *Nat Methods*, 2014. **11**: p. 737.

165. Liu, B., Xue, Y., Zhao, W., Chen, Y., Fan, C., Gu, L., Zhang, Y., Zhang, X., Sun, L., Huang, X., Ding, W., Sun, F., Ji, W., and Xu, T. Three-dimensional super-resolution protein localization correlated with vitrified cellular context. *Sci Rep*, 2015. **5**: p. 13017.

166. Kaufmann, R., Hagen, C., and Grünewald, K., Super-resolution Fluorescence Microscopy of Cryo-immobilized Samples, in *European Microscopy Congress 2016: Proceedings*. 2016, Wiley-VCH Verlag GmbH & Co. KGaA.

167. Afonso, C. L., Amarasinghe, G. K., Bányai, K., Bào, Y., Basler, C. F., Bavari, S., Bejerman, N., Blasdell, K. R., Briand, F.-X., Briese, T., Bukreyev, A., Calisher, C. H., Chandran, K., Chéng, J., Clawson, A. N., Collins, P. L., Dietzgen, R. G., Dolnik, O., Domier, L. L., Dürrwald, R., Dye, J. M., Easton, A. J., Ebihara, H., Farkas, S. L., Freitas-Astúa, J., Formenty, P., Fouchier, R. A. M., Fù, Y., Ghedin, E., Goodin, M. M., Hewson, R., Horie, M., Hyndman, T. H., Jiāng, D., Kitajima, E. W., Kobinger, G. P., Kondo, H., Kurath, G.,

Lamb, R. A., Lenardon, S., Leroy, E. M., Li, C.-X., Lin, X.-D., Liú, L., Longdon, B., Marton, S., Maisner, A., Mühlberger, E., Netesov, S. V., Nowotny, N., Patterson, J. L., Payne, S. L., Paweska, J. T., Randall, R. E., Rima, B. K., Rota, P., Rubbenstroth, D., Schwemmle, M., Shi, M., Smither, S. J., Stenglein, M. D., Stone, D. M., Takada, A., Terregino, C., Tesh, R. B., Tian, J.-H., Tomonaga, K., Tordo, N., Towner, J. S., Vasilakis, N., Verbeek, M., Volchkov, V. E., Wahl-Jensen, V., Walsh, J. A., Walker, P. J., Wang, D., Wang, L.-F., Wetzel, T., Whitfield, A. E., Xiè, J., Yuen, K.-Y., Zhang, Y.-Z., and Kuhn, J. H. Taxonomy of the order Mononegavirales: Update 2016. *Arch Virol*, 2016. **161**(8): p. 2351-2360.

168. Meng, J., Stobart, C. C., Hotard, A. L., and Moore, M. L. An overview of respiratory syncytial virus. *PLoS Pathog*, 2014. **10**(4): p. e1004016.

169. Chu, H. Y., Chin, J., Pollard, J., Zerr, D. M., and Englund, J. A. Clinical outcomes in outpatient respiratory syncytial virus infection in immunocompromised children. *Influenza Other Respir Viruses*, 2016. **10**(3): p. 205-210.

170. Collins, P. L. and Melero, J. A. Progress in understanding and controlling respiratory syncytial virus: Still crazy after all these years. *Virus Res*, 2011. **162**(1-2): p. 80-99.

171. Karron, R. A., Luongo, C., Thumar, B., Loehr, K. M., Englund, J. A., Collins, P. L., and Buchholz, U. J. A gene deletion that up-regulates viral gene expression yields an attenuated RSV vaccine with improved antibody responses in children. *Sci Transl Med*, 2015. **7**(312): p. 312ra175.

172. Meng, J., Lee, S., Hotard, A. L., and Moore, M. L. Refining the balance of attenuation and immunogenicity of respiratory syncytial virus by targeted codon deoptimization of virulence genes. *mBio*, 2014. **5**(5): p. e01704-14.

173. Rostad, C. A., Stobart, C. C., Gilbert, B. E., Pickles, R. J., Hotard, A. L., Meng, J., Blanco, J. C. G., Moin, S. M., Graham, B. S., Piedra, P. A., and Moore, M. L. A recombinant

respiratory syncytial virus vaccine candidate attenuated by a low-fusion F protein is immunogenic and protective against challenge in cotton rats. *J Virol*, 2016. **90**(16): p. 7508-7518.

174. Stobart, C. C., Rostad, C. A., Ke, Z., Dillard, R. S., Hampton, C. M., Strauss, J. D., Yi, H., Hotard, A. L., Meng, J., Pickles, R. J., Sakamoto, K., Lee, S., Currier, M. G., Moin, S. M., Graham, B. S., Boukhvalova, M. S., Gilbert, B. E., Blanco, J. C. G., Piedra, P. A., Wright, E. R., and Moore, M. L. A live RSV vaccine with engineered thermostability is immunogenic in cotton rats despite high attenuation. *Nat Commun*, 2016. **7**: p. 13916.

175. Neuzil, K. M. Progress toward a respiratory syncytial virus vaccine. *Clin Vaccine Immunol*, 2016. **23**(3): p. 186-188.

176. Jorquera, P. A., Anderson, L., and Tripp, R. A. Understanding respiratory syncytial virus (RSV) vaccine development and aspects of disease pathogenesis. *Expert Rev Vaccines*, 2016. **15**(2): p. 173-87.

177. Villafana, T., Falloon, J., Griffin, M. P., Zhu, Q., and Esser, M. T. Passive and active immunization against respiratory syncytial virus for the young and old. *Expert Rev Vaccines*, 2017. **16**(7): p. 1-13.

178. Kiss, G., Holl, J. M., Williams, G. M., Alonas, E., Vanover, D., Lifland, A. W., Gudheti, M., Guerrero-Ferreira, R. C., Nair, V., Yi, H., Graham, B. S., Santangelo, P. J., and Wright, E. R. Structural analysis of respiratory syncytial virus reveals the position of M2-1 between the matrix protein and the ribonucleoprotein complex. *J Virol*, 2014. **88**(13): p. 7602-7617.

179. Li, D., Jans, D. A., Bardin, P. G., Meanger, J., Mills, J., and Ghildyal, R. Association of respiratory syncytial virus M protein with viral nucleocapsids is mediated by the M2-1 protein. *J Virol*, 2008. **82**(17): p. 8863-8870.

180. Collins, P. L. and Graham, B. S. Viral and host factors in human respiratory syncytial virus pathogenesis. *J Virol*, 2008. **82**(5): p. 2040-55.

181. Collins, P. L., Chanock, R. M., Murphy, B. R., Knipe, D. M., and Howley, P. M., *Fields Virology*. 2001. 1443-1486.

182. Bermingham, A. and Collins, P. L. The M2–2 protein of human respiratory syncytial virus is a regulatory factor involved in the balance between rna replication and transcription. *Proc Natl Acad Sci U S A*, 1999. **96**(20): p. 11259-11264.

183. Jin, H., Cheng, X., Zhou, H. Z., Li, S., and Seddiqui, A. Respiratory syncytial virus that lacks open reading frame 2 of the M2 gene (M2-2) has altered growth characteristics and is attenuated in rodents. *J Virol*, 2000. **74**(1): p. 74-82.

184. Swedan, S., Musiyenko, A., and Barik, S. Respiratory syncytial virus nonstructural proteins decrease levels of multiple members of the cellular interferon pathways. *J Virol*, 2009. **83**(19): p. 9682-9693.

185. Lo, M. S., Brazas, R. M., and Holtzman, M. J. Respiratory syncytial virus nonstructural proteins NS1 and NS2 mediate inhibition of Stat2 expression and alpha/beta interferon responsiveness. *J Virol*, 2005. **79**(14): p. 9315-9319.

186. Shaikh, F. Y., Utley, T. J., Craven, R. E., Rogers, M. C., Lapierre, L. A., Goldenring, J. R., and Crowe, J. E., Jr. Respiratory syncytial virus assembles into structured filamentous virion particles independently of host cytoskeleton and related proteins. *PLoS One*, 2012. **7**(7): p. e40826.

187. Harrison, M. S., Sakaguchi, T., and Schmitt, A. P. Paramyxovirus assembly and budding: Building particles that transmit infections. *Int J Biochem Cell Biol*, 2010. **42**(9): p. 1416-29.

188. Lindquist, M. E., Lifland, A. W., Utley, T. J., Santangelo, P. J., and Crowe, J. E., Jr. Respiratory syncytial virus induces host RNA stress granules to facilitate viral replication. *J Virol*, 2010. **84**(23): p. 12274-84.

189. Brock, S. C., Goldenring, J. R., and Crowe, J. E. Apical recycling systems regulate directional budding of respiratory syncytial virus from polarized epithelial cells. *Proc Natl Acad Sci U S A*, 2003. **100**(25): p. 15143.

190. Utley, T. J., Ducharme, N. A., Varthakavi, V., Shepherd, B. E., Santangelo, P. J., Lindquist, M. E., Goldenring, J. R., and Crowe, J. E. Respiratory syncytial virus uses a Vps4-independent budding mechanism controlled by Rab11-FIP2. *Proc Natl Acad Sci U S A*, 2008. **105**(29): p. 10209.

191. McCurdy, L. H. and Graham, B. S. Role of plasma membrane lipid microdomains in respiratory syncytial virus filament formation. *J Virol*, 2003. **77**(3): p. 1747-56.

192. Kallewaard, N. L., Bowen, A. L., and Crowe, J. E., Jr. Cooperativity of actin and microtubule elements during replication of respiratory syncytial virus. *Virology*, 2005. **331**(1): p. 73-81.

193. Harpen, M., Barik, T., Musiyenko, A., and Barik, S. Mutational analysis reveals a noncontractile but interactive role of actin and profilin in viral RNA-dependent RNA synthesis. *J Virol*, 2009. **83**(21): p. 10869-76.

194. Burke, E., Dupuy, L., Wall, C., and Barik, S. Role of cellular actin in the gene expression and morphogenesis of human respiratory syncytial virus. *Virology*, 1998. **252**(1): p. 137-48.

195. Gower, T. L., Peeples, M. E., Collins, P. L., and Graham, B. S. RhoA is activated during respiratory syncytial virus infection. *Virology*, 2001. **283**(2): p. 188-96.

196. Shahriari, S., Gordon, J., and Ghildyal, R. Host cytoskeleton in respiratory syncytial virus assembly and budding. *Virol J*, 2016. **13**(1): p. 161.

197. Weiss, R. A. How does HIV cause AIDS? *Science*, 1993. **260**(5112): p. 1273-9.

198. Barouch, D. H. The quest for an HIV-1 vaccine--moving forward. *N Engl J Med*, 2013. **369**(22): p. 2073-6.

199. Stephenson, K. E., D'Couto, H. T., and Barouch, D. H. New concepts in HIV-1 vaccine development. *Curr Opin Immunol*, 2016. **41**: p. 39-46.

200. King, S. R. Hiv: Virology and mechanisms of disease. *Ann Emerg Med*, 1994. **24**(3): p. 443-449.

201. Mushahwar, I. K., *Human Immunodeficiency Viruses: Molecular Virology, Pathogenesis, Diagnosis and Treatment*. Vol. 13. 2006. 75-87.

202. Votteler, J. a. S., U., Human Immunodeficiency Viruses: Molecular Biology, in *Encyclopedia of Virology*, B.W.J. Mahy, and van Regenmortel, M.H.V., Editor. 2008. p. 517-525.

203. Montagnier, L., Human Immunodeficiency Viruses (Retroviridae), in *Encyclopedia of Virology*, W. Granoff A., R., Editor. 1999. p. 763-774.

204. Benko, D. M., Schwartz, S., Pavlakis, G. N., and Felber, B. K. A novel human immunodeficiency virus type 1 protein, tev, shares sequences with tat, env, and rev proteins. *J Virol*, 1990. **64**(6): p. 2505-2518.

205. Hirsch, M. S., Curran, J., Human Immunodeficiency Viruses, in *Fields Virology*, B.N. FIelds, Knipe, D.M., Howley, P.M., Editor. 1996, Lippincott-Raven: Philadelphia/New York. p. 1953-1975.

206. Miyauchi, K., Kim, Y., Latinovic, O., Morozov, V., and Melikyan, G. B. HIV enters cells via endocytosis and dynamin-dependent fusion with endosomes. *Cell*, 2009. **137**(3): p. 433-444.

207. Hernandez, L. D., Hoffman, L. R., Wolfsberg, T. G., and White, J. M. Virus-cell and cell-cell fusion. *Annu Rev Cell Dev Biol*, 1996. **12**: p. 627-61.

208. Doms, R. W. and Moore, J. P. HIV-1 membrane fusion: Targets of opportunity. *J Cell Biol*, 2000. **151**(2): p. f9-f14.

209. Campbell, E. M. and Hope, T. J. HIV-1 capsid: The multifaceted key player in HIV-1 infection. *Nat Rev Microbiol*, 2015. **13**(8): p. 471-483.

210. Ambrose, Z. and Aiken, C. HIV-1 uncoating: Connection to nuclear entry and regulation by host proteins. *Virology*, 2014. **0**: p. 371-379.

211. Fassati, A. Multiple roles of the capsid protein in the early steps of HIV-1 infection. *Virus Res*, 2012. **170**(1-2): p. 15-24.

212. Forshey, B. M., von Schwedler, U., Sundquist, W. I., and Aiken, C. Formation of a human immunodeficiency virus type 1 core of optimal stability is crucial for viral replication. *J Virol*, 2002. **76**(11): p. 5667-5677.

213. Francis, A. C., Marin, M., Shi, J., Aiken, C., and Melikyan, G. B. Time-resolved imaging of single HIV-1 uncoating in vitro and in living cells. *PLoS Pathog*, 2016. **12**(6): p. e1005709.

214. Neil, S. J., Zang, T., and Bieniasz, P. D. Tetherin inhibits retrovirus release and is antagonized by HIV-1 Vpu. *Nature*, 2008. **451**(7177): p. 425-30.

215. Van Damme, N., Goff, D., Katsura, C., Jorgenson, R. L., Mitchell, R., Johnson, M., Stephens, E. B., and Guatelli, J. The interferon-induced protein BST-2/CD317 restricts release of virions from infected cells and is down-regulated from the cell surface by HIV-1 Vpu. *Cell Host Microbe*, 2008. **3**(4): p. 245-252.

216. Ishikawa, J., Kaisho, T., Tomizawa, H., Lee, B. O., Kobune, Y., Inazawa, J., Oritani, K., Itoh, M., Ochi, T., Ishihara, K., and et al. Molecular cloning and chromosomal mapping of a bone marrow stromal cell surface gene, BST2, that may be involved in pre-B-cell growth. *Genomics*, 1995. **26**(3): p. 527-34.

217. Kupzig, S., Korolchuk, V., Rollason, R., Sugden, A., Wilde, A., and Banting, G. Bst-2/HM1.24 is a raft-associated apical membrane protein with an unusual topology. *Traffic*, 2003. **4**(10): p. 694-709.

218. Perez-Caballero, D., Zang, T., Ebrahimi, A., McNatt, M. W., Gregory, D. A., Johnson, M. C., and Bieniasz, P. D. Tetherin inhibits HIV-1 release by directly tethering virions to cells. *Cell*, 2009. **139**(3): p. 499-511.

219. Andrew, A. J., Miyagi, E., Kao, S., and Strebel, K. The formation of cysteine-linked dimers of BST-2/tetherin is important for inhibition of HIV-1 virus release but not for sensitivity to Vpu. *Retrovirology*, 2009. **6**: p. 80-80.

220. McNatt, M. W., Zang, T., and Bieniasz, P. D. Vpu binds directly to tetherin and displaces it from nascent virions. *PLoS Pathog*, 2013. **9**(4): p. e1003299.

221. Ackermann, H.-W., Phage Classification and Characterization, in *Bacteriophages: Methods and Protocols, Volume 1: Isolation, Characterization, and Interactions*, M.R.J. Clokie and A.M. Kropinski, Editors. 2009, Humana Press: Totowa, NJ. p. 127-140.

222. Braun, V., and Hantke, K., Bacterial Receptors for Phages and Colicins as Constituents of Specific Transport Systems, in *Microbial Interactions: Receptors and Recognition*, J.L. Reissig, Editor. 1977, Chapman and Hall: London. p. 101-130.

223. Schlesinger, M. Adsorption of bacteriophages to homologous bacteria. II. Quantitative investigation of adsorption velocity and saturation. Estimation of the particle size of the bacteriophage. *Immunitaetsforschung*, 1932. **114**: p. 149-160.

224. Sillankorva, S., Oliveira, R., Vieira, M. J., Sutherland, I., and Azeredo, J. *Pseudomonas fluorescens* infection by bacteriophage PhiS1: The influence of temperature, host growth phase and media. *FEMS Microbiol Lett*, 2004. **241**(1): p. 13-20.

225. Quiberoni, A. and Reinheimer, J. A. Physicochemical characterization of phage adsorption to *Lactobacillus helveticus* ATCC 15807 cells. *J Appl Microbiol*, 1998. **85**(4): p. 762-768.

226. Hershey, A. D., Kalmanson, G.M., Bronfenbrenner, J. Coordinate effects of electrolyte and antibody on the infectivity of bacteriophage. *J Immunol*, 1944. **48**(4): p. 221-238.

227. Delbrück, M. Adsorption of bacteriophage under various physiological conditions of the host. *J Gen Physiol*, 1940. **23**(5): p. 631-642.

228. Shin, H., Lee, J.-H., Kim, H., Choi, Y., Heu, S., and Ryu, S. Receptor diversity and host interaction of bacteriophages infecting *Salmonella enterica* serovar Typhimurium. *PLoS One*, 2012. **7**(8): p. e43392.

229. Rakhuba, D. V., Kolomiets, E. I., Dey, E. S., and Novik, G. I. Bacteriophage receptors, mechanisms of phage adsorption and penetration into host cell. *Pol J Microbiol*, 2010. **59**(3): p. 145-55.

230. Wilkinson, S. G. Bacterial lipopolysaccharides--themes and variations. *Prog Lipid Res*, 1996. **35**(3): p. 283-343.

231. Beveridge, T. J. and Graham, L. L. Surface layers of bacteria. *Microbiol Rev*, 1991. **55**(4): p. 684-705.

232. Yurewicz, E. C., Ghalambor, M. A., Duckworth, D. H., and Heath, E. C. Catalytic and molecular properties of a phage-induced capsular polysaccharide depolymerase. *J Biol Chem*, 1971. **246**(18): p. 5607-16.

233. Taylor, K. Enzymatic deacetylation of Vi-polysaccharide by Vi-phage. II. *Biochem Biophys Res Commun*, 1965. **20**(6): p. 752-6.

234. Taylor, K. Physical and chemical changes of Vi-polysaccharide due to Vi-phage II action. *Acta Biochim Polon*, 1966. **13**: p. 79-106.

235. Stirm, S., Bessler, W., Fehmel, F., Freund-Mölbrt, E., and Thurow, H. Isolation of spike-formed particles from bacteriophage lysates. *Virology*, 1971. **45**(1): p. 303-308.

236. Stirm, S., Bessler, W., Fehmel, F., and Freund-Mölbert, E. Bacteriophage particles with endo-glycosidase activity. *J Virol*, 1971. **8**(3): p. 343-346.

237. Park, B. H. An enzyme produced by a phage-host cell system: I. The properties of a *Klebsiella* phage. *Virology*, 1956. **2**(6): p. 711-718.

238. Chakrabarty, A. M., Niblack, J. F., and Gunsalus, I. C. A phage-initiated polysaccharide depolymerase in *Pseudomonas putida*. *Virology*, 1967. **32**(3): p. 532-4.

239. Luderitz, O., Jann, K., Wheat, R. Somatic and capsular antigens of gram-negative bacteria. *Comp Biochem*, 1968. **26A**: p. 105-228.

240. Schade, S. Z., Adler, J., and Ris, H. How bacteriophage χ attacks motile bacteria. *J Virol*, 1967. **1**(3): p. 599-609.

241. Lovett, P. S. Pbp1: A flagella specific bacteriophage mediating transduction in *Bacillus pumilus*. *Virology*, 1972. **47**(3): p. 743-752.

242. Lotz, W., Acker, G., and Schmitt, R. Bacteriophage 7-7-1 adsorbs to the complex flagella of *Rhizobium lupini* H13-3. *J Gen Virol*, 1977. **34**(1): p. 9-17.

243. Pate, J. L., Petzold, S. J., and Umbreit, T. H. Two flagellotropic phages and one pilus-specific phage active against *Asticcacaulis biprosthecum*. *Virology*, 1979. **94**(1): p. 24-37.

244. Steitz, J. A. Identification of the a protein as a structural component of bacteriophage r17. *J Mol Biol*, 1968. **33**(3): p. 923-936.

245. Steitz, J. A. Isolation of the a protein from bacteriophage R17. *J Mol Biol*, 1968. **33**(3): p. 937-945.

246. Roberts, J. W. and Steitz, J. E. The reconstitution of infective bacteriophage R17. *Proc Natl Acad Sci U S A*, 1967. **58**(4): p. 1416-1421.

247. Krahn, P. M., O'Callaghan, R. J., and Paranchych, W. Stages in phage R17 infection: VI: Injection of a protein and RNA into the host cell. *Virology*, 1972. **47**(3): p. 628-637.

248. Hohn, T. and Hohn, B. Structure and assembly of simple RNA bacteriophages. *Adv Virus Res*, 1970. **16**: p. 43-98.

249. Bamford, D. H., Palva, E. T., and Lounatmaa, K. Ultrastructure and life cycle of the lipid-containing bacteriophage phi 6. *J Gen Virol*, 1976. **32**(2): p. 249-59.

250. Skerker, J. M. and Shapiro, L. Identification and cell cycle control of a novel pilus system in *Caulobacter crescentus*. *EMBO J*, 2000. **19**(13): p. 3223-3234.

251. Meynell, G. G. and Lawn, A. M. Filamentous phages specific for the I sex factor. *Nature*, 1968. **217**(5134): p. 1184-6.

252. Loeb, T. Isolation of a bacteriophage specific for the F plus and Hfr mating types of *Escherichia coli* K-12. *Science*, 1960. **131**(3404): p. 932-3.

253. Caro, L. G. and Schnös, M. The attachment of the male-specific bacteriophage F1 to sensitive strains of *Escherichia coli*. *Proc Natl Acad Sci U S A*, 1966. **56**(1): p. 126-132.

254. Russel, M., Whirlow, H., Sun, T. P., and Webster, R. E. Low-frequency infection of F-bacteria by transducing particles of filamentous bacteriophages. *J Bacteriol*, 1988. **170**(11): p. 5312-5316.

255. Click, E. M. and Webster, R. E. The TolQRA proteins are required for membrane insertion of the major capsid protein of the filamentous phage F1 during infection. *J Bacteriol*, 1998. **180**(7): p. 1723-1728.

256. Molineux, I. J. and Panja, D. Popping the cork: Mechanisms of phage genome ejection. *Nat Rev Microbiol*, 2013. **11**: p. 194.

257. Koch, A. L. The biophysics of the gram-negative periplasmic space. *Crit Rev Microbiol*, 1998. **24**(1): p. 23-59.

258. Qiu, X., Rau, D. C., Parsegian, V. A., Fang, L. T., Knobler, C. M., and Gelbart, W. M. Salt-dependent DNA-DNA spacings in intact bacteriophage λ reflect relative importance of DNA self-repulsion and bending energies. *Phys Rev Lett*, 2011. **106**(2): p. 028102-028102.

259. Panja, D. and Molineux, I. J. Dynamics of bacteriophage genome ejection in vitro and in vivo. *Phys Biol*, 2010. **7**(4): p. 045006.

260. Lemay, S. G., Panja, D., and Molineux, I. J. Role of osmotic and hydrostatic pressures in bacteriophage genome ejection. *Phys Rev E Stat Nonlin Soft Matter Phys*, 2013. **87**(2): p. 022714.

261. Grayson, P. and Molineux, I. J. Is phage DNA "injected" into cells - biologists and physicists can agree. *Curr Opin Microbiol*, 2007. **10**(4): p. 401-409.

262. Zavriev, S. K. and Shemyakin, M. F. RNA polymerase-dependent mechanism for the stepwise T7 phage DNA transport from the virion into *E. coli*. *Nucleic Acids Res*, 1982. **10**(5): p. 1635-52.

263. Kemp, P., Garcia, L. R., and Molineux, I. J. Changes in bacteriophage T7 virion structure at the initiation of infection. *Virology*, 2005. **340**(2): p. 307-17.

264. Choi, K. H., McPartland, J., Kaganman, I., Bowman, V. D., Rothman-Denes, L. B., and Rossmann, M. G. Insight into DNA and protein transport in double-stranded DNA viruses: The structure of bacteriophage N4. *J Mol Biol*, 2008. **378**(3): p. 726-736.

265. Kazmierczak, K., Rothman-Denes, L., Bacteriophage N4, in *The Bacteriophages*, R. Calendar, Editor. 2006, Oxford University Press. p. 302-314.

266. Lanni, Y. T. First-step-transfer deoxyribonucleic acid of bacteriophage T5. *Bacteriol Rev*, 1968. **32**(3): p. 227-242.

267. Gonzalez-Huici, V., Salas, M., and Hermoso, J. M. Requirements for *Bacillus subtilis* bacteriophage phi29 DNA ejection. *Gene*, 2006. **374**: p. 19-25.

268. Gonzalez-Huici, V., Salas, M., and Hermoso, J. M. The push-pull mechanism of bacteriophage phi29 DNA injection. *Mol Microbiol*, 2004. **52**(2): p. 529-40.

269. Alcorlo, M., González-Huici, V., Hermoso, J. M., Meijer, W. J. J., and Salas, M. The phage φ29 membrane protein p16.7, involved in DNA replication, is required for efficient ejection of the viral genome. *J Bacteriol*, 2007. **189**(15): p. 5542-5549.

270. Summers, W. C. Bacteriophage therapy. *Annu Rev Microbiol*, 2001. **55**: p. 437-51.

271. Abedon, S. T., Kuhl, S. J., Blasdel, B. G., and Kutter, E. M. Phage treatment of human infections. *Bacteriophage*, 2011. **1**(2): p. 66-85.

272. Sulakvelidze, A., Alavidze, Z., and Morris, J. G. Bacteriophage therapy. *Antimicrob Agents Chemother*, 2001. **45**(3): p. 649-659.

273. Parasion, S., Kwiatek, M., Gryko, R., Mizak, L., and Malm, A. Bacteriophages as an alternative strategy for fighting biofilm development. *Pol J Microbiol*, 2014. **63**(2): p. 137-45.

274. Schmelcher, M. and Loessner, M. J. Application of bacteriophages for detection of foodborne pathogens. *Bacteriophage*, 2014. **4**: p. e28137.

275. Nobrega, F. L., Costa, A. R., Kluskens, L. D., and Azeredo, J. Revisiting phage therapy: New applications for old resources. *Trends Microbiol*, 2015. **23**(4): p. 185-91.

276. Meaden, S. and Koskella, B. Exploring the risks of phage application in the environment. *Front Microbiol*, 2013. **4**: p. 358.

277. Wittebole, X., De Roock, S., and Opal, S. M. A historical overview of bacteriophage therapy as an alternative to antibiotics for the treatment of bacterial pathogens. *Virulence*, 2014. **5**(1): p. 226-235.

278. Moradpour, Z., Sepehrizadeh, Z., Rahbarizadeh, F., Ghasemian, A., Yazdi, M. T., and Shahverdi, A. R. Genetically engineered phage harbouring the lethal catabolite gene activator protein gene with an inducer-independent promoter for biocontrol of *Escherichia coli*. *FEMS Microbiol Lett*, 2009. **296**(1): p. 67-71.

279. Örmälä, A.-M. and Jalasvuori, M. Phage therapy: Should bacterial resistance to phages be a concern, even in the long run? *Bacteriophage*, 2013. **3**(1): p. e24219.

280. Chan, B. K., Abedon, S. T., and Loc-Carrillo, C. Phage cocktails and the future of phage therapy. *Future Microbiol*, 2013. **8**(6): p. 769-83.

281. Drulis-Kawa, Z., Majkowska-Skrobek, G., Maciejewska, B., Delattre, A.-S., and Lavigne, R. Learning from bacteriophages - advantages and limitations of phage and phage-encoded protein applications. *Curr Protein Pept Sci*, 2012. **13**(8): p. 699-722.

282. Koch, R. An address on Cholera and its Bacillus. *Br Med J*, 1884. **2**(1235): p. 403-407.

283. Faruque, S. M., Albert, M. J., and Mekalanos, J. J. Epidemiology, genetics, and ecology of toxigenic *Vibrio cholerae*. *Microbiol Mol Biol Rev*, 1998. **62**(4): p. 1301-1314.

284. Knirel, Y. A., Widmalm, G., Senchenkova, S. N., Jansson, P. E., and Weintraub, A. Structural studies on the short-chain lipopolysaccharide of *Vibrio cholerae* O139 bengal. *Eur J Biochem*, 1997. **247**(1): p. 402-10.

285. Kenne, L., Lindberg, B., Unger, P., Gustafsson, B., and Holme, T. Structural studies of the *Vibrio cholerae* O-antigen. *Carbohydr Res*, 1982. **100**(1): p. 341-349.

286. Chatterjee, S. N. and Chaudhuri, K. Lipopolysaccharides of *Vibrio cholerae*: I. Physical and chemical characterization. *Biochim Biophys Acta, Mol Basis Dis*, 2003. **1639**(2): p. 65-79.

287. Lobitz, B., Beck, L., Huq, A., Wood, B., Fuchs, G., Faruque, A. S. G., and Colwell, R. Climate and infectious disease: Use of remote sensing for detection of *Vibrio cholerae* by indirect measurement. *Proc Natl Acad Sci U S A*, 2000. **97**(4): p. 1438-1443.

288. Lipp, E. K., Huq, A., and Colwell, R. R. Effects of global climate on infectious disease: The cholera model. *Clin Microbiol Rev*, 2002. **15**(4): p. 757-770.

289. Islam, M. S., Talukder, K. A., Khan, N. H., Mahmud, Z. H., Rahman, M. Z., Nair, G. B., Siddique, A. K., Yunus, M., Sack, D. A., Sack, R. B., Huq, A., and Colwell, R. R. Variation of

toxigenic *Vibrio cholerae* O1 in the aquatic environment of Bangladesh and its correlation with the clinical strains. *Microbiol Immunol*, 2004. **48**(10): p. 773-7.

290. Colwell, R. R. A voyage of discovery: Cholera, climate and complexity. *Environ Microbiol*, 2002. **4**(2): p. 67-9.

291. Colwell, R. R. Infectious disease and environment: Cholera as a paradigm for waterborne disease. *Int Microbiol*, 2004. **7**(4): p. 285-9.

292. Colwell, R. R. Global climate and infectious disease: The cholera paradigm. *Science*, 1996. **274**(5295): p. 2025-31.

293. Alam, M., Islam, A., Bhuiyan, N. A., Rahim, N., Hossain, A., Khan, G. Y., Ahmed, D., Watanabe, H., Izumiya, H., Faruque, A. S. G., Akanda, A. S., Islam, S., Sack, R. B., Huq, A., Colwell, R. R., and Cravioto, A. Clonal transmission, dual peak, and off-season cholera in Bangladesh. *Infect Ecol Epidemiol*, 2011. **1**: p. 10.3402/iee.v1i0.7273.

294. Alam, M., Hasan, N. A., Sadique, A., Bhuiyan, N. A., Ahmed, K. U., Nusrin, S., Nair, G. B., Siddique, A. K., Sack, R. B., Sack, D. A., Huq, A., and Colwell, R. R. Seasonal cholera caused by *Vibrio cholerae* serogroups O1 and O139 in the coastal aquatic environment of bangladesh. *Appl Environ Microbiol*, 2006. **72**(6): p. 4096-4104.

295. Bradford, A. K., A. B. Cheryl, and J. G. Wells., Isolation and Identification of *Vibrio cholerae* O1 from Fecal Specimens, in *Vibrio cholerae and Cholera: Molecular to Global Perspectives*, K. Wachsmut, Blake, P.A., and Olsvik, O., Editor. 1994, ASM Press: Washinton, DC. p. 3-25.

296. Kaper, J. B., Morris, J. G., and Levine, M. M. Cholera. *Clin Microbiol Rev*, 1995. **8**(1): p. 48-86.

297. Kaper, J., Lockman, H., Colwell, R. R., and Joseph, S. W. Ecology, serology, and enterotoxin production of *Vibrio cholerae* in chesapeake bay. *Appl Environ Microbiol*, 1979. **37**(1): p. 91-103.

298. Albert, M. J. Vibrio cholerae o139 bengal. *J Clin Microbiol*, 1994. **32**(10): p. 2345-2349.

299. Taylor, R. K., Miller, V. L., Furlong, D. B., and Mekalanos, J. J. Use of phoA gene fusions to identify a pilus colonization factor coordinately regulated with cholera toxin. *Proc Natl Acad Sci U S A*, 1987. **84**(9): p. 2833-2837.

300. Herrington, D. A., Hall, R.H., Losonsky, G., Mekalanos, J.J., Taylor, R.K., Levine, M.M. Toxin, toxin-coregulated pili, and the toxR regulon are essential for *Vibrio cholerae* pathogenesis in humans. *J Exp Med*, 1988. **168**(4): p. 1487-1492.

301. Cassel, D. and Pfeuffer, T. Mechanism of cholera toxin action: Covalent modification of the guanyl nucleotide-binding protein of the adenylate cyclase system. *Proc Natl Acad Sci U S A*, 1978. **75**(6): p. 2669-2673.

302. Nesper, J., Schild, S., Lauriano, C. M., Kraiss, A., Klose, K. E., and Reidl, J. Role of *Vibrio cholerae* O139 surface polysaccharides in intestinal colonization. *Infect Immun*, 2002. **70**(11): p. 5990-5996.

303. Schild, S., Lamprecht, A. K., Fourestier, C., Lauriano, C. M., Klose, K. E., and Reidl, J. Characterizing lipopolysaccharide and core lipid a mutant O1 and O139 *Vibrio cholerae* strains for adherence properties on mucus-producing cell line HT29-Rev MTX and virulence in mice. *Int J Med Microbiol*, 2005. **295**(4): p. 243-51.

304. Provenzano, D. and Klose, K. E. Altered expression of the Toxr-regulated porins OmpU and OmpT diminishes *Vibrio cholerae* bile resistance, virulence factor expression, and intestinal colonization. *Proc Natl Acad Sci U S A*, 2000. **97**(18): p. 10220-10224.

305. Chiang, S. L. and Mekalanos, J. J. rfb mutations in *Vibrio cholerae* do not affect surface production of toxin-coregulated pili but still inhibit intestinal colonization. *Infect Immun*, 1999. **67**(2): p. 976-980.

306. Thelin, K. H. and Taylor, R. K. Toxin-coregulated pilus, but not mannose-sensitive hemagglutinin, is required for colonization by *Vibrio cholerae* O1 El Tor biotype and O139 strains. *Infect Immun*, 1996. **64**(7): p. 2853-2856.

307. Yancey, R. J., Willis, D. L., and Berry, L. J. Role of motility in experimental cholera in adult rabbits. *Infect Immun*, 1978. **22**(2): p. 387-392.

308. Sack, D. A., Sack, R. B., Nair, G. B., and Siddique, A. K. Cholera. *Lancet*, 2004. **363**(9404): p. 223-33.

309. Waldor, M. K. and Mekalanos, J. J. Lysogenic conversion by a filamentous phage encoding cholera toxin. *Science*, 1996. **272**(5270): p. 1910-4.

310. Chaudhuri, K., Chatterjee, S.N., *Cholera Toxins*. 2009: Springer.

311. Wernick, N. L. B., Chinnapen, D. J.-F., Cho, J. A., and Lencer, W. I. Cholera toxin: An intracellular journey into the cytosol by way of the endoplasmic reticulum. *Toxins*, 2010. **2**(3): p. 310.

312. Tacket, C. O., Taylor, R. K., Losonsky, G., Lim, Y., Nataro, J. P., Kaper, J. B., and Levine, M. M. Investigation of the roles of toxin-coregulated pili and mannose-sensitive hemagglutinin pili in the pathogenesis of *Vibrio cholerae* O139 infection. *Infect Immun*, 1998. **66**(692-695): p. 692-695.

313. Karaolis, D. K. R., Johnson, J. A., Bailey, C. C., Boedeker, E. C., Kaper, J. B., and Reeves, P. R. A *Vibrio cholerae* pathogenicity island associated with epidemic and pandemic strains. *Proc Natl Acad Sci U S A*, 1998. **95**(6): p. 3134-3139.

314. Kojima, S., Yamamoto, K., Kawagishi, I., and Homma, M. The polar flagellar motor of *Vibrio cholerae* is driven by an Na^+ motive force. *J Bacteriol*, 1999. **181**(6): p. 1927-1930.

315. Wang, H., Zhang, L., Silva, A. J., and Benitez, J. A. A quinazoline-2,4-diamino analog suppresses *Vibrio cholerae* flagellar motility by interacting with motor protein PomB and induces envelope stress. *Antimicrob Agents Chemother*, 2013. **57**(8): p. 3950-3959.

316. Syed, K. A., Beyhan, S., Correa, N., Queen, J., Liu, J., Peng, F., Satchell, K. J. F., Yildiz, F., and Klose, K. E. The *Vibrio cholerae* flagellar regulatory hierarchy controls expression of virulence factors. *J Bacteriol*, 2009. **191**(21): p. 6555-6570.

317. Silva, A. J., Leitch, G. J., Camilli, A., and Benitez, J. A. Contribution of hemagglutinin/protease and motility to the pathogenesis of El Tor biotype cholera. *Infect Immun*, 2006. **74**(4): p. 2072-2079.

318. Häse, C. C. and Mekalanos, J. J. Effects of changes in membrane sodium flux on virulence gene expression in *Vibrio cholerae*. *Proc Natl Acad Sci U S A*, 1999. **96**(6): p. 3183-3187.

319. Hase, C. C. Analysis of the role of flagellar activity in virulence gene expression in *Vibrio cholerae*. *Microbiology*, 2001. **147**(Pt 4): p. 831-7.

320. Wai, S. N., Lindmark, B., Soderblom, T., Takade, A., Westermark, M., Oscarsson, J., Jass, J., Richter-Dahlfors, A., Mizunoe, Y., and Uhlin, B. E. Vesicle-mediated export and assembly of pore-forming oligomers of the enterobacterial ClyA cytotoxin. *Cell*, 2003. **115**(1): p. 25-35.

321. Vesy, C. J., Kitchens, R. L., Wolfbauer, G., Albers, J. J., and Munford, R. S. Lipopolysaccharide-binding protein and phospholipid transfer protein release lipopolysaccharides from gram-negative bacterial membranes. *Infect Immun*, 2000. **68**(5): p. 2410-2417.

322. Hoekstra, D., van der Laan, J. W., de Leij, L., and Witholt, B. Release of outer membrane fragments from normally growing *Escherichia coli*. *Biochim Biophys Acta, Biomembr*, 1976. **455**(3): p. 889-899.

323. Gankema, H., Wensink, J., Guinée, P. A. M., Jansen, W. H., and Witholt, B. Some characteristics of the outer membrane material released by growing enterotoxigenic *Escherichia coli*. *Infect Immun*, 1980. **29**(2): p. 704-713.

324. Fiocca, R., Necchi, V., Sommi, P., Ricci, V., Telford, J., Cover, T. L., and Solcia, E. Release of *Helicobacter pylori* vacuolating cytotoxin by both a specific secretion pathway and budding of outer membrane vesicles. Uptake of released toxin and vesicles by gastric epithelium. *J Pathol*, 1999. **188**(2): p. 220-226.

325. Devoe, I. W. and Gilchrist, J. E. Release of endotoxin in the form of cell wall blebs during in vitro growth of *Neisseria meningitidis*. *J Exp Med*, 1973. **138**(5): p. 1156-1167.

326. Dorward, D. W. and Garon, C. F. DNA-binding proteins in cells and membrane blebs of *Neisseria gonorrhoeae*. *J Bacteriol*, 1989. **171**(8): p. 4196-4201.

327. Kadurugamuwa, J. L. and Beveridge, T. J. Virulence factors are released from *Pseudomonas aeruginosa* in association with membrane vesicles during normal growth and exposure to gentamicin: A novel mechanism of enzyme secretion. *J Bacteriol*, 1995. **177**(14): p. 3998-4008.

328. Kondo, K., Takade, A., and Amako, K. Release of the outer membrane vesicles from *Vibrio cholerae* and *Vibrio parahaemolyticus*. *Microbiol Immunol*, 1993. **37**(2): p. 149-152.

329. Chatterjee, S. N. and Das, J. Electron microscopic observations on the excretion of cell-wall material by *Vibrio cholerae*. *J Gen Microbiol*, 1967. **49**(1): p. 1-11.

330. Beveridge, T. J. Structures of gram-negative cell walls and their derived membrane vesicles. *J Bacteriol*, 1999. **181**(16): p. 4725-4733.

331. Kuehn, M. J. and Kesty, N. C. Bacterial outer membrane vesicles and the host-pathogen interaction. *Genes Dev*, 2005. **19**(22): p. 2645-55.

332. Wensink, J. and Witholt, B. Outer-membrane vesicles released by normally growing *Escherichia coli* contain very little lipoprotein. *Eur J Biochem*, 1981. **116**(2): p. 331-335.

333. Post, D. M., Zhang, D., Eastvold, J. S., Teghanemt, A., Gibson, B. W., and Weiss, J. P. Biochemical and functional characterization of membrane blebs purified from *Neisseria meningitidis* serogroup B. *J Biol Chem*, 2005. **280**(46): p. 38383-94.

334. Kato, S., Kowashi, Y., and Demuth, D. R. Outer membrane-like vesicles secreted by *Actinobacillus actinomycetemcomitans* are enriched in leukotoxin. *Microb Pathog*, 2002. **32**(1): p. 1-13.

335. Rompikuntal, P. K., Vdovikova, S., Duperthuy, M., Johnson, T. L., Åhlund, M., Lundmark, R., Oscarsson, J., Sandkvist, M., Uhlin, B. E., and Wai, S. N. Outer membrane vesicle-mediated export of processed PrtV protease from *Vibrio cholerae*. *PLoS One*, 2015. **10**(7): p. e0134098.

336. Elluri, S., Enow, C., Vdovikova, S., Rompikuntal, P. K., Dongre, M., Carlsson, S., Pal, A., Uhlin, B. E., and Wai, S. N. Outer membrane vesicles mediate transport of biologically active *Vibrio cholerae* cytolysin (VCC) from *V. cholerae* strains. *PLoS One*, 2014. **9**(9): p. e106731.

337. Chatterjee, D. and Chaudhuri, K. Association of cholera toxin with *vibrio cholerae* outer membrane vesicles which are internalized by human intestinal epithelial cells. *FEBS Lett*, 2011. **585**(9): p. 1357-1362.

338. Schild, S., Nelson, E. J., and Camilli, A. Immunization with *vibrio cholerae* outer membrane vesicles induces protective immunity in mice. *Infect Immun*, 2008. **76**(10): p. 4554-4563.

339. O'Dwyer, C. A., Reddin, K., Martin, D., Taylor, S. C., Gorringe, A. R., Hudson, M. J., Brodeur, B. R., Langford, P. R., and Kroll, J. S. Expression of heterologous antigens in commensal *Neisseria* spp.: Preservation of conformational epitopes with vaccine potential. *Infect Immun*, 2004. **72**(11): p. 6511-6518.

340. Kesty, N. C. and Kuehn, M. J. Incorporation of heterologous outer membrane and periplasmic proteins into *escherichia coli* outer membrane vesicles. *J Biol Chem*, 2004. **279**(3): p. 2069-2076.

341. Schild, S., Nelson, E. J., Bishop, A. L., and Camilli, A. Characterization of *Vibrio cholerae* outer membrane vesicles as a candidate vaccine for cholera. *Infect Immun*, 2009. **77**(1): p. 472-484.

342. Poindexter, J. S. The Caulobacters: Ubiquitous unusual bacteria. *Microbiological Reviews*, 1981. **45**(1): p. 123-179.

343. Poindexter, J. S. Biological properties + classification of Caulobacter group. *Bacteriol Rev*, 1964. **28**(3): p. 231-&.

344. Degnen, S. T. and Newton, A. Chromosome replication during development in *Caulobacter crescentus*. *J Mol Biol*, 1972. **64**(3): p. 671-80.

345. Sommer, J. M. and Newton, A. Sequential regulation of developmental events during polar morphogenesis in *Caulobacter crescentus*: Assembly of pili on swarmer cells requires cell separation. *J Bacteriol*, 1988. **170**(1): p. 409-415.

346. Lagenaur, C. and Agabian, N. *Caulobacter crescentus* pili: Structure and stage-specific expression. *J Bacteriol*, 1977. **131**(1): p. 340-346.

347. Lagenaur, C. and Agabian, N. *Caulobacter* flagellar organelle: Synthesis, compartmentation, and assembly. *J Bacteriol*, 1978. **135**(3): p. 1062-1069.

348. Laub, M. T., McAdams, H. H., Feldblyum, T., Fraser, C. M., and Shapiro, L. Global analysis of the genetic network controlling a bacterial cell cycle. *Science*, 2000. **290**(5499): p. 2144-2148.

349. Holtzendorff, J., Hung, D., Brende, P., Reisenauer, A., Viollier, P. H., McAdams, H. H., and Shapiro, L. Oscillating global regulators control the genetic circuit driving a bacterial cell cycle. *Science*, 2004. **304**(5673): p. 983-7.

350. Hottes, A. K., Shapiro, L., and McAdams, H. H. DnaA coordinates replication initiation and cell cycle transcription in *Caulobacter crescentus*. *Mol Microbiol*, 2005. **58**(5): p. 1340-53.

351. Laub, M. T., Chen, S. L., Shapiro, L., and McAdams, H. H. Genes directly controlled by CtrA, a master regulator of the *Caulobacter* cell cycle. *Proc Natl Acad Sci U S A*, 2002. **99**(7): p. 4632-7.

352. Hahn, H. P. The type-4 pilus is the major virulence-associated adhesin of *Pseudomonas aeruginosa*--a review. *Gene*, 1997. **192**(1): p. 99-108.

353. Thanassi, D. G., Bliska, J. B., and Christie, P. J. Surface organelles assembled by secretion systems of gram-negative bacteria: Diversity in structure and function. *FEMS Microbiol Rev*, 2012. **36**(6): p. 1046-1082.

354. Berry, J.-L. and Pelicic, V. Exceptionally widespread nanomachines composed of type IV pilins: The prokaryotic swiss army knives. *FEMS Microbiol Rev*, 2015. **39**(1): p. 1-21.

355. Pelicic, V. Type iv pili: E pluribus unum? *Mol Microbiol*, 2008. **68**(4): p. 827-837.

356. Ellison, C. K., Kan, J., Dillard, R. S., Kysela, D. T., Ducret, A., Berne, C., Hampton, C. M., Ke, Z., Wright, E. R., Biais, N., Dalia, A. B., and Brun, Y. V. Obstruction of pilus retraction stimulates bacterial surface sensing. *Science*, 2017. **358**(6362): p. 535.

357. Zhang, H. Z., Lory, S., and Donnenberg, M. S. A plasmid-encoded prepilin peptidase gene from enteropathogenic *Escherichia coli*. *J Bacteriol*, 1994. **176**(22): p. 6885-6891.

358. Lory, S. and Strom, M. S. Structure-function relationship of type-IV prepilin peptidase of *Pseudomonas aeruginosa*--a review. *Gene*, 1997. **192**(1): p. 117-21.

359. Koo, J., Lamers, R. P., Rubinstein, J. L., Burrows, L. L., and Howell, P. L. Structure of the *Pseudomonas aeruginosa* type IVa pilus secretin at 7.4 Å. *Structure*, 2016. **24**(10): p. 1778-1787.

360. Collins, R. F., Frye, S. A., Kitmitto, A., Ford, R. C., Tonjum, T., and Derrick, J. P. Structure of the *Neisseria meningitidis* outer membrane PilQ secretin complex at 12 Å resolution. *J Biol Chem*, 2004. **279**(38): p. 39750-6.

361. Burkhardt, J., Vonck, J., and Averhoff, B. Structure and function of PilQ, a secretin of the DNA transporter from the thermophilic bacterium *Thermus thermophilus* HB27. *J Biol Chem*, 2011. **286**(12): p. 9977-9984.

362. Takhar, H. K., Kemp, K., Kim, M., Howell, P. L., and Burrows, L. L. The platform protein is essential for type IV pilus biogenesis. *J Biol Chem*, 2013. **288**(14): p. 9721-9728.

363. Chiang, P., Habash, M., and Burrows, L. L. Disparate subcellular localization patterns of *Pseudomonas aeruginosa* type IV pilus atpases involved in twitching motility. *J Bacteriol*, 2005. **187**(3): p. 829-839.

364. Gold, V. A. M., Salzer, R., Averhoff, B., and Kühlbrandt, W. Structure of a type IV pilus machinery in the open and closed state. *eLife*, 2015. **4**: p. e07380.

365. Chang, Y. W., Rettberg, L. A., Treuner-Lange, A., Iwasa, J., Sogaard-Andersen, L., and Jensen, G. J. Architecture of the type IVa pilus machine. *Science*, 2016. **351**(6278): p. aad2001.

366. Christen, M., Beusch, C., Bösch, Y., Cerletti, D., Flores-Tinoco, C. E., Del Medico, L., Tschan, F., and Christen, B. Quantitative selection analysis of bacteriophage ϕCbK susceptibility in *Caulobacter crescentus*. *J Mol Biol*, 2016. **428**(2, Part B): p. 419-430.

367. Thormann, K. M. and Paulick, A. Tuning the flagellar motor. *Microbiology*, 2010. **156**(Pt 5): p. 1275-83.

368. Tasteyre, A., Barc, M.-C., Collignon, A., Boureau, H., and Karjalainen, T. Role of FliC and FliD flagellar proteins of *Clostridium difficile* in adherence and gut colonization. *Infect Immun*, 2001. **69**(12): p. 7937-7940.

369. Erdem, A. L., Avelino, F., Xicohtencatl-Cortes, J., and Girón, J. A. Host protein binding and adhesive properties of H6 and H7 flagella of attaching and effacing *Escherichia coli*. *J Bacteriol*, 2007. **189**(20): p. 7426-7435.

370. Arora, S. K., Ritchings, B. W., Almira, E. C., Lory, S., and Ramphal, R. The *Pseudomonas aeruginosa* flagellar cap protein, FliD, is responsible for mucin adhesion. *Infect Immun*, 1998. **66**(3): p. 1000-1007.

371. Harshey, R. M. Bacterial motility on a surface: Many ways to a common goal. *Annu Rev Microbiol*, 2003. **57**: p. 249-73.

372. Prüß, B. M., Besemann, C., Denton, A., and Wolfe, A. J. A complex transcription network controls the early stages of biofilm development by *Escherichia coli*. *J Bacteriol*, 2006. **188**(11): p. 3731-3739.

373. Wang, Q., Suzuki, A., Mariconda, S., Porwollik, S., and Harshey, R. M. Sensing wetness: A new role for the bacterial flagellum. *EMBO J*, 2005. **24**(11): p. 2034-2042.

374. Blocker, A., Komoriya, K., and Aizawa, S.-I. Type III secretion systems and bacterial flagella: Insights into their function from structural similarities. *Proc Natl Acad Sci U S A*, 2003. **100**(6): p. 3027-3030.

375. Minamino, T., Imada, K., and Namba, K. Molecular motors of the bacterial flagella. *Curr Opin Struct Biol*, 2008. **18**(6): p. 693-701.

376. Minamino, T. and Namba, K. Self-assembly and type III protein export of the bacterial flagellum. *J Mol Microbiol Biotechnol*, 2004. **7**(1-2): p. 5-17.

377. Chevance, F. F. and Hughes, K. T. Coordinating assembly of a bacterial macromolecular machine. *Nat Rev Microbiol*, 2008. **6**(6): p. 455-65.

378. Faulds-Pain, A., Birchall, C., Aldridge, C., Smith, W. D., Grimaldi, G., Nakamura, S., Miyata, T., Gray, J., Li, G., Tang, J. X., Namba, K., Minamino, T., and Aldridge, P. D. Flagellin redundancy in *Caulobacter crescentus* and its implications for flagellar filament assembly. *J Bacteriol*, 2011. **193**(11): p. 2695-2707.

379. Lederberg, J. and Iino, T. Phase variation in *Salmonella. Genetics*, 1956. **41**(5): p. 743-757.

380. Pearce, U. B. and Stocker, B. A. Phase variation of flagellar antigens in *Salmonella*: Abortive transduction studies. *J Gen Microbiol*, 1967. **49**(2): p. 335-49.

381. Lambert, C., Evans, K. J., Till, R., Hobley, L., Capeness, M., Rendulic, S., Schuster, S. C., Aizawa, S.-I., and Sockett, R. E. Characterizing the flagellar filament and the role of motility in bacterial prey-penetration by *Bdellovibrio bacteriovorus*. *Mol Microbiol*, 2006. **60**(2): p. 274-286.

382. Ely, B., Ely, T. W., Crymes, W. B., and Minnich, S. A. A family of six flagellin genes contributes to the *Caulobacter crescentus* flagellar filament. *J Bacteriol*, 2000. **182**(17): p. 5001-5004.

383. Kostrzynska, M., Betts, J. D., Austin, J. W., and Trust, T. J. Identification, characterization, and spatial localization of two flagellin species in *Helicobacter pylori* flagella. *J Bacteriol*, 1991. **173**(3): p. 937-946.

384. McCarter, L. L. Polar flagellar motility of the *Vibrionaceae*. *Microbiol Mol Biol Rev*, 2001. **65**(3): p. 445-462.

385. Wu, J. and Newton, A. Regulation of the *Caulobacter* flagellar gene hierarchy; not just for motility. *Mol Microbiol*, 1997. **24**(2): p. 233-9.

386. Wu, J. G., Benson, A. K., and Newton, A. Global regulation of a sigma(54)-dependent flagellar gene family in *Caulobacter crescentus* by the transcriptional activator FlbD. *J Bacteriol*, 1995. **177**(11): p. 3241-3250.

387. Wingrove, J. A., Mangan, E. K., and Gober, J. W. Spatial and temporal phosphorylation of a transcriptional activator regulates pole-specific gene-expression in *Caulobacter*. *Genes Dev*, 1993. **7**(10): p. 1979-1992.

388. Ramakrishnan, G. and Newton, A. FlbD of *Caulobacter crescentus* is a homolog of the NtrC (NRI) protein and activates sigma-54-dependent flagellar gene promoters. *Proc Natl Acad Sci U S A*, 1990. **87**(6): p. 2369-2373.

389. Quon, K. C., Marczynski, G. T., and Shapiro, L. Cell cycle control by an essential bacterial two-component signal transduction protein. *Cell*, 1996. **84**(1): p. 83-93.

390. Mullin, D., Minnich, S., Chen, L. S., and Newton, A. A set of positively regulated flagellar gene promoters in *Caulobacter crescentus* with sequence homology to the nif gene promoters of *Klebsiella pneumoniae*. *J Mol Biol*, 1987. **195**(4): p. 939-943.

391. Benson, A. K., Ramakrishnan, G., Ohta, N., Feng, J. L., Ninfa, A. J., and Newton, A. The *Caulobacter crescentus* FlbD protein acts as ftr sequence elements both to activate and to repress transcription of cell-cycle-regulated flagellar genes. *Proc Natl Acad Sci U S A*, 1994. **91**(11): p. 4989-4993.

392. Ramakrishnan, G., Zhao, J. L., and Newton, A. Multiple structural proteins are required for both transcriptional activation and negative autoregulation of *Caulobacter crescentus* flagellar genes. *J Bacteriol*, 1994. **176**(24): p. 7587-7600.

393. Mangan, E. K., Bartamian, M., and Gober, J. W. A mutation that uncouples flagellum assembly from transcription alters the temporal pattern of flagellar gene-expression in *Caulobacter crescentus*. *J Bacteriol*, 1995. **177**(11): p. 3176-3184.

394. Driks, A., Bryan, R., Shapiro, L., and DeRosier, D. J. The organization of the *Caulobacter crescentus* flagellar filament. *J Mol Biol*, 1989. **206**(4): p. 627-636.

395. Nierman, W. C., Feldblyum, T. V., Laub, M. T., Paulsen, I. T., Nelson, K. E., Eisen, J., Heidelberg, J. F., Alley, M. R. K., Ohta, N., Maddock, J. R., Potocka, I., Nelson, W. C., Newton, A., Stephens, C., Phadke, N. D., Ely, B., DeBoy, R. T., Dodson, R. J., Durkin, A. S., Gwinn, M. L., Haft, D. H., Kolonay, J. F., Smit, J., Craven, M. B., Khouri, H., Shetty, J., Berry, K., Utterback, T., Tran, K., Wolf, A., Vamathevan, J., Ermolaeva, M., White, O., Salzberg, S. L., Venter, J. C., Shapiro, L., and Fraser, C. M. Complete genome sequence of *Caulobacter crescentus*. *Proc Natl Acad Sci U S A*, 2001. **98**(7): p. 4136-4141.

FIGURE LEGENDS

Figure 1. Cryo-EM workflow. Schematic illustration of options for cryo-EM sample preparation, imaging, and data processing. LM, light microscopy; HPF, high pressure freezing; SPRF, self-pressurized rapid freezing; FIB, focused ion beam; CLEM, correlated light and electron microscopy; EM, electron microscopy.

Figure 2. Affinity grid designed to selectively capture virus-like particles (VLPs). Cryo-EM images of HIV CD84 VLPs applied to an untreated grid (A) and a 20% Ni-NTA cryo-affinity grid with His-tagged Protein A and anti-Env polyclonal antibody (B). Use of the affinity capture method leads to increased VLP concentration and improved particle distribution on the grid. See Kiss *et al.* (49) for experimental detail. Scale bars, 1 μm.

Figure 3. Motion correction of data recorded on a Direct Electron DE-20 significantly improves image quality. 2D projection cryo-EM image of coliphage BA14 particles before (A) and after (B) motion correction using Direct Electron, LP scripts and the corresponding power spectra (insets). The image was recorded at a frame rate of 12 frames per second with an exposure time of 5 seconds. Scale bars, 50 nm.

Figure 4. Zernike phase plate imaging of a phage-lysed bacterial cell provides contrast, revealing internal features. Cryo-ET slices of ϕCbK phage-lysed *Caulobacter crescentus* cell using ZPC at zero defocus. (A) A top slice of the tomogram illustrating the hexagonal surface layer (SL), (B) a central slice revealing newly assembled phages within the lysing cell, and (C) a central slice showing an assembled phage capsid in the process of genome packaging. Fringing artifacts are evident, particularly at the edge of the cell. (D) Corresponding 3D segmentation showing surface layer, SL,

green; outer membrane, OM, gold; inner membrane, IM, red; and ϕCbK, magenta. Scale bars, 200 nm.

Figure 5. Hole-free phase plate (HFPP) imaging provides enhanced contrast without strong fringing artifacts. Cryo-EM images of reovirus T1L particles using HFPP slightly underfocus. (A and B) reovirus T1L particles displaying attachment fibers as indicated by white arrowheads. The black arrow points to a released viral genome in (B). Scale bars, 50 nm.

Figure 6. CLEM imaging of transfected mammalian cells provides multi-scale information. HT1080 cells grown on a gold London Finder grid and transfected with EGFP-tetherin (green) and mCherry-Gag (red) were imaged by live cell fluorescence microscopy (A and B), then plunge frozen and imaged by cryo-EM montaging (C and D), and cryo-ET (E and F). The mCherry-Gag (red) signal in (A) and (B) corresponds to electron density of a thin cellular extension in (C) and (D). The black arrowheads in (E) and (F) indicate a tether attaching 2 VLPs. Dashed boxes correspond to the enlarged image in the next panel. Adapted from Strauss *et al.* (158). Scale bars, (A and B) 25 μm, (C) 10 μm, (D) 500 nm, (E) 100 nm, and (F) 50 nm.

Figure 7. Cryo-CLEM imaging of transfected mammalian cells. HT1080 cells transfected with EGFP-tetherin (green) and mCherry-Gag (red) imaged by cryo-fluorescence microscopy (A), cryo-EM montaging (B), and cryo-ET (C). Dashed boxes correspond to the enlarged image in the next panel. The yellow signal in (A) (inset) indicates colocalization of EGFP-tetherin (green) and mCherry-Gag (red) signal and corresponds to a cluster of HIV-1 VLPs tethered to a cellular extension in (B) and (C). Adapted from Hampton *et al.* (159). Scale bars, (A) 50 μm, inset is 3X, (B) 2 μm, (C) 200 nm.

Figure 1

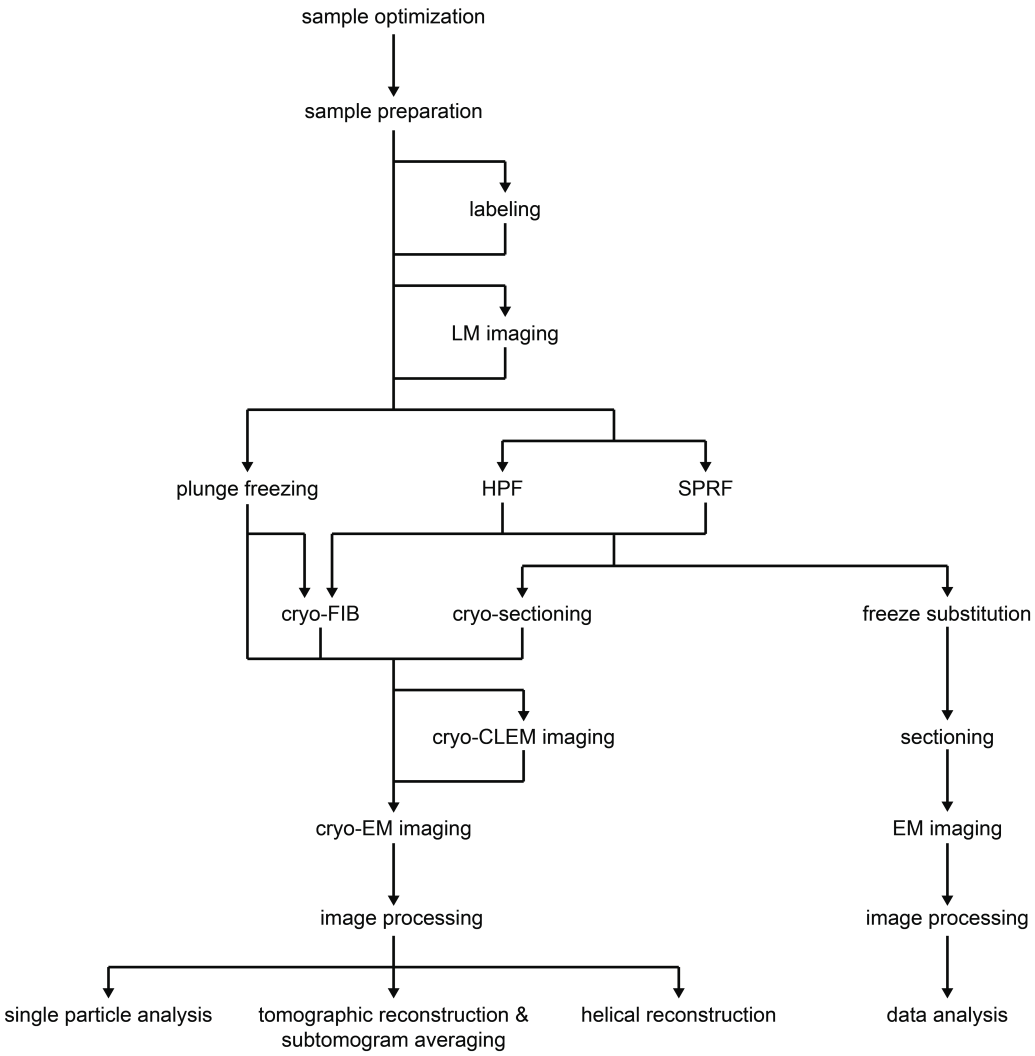
sample optimization
sample preparation
labeling
LM imaging
plunge freezing
HPF
SPRF
cryo-FIB
cryo-sectioning
freeze substitution
cryo-CLEM imaging
sectioning
cryo-EM imaging
EM imaging
image processing
image processing
single particle analysis
tomographic reconstruction & subtomogram averaging
helical reconstruction
data analysis

Figure 2

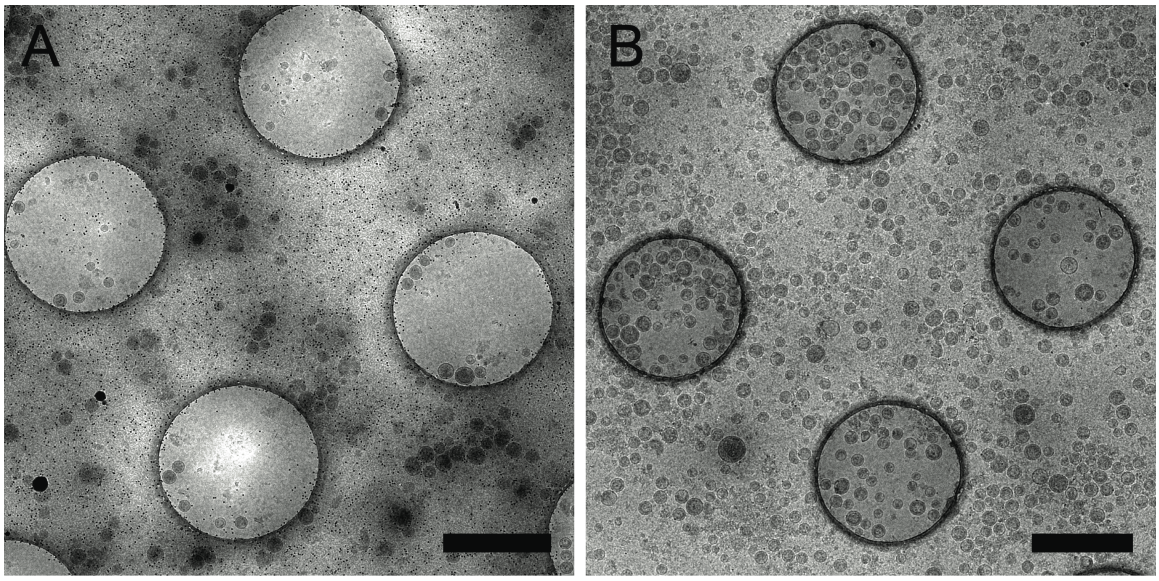

Figure 3

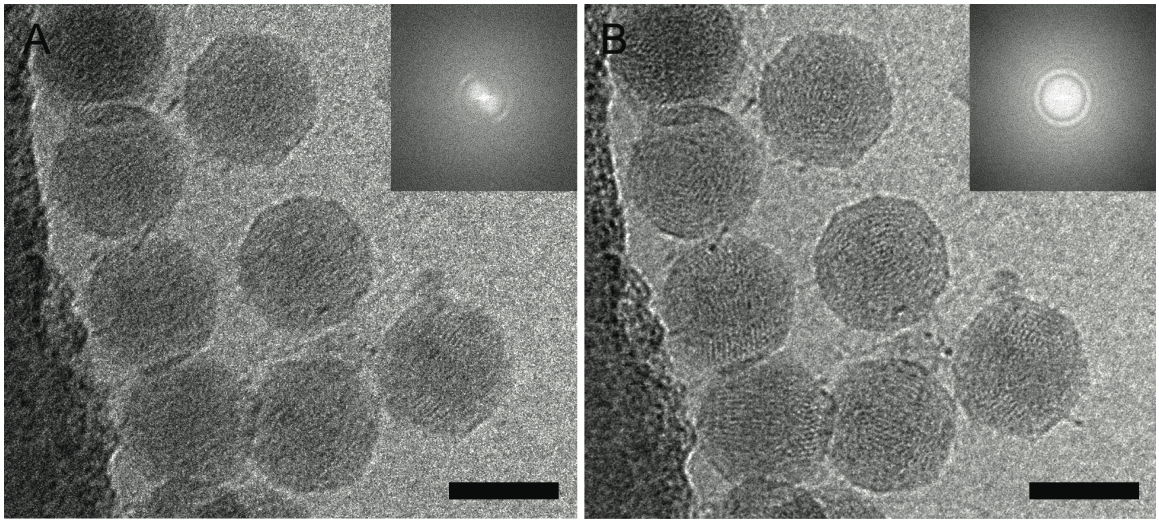

Figure 4

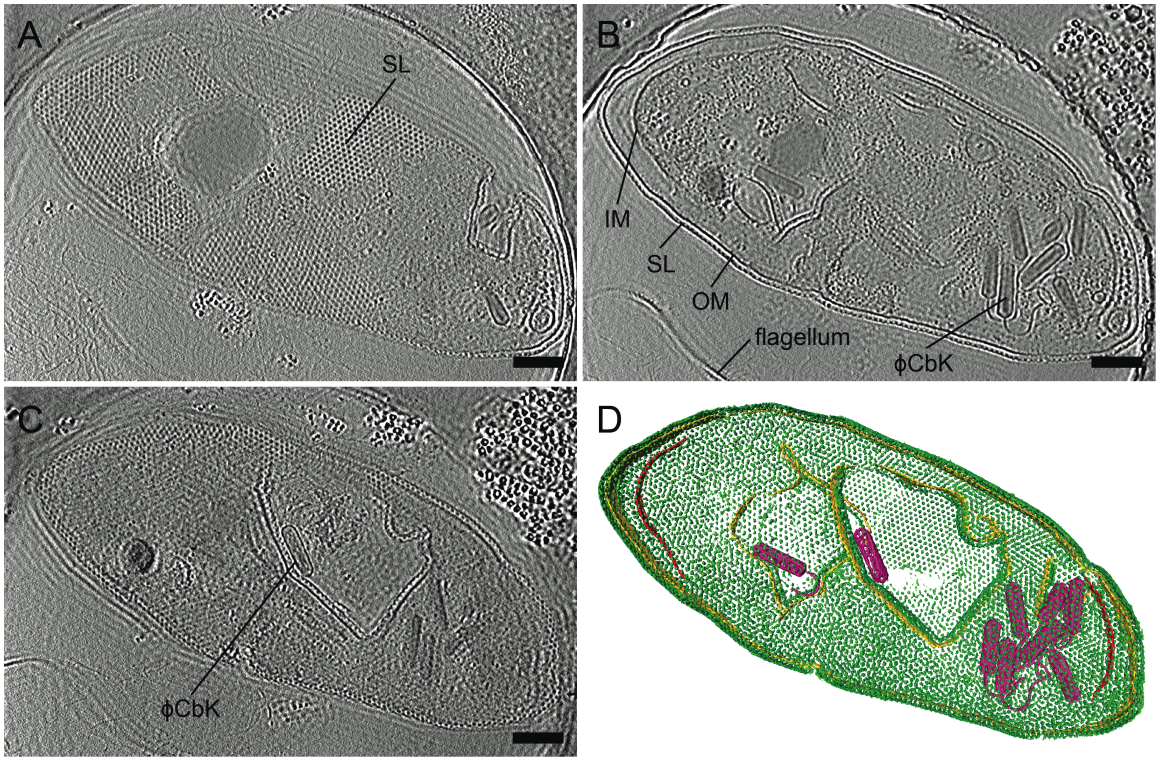

Figure 5

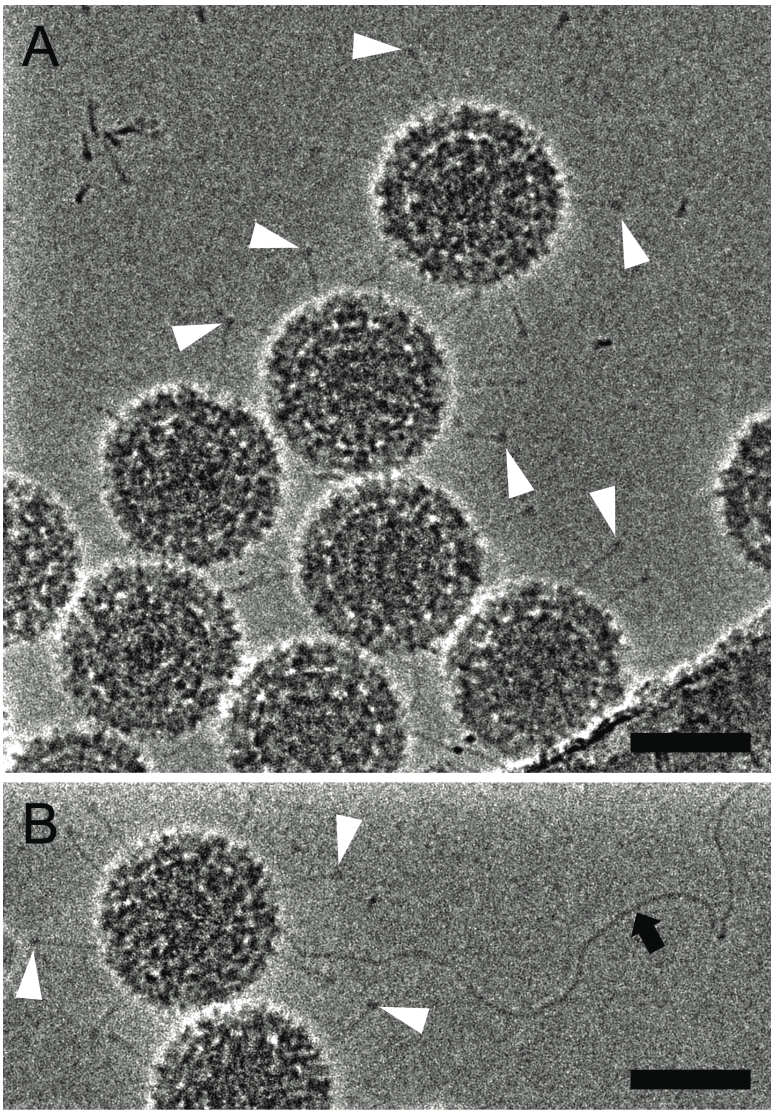

Figure 6

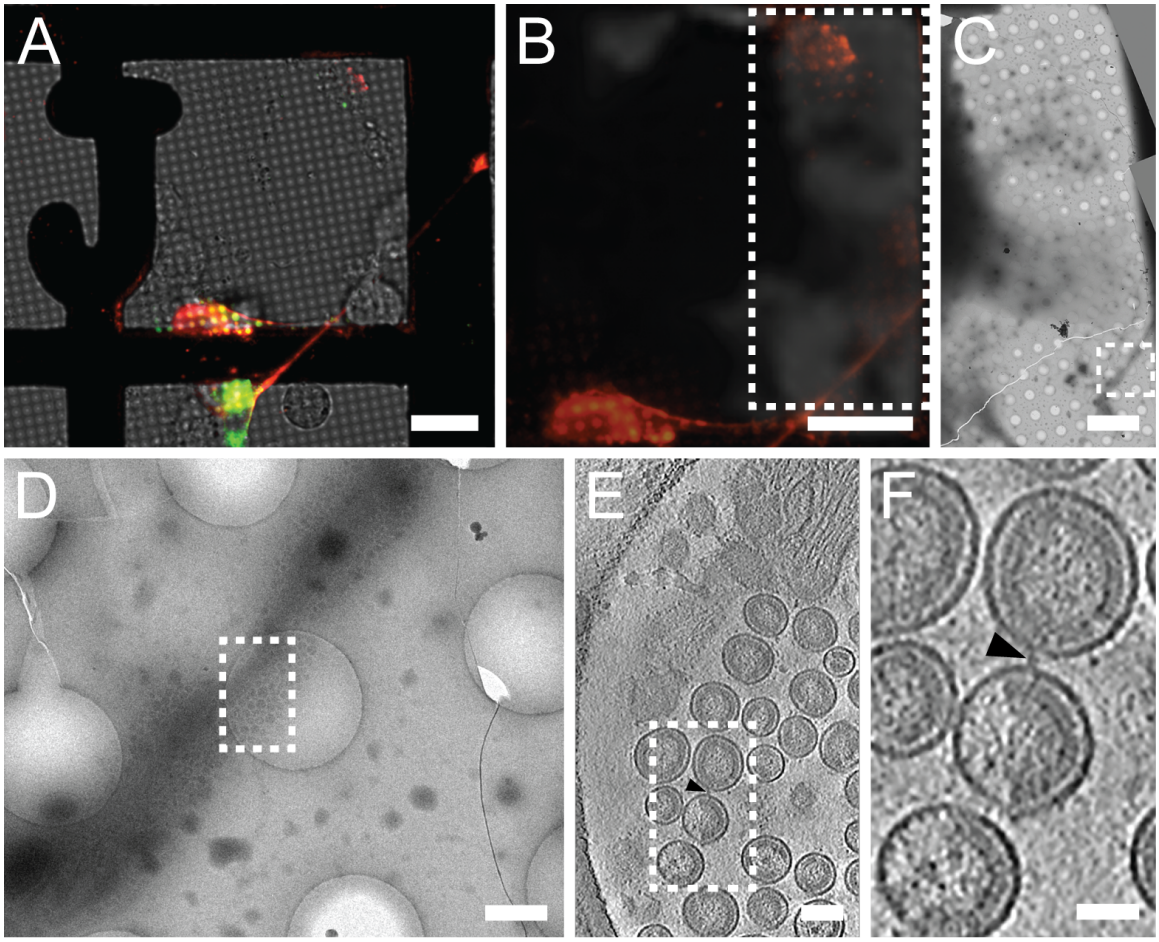

Figure 7

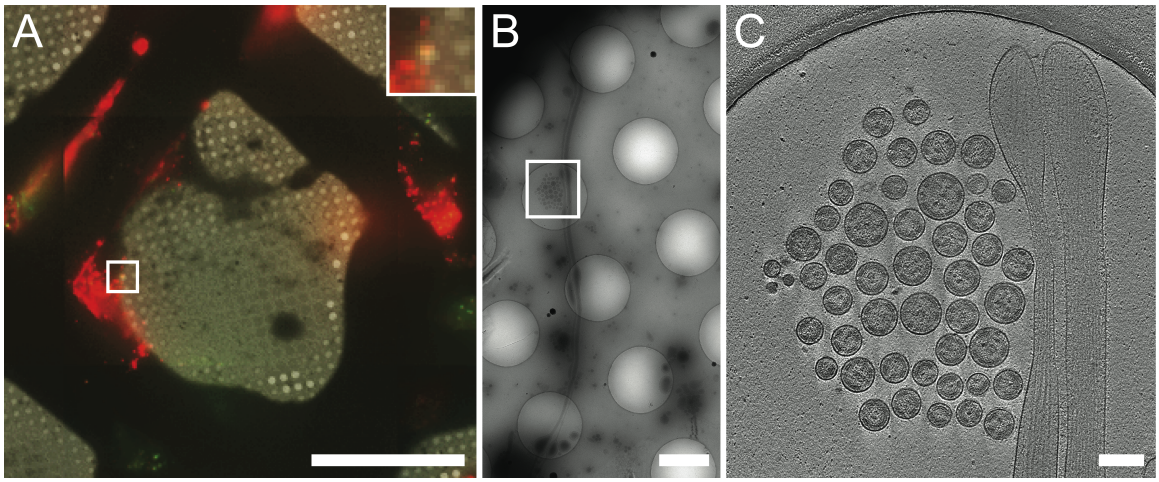

Chapter 2: Correlated fluorescence microscopy and cryo-electron tomography of virus-infected or transfected mammalian cells

Cheri M. Hampton,[1,5] Joshua D. Strauss,[1,5] Zunlong Ke,[2,5] Rebecca S. Dillard,[1,5] Jason E. Hammonds,[1] Eric Alonas,[3] Tanay M. Desai,[1] Mariana Marin,[1] Rachel E. Storms,[1] Fredrick Leon,[1] Gregory B. Melikyan,[1] Philip J. Santangelo,[3] Paul W. Spearman,[1] and Elizabeth R. Wright[1,4]

[1]Division of Infectious Diseases, Department of Pediatrics, Emory University School of Medicine, Children's Healthcare of Atlanta, Atlanta, GA

[2]School of Biology, Georgia Institute of Technology, Atlanta, GA

[3]Wallace H. Coulter Department of Biomedical Engineering, Georgia Institute of Technology and Emory University, Atlanta, GA

[4]Robert P. Apkarian Integrated Electron Microscopy Core, Emory University, Atlanta, GA

[5]These authors contributed equally to this work.

Published in:

Nature Protocols, 2017

Vol. 12, No. 1

p. 150-167

C.M.H. and E.R.W. wrote the manuscript. C.M.H., J.D.S., Z.K., R.S.D., J.E.H., E.A., T.M.D., M.M., G.B.M., P.J.S., P.W.S., and E.R.W. designed and performed the experiments, and edited the manuscript. R.E.S. and F.L. processed and analyzed data.

ABSTRACT

Correlative light and electron microscopy (CLEM) combines spatiotemporal information from fluorescence light microscopy (fLM) with high-resolution structural data from cryo-electron tomography (cryo-ET). These technologies provide opportunities to bridge knowledge gaps between cell and structural biology. Here we describe our protocol for correlated cryo-fLM, cryo-electron microscopy (cryo-EM), and cryo-ET (i.e., cryo-CLEM) of virus-infected or transfected mammalian cells. Mammalian-derived cells are cultured on EM substrates, using optimized conditions that ensure that the cells are spread thinly across the substrate and are not physically disrupted. The cells are then screened by fLM and vitrified before acquisition of cryo-fLM and cryo-ET images, which is followed by data processing. A complete session from grid preparation through data collection and processing takes 5–15 d for an individual experienced in cryo-EM.

INTRODUCTION

The first reported CLEM experiments were performed in the early 1960s and assessed the development of type 5 adenovirus in HEp-2 and HeLa cells [1, 2]. The experimental results defined the structural changes to the nucleus that occur due to infection with type 5 adenovirus and illustrated how the structure of the virus was affected by the preservation and fixation methods used. However, because the methodologies were not readily transferrable to other systems, and access to microscopes was limited, little progress was made in studies of viral replication using CLEM techniques.

As a substitute, indirect correlations have been made between live or fixed cell fluorescence images and high-resolution transmission electron microscope (TEM) images and structures. Fixation of cells is known to disrupt the integrity of cell membranes, and cell physiology, thus obscuring the native context of the viral replication event being imaged. Live-cell imaging occurs on the order of minutes before sample vitrification, and thus relocating the regions of interest (ROIs) once in the TEM can be highly inaccurate. This is because the cells either grow and shift positions on the grid, or are perturbed on the carbon substrate during the blotting process.

However, in the intervening years, cell biologists, molecular biologists, virologists, and structural biologists have made substantial technical advances that make widespread adoption of CLEM more feasible. Such advances include the following: strategies for manipulating and preserving cells and viruses; design of macro-molecular-complex-specific fluorescent labels; and engineering of new microscope hardware and software [3-13]. Developments in, and strategies for, cryo-CLEM have been reviewed previously in Briegel *et al.* [13]. These technological advances have generated renewed interest in examining many of the processes associated with viral replication using CLEM and, more

recently, cryo-CLEM approaches. The development of the cryo-fLM stage has made possible the direct correlation of the same vitrified, close-to-native-state fluorescently labeled sample at both the light microscope and TEM levels. The ability to instantaneously vitrify whole cells at a given time point and to image fluorescently labeled virus under cryo conditions, while static, offers a genuine and accurate cellular context in which to study the stages of virus–host cell interactions. Direct methods for structural cell biology were also hampered by a lack of non-physiology-altering labeling methods.

Now, with the development of a variety of CLEM imaging techniques, structural cell biology no longer exists apart from physiology, a situation in which only indirect inferences to physiological data were possible.

Development and overview of the protocol

We previously used live-cell fluorescence imaging before vitrification to identify fluorescently tagged ROIs within the cell [14]. Although this approach is useful for targeting cells expressing the labeled protein, it is difficult to obtain exact coordinates for CLEM because cells can grow and move on the grid between the live-cell imaging and freezing steps. Similarly, we have demonstrated the utility of native immunogold labeling of cell surface proteins and viral glycoproteins for cryo-EM and cryo-ET applications [15]. However, this technique relies on indirect labeling and is applicable only to cell and viral surface proteins. By incorporating cryo-based fluorescence imaging into our workflow, we have been able to increase the spatial precision with which we can locate tagged molecules, both on and in the cell.

Here we present a detailed cryo-CLEM protocol for native-state structural analysis of virus-infected or transfected mammalian cells, the stages of which are summarized in Figure 1. In particular, we take advantage of fluorescence labeling techniques to better locate points of interest in or on the cell. For cryo-CLEM studies of mammalian cells, samples are prepared by culturing cells of interest on carbon-coated gold or nickel EM grids (Steps 8–14). This is followed by infection or transfection of the cultured cells with fluorescently tagged viruses or viral cDNA, respectively (Step 15). The specimens are incubated and monitored by live-cell fluorescence microscopy for a specified period of time post infection or transfection, and are then plunge-frozen in liquid ethane (Steps 16–27). Cryo-fLM data are collected using either an inverted or upright light microscope outfitted with a liquid-nitrogen-cooled cryo-stage [13] (Steps 28–36). Once cryo-fLM imaging is complete, the specimen is transferred to the cryo-electron microscope for EM-level data collection. We use SerialEM [16] under low-dose conditions for grid mapping (Steps 37–40), correlation functions (Steps 41–45), intermediate magnification image montaging (Steps 46–47), and tilt series data collection (Steps 48–51) with the electron microscope. Once suitable positions are identified, low-dose higher-magnification image montages of specific cells are acquired in order to select fields for cryo-ET tilt series acquisition. Tilt series images are acquired with SerialEM software and processed into tomograms using eTomo (Steps 55–59). Subvolumes can be aligned, classified, and averaged using the PEET package or EMAN2 (Step 64). Alternatively, the tilt series 2D images and the 3D volumes can be ported into any other available software package, such as Relion [17], pyTom [18], jsubtomo [19], Bsoft [20], or Dynamo [21].

To successfully implement this protocol, the investigator should be comfortable with the following: cell culture techniques; the generation of fluorescent fusion proteins or other labeling schemes; and the operation of both fluorescence microscopes and TEMs. It should be noted that within the field

of cryo-EM the procedures and instrumentation used for CLEM and cryo-CLEM may vary and are dependent on the biological questions to be addressed [22, 23]. In this protocol, we describe the CLEM and cryo-CLEM approaches that we have adapted for use on specific biological targets of interest to us, and with the hardware and software available to us [14, 15]. However, the streamlined procedures for sample preparation and generation of multiscale image maps for correlation should be applicable to a broad range of cryo-CLEM experiments.

Applications of the method

Cryo-CLEM methods have been used to identify viruses in virus-infected cells to understand mechanisms associated with HIV-1 entry and herpes-simplex virus type 1 (HSV-1) transport in neurons, and to develop improved correlation workflows [24-26]. In addition, (cryo-)CLEM procedures were used to determine the arrangement of HIV-1 particles anchored to cell plasma membranes via tetherin, a host cellular restriction factor that inhibits enveloped virus release [14]. Cryo-CLEM of prokaryotes has also been described [22, 27-29] and sections of this protocol that describe imaging and analysis parameters are also relevant to studies of these systems. With further development of cryo-CLEM technologies [13, 24, 26] and macromolecular-labeling strategies [30-32], we anticipate that CLEM and cryo-CLEM methods will be routinely used for investigations of virus replication and broader topics in structural cell biology.

Comparison with other methods

Other methods for studying the viral replication cycle within cells typically include immunolabeled, thin-sectioned cells as an ultrastructural complement to live-cell imaging. The amount of chemical fixation and processing required for making these samples electron-dense can alter membranes and obscure the finer cytoskeletal details required for interpretation. Furthermore, although immuno-

EM techniques can effectively label and provide localization information about the virus, the method is unable to provide a comparable level of resolution for 3D assemblies afforded by using cryo-ET and subvolume averaging.

Limitations of the protocol

The electron beam of an intermediate voltage TEM is unable to penetrate sample thicknesses >~1 μm (ref. 33). Thus, whole-cell cryo-CLEM methods are best suited to specimens in which cryo-EM imaging can be targeted to regions <~750 nm thick, such as the thin lamella or other protrusions of vitrified cells. Thicker regions, such as the cell interior surrounding the nucleus, can be investigated using several other complementary techniques, including sectioning-based approaches such as cryo-ultramicrotomy (i.e., CEMOVIS) [33, 34] and cryo-focused ion beam milling [35, 36], or through scanning TEM-tomography approaches [37]. With the sectioning methods, additional experimental steps will be required so that the correlations to the fluorescent markers remain viable [38]. Another limitation of (cryo-)CLEM is the inability to precisely localize very small (<200-nm) molecules within a cell. Refined strategies for registration of both large and small fiducials have been proposed [26, 39]. Localization, therefore, is limited by the precision of fiducial registration, whereas resolution is limited by the 200-nm diffraction limit. To this end, super-resolution cryo-light microscopy is currently under development [29, 40, 41].

EXPERIMENTAL DESIGN

Sample preparation: choice of substrate

Choice of substrate is critical for cells to grow, adhere, and spread well. Because standard copper EM grids are toxic to cells, most cell culture is done using gold EM grids. It is standard practice for most experiments to use gold NH2 London Finder grids with Quantifoil holey carbon film. The grids are very malleable and must be handled with extreme care. Alternatively, 200-mesh gold Quantifoil grids that are sturdier can be used if adequate fiducials are used for localization [26, 39]. The selection of hole size and spacing will depend on the magnification used for data collection. The diameter of the holes present on the Quantifoil film should be at least 2 μm to permit an imaging area (between 1.5 × 1.29–3.14 × 2.36 μm) that is large enough for tilt series acquisition, and spacing between holes should be either 1 or 2 μm.

Sample preparation: choice of cell line

Choice of cell line is also a critical consideration in regard to optimal cell thickness for supporting large imaging areas, as well as to permissivity of infection. This step may require some optimization, as different cell types have different growth and adhesion characteristics. The cells should be adherent and spread readily across the substrate. In some cases, we may apply extracellular matrix proteins, namely collagen, poly-L-lysine, or fibronectin, to the surface of the grid to improve cell distribution and spreading. Relative cell thickness can be determined beforehand using either live-cell or fixed-immunostained approaches (Figure 2) to validate the utility of the biological specimen for cryo-CLEM analyses. In our case, we use confocal microscopy to capture serial optical sections of cells of variable thickness at a suitable resolution to resolve immunostained viral and cellular components.

Sample vitrification

Several automated cryo-plunge units are commercially available, as well as various homemade manual units. Here we describe blotting and plunge-freezing using the Gatan CryoPlunge3 system with GentleBlot blotters. GentleBlot blotters are engineered to require less pneumatic force than other models, which can tear or disrupt the thin carbon film on the grids. They allow the pressure on the specimen to be adjusted (from −1.0 to 0 mm). Blotting can also be rapidly optimized for single- or double-sided approaches. Our system works reproducibly with both blotters set to 0 mm using Whatman no. 1 filter paper custom-punched for these blotters. Blotters are rotated manually between grids up to four times, after which the filter paper must be changed to prevent saturation from media, buffers, and the relative humidity of the unit. We use 10-nm gold as fiducials for alignment of tilt series images and 100–200 nm TetraSpeck or FluoSpheres as registration fiducials. These can be combined at the proper ratio and applied to the grids just before blotting.

Cryo-fLM and Cryo-TEM

Cryo-fLM imaging typically requires the use of a liquid-nitrogen-cooled stage to keep the sample below the vitrification temperature. Several cryo-CLEM stages are commercially available: the Linkam BCS196 cryobiology stage (Linkam) [23], the Instec CLM77K or CLM77Ki (inverted) [42], and the FEI cryostage 2 [43, 44]. These cryostages may be engineered to be mounted to a number of commercially available upright or inverted microscopes. The drawback to these setups is that they necessitate the use of long (or extra-long)-working- distance objectives, resulting in a theoretical resolution limit of ~400 nm [23]. Alternatively, an integrated light and electron microscope can be used, which combines both cryo-fLM and cryo-EM imaging sources in the column of the TEM [45]. The Leica cryo-CLEM system [46] has the advantage of using a unique ceramic-tipped, short-working-distance objective with a resolution limit of ~200 nm. Our decision to use the Leica cryo-

CLEM system was also driven by the seamless nature of the hardware and software, which facilitates the direct registration of coordinates between the two imaging platforms and eliminates time-consuming generation of LM–TEM overlay images before collecting high- resolution cryo-ET data. Alternatively, external Matlab scripts have been developed for this purpose [26, 39].

We recommend testing a number of cryo-fLM configurations to determine which will perform best with the selected cell types, macromolecular targets, and fluorophores. There are a few critical points about the system that should be considered.

- It is essential that the temperature of the unit remain well below the ice transition temperature (approximately −150 °C) during the processes associated with specimen imaging and transfer; otherwise, crystalline ice artifacts will ruin the specimen.
- Care should be taken in the selection of the microscope objective lens because of its impact on the resolution of the cryo-fLM data, specifically for correlation and colocalization information. Currently, most objective lenses for cryo-fLM are long- or extra- long-working-distance air objectives, to avoid heat transfer to the specimen.
- It is also advisable that the cryo-fLM stage be motorized and automated to improve the speed of data acquisition, in order to limit the time that each cryo-specimen remains at room humidity levels.
- The cryo-fLM software should be sufficiently extensible to facilitate the acquisition and transfer of a grid map and coordinates to the cryo-EM data collection software.

Multiscale cryo-TEM imaging

Once the grid is transferred into the TEM, a grid map is acquired at ~100× in order to correlate directly with the map from the cryo-fLM. Through a series of manipulations of coordinate text files (Steps 41–45), coordinates and points of interest from the cryo-fLM and cryo-TEM maps will be correlated. Intermediate magnification (10,000×) montage maps are routinely acquired because they provide context for the condition of the cell of interest. Projection imaging at this magnification reveals whether the cell membranes are healthy and intact before lengthy tilt series acquisition. These maps can also be used for finer correlations with cryo-fLM maps. In addition, we use these maps for creating figures that explain the context of the structural data. Tilt series data acquisition can then be targeted to regions where cryo-fLM maps indicate appropriate levels of fluorescently tagged protein expression or individual virus fusion events. Preferences used for tilt series collection, such as the total electron dose, magnification, defocus (if applied), and other settings, will be dependent on the specimen, downstream data analysis, and information needs of the investigator.

Image processing

Several software packages are available for tomogram generation. We use IMOD's eTomo module, as it is contiguous with the SerialEM data acquisition software. For our subvolume analyses, we have been using EMAN2 [47, 48] and PEET [49, 50] (via IMOD) for subvolume averaging. However, a number of subvolume-processing software packages are available, and one should determine which will perform best with the selected macromolecular targets [18, 20, 21, 51, 52]. Segmentation of tomographic data can be done with IMOD, Amira (FEI Visualization Sciences Group), or other programs. Quantitative measurements can be generated and the distribution of objects analyzed using the model surfaces created.

MATERIALS

Reagents

- Appropriate cell line(s): cell lines used as examples in this protocol are as follows: A549 (ATCC CCL-185), BEAS-2B (ATCC CRL-9609), CV-1 (ATCC CCL-70), HeLa (ATCC CCL-2), HEL 299 (ATCC CCL-137), HT1080 (ATCC CCL-121), and MRC-5 (ATCC CCL-171) cells

  ! CAUTION The cell lines used in your research should be regularly checked to ensure that they are authentic and are not infected with mycoplasma.
- Viral stocks of interest: viruses used as examples in this protocol are measles and RSV
- Appropriate plasmids encoding fluorescently tagged proteins of interest
- Dulbecco's PBS, Ca^{2+} and Mg^{2+} free (DPBS; Lonza, cat. no. 17-512F)
- DMEM with 4.5 g/l glucose (Lonza, cat. no. 12-604F)
- Eagle's Minimum Essential Medium (EMEM; ATCC, cat. no. 30-2003)
- RPMI-1640 medium with L-glutamine (Lonza, cat. no. 12-702F)
- FBS (HyClone, cat. no. SH30071)
- PSA antibiotic–antimycotic solution, 100× (penicillin, streptomycin, and amphotercin B; Corning, cat. no. 30-004-CI)
- 70% Ethanol (from 200-proof; Decon, cat. no. DSP-MD43)
- MilliQ water or molecular-grade water (Corning, cat. no. 46-000-CM)
- Trypsin/EDTA (Sigma-Aldrich, cat. no. T4049)
- Trypan blue (HyClone, cat. no. SV30084.01)
- Collagen, type 1, rat tail (Corning, cat. no. 354236)
- jetPRIME transfection reagent (Polyplus Transfection, cat. no. 114-15)

- Live Cell Imaging Solution (Thermo Fisher Scientific, cat. no. A14291DJ)
- Fluorescent microspheres, 200 nm (TetraSpeck, cat. no. T7280, or FluoSpheres, Molecular Probes, cat. no. F-8809)
- BSA-treated tracers, EM grade (EMS, cat. no. 25486)
- Liquid nitrogen (NexAir, cat. no. LN NI-250)

  ! CAUTION Liquid nitrogen is a cryogen. Handling of liquid nitrogen should be done in a fume hood, under a venting snorkel, or in a well-ventilated area. All cryogens and cryogenic materials are extremely cold and personnel should wear the necessary personal protective equipment (PPE: gloves, goggles, lab coat, and closed-toed shoes).
- Ethane (99.999% purity; NexAir, cat. no. SG ETHANE_RG_RB)

  ! CAUTION Ethane is a fire hazard and an asphyxiant. Do not use it near an open flame. Work with ethane should be done in a fume hood, under a venting snorkel, or in a well-ventilated area. Personnel should wear the necessary PPE: gloves, goggles, lab coat, and closed-toed shoes.

EQUIPMENT

- Forceps, thin-tip, style 55 (Dumont, cat. no. 0203-55-PO)
- Forceps, thin, bent-tip, style 5/15 (Dumont, cat. no. 0203-5/15-PO)
- Gold Finder grids with Quantifoil R 2/1 carbon film (Quantifoil, cat. no. NH2 Au-R2/1)
- Gold 200 mesh grids with Quantifoil R 2/1 carbon film (Quantifoil, cat. no. Au R2/1 200)
- MatTek dishes (MatTek, cat. no. P35G-0-20-C)
- T25 and T75 flasks, TC treated and vented (Olympus, cat. nos. 25-207 and 25-209)
- Gloves (Genesee, cat. no. 44-103M)
- 0.22-μm polyethersulfone (PES) filter, 500 ml (Olympus, cat. no. 25-227)
- 1.5-ml Microcentrifuge tubes (Corning, cat. no. MCT-150-C)
- C-Chip hemocytometer (Incyto, cat. no. DHC-N01)
- 1-, 5-, 10-, and 25-ml Serological pipettes (Genesee, cat. nos. 12-102, 12-104, 12-106, and 12-107)
- 5-ml Aspirating pipette (Celltreat, cat. no. 229265)
- Pipet-Aid (Drummond, cat. no. 175705)
- 10-, 20-, 200-, 1,000-μl Barrier pipette tips (Olympus, cat. nos. 24-401, 24-404, 24-412, and 24-430)
- 1,000-μl Standard pipette tips (Olympus, cat. no. 24-430)
- Whatman qualitative filter paper, grade 1 (Sigma-Aldrich, cat. no. 1001-055)
- Denton Benchtop Turbo thin-film evaporator apparatus (Denton Vacuum)
- Carbon rods (EMS, cat. no. 70220-01)
- Piezo transducer gauge (to monitor the thickness of the carbon; Inficon, cat. no. SQM-160)
- Plasma cleaner (Harrick, cat. no. PDC-32G)

- Vacuum gauge for plasma cleaner
- Mammalian CO_2-charged cell culture incubator (Forma Scientific, cat. no. 3110)
- Biosafety cabinet
- Light microscope, Evos (AMG)
- Zeiss LSM780 confocal microscope or equivalent
- Cryoplunge3 System with GentleBlot (Gatan, cat. no. 930.GB)
- Cryo-grid storage boxes (Pacific Grid Tech, cat. no. GB-4R)
- Liquid nitrogen Dewar flask(s)
- Leica EM Cryo CLEM system (Leica, cat. no. EM cryo_CLEM DM6 FS)
- Cryo-transmission electron microscope (Jeol, model no. JEM-2200FS)
- High-tilt cryo-specimen holder and holder transfer system (Gatan, model no. 914)
- US4000 charge-coupled device (CCD) camera (Gatan, model no. 895)
- DE-20 camera system (Direct Electron)
- Wacom Cintiq monitor
- Computers (Mac or Linux) with 16 GB or more RAM, 1 T or more storage space

Software

- LASX (Leica): fLM imaging software for obtaining single images or grid maps; it allows selection of coordinates for transfer to the TEM
- TEMCon (Jeol): TEM controller
- DigitalMicrograph (Gatan): image acquisition software
- DE-IM (Direct Electron): detector configuration and image acquisition software
- PhotoShop (Adobe): used for overlaying fLM and TEM images
- SerialEM [16]: TEM and tomography software

- Motion correction Python scripts for frame alignment (Direct Electron)
- 3dmod [53]: for alignment of tilt series, assembly of montages, measurements, and image processing
- CTFFIND4 [54]: contrast transfer function (CTF) estimation
- PEET [49, 50]: subvolume alignment and classification
- EMAN2 [48]: CTF estimation, subvolume alignment, and classification
- Amira (FEI Visualization Sciences Group): segmentation (3D rendering) of tomograms and quantitative measurements

REAGENT SETUP

Cell cultures, virus stocks, and transfection reagents

These materials should be acquired from the ATCC, other bioreagent sources, and collaborators. The cells and viruses should be propagated using standard cell culture and virological procedures supplied by either the manufacturers or collaborators [11, 12, 14, 15]. HeLa, A549, and MRC-5 cells should be maintained in filtered (0.22 μm) DMEM with 4.5 g/l glucose, 10% FBS, and 1% PSA antibiotic–antimycotic solution (final concentration: 100 IU/ml penicillin, 100 μg/ml streptomycin, and 0.25 μg/ml amphotercin B). The transformed human bronchial epithelium cell line BEAS-2B should be maintained in RPMI-1640 medium (Lonza, 12-702F, with L-glutamine). The human lung fibroblast cell line HEL 299 should be maintained in EMEM complete medium (ATCC). Transfection protocols should be adapted from source material provided by the vendor in order to suit correlative imaging studies [14].

EQUIPMENT SETUP

Tissue culture and plunge-freezing apparatus

To maintain both a nonhazardous and a contamination-free environment for working with mammalian cells and virus-infected or transfected mammalian cells, all cell culture and plunge-freezing equipment should be housed in a biosafety-level 2 (BSL 2) room isolated from common laboratory space. In our case, the room contains a biosafety cabinet; a CO_2-charged, water-jacketed cell culture incubator; a refrigerator; a plasma cleaner; several plunge-freezing apparatuses; liquid nitrogen Dewar flasks (daily use and storage); necessary gas cylinders; and miscellaneous plasticware and supplies.

Cryo-fLM and cryo-TEM

To minimize the impact of relative humidity on the stability and longevity of cryo-specimens and the success of prolonged cryo-imaging sessions, cryo-fLM and cryo-TEM systems should be contained in environmentally controlled rooms. In our laboratory, the cryo-fLM and the cryo-TEM are located in adjacent rooms, where the temperature is maintained at ~21 °C and the relative humidity level at 30% or less.

PROCEDURE

Preparation of EM grids ● TIMING ~1–2 d

1. Take 4–20 gold Quantifoil grids (either 200 mesh or NH2 Finder-style) and screen them on a light microscope to confirm that the carbon film is intact.
2. Place a group of screened grids in the center of a glass Petri dish lined with Whatman filter paper and set the two carbon graphite rods, one single-pointed, the other flat, at an appropriate distance (12 cm) from the grids to achieve adequate evaporation (Figure 3).
3. Reinforce the carbon film on the grids by evaporating an extra ~4–5 nm of carbon over the grids in a Denton Benchtop Turbo carbon evaporator or similar device; this step prevents the carbon from becoming too brittle during blotting and plunge-freezing (Step 26). The thickness of the carbon is determined with a calibrated piezo transducer gauge and may be estimated by the color of carbon that has evaporated onto the filter paper: a very light tan/gray color is all that is required.
4. Once the appropriate thickness of carbon has been attained, remove the grids from the carbon evaporator and place them in a storage box until required.

   ▲ **CRITICAL STEP** Jarring or percussive dropping of the grid storage box can result in torn and broken carbon films.

   ■ **PAUSE POINT** Grids can be stored under vacuum at room temperature (20–22 °C) for several weeks, but they are ready to be used the same day.
5. Sterilize the carbon film side of the grids by plasma cleaning in a glow discharge system under vacuum (0.15 Torr) for 10–30 s on the highest radio frequency setting. This procedure also imparts a slight positive charge to the carbon film.
6. Perform a second sterilization step by placing the grids in 2 ml of 70% ethanol in MatTek dishes (35-mm dish diameter, 20 mm glass) in a biosafety cabinet; place up to three grids per

dish. Introduce the grids slowly and vertically using forceps to avoid damaging the carbon film. Once the grid is fully submerged, lay it flat on the bottom of the dish with the carbon film side up. Let the grids remain in the 70% ethanol solution for 5 min. Alternatively, simply dip the grids vertically in and out of 70% ethanol one to two times.

▲ **CRITICAL STEP** Do not place the grids flat on the liquid surface; this will tear the carbon film because of surface tension and/or trap air under the carbon film, causing the grids to float on the surface of the medium and other reagents in subsequent steps.

7. (Optional) If required for the cell line of interest, perform the steps in Box 1 to coat the grid carbon film with extracellular matrix protein, e.g., collagen, poly-L-Lysine or fibronectin, to enhance cell adhesion to the carbon.

▲ **CRITICAL STEP** This step may require repeated trials until suitable conditions have been determined.

Culture of cells on EM grids ● TIMING 1–2 d

8. Aspirate the cell medium from a culture of low-passaged cells of choice (fewer than 20 total passages; ideally fewer than 10) in a T75 flask, wash the cells with 5–10 ml of DPBS and aspirate.
9. Add 1–2 ml of trypsin and incubate for ~5 min at 37 °C.
10. Add 5 ml of complete medium to dilute the cell suspension and mix by pipetting up and down a few times with a Pipet-Aid to break up any clumps of cells.
11. Take an aliquot of cells and dilute in trypan blue at a ratio of 1:4 (cells/trypan blue) and apply to a hemocytometer or cell counter for counting.
12. Carefully aspirate the ethanol (or medium, if steps in Box 1 were performed) from the MatTek dish containing the EM grids (from Step 6 or Box 1, step 4) and replace with fresh

complete medium. Some cells may require the addition of growth factors to the medium to encourage cell spreading.

13. Add the trypsinized cells in complete medium (from Step 10) to the MatTek dishes (from Step 12) and swirl the dish to ensure even distribution of cells.

    ▲ **CRITICAL STEP** It is recommended to initially seed cells at both high and low density—for example, 50,000 and 100,000 total cells—and then examine the grids under the light microscope before infection or transfection, and again before freezing, to make sure that the cell density is appropriate for cryo-ET (Figure 4). Seeding density is dependent on factors that are specific to each cell line, such as overall size and tendency to spread, as well as mitotic index. Some cell lines do not grow well when plated too sparsely. Addition of growth factors to the medium may help. In addition, it is important to monitor cell morphology. If the cells are round and not spreading, they will not be suitable for imaging by cryo-EM methods.

14. Place the dishes in the incubator at 37 °C with 5% CO_2 and monitor cell growth under a light microscope every 4–6 h to determine when the appropriate confluency of attached cells has been reached on the TEM grid. Typical confluency is 30–50%, with optimally one to two cells per grid square (Figure 4).

    ▲ **CRITICAL STEP** Cells growing on the dish will spread and become confluent faster than cells growing on the grids. The cells on the TEM grids should not be allowed to become 100% confluent, as they will not be spread thinly enough to allow adequate vitrification, resulting in cubic ice formation and large areas of overlapping cells that are too thick to be penetrated by the electron beam.

Introduction of virus to cells ● TIMING 30 min to 3 d

15. Virus can be introduced into cells in a number of ways. Transfection of plasmid-encoded viral cDNA can be used to create a noninfectious version of the virus while simultaneously adding a fluorescent tag to a viral protein of interest. Cells can also be co-transfected with DNA plasmids for labeled endogenous cell proteins for colocalization studies. Infection of cultured cells to study assembly and release of newly synthesized virus is done by adding viral particles directly to cultured cells. For fusion or transduction, pseudo-typed viral strains are added to study early events, and no new virus is produced. For transfection, follow option A, for infection, follow option B, and for fusion or transduction, use option C.

    ! CAUTION This step, including live-cell imaging, should be performed in BSL 2 rooms, and procedures associated with virus infection/transfection should be completed within a biosafety cabinet with the appropriate PPE (gloves, goggles, lab coat, and closed-toed shoes) to minimize external contamination of the cell cultures and for personal health safety when handling virus stocks.

    (A) Transfection of cells with virus-encoding plasmid ● TIMING 1–2 d

        i. In a 1.5-ml Eppendorf tube, add 200 µl of jetPrime diluent per transfection and 1 µg of total plasmid DNA and mix according to the manufacturer's instructions [14, 15].

        ii. Add jetPrime (2:1 (vol/vol) ratio) and mix. Incubate the mixture for 15 min at room temperature and then evenly pipette the mixture onto the cells in the MatTek dishes (from Step 14).

        iii. Put the MatTek dishes back into the tissue culture incubator and monitor cell density, cell morphology, and transfection efficiency using fLM to determine when cells are ready for plunge-freezing (typically 24–36 h post transfection).

Determining factors for the freezing time point include levels of fluorescent protein expression, as well as cytotoxic effects on cell morphology. Alternatively, cells grown in additional MatTek dishes can be fixed and immunolabeled for viral proteins.

(B) Infection of cells with viral particles (e.g., with RSV, measles, or pseudotyped HIV) ● TIMING 1–3 d

i. Infect cells of the correct confluency (from Step 14) by adding virus at an appropriate multiplicity of infection (MOI).

▲ **CRITICAL STEP** Determination of the appropriate MOI and timing of virus application are essential for optimal viral density and imaging.

ii. Incubate the cells for 24–36 h.

iii. Image cells via a light microscope to determine when to plunge-freeze, typically when cytopathic effects appear, defined by the presence of large syncytial cells, which can be directly visualized by inverted phase-contrast microscopy 24–48 h post infection.

Fusion or transduction (e.g., of pseudotyped HIV-1 to CV-1 cells) ● TIMING 30–60 min

(C) Fusion or transduction (e.g., of pseudotyped HIV-1 to CV-1 cells) ● TIMING 30–60 min

i. Remove most, but not all, of the medium from the cells (from Step 14).

ii. Add virus diluted in cold Live Cell Imaging Solution at an appropriate MOI.

iii. Incubate the virus and cells at 4 °C for ~30 min to prebind the virus and synchronize timing of fusion. Length of time will vary based on virus and should be determined empirically (Step 15C(vi)).

iv. Remove the unbound virus solution and wash the once with 2 ml of cold PBS.

v. Return the dish to the 37 °C incubator to allow fusion to proceed, and cells and cytoskeletal components, e.g., microtubules, to recover from cold temperature so that cell structure is preserved.

vi. To determine the time point for freezing, add 2 ml of cold Live Cell Imaging Solution and image the grids at room temperature on a Zeiss LSM780 confocal microscope (or equivalent). Early-stage uptake of the virus is characterized by observation of canonical 'omega' structures or clathrin-coated pits, whereas later events such as uncoating and transport are characterized by observation of viral cores and/or association with cytoskeletal networks.

▲ **CRITICAL STEP** For investigations of virus fusion, the prebinding of the virus in the cold (4 °C) blocks fusion events and promotes synchronization, although the cold temperatures may also cause cytoskeletal components—e.g., microtubules—to disassemble, thus preventing a true contextual interpretation of cell structure.

Vitrification of grids by plunge-freezing ● TIMING 1 h

▲ **CRITICAL** Here we describe vitrification using the Gatan CryoPlunge3 system with GentleBlot blotters. Other systems can be used, but Steps 16–27 will need to be modified accordingly.

▲ **CRITICAL** Warm the Gatan forceps, BSA-gold, media, and DPBS in the tissue culture incubator before cryo-plunging. Maintain a stable working temperature around the freezing apparatus (~20 °C). The plunger should be located directly next to the cell culture incubator to facilitate rapid transfer. We use a thick piece of Styrofoam as an insulated working platform to prevent contact of culture dishes and media with the cold laboratory bench.

16. Set up the plunge-freezing apparatus (Steps 16–19; Figure 5). Set the pressure on the nitrogen gas tank to 60 psi.
17. Wet the sponges with warm water to humidify the chamber (80–90% humidity when freezing). If the experiments require a long session time to freeze many grids, sponges should be periodically re-wetted to maintain optimal humidity.
18. Fill the cooling workstation with liquid nitrogen and allow the temperature to stabilize at approximately -194 °C (~10 min).
19. Once the workstation is adequately cooled, condense the ethane gas into the cup. The temperature for the ethane cup should be set to −168 to −170°C to maintain the ethane at its melting point. This has the advantage of a longer working time and a more stable vitrification temperature.
20. *Transfer and vitrification of grids* (*Steps 20–27*). Preload a pipette with 5 µl of well-mixed fiducial solution (or DPBS, if fiducials are not being used) in readiness for Step 23 so as to minimize exposure of the grid to air.
21. At the appropriate time point, gently remove a grid from the MatTek dish (from Step 15) using the Gatan-supplied plunging forceps and secure the grid in the forceps with the black sliding clip. Lift the grid vertically from the culture medium.

    ▲ **CRITICAL STEP** To lift the flat grid from the surface of the dish, it is recommended to use well-maintained forceps. Do not push the grid against the edges of the dish, as this may result in bending of the grid and tearing of the carbon film. A gentle top-to-bottom motion along the edge of the TEM grid is enough to slide the bottom tip of the forceps under the edge. Be sure to grip the grid only by the outer rim, to avoid puncturing the carbon film and to ensure even blotting.
22. Dip the grid vertically into a small container of prewarmed DPBS (37 °C) for a few seconds.

23. Immediately pipette onto the grid the 5 μl of pre-prepared fiducials (from Step 20) and wait for 10–30 s. If fiducial markers are not being used, add the 5 μl of DPBS to the carbon side of the TEM grid immediately before transfer to the humidity chamber; this prevents excessive evaporation and allows for more consistent blotting times.
24. Transfer the grid to the plunge rod and raise the forceps into the humidity chamber; this should be done quickly to prevent any evaporation of buffer, which may result in an increased salt concentration on the grid and can cause cell membranes to rupture.
25. Set the blot time to 6 s to achieve thin ice suitable for tomography along cell edges and cell protrusions. It is estimated that the blotting rate for Whatman no. 1 filter paper is 1 μl of liquid per second. The blot force should be determined empirically and may differ between individual units.
26. Rotate the plunging rod so that the TEM grid is parallel to the blotting paper, and press the start button to activate the automated blotting and plunging process.

    ▲ **CRITICAL STEP** Remember to rotate the blotters between grids to avoid saturating the blotting papers with media and other solutions.
27. Transfer the grid to a grid storage box under liquid nitrogen, and store it in a liquid nitrogen Dewar flask until imaging. Repeat Steps 20–27 until sufficient grids have been vitrified.

    ! CAUTION Handling of liquid nitrogen and liquid ethane should be done in a fume hood, under a venting snorkel, or in a well-ventilated area. All cryogens and cryogenic materials are extremely cold, and personnel should wear the necessary PPE (gloves, goggles, lab coat, and closed-toed shoes). Liquid ethane is explosive; handle it with care. When you have finished plunge-freezing samples, allow the liquid ethane to evaporate in a fume hood or under a venting snorkel.

■ **PAUSE POINT** Grids, once frozen, may be stored in liquid nitrogen indefinitely. Alternatively, one may proceed immediately to cryo-fLM imaging (Step 28).

Cryo-fLM imaging ● TIMING 30–45 min

28. Load the grid into the cryo stage (Steps 28–30, Figure 6). Turn on the liquid nitrogen pump to cool the cryo-fLM stage to −195 °C. Fill the cryo-transfer box with liquid nitrogen.
29. When the temperature has stabilized (~15 min), place the grid storage box in the loading area (Figure 6b, ii). With precooled bent-tip forceps, transfer the grid, carbon side up, to the copper cartridge (Figure 6c). Gently lower the cartridge clips onto the grid edges. Using the clamp on the transfer rod (Figure 6b, iii), retrieve the loaded cartridge from the loading block and slide the loading block out of the transfer rod path.
30. Carry the transfer station to the microscope and slide it into the loading port. Make certain that the cryo objective is raised (~2 mm), and open both gates to the cryo stage. Slide the transfer rod and cartridge into place in the cryo stage, and then open the clamp on the transfer rod and retract the rod from the stage, closing the gates behind.
31. *Cryo-fluorescent imaging of the grid* (*Steps 31–35*). Lower the objective lens (50×, ceramic-tipped, and short working distance (numerical aperture = 0.90), paired with a 1.25× magnification booster for a working magnification of 62.5×), and determine focus. Set the intensity levels for the fluorescent channels.
32. Create a focus map of the area to be imaged using the microscope software. Leica LASX software allows creation of acquisition templates for overlapping (10%) image tiles of the grid. In the interest of a shorter acquisition time and limiting our focus to areas useful for tomography, we generally use a 3 × 3 template of the center region of the grid (corresponding to an area of 401.78 × 300.02 μm) and an image binning setting of 2 for

autofocus. The focus map is useful because the TEM grids are rarely flat and level, creating a focus gradient from one side of the grid to the other.

▲ **CRITICAL STEP** Creation of the focus map can be done using bright-field imaging; however, this usually focuses on the holey carbon film. Note that for fluorescence imaging, the desired focus is often at a different *z* height. Therefore, a second focus map using a fluorescence channel may be useful. However, note that attempts to use a fluorescence channel for the focus map may result in the focus being on the grid bar edges instead of the sample if there is insufficient fluorescence contrast on the cell.

33. Acquire the image map at a binning setting of 1 (20–40 min for three-channel *z* stacks).
34. (Optional) If desired, reacquire *z* stacks of cells of particular interest at a binning setting of 1 for further image processing (Figure 7).
35. Remove the grid and cartridge by raising the objective lens, and retrieving them with the well-chilled transfer rod. Place the grid back into the grid box for transfer to the TEM.
36. *Selection of registration and ROI points.* Open the image map in the CLEM viewer module. This software allows for placement of landmark registration points on the imaged area for alignment to the cryo-TEM map. Then add as many ROI markers as needed. The software saves all text coordinates, overview, and thumbnail images to aid in relocation at the TEM (Figure 7).

▲ **CRITICAL STEP** Be careful when selecting registration points that are in areas of thick ice, especially next to grid bars or in corners, as these will not be penetrable by the electron beam. Instead, choose clusters of cells, fiducials, or unique cell morphologies near the central *z* image.

Creation of low-magnification cryo-TEM maps ● TIMING 20–30 min

37. Load the grid into a Gatan 914 holder, or another cryo-transfer device, and insert it into the microscope. Allow time (~15–20 min) for the microscope vacuum to recover, as the grid may have acquired moisture from the atmosphere.
38. Using SerialEM software, acquire a low-magnification (100–150×) map of the entire grid. The full grid montage requires an image overlap of 15–20%, depending on the microscope stage accuracy.
39. Save the stitched map image to a new window to prevent overwriting it during tilt series acquisition.
40. *Alignment of the low-magnification map to actual stage coordinates*. Add a point on an obvious feature in the map and navigate to it using navigator 'Go to XY'. There is often a substantial offset between the map and stage coordinates, in which case move the stage to the actual feature. Take a record image. Left-click in the image to place a green cross at the desired point and select 'Shift to Marker' under the navigator tab. Save the navigator file.

Correlation of the TEM map with the CLEM map ● TIMING 30 min

41. *Importing of the CLEM map into the SerialEM software on the TEM*. Using the navigator tab, use 'Import Map' to select your_CLEM_map.tif imported from the LASX software. Double-clicking will load it as a new map number 2 (red).
42. *Adding of the CLEM coordinates to the navigator file*. Using a text editor, open the your_CLEM_map.nav file and copy the x, y, and z coordinates and paste them into the current saved (TEM) navigator file (Step 40). Save the file, and then under the SerialEM navigator tab choose 'Read' and 'Open' to reload it. Select each of the CLEM registration

points in the navigator window and set labels to '2R1', '2R2', and so on, using the check box at the top of the window, and change the label color to red. Save the navigator file again.

43. *Adding of the registration points to the TEM map*. On the TEM map, add registration points to match those from the CLEM map, using the .tif CLEM image as a guide, set labels to '1R1', '1R2', and so on, and change the label color to blue.
44. *Registration of TEM and CLEM maps to one another*. Under the navigator tab, select 'Transform Items.' Save, read, and open the TEM navigator file again to see these points on the cryo-TEM map.
45. *Adding of the ROI points to the TEM map*. Repeat the copy-and-paste procedure (Step 42) for the ROI points in the CLEM navigator file. Read and open the navigator file again, and set these points to be green. Select 'Transform Items' again and the points should be placed on the cryo TEM map. Use the navigator 'Go to XY' command to move the stage to the coordinates (Figure 8).

Cryo-TEM data acquisition ● TIMING 6–18 h

46. *Intermediate-magnification montaging* (*Steps 46–47*). Identify a cell region surrounding a marked ROI. Using the Gatan US4000 CCD camera, set up low-dose record properties at a magnification of 10,000× with enough defocus (−15 to −20 μm) to see the structural detail of the viruses, including viral glycoproteins and known internal structures. Keep the beam slightly larger than the detector area, and set the dose to ~1 electron per square Ångstrom (~1 e/Å^2). This will result in an additional ~5 e/Å^2 exposure for each image of the montage.
47. In the navigator window, select 'Add Polygon.' Click points on the TEM map to define the region. Under the navigator tab, select 'Montage' 'Setup Polygon Montage.' Set the image overlap to 15–20% and start montage acquisition. These maps are useful for CLEM—

identifying areas to image by tomography, assessing ice thickness, determining whether cell membranes are intact, providing cell and virus context information for tomograms, and obtaining quantitative data—and for the preparation of figures (Figures 9–11).

48. *Tilt series acquisition* (*Steps 48–51*). Select a location to image by using the low-magnification TEM map to identify viral targets from the correlated cryo-fLM points. Next, refer to the intermediate-magnification map to evaluate whether the ROI is thin enough for tomography and has intact cell membranes and other structures.

    ▲ **CRITICAL STEP** When selecting an area for tilt series acquisition, it is advisable to consider location of the tilt axis and where the focus and trial positions are located with respect to the rest of the cell, to avoid exposing nearby ROI.

49. Set imaging conditions for tilt series acquisition as indicated in the table below. The magnification used depends on the desired pixel size. For downstream processing such as subvolume averaging, we use a smaller pixel size of ~3 Å (or less) per pixel (corresponding to a magnification of 20,000× (or greater) for the DE-20). For general morphology and cell structure data, we use ~6 Å per pixel (corresponding to a magnification of 10,000× for the DE-20). Total dose should be limited to ~100–150 e/Å^2 (including the 5 e/Å^2 from the previous montage). The beam should be small (for 20,000×, ~2 μm in diameter) and the distance between the focus and record areas should be sufficient to prevent overlap (5–6 μm).

50. Acquire tilt series as indicated in the table below. There are many options for data collection schemes, with the main priority being preservation of high-resolution information while limiting beam damage. To this end, tilt series should be collected using the bidirectional option from a zero-degree tilt to a final tilt of between 60° and 65°, at 1° to 2° tilt increments. Other collection schemes, such as the alternating dose symmetric scheme [55],

are now commonly used. In addition, it is important to minimize alterations to the electron beam by keeping the beam intensity constant and instead varying the exposure time by using the $1/\cos ine^{1/5}$ weighting option in SerialEM (i.e., to vary the exposure time as a function of specimen thickness, with higher tilt angles receiving slightly longer exposure times). To aid in focusing and tracking, image binning should be set to 2 or 4 to increase the image contrast. Use an additional offset of 2–3 μm for focusing to provide enough contrast for accurate estimation. Tilt series should be acquired with a Direct Electron DE-20 direct detector at 12–24 frames per s, depending on record exposure time, not only for its increased resolution but also for its large imaging area (field of view). In this way, more of the cellular structural context is retained and more subvolumes can be extracted from a given tomogram.

51. Repeat Steps 48–50 for each ROI.

▲ **CRITICAL STEP** A best-practice approach to determining the maximum amount of electron dose for a sample is to collect an extended dose series of exposures to determine the beam sensitivity of the specimen, including cell (and viral) membranes and internal structural proteins.

Processing and combining of high-resolution CLEM overlay images ● TIMING 1 d

52. Perform ɀ cropping, background adjustment, deconvolution, projection, and channel merging of cryo-fLM images (from Step 34) using the LASX software. For best results, separate the three channels and process them individually before merging them back together. The fluorescence signal of the specific probes is well maintained at cryo-fLM temperatures because there is minimal photobleaching [42, 56, 57], and the close working distance of the objective lens ensures that there is robust signal over background

fluorescence. Merged fluorescence channels can be saved with and without the bright-field image.

53. Stitch together cryo-TEM montages (from Steps 46–47) to form maps using the eTomo software 'Align Serial Sections/ Blend Montages' function.
54. Scale and overlay both cryo-fLM and cryo-TEM maps in PhotoShop using layers. It is convenient to use the size and orientation of the holes in the carbon film to scale and rotate the images to one another (Figures 9–11).

Processing of tilt series data ● TIMING 5–6 h per data set

55. Motion-correct the raw frames from the direct detector using the Python scripts (DE_combine_references.py and DE_process_frames.py) provided by Direct Electron (or other sources for different detectors). The total number of frames per image varies with the tilt angle because of the $1/\cos^{1/5}$ exposure setting.
56. Recombine the corrected images using IMOD's 'newstack' command. For bidirectional tilt series, we use the 'reverse' option. Create a corresponding rawtilt file containing all angles for the tilt series.
57. Launch 3dmod's eTomo module, import the tilt series, and select 'Tilt angles in existing rawtlt file'.
58. Perform coarse alignment, fiducial-based fine alignment, and tomogram positioning using the eTomo user interface.
59. Correct the CTF, create the full aligned stack, and then proceed with r-weighted back-projection [53, 58]. It is advisable to do binned and full versions of tomograms within the eTomo module by going back to the 'Create Full Aligned Stack' module in eTomo to create consistently scaled maps. Be sure to change the output .rec filename so that it is not

overwritten. Tomograms may be optionally filtered or denoised by nonlinear anisotropic diffusion, or other filters such as band-pass, bilateral, or median filters, before segmentation [20, 48, 53, 59, 60].

60. Segmentation of densities in the tomogram is useful for illustrative purposes and to obtain quantitative measurements from surface data. Two options are currently available: the basic modeling tools in 3dmod, and the more detailed 3D segmentations in Amira.

(A) Performance of initial contour segmentation of proteins and cell and viral membranes in 3dmod

i. Filter the tomogram (nonlinear anisotropic diffusion), if needed.

ii. Create contours of components that are then meshed into surfaces using imodmesh.

iii. Take manual measurements with the drawing tools feature, saving the 'info text' dialog to file.

iv. Run and plot statistical analyses such as neighbor density analysis (nda program) and distances between objects (mtk program).

(B) Performance of detailed segmentation of membranes and molecules of interest in Amira

i. Import the binned and/or filtered tomogram into Amira and filter to smooth pixel edges and display as orthoslices.

▲ **CRITICAL STEP** Make sure that Amira does not flip the data. To correct improper flipping, select 'rotate around y-axis' after the volume is initially imported into the program.

ii. Segment tomographic data semiautomatically in Amira. Use of the masking option is helpful in selecting continuous membranes. Note that the use of a Wacom Cintiq monitor is very helpful for direct, on-screen drawing of contours.

iii. Create surfaces using 'SurfaceGen' and 'Smooth Surface' under the project tab to create a smoothed 3D surface model, then select 'Surface View' for visualization.

iv. After segmentation, label objects with the 3D annotation tool, which is useful for making measurements. For segmented data, measurements can be made using the 2D and 3D length and angle tools. 2D and 3D measurements can be made in the orthoslice view and surfaces can be measured in 3D. Similarly, angles can be measured in both 2D and 3D. Make sure to name each measurement in the 'measurement properties' window, and then export them to a spreadsheet for quantification (Figures 10–12).

Particle picking for subvolume averaging ● TIMING 1 d

61. *Selection of particles using EMAN2 [48].* Load the tomogram (Step 59) into EMAN2's boxer graphical user interface with the following example command line:

```
e2spt_boxer.py tomogram.rec --invert --inmemory --low-pass=80
```

Set the box size relatively small (4–10 pixels) to begin with to avoid box overlaps when selecting closely spaced particles. Use the *xyz* views to make certain that the boxes are well centered on the densities. Save the coordinates as 'box file'.

62. Using IMOD's 'point2mod' command, convert the boxed particle coordinates to a model file for use in alignment and averaging in PEET (Step 64).

63. *Editing of the model file.* Open the tomogram (from Step 59) and model file (from Step 62) with IMOD and save the model object points as 'Scattered'. The IMOD command 'imodtrans' can be used to scale the model files so that particles can be picked in a binned tomogram and a corresponding model file can be made for the unbinned tomogram.

Subvolume alignment, averaging, and classification ● TIMING 1–6 months

64. There are several image processing packages that incorporate subvolume analysis, and here we highlight two that are commonly used in our group. Use option A to align and classify subvolumes using PEET and option b to do so using EMAN2.

(A) Alignment and classifying of subvolumes using PEET

i. Scale the PEET [49, 50] motive list (.csv files) generated after initial alignments (in Excel) to match unbinned tomographic data. Use this file as input (under the PEET 'Setup' tab 'Initial Motive List') for running fine alignment. When running PEET, we typically select the option 'save individual aligned particles' (under the PEET 'Run' tab 'Optional / Advance Features'). The individual aligned particles can be inspected in IMOD and screened manually to ensure that no misaligned particles are used to generate the final subvolume average. A final subvolume average of the manually screened aligned particles can be generated using the PEET command 'averageAll' or the IMOD command 'clip'.

(B) Alignment and classification using EMAN2

i. With EMAN2's 'e2spt_classaverage.py' script [47], use binned tomograms (binned by a factor of 2 or 4) to generate an initial subvolume average and to explore different alignment parameters, including box size, angular search range and search distance, and masking options, and selection of an appropriate starting reference.

TROUBLESHOOTING

Trouble shooting advice can be found in Table 1.

TIMING

Steps 1–7, preparation of EM grids: ~1–2 d

Steps 8–14, culture of cells on EM grids: 1–2 d

Step 15, introduction of virus to cells: 30 min to 3 d

Steps 16–27, vitrification of grids by plunge-freezing: 1 h

Steps 28–36, cryo-fLM imaging: 30–45 min

Steps 37–40, creation of low-magnification cryo-TEM maps: 20–30 min

Steps 41–45, correlation of the TEM map with the CLEM map: 30 min

Steps 46 and 47, intermediate-magnification montaging: 30–60 min

Steps 48–51, tilt series acquisition: 6–18 h

Steps 52–54, processing and combining of high-resolution CLEM overlay images: 1 d

Steps 55–59, processing of tilt series data: 5–6 h per data set

Step 60, segmentation of tomograms: 1–3 d

Steps 61–63, particle picking for subvolume averaging: 1 d

Step 64, subvolume alignment, averaging, and classification: 1–6 months

Box 1, coating of grids with extracellular matrix components: 8–24 h

ANTICIPATED RESULTS

This protocol describes how to perform cryo-CLEM on intact, virus-infected or transfected mammalian cells. The success and quality of the acquired data depend heavily on the handling of the TEM grids during grid preparation, especially during transfers from the plunge-freezing apparatus to grid boxes and the microscopes. Figure 13 provides examples of suboptimal grids for cryo-CLEM imaging. Examples of ice contamination from the atmosphere and ice morphological changes due to warming are shown, as well as how grids that are bent or otherwise uneven do not produce maps that correlate well in either microscope.

ACKNOWLEDGEMENTS

We thank the Robert P. Apkarian Integrated Electron Microscopy Core of Emory University for microscopy services and support. This work was supported in part by grants from Emory University, Children's Healthcare of Atlanta, and the Georgia Research Alliance to E.R.W.; a grant from the Center for AIDS Research at Emory University (P30 AI050409); a grant from the James B. Pendleton Charitable Trust to E.R.W. and P.W.S.; public health service grants R01GM104540, R21AI101775, and R01GM104540-03S1 from the NIH to E.R.W.; NSF grant 0923395 to E.R.W.; public health service grant R01GM114561 from the NIH to E.R.W. and P.J.S.; public health service grant R01AI058828 from the NIH to P.W.S.; public health service grants R01GM054787 and R01AI053668 from the NIH to G.B.M.; public health service grant R01GM094198 from the NIH to P.J.S.; and public health service grant F32GM112517 from the NIH to J.D.S. The funders had no role in study design, data collection and interpretation, or the decision to submit the work for publication.

REFERENCES

1. Morgan, C., Godman, G. C., Breitenfeld, P. M., and Rose, H. M. A correlative study by electron and light microscopy of the development of type-5 adenovirus. 1. Electron microscopy. *J Exp Med*, 1960. **112**(2): p. 373-382.
2. Godman, G. C., Morgan, C., Breitenfeld, P. M., and Rose, H. M. A correlative study by electron and light microscopy of the development of type-5 adenovirus. 2. Light microscopy. *J Exp Med*, 1960. **112**(2): p. 383-402.
3. Dubochet, J., Adrian, M., Chang, J. J., Homo, J. C., Lepault, J., McDowall, A. W., and Schultz, P. Cryo-electron microscopy of vitrified specimens. *Q Rev Biophys*, 1988. **21**(2): p. 129-228.
4. Mancini, E. J., deHaas, F., and Fuller, S. D. High-resolution icosahedral reconstruction: Fulfilling the promise of cryo-electron microscopy. *Structure*, 1997. **5**(6): p. 741-750.
5. Steven, A. C. and Aebi, U. The next ice age: Cryo-electron tomography of intact cells. *Trends Cell Biol*, 2003. **13**(3): p. 107-110.
6. Risco, C. and Carrascosa, J. L. Visualization of viral assembly in the infected cell. *Histol Histopathol*, 1999. **14**(3): p. 905-926.
7. Schroder, R. R. Advances in electron microscopy: A qualitative view of instrumentation development for macromolecular imaging and tomography. *Arch Biochem Biophys*, 2015. **581**: p. 25-38.
8. McDonald, K. L. A review of high-pressure freezing preparation techniques for correlative light and electron microscopy of the same cells and tissues. *J Microsc*, 2009. **235**(3): p. 273-281.
9. Carroni, M. and Saibil, H. R. Cryo electron microscopy to determine the structure of macromolecular complexes. *Methods*, 2016. **95**: p. 78-85.

10. Giepmans, B. N. G., Adams, S. R., Ellisman, M. H., and Tsien, R. Y. Review - the fluorescent toolbox for assessing protein location and function. *Science*, 2006. **312**(5771): p. 217-224.

11. Desai, T. M., Marin, M., Sood, C., Shi, J., Nawaz, F., Aiken, C., and Melikyan, G. B. Fluorescent protein-tagged Vpr dissociates from HIV-1 core after viral fusion and rapidly enters the cell nucleus. *Retrovirology*, 2015. **12**.

12. Padilla-Parra, S., Marin, M., Gahlaut, N., Suter, R., Kondo, N., and Melikyan, G. B. Fusion of mature HIV-1 particles leads to complete release of a Gag-GFP-based content marker and raises the intraviral pH. *PLoS One*, 2013. **8**(8).

13. Briegel, A., Chen, S., Koster, A. J., Plitzko, J. M., Schwartz, C. L., and Jensen, G. J. Correlated light and electron cryo-microscopy, in *Methods Enzymol*, G.J. Jensen, Editor. 2010. p. 317-341.

14. Strauss, J. D., Hammonds, J. E., Yi, H., Ding, L., Spearman, P., and Wright, E. R. Three-dimensional structural characterization of HIV-1 tethered to human cells. *J Virol*, 2016. **90**(3): p. 1507-1521.

15. Yi, H., Strauss, J. D., Ke, Z., Alonas, E., Dillard, R. S., Hampton, C. M., Lamb, K. M., Hammonds, J. E., Santangelo, P. J., Spearman, P. W., and Wright, E. R. Native immunogold labeling of cell surface proteins and viral glycoproteins for cryo-electron microscopy and cryo-electron tomography applications. *J Histochem Cytochem*, 2015. **63**(10): p. 780-792.

16. Mastronarde, D. N. Automated electron microscope tomography using robust prediction of specimen movements. *J Struct Biol*, 2005. **152**(1): p. 36-51.

17. Bharat, T. A., Russo, C. J., Lowe, J., Passmore, L. A., and Scheres, S. H. Advances in single-particle electron cryomicroscopy structure determination applied to sub-tomogram averaging. *Structure*, 2015. **23**(9): p. 1743-53.

18. Hrabe, T. Localize.Pytom: A modern webserver for cryo-electron tomography. *Nucleic Acids Res*, 2015. **43**(W1): p. W231-W236.

19. Huiskonen, J. T., Parsy, M.-L., Li, S., Bitto, D., Renner, M., and Bowden, T. A. Averaging of viral envelope glycoprotein spikes from electron cryotomography reconstructions using Jsubtomo. *J Visualized Exp*, 2014(92).

20. Heymann, J. B., Cardone, G., Winkler, D. C., and Steven, A. C. Computational resources for cryo-electron tomography in Bsoft. *J Struct Biol*, 2008. **161**(3): p. 232-242.

21. Castano-Diez, D., Kudryashev, M., Arheit, M., and Stahlberg, H. Dynamo: A flexible, user-friendly development tool for subtomogram averaging of cryo-EM data in high-performance computing environments. *J Struct Biol*, 2012. **178**(2): p. 139-51.

22. Koning, R. I., Celler, K., Willemse, J., Bos, E., van Wezel, G. P., and Koster, A. J. Correlative cryo-fluorescence light microscopy and cryo-electron tomography of streptomyces, in *Correlative Light and Electron Microscopy II*, T. MullerReichert and P. Verkade, Editors. 2014. p. 217-239.

23. van Driel, L. F., Valentijn, J. A., Valentijn, K. M., Koning, R. I., and Koster, A. J. Tools for correlative cryo-fluorescence microscopy and cryo-electron tomography applied to whole mitochondria in human endothelial cells. *Eur J Cell Biol*, 2009. **88**(11): p. 669-84.

24. Jun, S., Ke, D., Debiec, K., Zhao, G., Meng, X., Ambrose, Z., Gibson, G. A., Watkins, S. C., and Zhang, P. Direct visualization of HIV-1 with correlative live-cell microscopy and cryo-electron tomography. *Structure*, 2011. **19**(11): p. 1573-1581.

25. Ibiricu, I., Huiskonen, J. T., Doehner, K., Bradke, F., Sodeik, B., and Gruenewald, K. Cryo electron tomography of herpes simplex virus during axonal transport and secondary envelopment in primary neurons. *PLoS Pathog*, 2011. **7**(12).

26. Schorb, M. and Briggs, J. A. Correlated cryo-fluorescence and cryo-electron microscopy with high spatial precision and improved sensitivity. *Ultramicroscopy*, 2014. **143**: p. 24-32.

27. Briegel, A., Ding, H. J., Li, Z., Werner, J., Gitai, Z., Dias, D. P., Jensen, R. B., and Jensen, G. J. Location and architecture of the *Caulobacter crescentus* chemoreceptor array. *Mol Microbiol*, 2008. **69**(1): p. 30-41.

28. Swulius, M. T., Chen, S., Ding, H. J., Li, Z., Briegel, A., Pilhofer, M., Tocheva, E. I., Lybarger, S. R., Johnson, T. L., Sandkvist, M., and Jensen, G. J. Long helical filaments are not seen encircling cells in electron cryotomograms of rod-shaped bacteria. *Biochem Biophys Res Commun*, 2011. **407**(4): p. 650-655.

29. Chang, Y.-W., Chen, S., Tocheva, E. I., Treuner-Lange, A., Löbach, S., Søgaard-Andersen, L., and Jensen, G. J. Correlated cryogenic photoactivated localization microscopy and cryo-electron tomography. *Nat Methods*, 2014. **11**: p. 737.

30. Wang, Q., Mercogliano, C. P., and Loewe, J. A ferritin-based label for cellular electron cryotomography. *Structure*, 2011. **19**(2): p. 147-154.

31. Gold, V. A. M., Ieva, R., Walter, A., Pfanner, N., van der Laan, M., and Kuehlbrandt, W. Visualizing active membrane protein complexes by electron cryotomography. *Nat Commun*, 2014. **5**.

32. Mercogliano, C. P. and DeRosier, D. J. Concatenated metallothionein as a clonable gold label for electron microscopy. *J Struct Biol*, 2007. **160**(1): p. 70-82.

33. Al-Amoudi, A., Chang, J. J., Leforestier, A., McDowall, A., Salamin, L. M., Norlen, L. P., Richter, K., Blanc, N. S., Studer, D., and Dubochet, J. Cryo-electron microscopy of vitreous sections. *EMBO J*, 2004. **23**(18): p. 3583-8.

34. Gruska, M., Medalia, O., Baumeister, W., and Leis, A. Electron tomography of vitreous sections from cultured mammalian cells. *J Struct Biol*, 2008. **161**(3): p. 384-392.

35. Engel, B. D., Schaffer, M., Cuellar, L. K., Villa, E., Plitzko, J. M., and Baumeister, W. Native architecture of the *Chlamydomonas* chloroplast revealed by in situ cryo-electron tomography. *eLife*, 2015. **4**.

36. Marko, M., Hsieh, C., Schalek, R., Frank, J., and Mannella, C. Focused-ion-beam thinning of frozen-hydrated biological specimens for cryo-electron microscopy. *Nat Methods*, 2007. **4**(3): p. 215-7.

37. Wolf, S. G., Houben, L., and Elbaum, M. Cryo-scanning transmission electron tomography of vitrified cells. *Nat Methods*, 2014. **11**(4): p. 423-428.

38. Bykov, Y. S., Cortese, M., Briggs, J. A. G., and Bartenschlager, R. Correlative light and electron microscopy methods for the study of virus-cell interactions. *FEBS Lett*, 2016. **590**(13): p. 1877-1895.

39. Schellenberger, P., Kaufmann, R., Siebert, C. A., Hagen, C., Wodrich, H., and Gruenewald, K. High-precision correlative fluorescence and electron cryo microscopy using two independent alignment markers. *Ultramicroscopy*, 2014. **143**: p. 41-51.

40. Liu, B., Xue, Y., Zhao, W., Chen, Y., Fan, C., Gu, L., Zhang, Y., Zhang, X., Sun, L., Huang, X., Ding, W., Sun, F., Ji, W., and Xu, T. Three-dimensional super-resolution protein localization correlated with vitrified cellular context. *Sci Rep*, 2015. **5**: p. 13017.

41. Wolff, G., Hagen, C., Grunewald, K., and Kaufmann, R. Towards correlative super-resolution fluorescence and electron cryo-microscopy. *Biol Cell*, 2016. **108**(9): p. 245-258.

42. Schwartz, C. L., Sarbash, V. I., Ataullakhanov, F. I., McIntosh, J. R., and Nicastro, D. Cryo-fluorescence microscopy facilitates correlations between light and cryo-electron microscopy and reduces the rate of photobleaching. *J Microsc*, 2007. **227**(2): p. 98-109.

43. Sartori, A., Gatz, R., Beck, F., Rigort, A., Baumeister, W., and Plitzko, J. M. Correlative microscopy: Bridging the gap between fluorescence light microscopy and cryo-electron tomography. *J Struct Biol*, 2007. **160**(2): p. 135-45.

44. Rigort, A., Baeuerlein, F. J. B., Leis, A., Gruska, M., Hoffmann, C., Laugks, T., Boehm, U., Eibauer, M., Gnaegi, H., Baumeister, W., and Plitzko, J. M. Micromachining tools and correlative approaches for cellular cryo-electron tomography. *J Struct Biol*, 2010. **172**(2): p. 169-179.

45. Faas, F. G. A., Barcena, M., Agronskaia, A. V., Gerritsen, H. C., Moscicka, K. B., Diebolder, C. A., van Driel, L. F., Limpens, R. W. A. L., Bos, E., Ravelli, R. B. G., Koning, R. I., and Koster, A. J. Localization of fluorescently labeled structures in frozen-hydrated samples using integrated light electron microscopy. *J Struct Biol*, 2013. **181**(3): p. 283-290.

46. Schorb, M., Gaechter, L., Avinoam, O., Sieckmann, F., Clarke, M., Bebeacua, C., Bykov, Y. S., Sonnen, A. F. P., Lihl, R., and Briggs, J. A. G. New hardware and workflows for semi-automated correlative cryo-fluorescence and cryo-electron microscopy/tomography. *J Struct Biol*, 2017. **197**(2): p. 83-93.

47. Galaz-Montoya, J. G., Flanagan, J., Schmid, M. F., and Ludtke, S. J. Single particle tomography in EMAN2. *J Struct Biol*, 2015. **190**(3): p. 279-90.

48. Tang, G., Peng, L., Baldwin, P. R., Mann, D. S., Jiang, W., Rees, I., and Ludtke, S. J. Eman2: An extensible image processing suite for electron microscopy. *J Struct Biol*, 2007. **157**(1): p. 38-46.

49. Nicastro, D., Schwartz, C., Pierson, J., Gaudette, R., Porter, M. E., and McIntosh, J. R. The molecular architecture of axonemes revealed by cryoelectron tomography. *Science*, 2006. **313**(5789): p. 944-948.

50. Heumann, J. M., Hoenger, A., and Mastronarde, D. N. Clustering and variance maps for cryo-electron tomography using wedge-masked differences. *J Struct Biol*, 2011. **175**(3): p. 288-299.

51. Winkler, H. 3D reconstruction and processing of volumetric data in cryo-electron tomography. *J Struct Biol*, 2007. **157**(1): p. 126-137.

52. Huiskonen, J. T., Hepojoki, J., Laurinmaki, P., Vaheri, A., Lankinen, H., Butcher, S. J., and Gruenewald, K. Electron cryotomography of Tula hantavirus suggests a unique assembly paradigm for enveloped viruses. *J Virol*, 2010. **84**(10): p. 4889-4897.

53. Kremer, J. R., Mastronarde, D. N., and McIntosh, J. R. Computer visualization of three-dimensional image data using IMOD. *J Struct Biol*, 1996. **116**(1): p. 71-76.

54. Rohou, A. and Grigorieff, N. Ctffind4: Fast and accurate defocus estimation from electron micrographs. *J Struct Biol*, 2015. **192**(2): p. 216-21.

55. Hagen, W. J. H., Wan, W., and Briggs, J. A. G. Implementation of a cryo-electron tomography tilt-scheme optimized for high resolution subtomogram averaging. *J Struct Biol*, 2017. **197**(2): p. 191-198.

56. Moerner, W. E. and Orrit, M. Illuminating single molecules in condensed matter. *Science*, 1999. **283**(5408): p. 1670-1676.

57. Kaufmann, R., Hagen, C., and Gruenewald, K. Fluorescence cryo-microscopy: Current challenges and prospects. *Curr Opin Chem Biol*, 2014. **20**: p. 86-91.

58. Xiong, Q., Morphew, M. K., Schwartz, C. L., Hoenger, A. H., and Mastronarde, D. N. CTF determination and correction for low dose tomographic tilt series. *J Struct Biol*, 2009. **168**(3): p. 378-387.

59. Heymann, J. B. and Belnap, D. M. Bsoft: Image processing and molecular modeling for electron microscopy. *J Struct Biol*, 2007. **157**(1): p. 3-18.

60. Heymann, J. B. Bsoft: Image and molecular processing in electron microscopy. *J Struct Biol*, 2001. **133**(2-3): p. 156-169.

FIGURE LEGENDS

Figure 1. Flowchart of the steps for CLEM of mammalian cells. The protocol begins with the selection of the mammalian cells, the culturing of the cells on EM substrates, the infection or transfection protocol, and specimen evaluation by light microscopy. Next, the samples are plunge-frozen with an automated vitrification system. The frozen grids are then imaged and mapped by cryo-fLM and cryo-TEM instruments. Map coordinates from cryo-fLM and cryo-TEM are combined for correlation purposes to facilitate cryo-EM data collection. From the correlation map(s) and images, intermediate-magnification montages and cryo-ET data are acquired. The imaging data are then evaluated for further image processing, to include segmentation, quantification, and subvolume analysis.

Figure 2. Use of fLM to determine cross-sectional cell thickness and cell permissivity to RSV. (**a**) Extended-focus images of six cell lines infected with RSV and immunostained for the RSV fusion protein (red), nucleocapsid protein (green), and nucleus (DAPI, blue). Colocalization of viral proteins indicates that the cells are actively producing virus for imaging. (**b**) Single-axial section through the middle of each cell shown in (**a**). The XZ view in **b** illustrates the relative thickness of the cultured cells and shows that the cells will be thin enough at the periphery for TEM imaging. Spinning-disk confocal and laser-scanning confocal images are shown. Scale bars, (**a**) 10 μm, (**b**) 1 μm. NPC, Niemann–Pick type C.

Figure 3. Carbon evaporation onto gold Finder EM grids. (**a**) Carbon evaporation setup: (i) carbon rods, (ii) shield, and (iii) EM grids in the Petri dish. (**b**) Result of carbon evaporation. Displaced EM grid shows qualitatively how much carbon was evaporated, which corresponds to ~5 nm, according to the calibrated piezo transducer gauge.

Figure 4. Representative light microscopy image of the ideal cell density present on an EM grid. MRC-5 cells cultured on a carbon-coated gold EM grid before infection or plunge-freezing. Asterisks identify representative healthy MRC-5 cells that are spreading across the carbon film of the EM grid.

Figure 5. Gatan Cryoplunge3 system setup for plunge-freezing. Note that tissue culture incubator (not shown) is located immediately to the left of the unit. (**a**) Complete setup showing the following: (i) ethane temperature control, (ii) blot timer, (iii) relative humidity and temperature gauge, (iv) wet sponges for chamber humidification, (v) Gentle Blot blotters, (vi) plunge rod, and (vii) liquid nitrogen Dewar flask containing liquid ethane cup. (**b**) Work-space setup on Styrofoam surface for freezing: (i) small cap full of prewarmed PBS for washes, (ii) prepared fiducials, (iii) MatTek dish containing grids for freezing, and (iv) forceps for loading into plunge rod. (**c**) Forceps with grid in place between the GentleBlot blotters with blotting paper.

Figure 6. Leica EM Cryo CLEM system. (**a**) System setup consisting of the following: (i) liquid nitrogen pump, (ii) temperature control unit, (iii) Leica DM6 light microscope with motorized stage, (iv) 50× cryo objective HCX FL Apo, NA 0.9, WD 0.28 mm, (v) cryo CLEM stage, (vi) microscope control unit, (vii) STP stage controller, (viii) cryo-transfer shuttle, (ix) fluorescence light source, and (x) PC with LAS X software. (**b**) Inside of the cryo-transfer shuttle, showing the following: (i) cartridge-loading block, (ii) grid storage box, and (iii) transfer rod cartridge gripper. (**c**) Vitrified TEM grid (circled) loaded into cartridge for transfer.

Figure 7. Cryo-fluorescence microscopy grid map of HIV-1 virus-like particles tethered to HT1080 cells collected using the Leica LASX software. Cells were transfected with a 3:1 ratio of pVRC-

3900/GagOpt-mCherry and pEGFP-tetherin. Region from a central 3 × 3 grid of images with 10% overlap collected in (**a**) bright-field**,** (**b**) HIV-1 mCherry-Gag (red—Texas Red filter), and (**c**) EGFP-tetherin (green—GFP filter) microscopy. Red boxes in all three panels indicate registration points. Green boxes in all three panels denote data acquisition points.

Figure 8. Cryo-TEM map of grid with coordinates imposed from Leica LASX software. (Left) cryo-CLEM workflow viewed through SerialEM navigator window on the cryo-TEM computer. Cryo-TEM map in the center window with red registration numbers and green data acquisition points is derived from cryo-fLM map and navigator file. Cryo-fLM map in the right-hand window highlights the same registration numbers and data acquisition points that are present on the cryo-TEM map (center).

Figure 9. Entire cryo-CLEM imaging workflow with an HIV-1 Gag-tetherin specimen. (**a**) Overlay of cryo-fLM and cryo-TEM montage. Inset is the point of interest, with yellow fluorescent signal representing colocalization of mCherry-Gag (red) and EGFP-tetherin (green). (**b**) 10,000× polygon montage. White box indicates area where tilt series was collected. (**c**) Tomographic slice (6.14 nm) through a cluster of HIV-1 VLPs tethered to HT1080 cell extension. Scale bars, (**a**) 50 μm (inset is 3×), (**b**) 2 μm, and (**c**) 200 nm.

Figure 10. Cryo-CLEM imaging of retroviral endocytosis and fusion. (**a**–**c**) Double-labeled HIV-1 particles pseudotyped with avian sarcoma and leukosis virus (ASLV) Env glycoprotein. (**a**) Cryo-CLEM of ASLV Env pseudotyped HIV-1 particles bound to CV-1/TVA950 cells. Central region is the overlay of the cryo-EM montage onto the cryo-fLM image. Red square indicates the tomography data in **b** and **c**. (**b**) Tomographic slice, with segmentation, of ASLV Env pseudotyped HIV-1

particles undergoing endocytosis. The viral membrane (light blue) and mature core (yellow) are rendered. Clathrin cages (purple) surround several viral particles. (**c**) Enlargement of one clathrin cage (purple) surrounding a viral particle (light blue). Scale bars, (**b**) 250 nm, (**c**) 100 nm.

Figure 11. Montage maps provide cellular context for cryo-ET data. (**a**) Montage of RSV A2-infected A549 cells taken at 10,000× using the energy filter for improved contrast. The cell membrane is regular and intact, with filamentous RSV protruding from it. Scale bar, 2 μm; inset scale bar, 500 nm. (**b**) Segmented cryo-ET data from inset in **a** indicating membrane (cyan), glycoproteins (yellow), RNP (red), and actin filaments (magenta). Data were collected at 8,000× on a DE-20 camera system. Binned by 2, pixel size is 14.94 Å. Scale bar, 500 nm.

Figure 12. Quantitative segmentation data of HIV-1 particles with tetherin. Cells are transfected with pNLenv1-deltaU and pEGFP-tetherin. Measurements made along segmented tethers (red) connecting HIV-1 virions (yellow, transparent) to each other, as indicated by the thin white lines. Orientation axes of the mature HIV-1 core (purple) are identified as black lines. Scale bar, 50 nm.

Figure 13. Examples of poor-quality grids for cryo-CLEM imaging. (**a**) A cryo-fLM map of a slightly bent grid produces focus gradients within each stitched image, preventing accurate localization of regions of interest. (**b**) A low-magnification cryo-EM grid map of a 3-mm grid that has been bent before cryo-EM imaging. Aside from the obvious missing carbon in most grid squares, there are large variations in z height. (**c**) Image showing ice over 2-μm holes in the Quantifoil carbon film. W indicates ice that has warmed above the transition temperature (~−150 °C) to create crystalline artifacts. x indicates ice contamination from the atmosphere that has landed on the grid. Both can be attributed to transfer steps.

Figure 1.

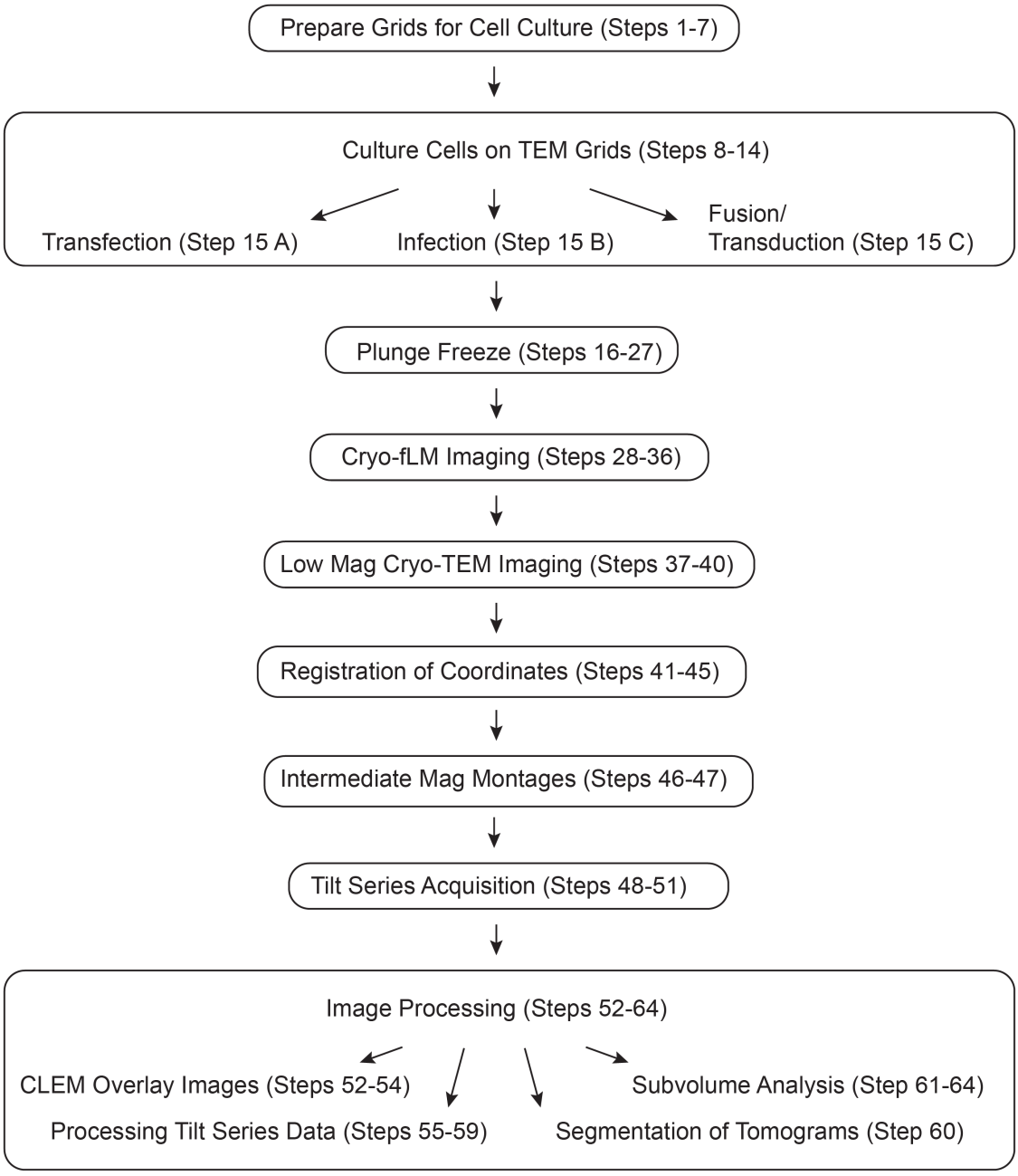
Prepare Grids for Cell Culture (Steps 1-7)
Culture Cells on TEM Grids (Steps 8-14)
Transfection (Step 15 A)
Infection (Step 15 B)
Fusion/
Transduction (Step 15 C)
Plunge Freeze (Steps 16-27)
Cryo-fLM Imaging (Steps 28-36)
Low Mag Cryo-TEM Imaging (Steps 37-40)
Registration of Coordinates (Steps 41-45)
Intermediate Mag Montages (Steps 46-47)
Tilt Series Acquisition (Steps 48-51)
Image Processing (Steps 52-64)
CLEM Overlay Images (Steps 52-54)
Processing Tilt Series Data (Steps 55-59)
Segmentation of Tomograms (Step 60)
Subvolume Analysis (Step 61-64)

Figure 2.

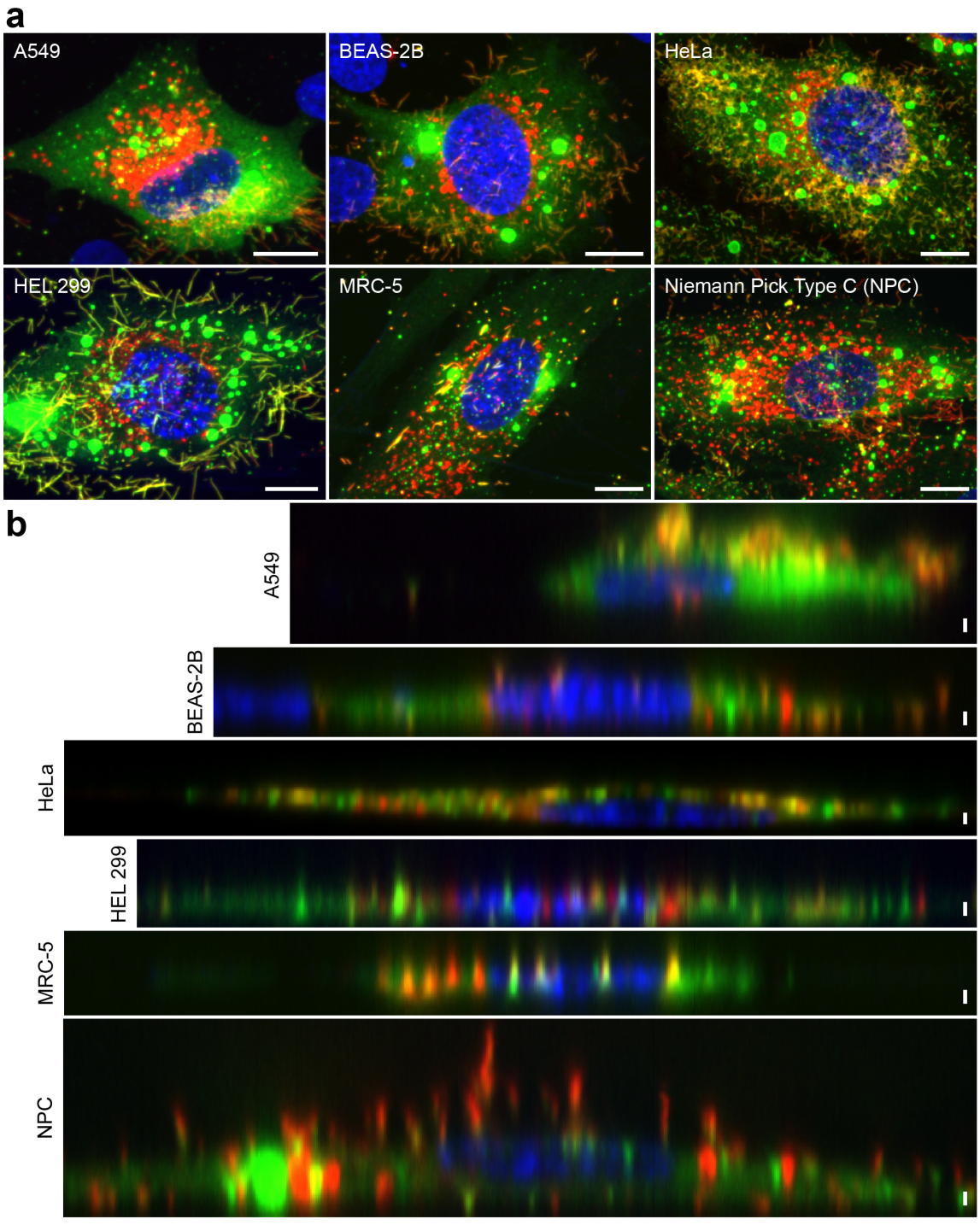
a
A549
BEAS-2B
HeLa
HEL 299
MRC-5
Niemann Pick Type C (NPC)
b
A549
BEAS-2B
HeLa
HEL 299
MRC-5
NPC

Figure 3.

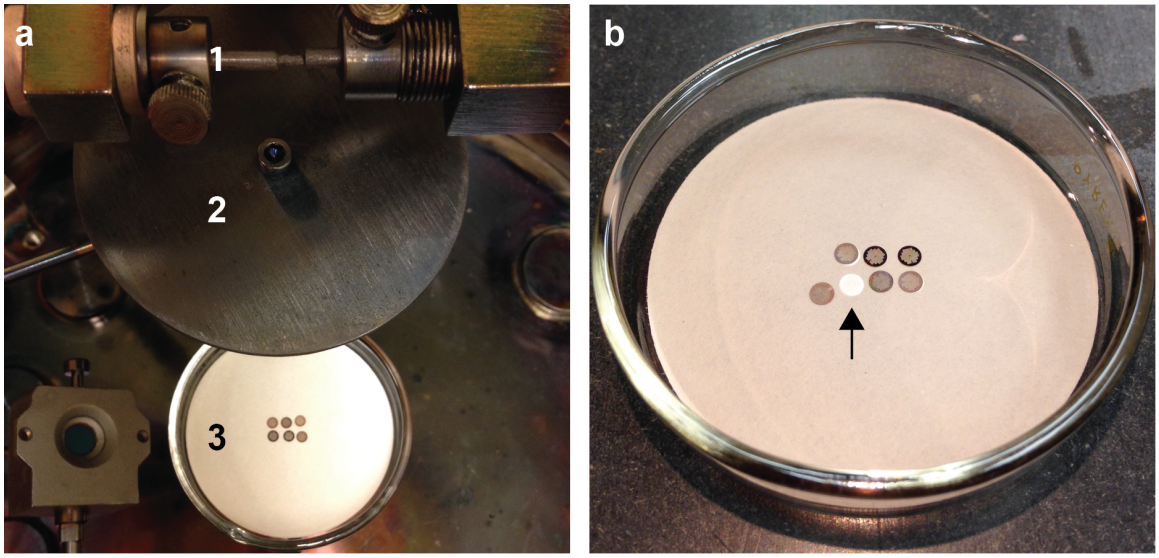

Figure 4.

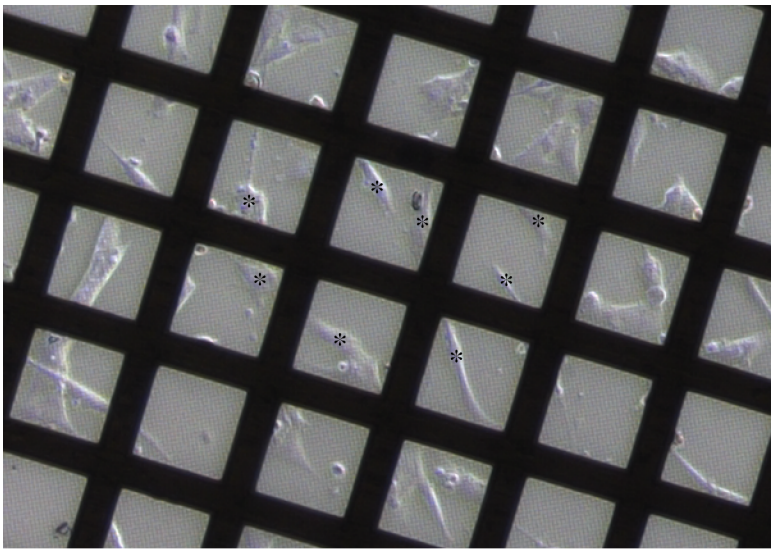

Figure 5.

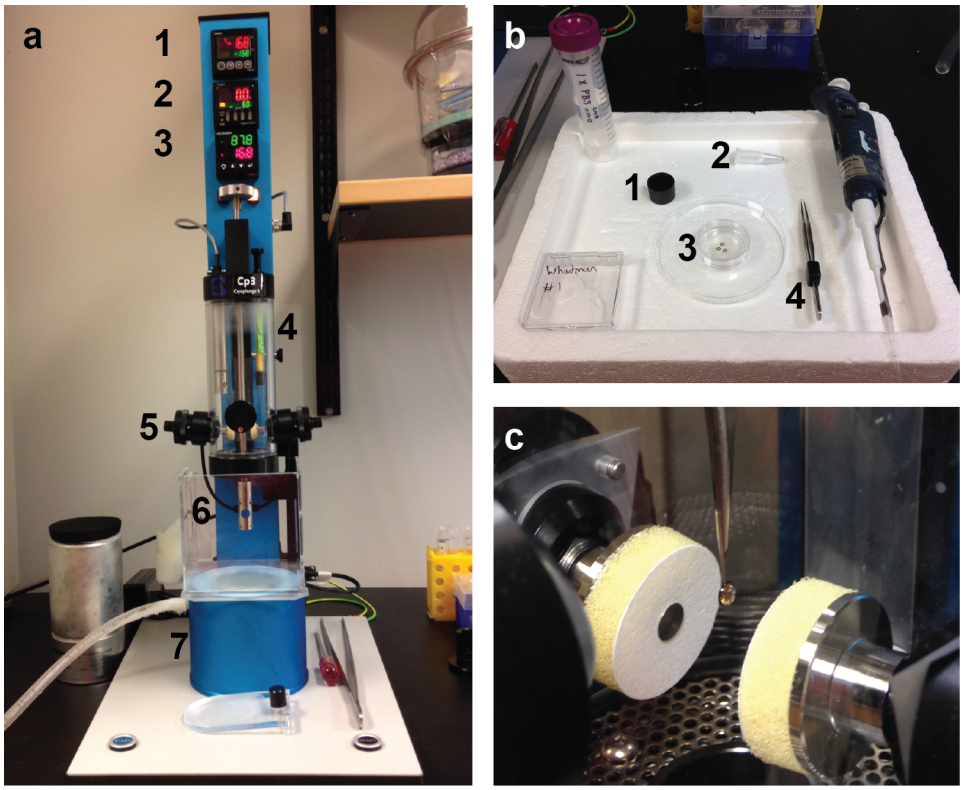

Figure 6.

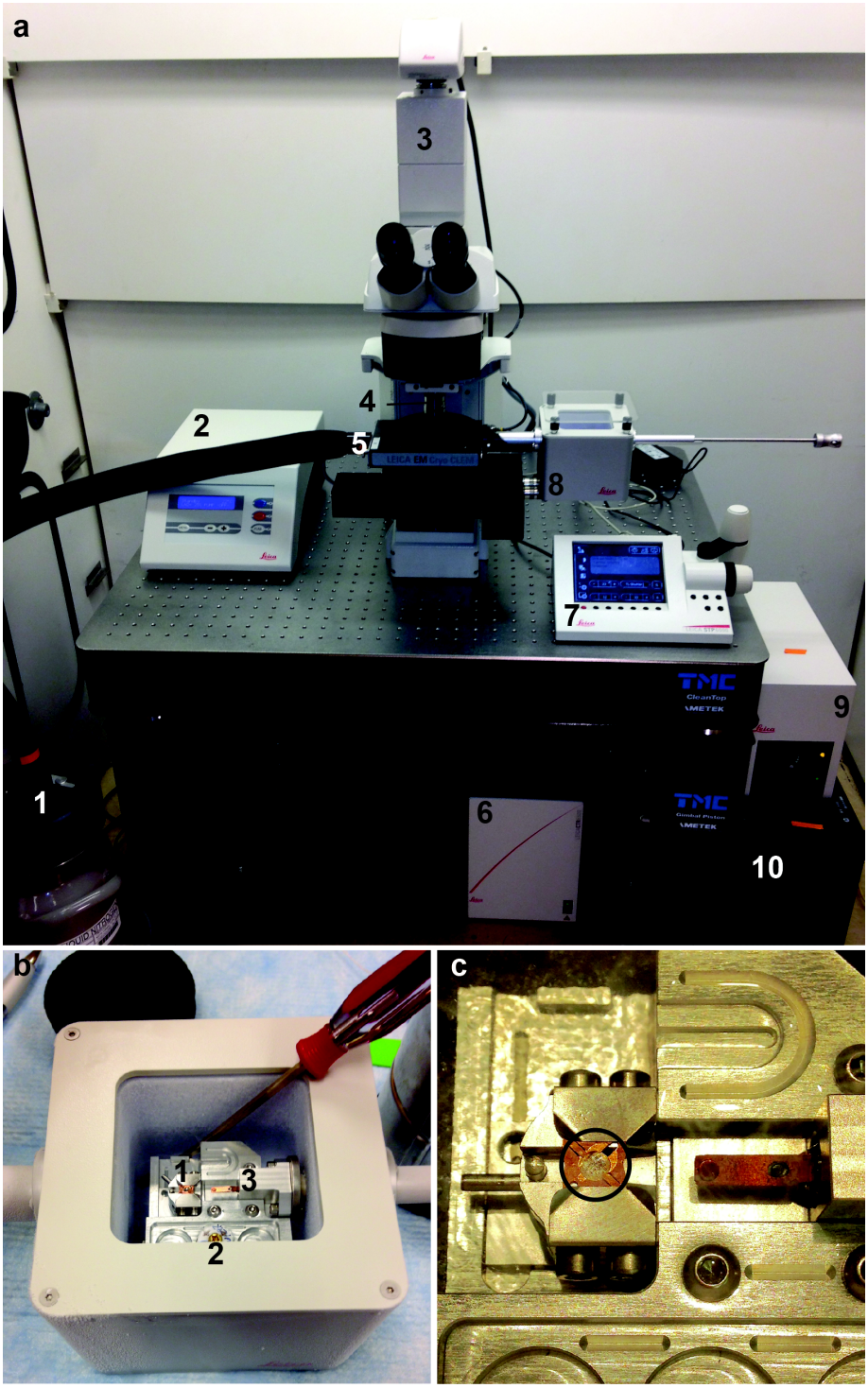

Figure 7.

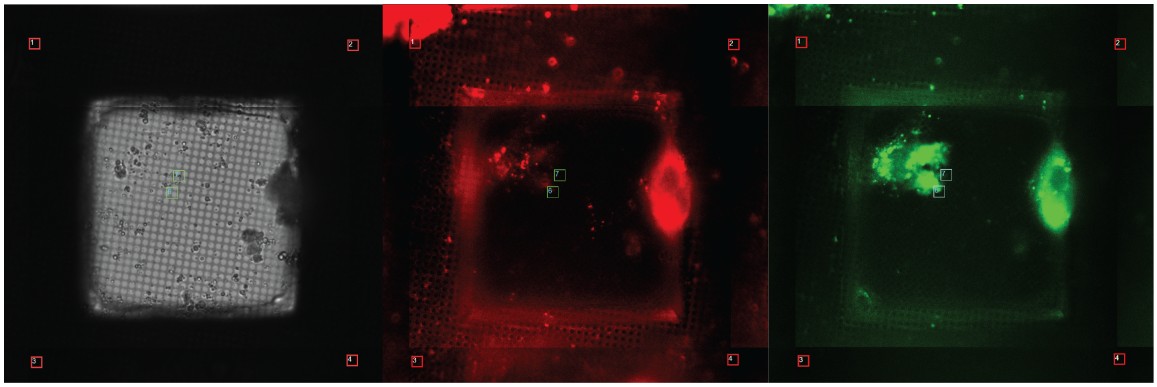

Figure 8.

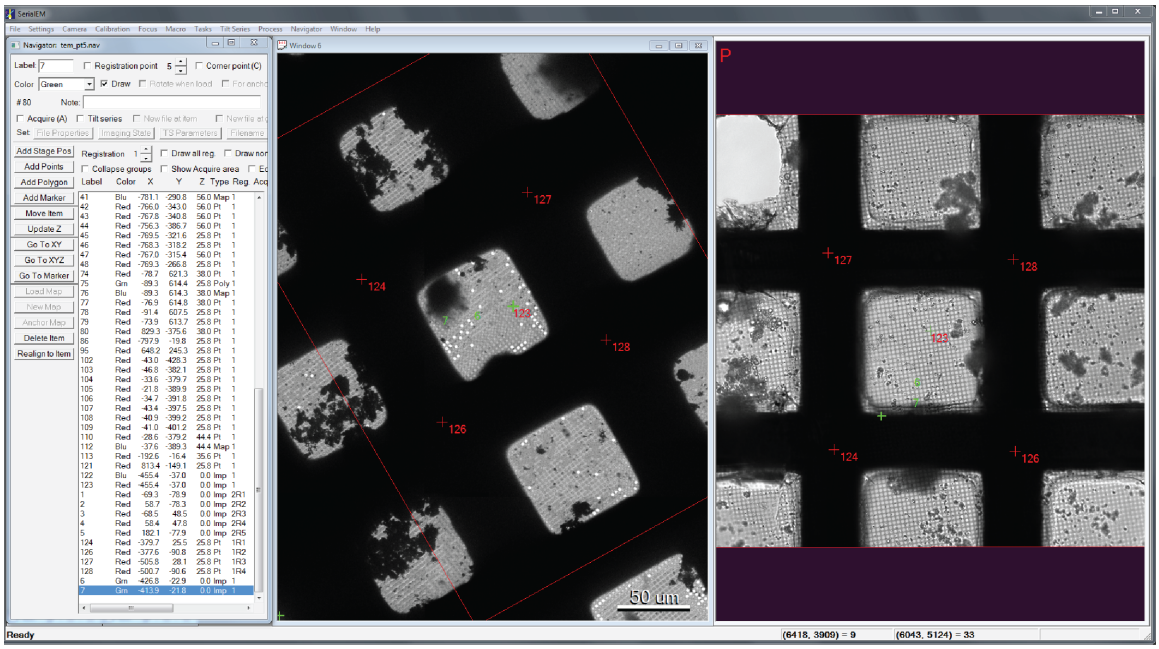
127
124
123
128
126
50 um
P
127
128
123
124
126
Ready
(6418, 3909) = 9
(6043, 5124) = 33

Figure 9.

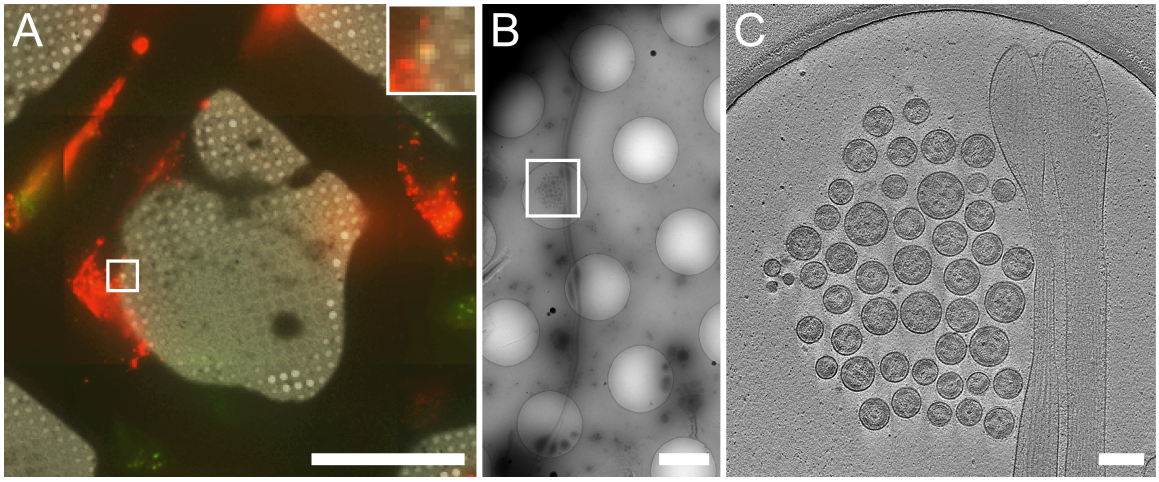

Figure 10.

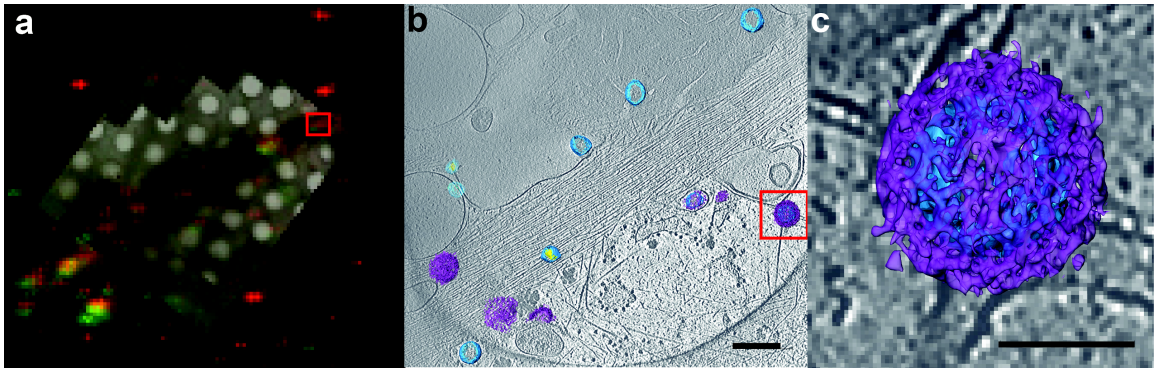

Figure 11.

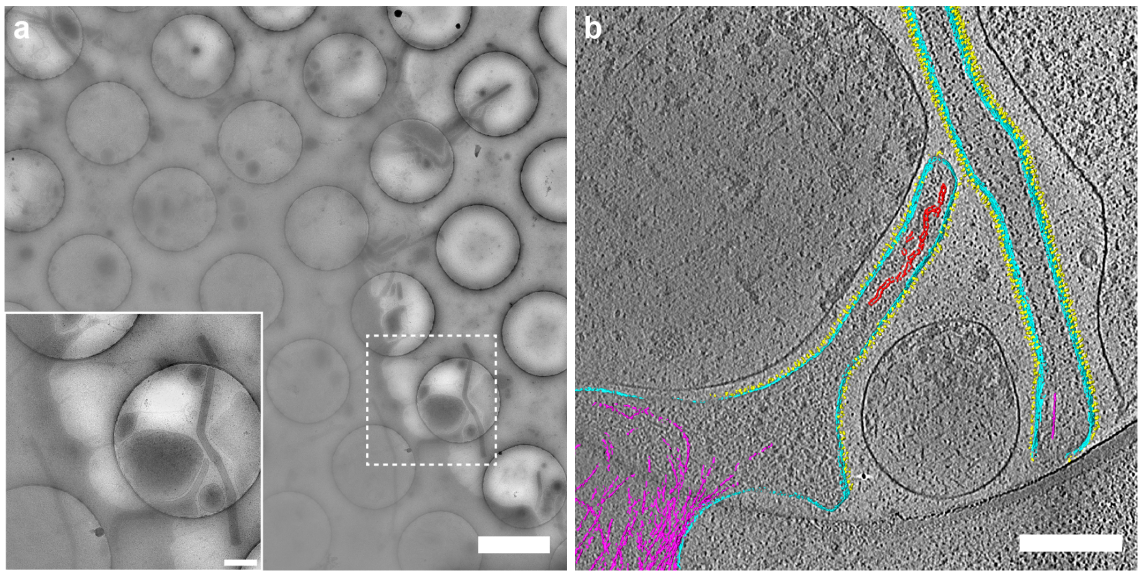

Figure 12.

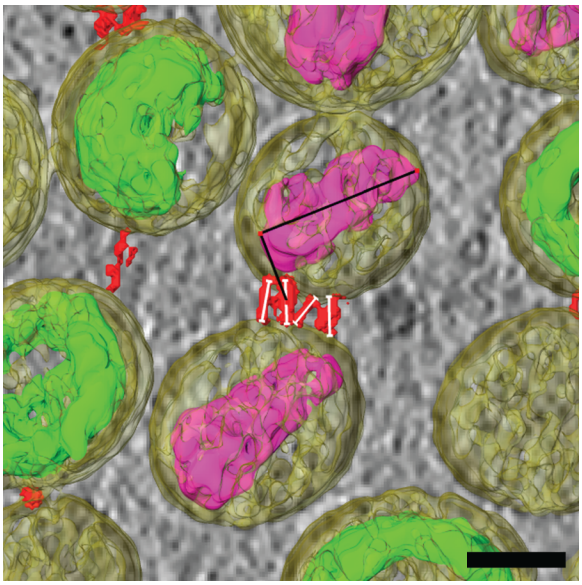

Figure 13.

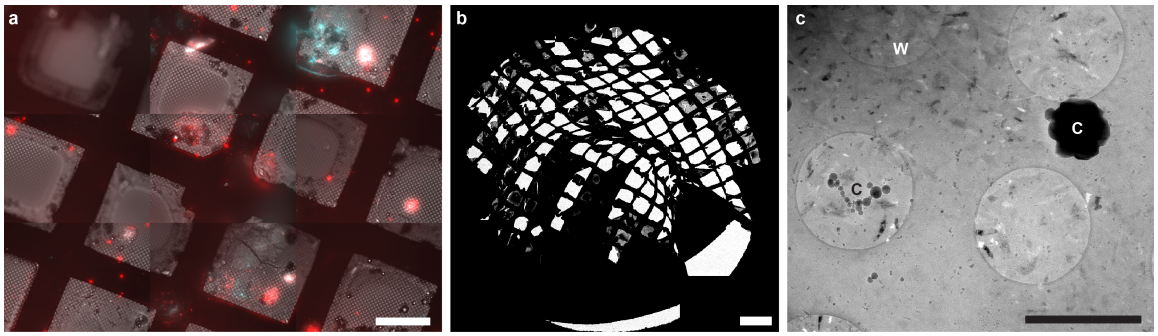

Table 1. Troubleshooting table

Step	Problem	Possible reason	Solution
6	Grids float on the medium	Surface of grids is hydrophobic because of insufficient glow discharging Air bubbles are attached to the grid	Adjust the settings on the plasma cleaner (Step 5) Introduce grids into solutions slowly and vertically to avoid formation of bubbles (Step 6)
15, 31, 38	Carbon film is torn	Rough handling of the grids Forceps have been damaged Grids were allowed to dry out Carbon film was damaged during blotting	Handle grids gently Avoid using forceps with bent tips Do not aspirate grids to dryness (Steps 8 and 12; Box 1) Reduce compressed nitrogen gas PSI on Gatan CryoPlunge3 unit (Step 16)
	Too many cells on the grid	Seeding density is high Cells are over confluent	Use a lower initial seeding density (Step 13) Grow the cells for a shorter time (Step 14)
	Not enough cells on the grid	Low initial seeding density Cells are not adhering to the grid	Seed at a higher density (Step 13) Include growth factors or coat carbon with extracellular matrix proteins (Step 7; Box 1)
	Cells are too rounded	Low initial seeding density No extracellular matrix solutions applied to the grids Virus infection is too high	Seed at a higher density (Step 13) Coat carbon with extracellular matrix proteins (Step 7; Box 1) Lower MOI of virus (Step 15)
31, 38	Ice is too thick	Blotting conditions are inadequate Cells are too confluent	Use a longer blot time (Step 25) Remember to rotate blotters (Step 26) Reduce the seeding density (Step 14)
38	Ice is too thick on one half of the grid	Grid is not centered and held evenly in plunge device forceps	Make sure that tips of forceps do not extend past the rim of the grid (Step 21)
38, 48	Ice on the grid has a freckled appearance	Warming past the vitrification point (i.e., above –150 °C) has occurred	Check the temperature of the cryo-fLM stage (Step 28) and expedite grid transfers (Steps 27, 29, 35, and 37)
	Lots of cell debris in the ice	Cytotoxicity from virus infection or transfection Cells were damaged during blotting	Cryo-plunge at an earlier time point (Step 15) Add an extra or longer DPBS wash to remove debris (Step 22) Adjust the blot settings (Step 25)
	Cell membranes appear ruptured or blebby	Blotting conditions are too severe Grid became too dry before blotting Cells were exposed to low temperatures	Lessen the blot force (Step 25) Reduce exposure to air and evaporation (Steps 21–26) Reduce time spent out of the incubator Do not place culture dishes on a cold benchtop and avoid holding the grid near liquid nitrogen while loading the plunge rod

Step	Problem	Possible reason	Solution
			(Step 24)
	Large amounts of solid ice particles on grid surface	Ice contamination from atmosphere	Do grid transfers in a humidity-controlled room (relative humidity <30%) Use Plexiglas shields or wear a facemask when transferring (Steps 27, 29, 35, and 37)
48	Gold fiducials aggregated in the ice	Initial solution of gold fiducials has precipitated	Vortex gold fiducial solution before use (Step 20)

Chapter 3: *Vibrio cholerae* outer membrane vesicles inhibit bacteriophage infection

Tamara Reyes-Robles[1,*], Rebecca S. Dillard[2,*], Lynne S. Cairns[1], Cecilia A. Silva-Valenzuela[1], Max Housman[2], Afsar Ali[3,4], Elizabeth R. Wright[2], and Andrew Camilli[1]

[1]Department of Molecular Biology and Microbiology, Howard Hughes Medical Institute, Tufts University School of Medicine, Boston, MA

[2]Department of Department of Pediatrics, Division of Infectious Diseases, Emory University School of Medicine, Atlanta, GA

[3]Emerging Pathogens Institute, University of Florida, Gainesville, FL

[4]Department of Environmental and Global Health, College of Public Health and Health Professions, University of Florida, Gainesville, FL

[*]These authors contributed equally to this work.

In revision at *Journal of Bacteriology*

R.S.D. performed cryo-electron microscopy experiments and contributed to the writing of the manuscript.

ABSTRACT

Novel preventatives could help in efforts to limit *Vibrio cholerae* infection and the spread of cholera. Bacteriophage (or phage) treatment has been proposed to be an alternative intervention, given the rapid replication of virulent phages, prey specificity, and relative ease of finding new virulent phages. Phage tropism is dictated in part by the presence of phage receptors on the bacterial surface. While many phages that can kill *V. cholerae* have been isolated, whether this pathogen is able to defend itself by neutralizing phage binding is unknown. Here we show that secreted outer membrane vesicles (OMVs) act as a defense mechanism that confers protection to *V. cholerae* against phage predation and that this OMV-mediated inhibition is phage receptor-dependent. Our results suggest that phage therapy or prophylaxis should take into consideration the production of OMVs as a bacterial decoy mechanism that could influence the outcome of phage treatment.

IMPORTANCE

Phages have been increasingly realized for the significance of their interactions with bacterial cells in multiple environments. Bacteria use myriad strategies to defend against phage infection, including: restriction modification, abortive infection, phase variation of cell surface receptors, phage-inducible chromosomal islands, and CRISPR-Cas systems. The data presented here suggest that the apparently passive process of OMV release can also contribute to phage defense. By considering the effect of OMVs on infection of *V. cholerae* by three unique virulent phages, ICP1, ICP2 and ICP3, we show that, *in vitro,* a reproducible reduction in bacterial killing is both dose- and phage receptor-dependent. This work supports a role for OMVs as natural decoys to defend bacteria from phage predation.

INTRODUCTION

Cholera, caused by toxigenic strains of *V. cholerae*, is a profuse secretory diarrheal disease endemic to many countries with poor sanitation infrastructure and limited access to clean water and food [1]. It is estimated that 1.3 to 4 million cases of cholera occur annually with 23,000 to 143,000 deaths [2]. Cholera symptoms can be ameliorated with the standard care of oral rehydration therapy or fluids administered intravenously for severe cases, yet if left untreated can result in death within several hours [3].

Given the explosive rapid onset of disease and risk of mortality, control efforts have focused on generating and administering vaccines against cholera. Whole cell killed and live attenuated cholera oral vaccines are available (reviewed in [4]. Additional alternative approaches are being pursued to prevent *V. cholerae* infection, including phage prophylaxis [5, 6] and an outer membrane vesicle (OMV)-based vaccine [7-10]. Recently, oral administration of a cocktail of three virulent phages, named ICP1, ICP2, and ICP3, which were isolated from rice-water stool samples of cholera patients in Bangladesh [11], was shown to protect against *V. cholerae* infection in infant mice and infant rabbit models of colonization and disease [6]. Potentially, phages could also be used to reduce the numbers of *V. cholerae* or other water-borne bacterial pathogens in aquatic reservoirs.

OMVs are non-replicating, spherical nanostructures produced during bacterial growth. These outer membrane enclosed structures are composed of outer membrane lipids, outer membrane proteins, and periplasmic components. It has been shown that OMVs play several roles in bacterial biology, including assisting interactions between bacterial cells and delivering of cargo proteins, toxins, and nucleic acids to neighboring bacteria and host cells [12-15]. *V. cholerae* OMVs are immunogenic and it has been shown that mucosal immunization of adult female mice with OMVs provides maternal

protection to their suckling pups from *V. cholerae* colonization [7-10]. Similar immunization strategies and outcomes have been observed with OMVs against other pathogenic bacteria [16, 17].

Given that OMVs are comprised of bacterial membrane components, their potential to act as decoys – defense mechanisms that bacteria employ to protect themselves against external insults, including antibiotics, antimicrobial peptides, and bacteriophage infection – has been explored by others [14, 18]. In this work, we set out to explore whether *V. cholerae* OMVs can act as a defense mechanism against predation by the virulent phages ICP1, ICP2, and ICP3. We show that OMVs produced by two representative modern cholera pandemic strains can inhibit (neutralize) all three phages, and we show this neutralization is receptor-dependent for two of the phages whose receptors have been identified.

MATERIALS AND METHODS

Bacterial strains and growth conditions

For all experiments, *V. cholerae* and isogenic mutants were routinely grown in Luria-Bertani Miller (LB) broth or on LB agar (Thermo Fisher Scientific) at 37°C with aeration. *V. cholerae* strains and phages used in this study are listed in Table 1. *V. cholerae* HC1037 was isolated at the Cholera Treatment Center Jacmel, Haiti, in January of 2014 from a cholera patient rice-water stool sample.

Bacteriophage stock preparation

To obtain high titer phage stocks, 40 ml cultures of *V. cholerae* E7946 were grown to mid-exponential phase (absorbance OD600 nm = 0.2-0.3). A single plaque stock was inoculated into the culture and supplemented with calcium chloride at a final concentration of 5 mM to aid phage adsorption. The infected culture was incubated at 37°C with aeration for 1.5 hours and then treated with sodium citrate at a final concentration of 50 mM to block further phage adsorption. The infected culture was centrifuged for 15 minutes at 8,000 x *g* and the supernatant was transferred to a 50 ml conical tube. The supernatant was filter-sterilized using a 0.22 μm filter (Millipore). A 0.2 volume of 5x phage precipitation buffer (20% Polyethylene glycol MW 8000, 2.5 M NaCl) was added and mixed by inversion. The mixture was incubated for 24-48 h at 4°C to precipitate the phage, after which the phage was pelleted by centrifugation for 15 minutes at 10,000 x *g* at 4°C using a Beckman Coulter floor centrifuge with a F13-14x50Cy rotor. The supernatant was removed by decanting, and the tube was centrifuged again for 1 minute at 7,000 x *g* to allow subsequent removal of the last traces of supernatant. The phage pellet was resuspended in STE Buffer (100 mM NaCl, 10 mM Tris-HCl pH 7.5, 1 mM EDTA) supplemented with 10 mM MgSO4 to help stabilize the phage and stored at 4°C until use.

Outer membrane vesicle isolation

To isolate OMVs, *V. cholerae* was struck out on an LB agar plate and incubated overnight at 37°C. The following day, an individual colony was inoculated into 6 ml of LB broth and grown for ~8 hours at 37°C with aeration in a roller drum. This culture was then sub-cultured in a 1:100 ratio in 600 ml of LB broth and incubated overnight at 37°C with aeration. Cultures were chilled in an ice-water bath for ~10 minutes, then centrifuged for 10 minutes at 10,000 x *g* to pellet bacterial cells. The supernatants, which contained the OMVs, were filtered through a SteriCup 0.22 μm filter system (Millipore) to remove any remaining bacterial cells, and an EDTA-free protease inhibitor cocktail (Roche) was added. OMVs were pelleted from culture filtrates by centrifugation at 28,000 RPM for 3 hours and 15 minutes using a Beckman Coulter Optima L-90K ultracentrifuge with an SW 32 Ti rotor. After removal of supernatants by decanting, OMV pellets originating from one 600 ml culture were resuspended in a total of 0.5 ml of phosphate buffered saline (Boston BioProducts) and stored in aliquots at -80°C. OMV protein concentration was measured using the Modified Lowry Protein Assay kit (Thermo Fisher Scientific).

Phage neutralization assays

For phage neutralization assays, 10,000 plaque-forming units (PFU) of phage were added to OMVs at the specified amount (25, 10, 1, or 0.2 μg) in a final volume of 200 μl LB and vortexed to mix. Mixed samples were incubated for 1 hour at room temperature. Mid-exponential growth phase cultures of wild type *V. cholerae* E7946 or HC1037 were used as host bacteria for plaque assays. Cultures of the host bacteria were centrifuged for 5 minutes at 4,000 x *g*, washed once in LB broth, and adjusted to an absorbance (OD600 nm) of 0.5. Phage alone or phage/OMV mixtures in a total volume of 90 μl were added to 100 μl of host *V. cholerae* and were allowed to adsorb for 10 minutes at room temperature. The mixtures were then transferred to 6-well, clear, untreated tissue culture

plates (Corning). To each well, 3 ml of molten 47˚C 0.3% agarose in LB broth was added, mixed by gentle swirling, and allowed to cool and solidify. The plates were incubated for ~4 hours at 37˚C to allow plaque formation. After visually counting plaques, the titer of plaque-forming units per ml of phage added was calculated. Results are shown as log change in PFU ml-1 compared to the phage only (no OMVs added) control.

Bacteriophage-OMV imaging using cryo-electron tomography

The interactions between OMVs and ICP phages were characterized using cryo-electron tomography (cryo-ET). One μl of *V. cholerae* HC1037 OMVs at a concentration of 8.4 mg ml-1 (protein content) was added to 100 μl of phage at a titer of ~1010 PFU ml-1 in phosphate buffered saline and incubated for 1 hour at room temperature. After incubation, 10 nm BSA-treated colloidal gold fiducials (Electron Microscopy Sciences, Hatfield, PA) were added as alignment markers. The sample (4 μl) was applied to glow discharged, 200 mesh copper Quantifoil R 2/1 TEM grids (Quantifoil Micro Tools Gmbh, Jena, Germany) before plunge freezing with a Vitrobot Mark III system (FEI, Hillsboro, OR). Images were acquired on a JEOL JEM-2200FS field emission TEM (JEOL Ltd., Japan) operating at 200 kV and equipped with an in-column Omega energy filter (slit width of 20 eV) and a Direct Electron DE-20 (Direct Electron, LP, San Diego, CA). Bi-directional tilt series were collected at 10,000. nominal magnification (6.14 Å/pixel) semi-automatically using the SerialEM software package [31]. Data sets were acquired with a tilt range of -62° to +62° at 2° increments, a defocus of -6 μm, and a total electron dose of ~120 e-/Å2 [32, 33]. Images were recorded at 12 frames per second and motion corrected using scripts provided by Direct Electron. IMOD software [34] was used for CTF-correction of the images by phase inversion and for three-dimensional (3D) reconstruction of the tomograms by r-weighted back-projection. 3D segmentations were done manually using the Amira package (FEI Visualization Sciences Group,

Hillsboro, OR).

Statistical analyses

Graphs were plotted using Prism 7 software (GraphPad) and statistical analyses were done using Student's two-tailed *t*-test.

RESULTS

V. cholerae OMVs inhibit phage infection

To evaluate whether *V. cholerae* OMVs inhibit phage predation, OMVs isolated from spent culture supernatants of wild type *V. cholerae* O1 El Tor strain E7946 [19] were incubated with the *V. cholerae* O1-specific virulent phage ICP1 [11, 20] prior to measuring bacterial killing, using plaque formation on the *V. cholerae* E7946 strain as a proxy (Figure 1). We observed a significant and dose-dependent inhibition of plaque formation by OMVs. It has been shown that the O1-antigen of the *V. cholerae* lipopolysaccharide (LPS) is the receptor for ICP1 [11, 21]. To test whether the observed phage neutralization is receptor-dependent, we performed plaque assays using OMVs from an acapsular derivative of the *V. cholerae* O139 serogroup strain MO10, as well as OMVs from an E7946 Δ*wbeL* rough mutant that fails to synthesize O1-antigen [21]. Addition of OMVs from either the O139 strain or the E7946 rough mutant did not reduce ICP1 infection, indicating that the presence of O1-antigen in OMVs is required to neutralize this phage (Figure 1).

To investigate whether the neutralizing effect observed for *V. cholerae* O1 OMVs on ICP1 was a general phenomenon, we performed similar neutralization assays using two additional virulent phages, ICP2 and ICP3. We observed that while there was a significant, dose-dependent inhibition of ICP2, the magnitude of inhibition was approximately half of that observed for ICP1 (0.5 logs less) and only at the two highest OMV doses tested (25 and 10 μg) (Figure 2). The receptor for ICP2 was previously shown to be the outer membrane porin OmpU [22]. We hypothesize that the lower level of neutralization of ICP2 by OMVs may be due to the known low level of expression of OmpU during growth *in vitro* in Luria-Bertani Miller (LB) broth [23]. Despite the low level of expression of OmpU under the conditions tested, we observed that OMVs purified from E7946 OmpU G325D, which is an ICP2 resistant point mutant [22], failed to neutralize ICP2 at the highest

OMV dose tested (Figure 2). These results indicate that OMV-mediated neutralization of ICP2 is dependent on the presence of the ICP2 receptor, OmpU.

As observed for ICP1 and ICP2 neutralization, addition of OMVs showed a dose-dependent reduction in the ability of ICP3 to infect (Figure 3), albeit again to a lower magnitude than ICP1 inhibition (Figure 1). The receptor for ICP3 is currently unknown.

Modern (7th pandemic) cholera epidemics have been attributed to a succession of three types of *V. cholerae* O1 El Tor strains, called Wave 1, 2, and 3, with *V. cholerae* E7946 belonging to Wave 1 [24]. Wave 2 have replaced Wave 1 strains beginning in the late 1970s, and Wave 3 have subsequently replaced Wave 2 strains beginning in the late 1980s. Wave 3 strains, which now dominate as the cause of cholera epidemics in South Asia, Africa, and Haiti, have recently been shown to be hypervirulent [25]. To evaluate whether ICP1, ICP2, and ICP3 can also be inhibited by OMVs from a Wave 3 strain, plaque assays were performed using a *V. cholerae* clinical isolate, HC1037, from the ongoing epidemic in Haiti. We observed an order of magnitude reduction in plaque formation for all three phages (Figure 4), indicating that OMVs from distinct *V. cholerae* strains, including the most current pandemic strain, can neutralize virulent phages.

Our results thus far suggest that *V. cholerae* OMVs are able to neutralize phages by acting as decoys, whereby presumably the phage tail fibers bind to receptors on the OMV surface, therefore precluding the tail fibers from interacting with bacteria. We sought to directly visualize and confirm these interactions using cryo-electron tomography (cryo-ET). OMVs purified from HC1037 were used to neutralize phages ICP1, ICP2, and ICP3 and samples were applied to copper TEM grids, immediately flash frozen in liquid ethane, and stored in liquid nitrogen. Grids were then imaged by

cryo-electron microscopy to observe phages and OMVs. For a subset of individual phages bound to OMVs, tilt series were acquired and reconstructed via cryo-ET. Three representative tomograms of phages bound to OMVs are shown in Figure 5. A slice through the three-dimensional volume is displayed, and thus the OMVs appear as circles. The sizes and morphologies of all three phages were consistent with a previous work using traditional transmission electron microscopy [11]. We often observed direct contact between phages and one, sometimes two, OMVs, with the contact being exclusively at the tail end of the phages. Quantification of phages bound to OMVs was not possible by this method because we observed a large difference in binding between phages and OMVs to the carbon substrate on the copper TEM grids. Contact between a subset of the phage tail fibers and individual OMVs can be seen in each example, with the bound OMV being offset from the central axis of the phage tail. The phage tails were not observed to be contracted nor was DNA ejected from the capsids.

Altogether, our data indicates that OMVs can neutralize virulent phages by engagement of phage tail fibers with phage receptors on the OMV surface. This engagement presumably prevents or interferes with productive phage adsorption to the *V. cholerae* surface.

DISCUSSION

OMVs are naturally secreted by gram-negative bacteria and have been implicated in a diversity of biological roles, including cell-to-cell communication and biofilm integrity (reviewed in [12-15]). Because OMVs have essentially the same surface protein, lipid, and carbohydrate structures as the bacterial cells that produce them, they may serve as natural decoys to defend the bacteria that secrete them against harmful products. Indeed, OMVs have been described as a virulence mechanism, where their secretion dampens the effects of host antimicrobial peptides and administered antibiotics, which target the OMVs instead of the bacterial cells (reviewed in [14]).

Similarly, OMVs would seem to be natural decoys to protect bacteria from virulent phages. However there have been few reports demonstrating this. *Escherichia coli* OMVs were previously shown to neutralize bacteriophage T4 175 [18, 26], while the cyanophage PHM-2 can directly interact with *Prochlorococcus*, resulting in contraction of the phage tail, and ultimately DNA release [27]. Here we provide further support for this biological function of OMVs by showing that OMVs produced by pathogenic strains of *V. cholerae* can neutralize three different virulent phages. The three virulent phages we tested, ICP1, ICP2, and ICP3, are naturally found in association with pathogenic *V. cholerae* in patient stool samples from Bangladesh, and thus the frequency of interaction between them is likely high. In this work, we show that OMVs reduced phage predation in a dose- and receptor-dependent manner.

Because the concentrations of OMVs that naturally accumulate in the vicinity of *V. cholerae* in aquatic reservoirs, in biofilms, and in the human intestinal tract are unknown, it is not possible at present to positively state that *V. cholerae* OMVs neutralize phages in nature. Additionally, mutants of *V. cholerae* that fail to make OMVs have not been isolated as yet, and so it is not possible to

quantify the role of OMVs in protection from phage predation during infection or in aquatic environment microcosms. However, because *V. cholerae* does produce OMVs, it is reasonable to assume that they protect *V. cholerae* from phage predation to an extent commensurate with the rate of OMV production and accumulated OMV concentration.

Multiple phage defense strategies are used by bacteria, each targeting different stages of phage infection. Phase variation or mutation of cell surface receptors, restriction-modification systems, abortive infection, CRISPR-Cas, phage-inducible chromosomal islands, and bacteriophage-exclusion systems [28] have all been shown to contribute to the protection of bacterial cells. How these processes are regulated and integrated to ensure bacterial cell survival remains to be fully understood. We suggest that the data presented here further supports the idea that OMVs can also contribute toward phage-defense, by acting as decoys in a receptor-dependent manner.

Our results add to the increasing recognition of OMVs as important bacterial secreted products. OMVs have potentially important differences with other canonical secretion systems, including continuous OMV production, exacerbated OMV production under stressful conditions to the bacteria, and encasing of virulence factors and signaling molecules by a membrane lipid bilayer that is protective against degradative enzymes [29, 30]. Our findings add to a growing body of data showing that OMVs act as a first line of defense against external insults.

ACKNOWLEDGMENTS

This work was supported in part by NIH grant R01 GM104540, NSF grant 0923395, grants from Emory University, Children's Healthcare of Atlanta, the Georgia Research Alliance, the Center for AIDS Research at Emory University (P30 AI050409), and the James B. Pendleton Charitable Trust to E.R.W; NIH T32 AI007329 to T.R.R.; a Pew Latin American Fellows Program in the Biomedical Sciences and a CONICYT Becas Chile postdoctoral fellowship to C.A.S.V.; NIH R01 AI12875 to A.A.; and NIH R01 AI055058 to A.C. A.C. is a Howard Hughes Medical Institute Investigator. We thank the Robert P. Apkarian Integrated Electron Microscopy Core facility of Emory University for microscopy services and support.

REFERENCES

1. Clemens, J. D., Nair, G. B., Ahmed, T., Qadri, F., and Holmgren, J. Cholera. *The Lancet*, 2017. **390**(10101): p. 1539-1549.
2. Ali, M., Nelson, A. R., Lopez, A. L., and Sack, D. A. Updated global burden of cholera in endemic countries. *PLoS Neglected Trop Dis*, 2015. **9**(6): p. e0003832.
3. Harris, J. B., LaRocque, R. C., Qadri, F., Ryan, E. T., and Calderwood, S. B. Cholera. *The Lancet*, 2012. **379**(9835): p. 2466-2476.
4. Bishop, A. L. and Camilli, A. *Vibrio cholerae*: Lessons for mucosal vaccine design. *Expert Rev Vaccines*, 2011. **10**(1): p. 79-94.
5. Jaiswal, A., Koley, H., Ghosh, A., Palit, A., and Sarkar, B. Efficacy of cocktail phage therapy in treating *Vibrio cholerae* infection in rabbit model. *Microbes Infect*, 2013. **15**(2): p. 152-6.
6. Yen, M., Cairns, L. S., and Camilli, A. A cocktail of three virulent bacteriophages prevents *Vibrio cholerae* infection in animal models. *Nat Commun*, 2017. **8**: p. 14187.
7. Wang, Z., Lazinski, D. W., and Camilli, A. Immunity provided by an outer membrane *Vibrio cholerae* vaccine is due to O-antigen-specific antibodies inhibiting bacterial motility. *Infect Immun*, 2017. **85**(1): p. e00626-16.
8. Schild, S., Nelson, E. J., and Camilli, A. Immunization with *Vibrio cholerae* outer membrane vesicles induces protective immunity in mice. *Infect Immun*, 2008. **76**(10): p. 4554-4563.
9. Bishop, A. L., Schild, S., Patimalla, B., Klein, B., and Camilli, A. Mucosal immunization with *Vibrio cholerae* outer membrane vesicles provides maternal protection mediated by antilipopolysaccharide antibodies that inhibit bacterial motility. *Infect Immun*, 2010. **78**(10): p. 4402-4420.

10. Bishop, A. L., Tarique, A. A., Patimalla, B., Calderwood, S. B., Qadri, F., and Camilli, A. Immunization of mice with *Vibrio cholerae* outer-membrane vesicles protects against hyperinfectious challenge and blocks transmission. *J Infect Dis*, 2012. **205**(3): p. 412-421.

11. Seed, K. D., Bodi, K. L., Kropinski, A. M., Ackermann, H.-W., Calderwood, S. B., Qadri, F., and Camilli, A. Evidence of a dominant lineage of *Vibrio cholerae*-specific lytic bacteriophages shed by cholera patients over a 10-year period in Dhaka, Bangladesh. *mBio*, 2011. **2**(1): p. e00334-10.

12. Ellis, T. N. and Kuehn, M. J. Virulence and immunomodulatory roles of bacterial outer membrane vesicles. *Microbiol Mol Biol* Rev, 2010. **74**(1): p. 81-94.

13. Kulp, A. and Kuehn, M. J., Biological functions and biogenesis of secreted bacterial outer membrane vesicles. *Annu Rev Microbiol*, 2010. **64**: p. 163-184.

14. Schwechheimer, C. and Kuehn, M. J. Outer-membrane vesicles from gram-negative bacteria: Biogenesis and functions. *Nat Rev Microbiol*, 2015. **13**(10): p. 605-619.

15. Jan, A. T. Outer membrane vesicles (OMVs) of gram-negative bacteria: A perspective update. *Front Microbiol*, 2017. **8**: p. 1053.

16. Roier, S., Leitner, D. R., Iwashkiw, J., Schild-Prüfert, K., Feldman, M. F., Krohne, G., Reidl, J., and Schild, S. Intranasal immunization with nontypeable *Haemophilus influenzae* outer membrane vesicles induces cross-protective immunity in mice. *PLoS One*, 2012. **7**(8): p. e42664.

17. Huang, W., Wang, S., Yao, Y., Xia, Y., Yang, X., Li, K., Sun, P., Liu, C., Sun, W., Bai, H., Chu, X., Li, Y., and Ma, Y. Employing *Escherichia coli*-derived outer membrane vesicles as an antigen delivery platform elicits protective immunity against *Acinetobacter baumannii* infection. *Sci Rep*, 2016. **6**: p. 37242.

18. Manning, A. J. and Kuehn, M. J. Contribution of bacterial outer membrane vesicles to innate bacterial defense. *BMC Microbiology*, 2011. **11**: p. 258-258.

19. Levine, M. M., Black, R. E., Clements, M. L., Cisneros, L., Saah, A., Nalin, D. R., Gill, D. M., Craig, J. P., Young, C. R., and Ristaino, P. The pathogenicity of nonenterotoxigenic *Vibrio cholerae* serogroup O1 biotype El Tor isolated from sewage water in Brazil. *J Infect Dis*, 1982. **145**(3): p. 296-9.

20. Seed, K. D., Lazinski, D. W., Calderwood, S. B., and Camilli, A. A bacteriophage encodes its own CRISPR/Cas adaptive response to evade host innate immunity. *Nature*, 2013. **494**(7438): p. 489-491.

21. Seed, K. D., Faruque, S. M., Mekalanos, J. J., Calderwood, S. B., Qadri, F., and Camilli, A. Phase variable O antigen biosynthetic genes control expression of the major protective antigen and bacteriophage receptor in *Vibrio cholerae* O1. *PLoS Pathog*, 2012. **8**(9): p. e1002917.

22. Seed, K. D., Yen, M., Shapiro, B. J., Hilaire, I. J., Charles, R. C., Teng, J. E., Ivers, L. C., Boncy, J., Harris, J. B., and Camilli, A. Evolutionary consequences of intra-patient phage predation on microbial populations. *eLife*, 2014. **3**: p. e03497.

23. Miller, V. L. and Mekalanos, J. J. A novel suicide vector and its use in construction of insertion mutations: Osmoregulation of outer membrane proteins and virulence determinants in *Vibrio cholerae* requires ToxR. *J Bacteriol*, 1988. **170**(6): p. 2575-2583.

24. Mutreja, A., Kim, D. W., Thomson, N., Connor, T. R., Lee, J. H., Kariuki, S., Croucher, N. J., Choi, S. Y., Harris, S. R., Lebens, M., Niyogi, S. K., Kim, E. J., Ramamurthy, T., Chun, J., Wood, J. L. N., Clemens, J. D., Czerkinsky, C., Nair, G. B., Holmgren, J., Parkhill, J., and Dougan, G. Evidence for multiple waves of global transmission within the seventh cholera pandemic. *Nature*, 2011. **477**(7365): p. 462-465.

25. Satchell, K. J. F., Jones, C. J., Wong, J., Queen, J., Agarwal, S., and Yildiz, F. H. Phenotypic analysis reveals that the 2010 Haiti cholera epidemic is linked to a hypervirulent strain. *Infect Immun*, 2016. **84**(9): p. 2473-2481.

26. Loeb, M. R. Bacteriophage T4-mediated release of envelope components from *Escherichia coli*. *J Virol*, 1974. **13**(3): p. 631-641.

27. Biller, S. J., Schubotz, F., Roggensack, S. E., Thompson, A. W., Summons, R. E., and Chisholm, S. W. Bacterial vesicles in marine ecosystems. *Science*, 2014. **343**(6167): p. 183.

28. Goldfarb, T., Sberro, H., Weinstock, E., Cohen, O., Doron, S., Charpak-Amikam, Y., Afik, S., Ofir, G., and Sorek, R. BREX is a novel phage resistance system widespread in microbial genomes. *EMBO J*, 2015. **34**(2): p. 169-183.

29. Guerrero-Mandujano, A., Hernandez-Cortez, C., Ibarra, J. A., and Castro-Escarpulli, G. The outer membrane vesicles: Secretion system type zero. *Traffic*, 2017. **18**(7): p. 425-432.

30. Bonnington, K. E. and Kuehn, M. J. Protein selection and export via outer membrane vesicles. *Biochim Biophys Acta*, 2014. **1843**(8): p. 1612-1619.

31. Mastronarde, D. N. Automated electron microscope tomography using robust prediction of specimen movements. *J Struct Biol*, 2005. **152**(1): p. 36-51.

32. Hampton, C. M., Strauss, J. D., Ke, Z., Dillard, R. S., Hammonds, J. E., Alonas, E., Desai, T. M., Marin, M., Storms, R. E., Leon, F., Melikyan, G. B., Santangelo, P. J., Spearman, P. W., and Wright, E. R. Correlated fluorescence microscopy and cryo-electron tomography of virus-infected or transfected mammalian cells. *Nat Protoc*, 2017. **12**(1): p. 150-167.

33. Ellison, C. K., Kan, J., Dillard, R. S., Kysela, D. T., Ducret, A., Berne, C., Hampton, C. M., Ke, Z., Wright, E. R., Biais, N., Dalia, A. B., and Brun, Y. V. Obstruction of pilus retraction stimulates bacterial surface sensing. *Science*, 2017. **358**(6362): p. 535.

34. Kremer, J. R., Mastronarde, D. N., and McIntosh, J. R. Computer visualization of three-dimensional image data using IMOD. *J Struct Biol*, 1996. **116**(1): p. 71-76.

35. Nesper J, Kraiss A, Schild S, Blass J, Klose KE, Bockemühl J, Reidl J. Comparative and genetic analyses of the putative *Vibrio cholerae* lipopolysaccharide core oligosaccharide biosynthesis (*wav*) gene cluster. *Infect Immun*, 2002. 70:2419-33.

FIGURE LEGENDS

Figure 1. LPS O1-antigen in OMVs is required to neutralize ICP1. Titration of *V. cholerae* E7946 OMVs, or OMVs from *V. cholerae* O139 or E7946 D*wbeL*, on a fixed concentration of prey (E7946) and phage ICP1 (~10,000 PFU). *n* = 3 for all, except for 25 μg of OMVs where n = 6. The horizontal solid lines indicate mean ± standard deviation. ***P* = 0.0018 for 25 μg, **P* = 0.036 for 10 μg, **P* = 0.0398 for 1 μg and **P* = 0.019 for 0.2 μg.

Figure 2. OmpU in OMVs is required to neutralize ICP2. Titration of *V. cholerae* E7946 OMVs, or OMVs from E7946 OmpU G235D mutant (OmpU*), on a fixed concentration of prey (E7946) and phage ICP2 (~10,000 PFU). *n* = 10 for 25 μg; *n* = 4 for 10, 1, and 0.2 μg of OMVs; and *n* = 6 for OmpU G325D. The horizontal solid lines indicate mean ± standard deviation. *****P* = <0.0001 for 25 μg, **P* = 0.0121 for 10 μg and **P* = 0.0135 for OmpU G325D.

Figure 3. OMVs neutralize ICP3. Titration of *V. cholerae* E7946 OMVs on a fixed concentration of prey (E7946) and ICP3 (~10,000 PFU). *n* = 6 for all. The horizontal solid lines indicate mean ± standard deviation. ****P* = 0.0006 for 25 and 10 μg, ***P* = 0.0053 for 1 μg and **P* = 0.0224 for 0.2 μg.

Figure 4. OMVs from a *V. cholerae* Wave 3 pandemic strain neutralizes all three ICP phages. Titration of *V. cholerae* HC1037 OMVs on a fixed concentration of prey (HC1037) and ICP1, ICP2, and ICP3 (~10,000 PFU). *n* = 3 for all. The horizontal solid lines indicate mean ± standard deviation. **P* = 0.0076 for ICP1, ***P* = 0.02, **P* = 0.0093.

Figure 5. Tail fibers of ICP phages interact with *V. cholerae* outer membrane vesicles (OMVs). Cryo-electron tomography slices and 3D segmentations of *V. cholerae* HC1037 OMVs free or bound to tail fibers of (**A**) 459 ICP1, (**B**) ICP2, and (**C**) ICP3. Not all OMVs are shown in the 3D segmentation 460 panels. Scale bars, 100 nm.

Figure 1

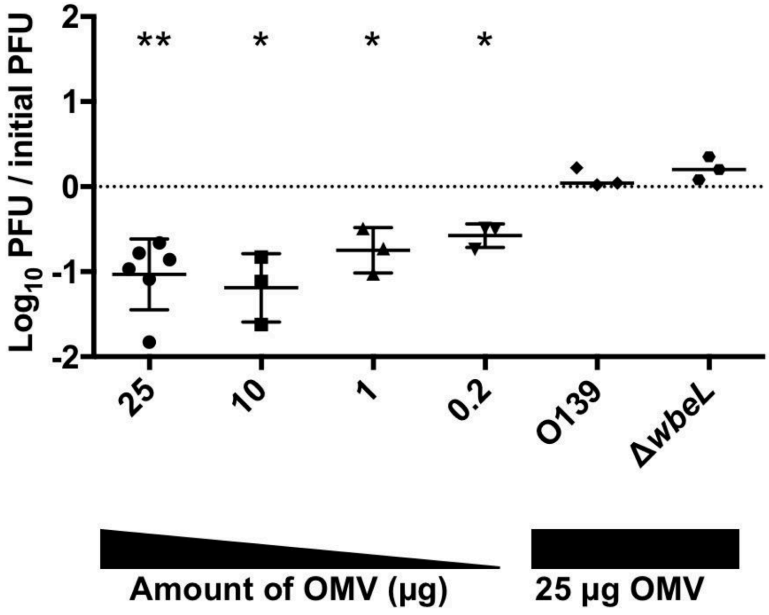
Log10 PFU / initial PFU
2
1
0
-1
-2
**
*
*
*
25
10
1
0.2
O139
ΔwbeL
Amount of OMV (μg)
25 μg OMV

Figure 2

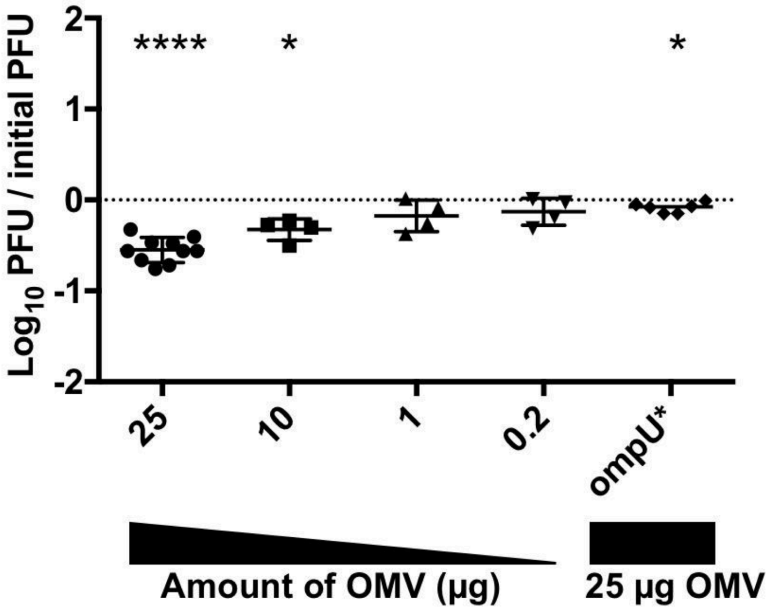
Log10 PFU / initial PFU
2
1
0
-1
-2
****
*
*
25
10
1
0.2
ompU*
Amount of OMV (µg)
25 µg OMV

Figure 3

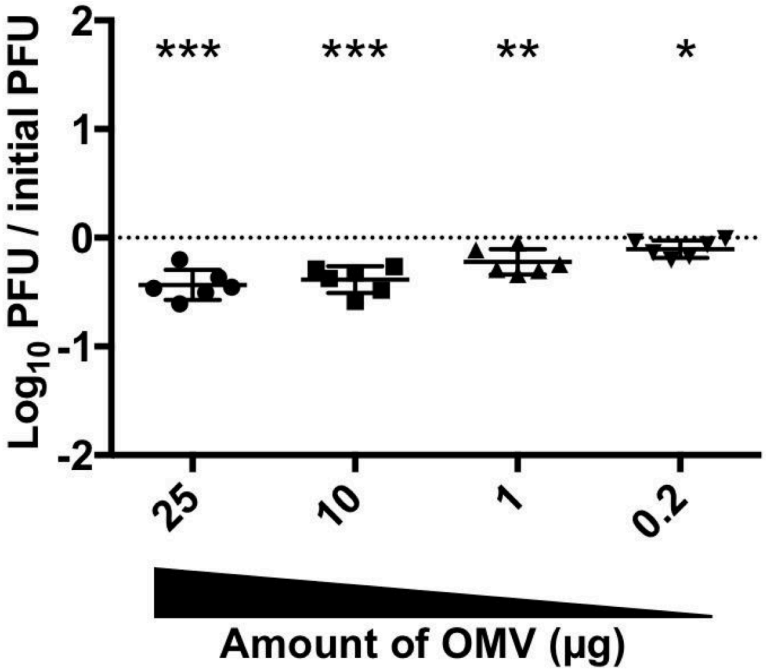

Figure 4

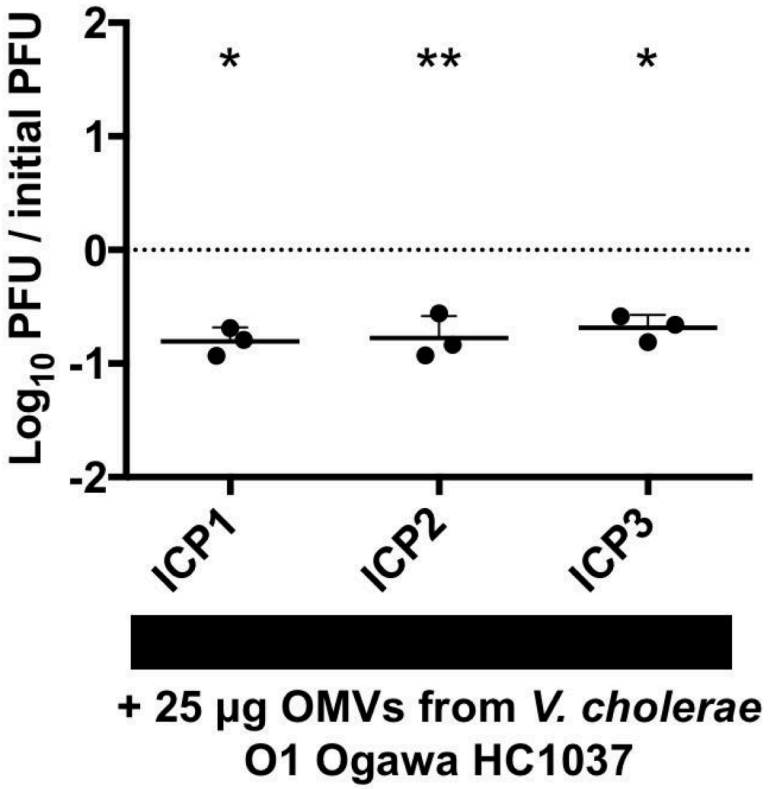
2
1
0
-1
-2
Log10 PFU / initial PFU
*
**
*
ICP1
ICP2
ICP3
+ 25 µg OMVs from V. cholerae
O1 Ogawa HC1037

Figure 5

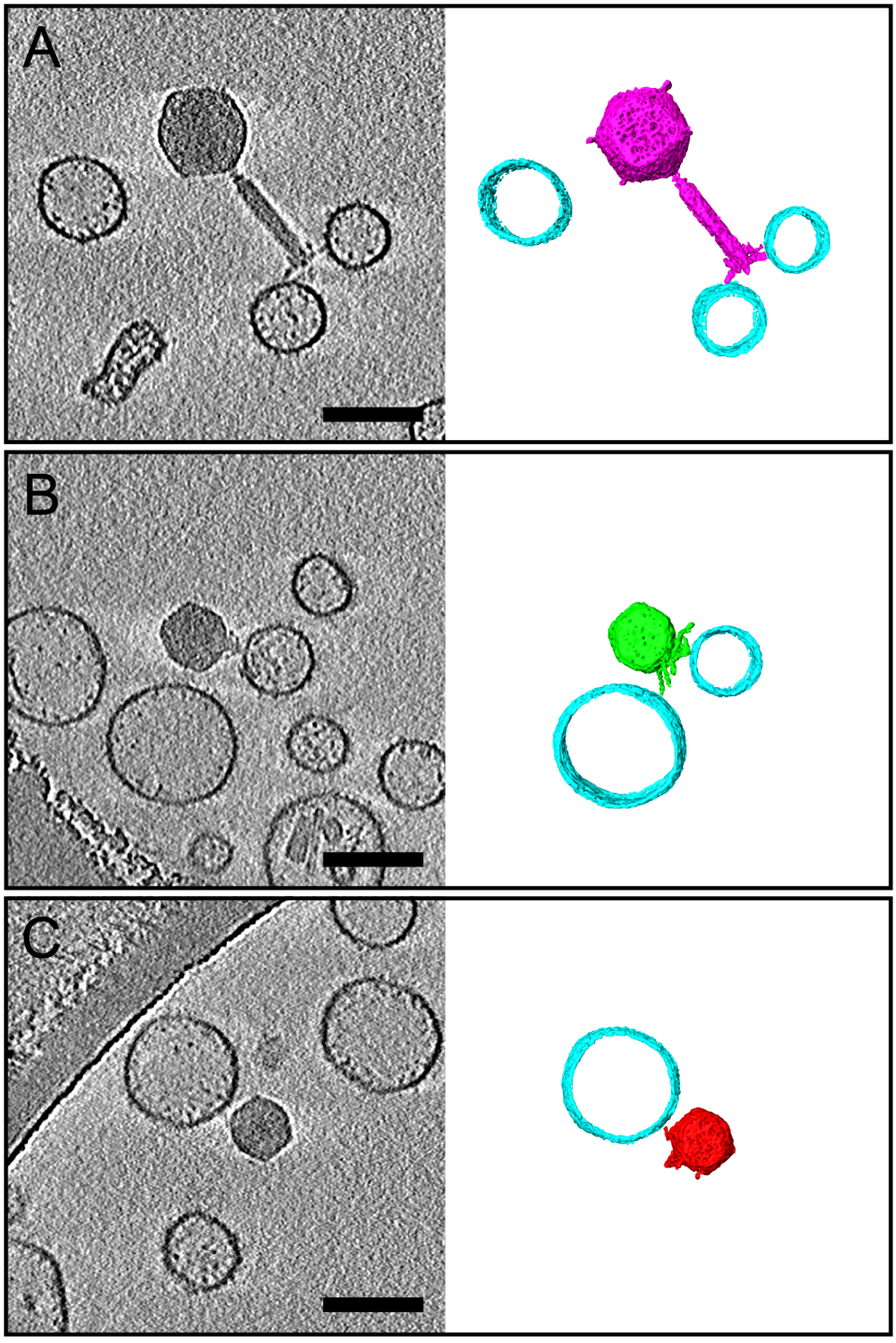

Table 1. Bacterial strains and bacteriophages used in this study.

Strain	Genotype and description	Reference
AC53	*V. cholerae* O1 El Tor Ogawa E7946	19
AC5423	*V. cholerae* O1 El Tor Ogawa HC1037	This study
AC4623	E7946 Δ*wbeL*	21
AC3276	*V. cholerae* O139 MO10 *ontA*::pGP	35
AC4682	E7946 OmpU G325D	22
ICP1	Bacteriophage ICP1_2011_A; *Myoviridae* family	11,20
ICP2	Bacteriophage ICP2_2004; *Podoviridae* family	11
ICP3	Bacteriophage ICP3_2007; *Podoviridae* family	11

Chapter 4: Pilus retraction in *Caulboacter crescentus* is required for ϕCbK infection

Rebecca S. Dillard[1], Rachel E. Storms[1], Leon De Masi[1], Deanna Altomara[1], Gaël Panis[2], Patrick H. Viollier[2], Elizabeth R. Wright[1,3]

[1]Division of Pediatric Infectious Diseases. Emory University School of Medicine. Children's Healthcare of Atlanta. Atlanta, GA 30322

[2]Department of Microbiology and Molecular Medicine. Centre Medicale Universitaire, Faculty of Medicine, University of Geneva, CH-1211 Geneva 4, Switzerland

[3]Robert P. Apkarian Integrated Electron Microscopy Core, Emory University, Atlanta, GA 30322

This manuscript was written by R.S.D. and L.D.M.

All experiments were performed by R.S.D. with the exception of Figure 1B.

ABSTRACT

Caulobacter crescentus is a gram-negative bacterium that divides asymmetrically to produce a sessile stalked cell and a motile swarmer cell, which expresses a polar flagellum and polar type IVc pili. ϕCbK is a bacteriophage that initially adsorbs to the *C. crescentus* flagellum through a head filament and uses flagellar rotation to reach the cell pole. It has been hypothesized that ϕCbK uses pilus retraction to position itself for attachment at the pilus portals, although there is no known retraction ATPase in the *C. crescentus* assembly complex. Treatment with anti-PilA antibody reduced both motility and ϕCbK adsorption, suggesting that antibody binding blocks pilus retraction and prevents the phage from reaching the receptor at the cell pole. ϕCbK adsorption is also negatively impacted by the addition of CCCP, indicating that the proton motive force is involved in pilus dynamics. Negative stain and cryo-electron microscopy indicate that antibody treatment increases the number of cells with extended pili, demonstrating that pilus retraction has been stalled. This study demonstrates the role of type IVc pilus retraction in ϕCbK adsorption. The data support a model of ϕCbK adsorption in which the phage localizes at the cell pole using flagellar rotation, attaches to the pilus filament through its tail fiber, and then uses retraction of the pilus to reach the pilus portal where it injects the genome.

INTRODUCTION

Type IV Pili (T4P) are the most widespread class of pili in bacteria [1]. T4P are found in multiple bacterial species, from pathogens such as Enteropathogenic *Escherichia coli* [2], *Vibrio cholerae* [3], *Neisseria meningitidis* [4], and *Pseudomonas aeruginosa* [5], plant pathogens such as *Xanthomonas campestris* [6], and even archaeal species [7]. T4P are highly flexible and extremely thin ranging from 5 to 8 nm in diameter, yet capable of growing to several micrometers in length. T4P systems were historically subdivided into two classes by amino acid sequence similarity and length, type IV pilus class A (T4aP) and type IV pilus class B (T4bP) [8, 9]. The T4aP found in *P. aeruginosa* has a 5-6 amino acid long leader sequence and a mature pilin length averaging 150 amino acids. T4aPs are present in many Gram-negative bacteria and the machinery components necessary for expression of a T4aP are encoded on multiple segments throughout a bacterial species genome [10].

T4bP pilins in contrast typically have a leader sequence of 15-30 amino acids and a mature length of approximately 190 amino acids [8]. This class has been found on enteric bacteria colonizing the intestine such as EPEC, ETEC, and *V. cholerae*. The components of T4bP systems are encoded on contiguous operons [10]. A subgroup of T4bP are the Tight Adherence (Tad) or Fimbrial low-molecular weight protein (Flp) pili, which like T4aP are found on a broad spectrum of bacteria [11], but encode a very small pilin of 40 to 80 amino acids and whose only known function is adherence to a surface [9]. Flp pili are found on a diverse range of pathogenic bacteria, such as *P. aeruginosa* [12] *Haemophilus ducreyi* [13, 14] and *Aggregatibacter actinomycetemcomitans* [13, 15].

Caulobacter crescentus is a non-pathogenic bacterium that divides in an unusually polar manner, forming a daughter sessile stalked cell and a daughter swarmer cell [16]. The species has long been a model system for the bacterial cell cycle [17] and the bacterial flagellum [18-20] because of its non-

pathogenic nature and polymorphic lifecycle. This species expresses polar pili (Caulobacter pilus assembly, Cpa) [21], previously categorized as Flp pili because the 14 amino acid leader sequence is cleaved from the prepilin to produce a 45 amino acid mature pilin and the genes for the pilus and the pilus assembly apparatus are encoded on an operon [22]. Recent phylogenetic analysis by Ellison *et al.*, however revealed a more distantly related class, type IV pilus class C (T4cP), to which the Cpa pilus belongs [23]. The T4cP lack homologues to the retraction ATPases found in T4aP and some T4bP, although retraction of Cpa pili has been directly visualized [23].

C. crescentus expresses several global regulatory proteins that control the transformation of a swarmer cell into a sessile cell once a bacterium attaches to a surface. Some of the most important cell cycle regulation proteins are TacA, SpmX, and CtrA, with CtrA controlling expression of the Cpa operon [24]. Expression of each regulatory protein is highly controlled, and abnormal expression of any one regulatory protein causes severe growth defects [25-29]. Swarmer cells express both a flagellum for motility and surface sensing [30-32] and Cpa pili, which are used by *C. crescentus* to anchor the bacterium to a surface [21]. The pilus enables the cell to adhere to the bottom of a freshwater streambed, form a holdfast structure [32], and transform into a sessile cell, where it can begin cell division. Lack of pilus expression alters biofilm formation in *C. crescentus* [33] and the bacteria become unable to tether themselves to a single point in a freshwater environment. The Cpa pilus has several core proteins found in other T4P systems, such as a main pilin subunit, PilA, assembly ATPases, CpaE and CpaF, and a dodecameric secretin, CpaC [22, 34]. It contains several associated proteins, such as outer membrane, periplasmic, and inner membrane assembly proteins, as well as proteins of unknown function [34]. The pilus portal is believed to be the receptor for irreversible attachment for *C. crescentus* phages such as ϕCbK, a large prolate siphophage that initially adsorbs to the *C. crescentus* flagellum using a head filament [35]. Strains which lack pilus expression are resistant

to phage infection [28], and it has been hypothesized that retraction of the pilus plays an important role in bringing the phage body into contact with the bacterial cell membrane [36]. We therefore sought to investigate the interactions between ϕCbK and *C. crescentus* by blocking pilus retraction using antibody binding and to better understand T4cP retraction in *C. crescentus* by dissipating the proton motive force.

MATERIALS AND METHODS

Strains and Growth Conditions

The *Caulobacter crescentus* strains, such as NA1000 and its derivatives, used in this study are listed in Table 1. All Strains were grown for overnight at 30°C with aeration in peptone yeast extract (PYE; 0.2% peptone, 0.1% yeast extract, 1 mM $MgSO_4$, 0.5 mM $CaCl_2$). These cultures were used in the protocols listed below.

Motility Assay

20 one μL drops of culture were placed on semi-solid PYE plates with 0.3% agar and grown for 48 hours at 30°C. Diameters of the motility zones formed from each drop were measured at 24 and 48 hours post inoculation. For cultures exposed to anti-PilA antibody, cells were incubated with dilutions of the antibody 45 minutes prior to inoculation on semi-solid plates. For motility assays with CCCP, CCCP was added to the semi-solid agar at the concentrations ranging from 1 – 50 μM.

Determination of Phage Adsorption Efficiency

The method used was adapted from the double overlay agar assay previously described [37, 38]. Briefly, 30 mL of an overnight culture of *C. crescentus* NA1000 grown in 1 mM $MgSO_4$ PYE was centrifuged for five minutes at 8000 x g and the supernatant decanted. The cell pellet was resuspended and then diluted in PYE adsorption media (4 mM $MgSO_4$) to obtain an OD_{600} of 0.6. Nine mL of the diluted culture was placed in an 125 mL Erlenmeyer flask and incubated for 30 minutes at 30°C and 60 rpm with and without the addition of dilutions of the anti-PilA antibody or CCCP. One mL of 1 x 10^6 PFU/mL ϕCbK in 4 mM $MgSO_4$ PYE was mixed with the 9 mL of diluted culture for a multiplicity of infection (MOI) of 0.001. Every 5 minutes, 100 μL aliquots of the *C. crescentus* cultures were removed from the flask and mixed in Eppendorf tubes containing 900

μL of ice-cold PYE and 30 μL chloroform for 45 minutes, as the ϕCbK completes its lytic cycle in *C. crescentus* at 50 minutes or later. Once all time points were collected, the Eppendorf tubes were centrifuged at 4°C for five minutes at 12000 × g. 100 μL of the phage-containing supernatant was mixed with 400 μL of a phage infection indicator strain (bNY304; OD_{600} = 0.3), mixed with 4.5 mL of molten 0.5% 1 mM $MgSO_4$ PYE agar and overlaid on a plate containing 20 mL of 1.5% 1 mM $MgSO_4$ PYE agar. The plates were incubated overnight at 30°C before counting PFU. A control flask containing only phage was maintained in parallel for the duration of the experiment. The adsorption rate constant (K-value) was calculated by plotting relative PFU over time for each adsorption and dividing the slope of the regression line by the viable bacteria cell number. K-values listed in Tables 2 and 3 are means of 3 separate regression lines.

Preparation of Grids for Transmission Electron Microscopy

Negatively stained grids. 400-mesh carbon-formvar copper grids (EM Sciences; Hatsfield, PA) were glow discharged for 30 seconds. *C. crescentus* cultures were treated with 1:500 anti-PilA antibody or 10 μM CCCP for fifteen minutes then four μL were applied to the grids and allowed to adsorb for five minutes. Grids were washed once with distilled water, stained for 45 seconds with 1% uranyl acetate (UA), and allowed to air dry.

Cryo-grids. C. crescentus cultures were treated with 1:500 anti-PilA antibody or 10 μM CCCP for fifteen minutes then mixed with 10 nm BSA-treated colloidal gold (Electron Microscopy Sciences, Hatfield, PA). To visualize ϕCbK adsorption, ϕCbK was added to the cultures 10 minutes prior to plunge-freezing at an MOI of 10. Four μL aliquots were applied to Quantifoil Cu R 2/1 200 mesh grids and

plunge-frozen using an FEI Vitrobot Mark III (FEI, Hillsboro, Oregon). Grids were stored in liquid nitrogen prior to imaging.

Transmission Electron Microscopy

Negatively stained specimens were imaged on a JEOL JEM-1400 transmission electron microscope (TEM; JEOL, Ltd., Japan) equipped with a LaB_6 filament and operated at an accelerating voltage of 120 kV. Images were digitally captured on a Gatan US1000 (2k × 2k) CCD camera (Gatan, Pleasanton, CA).

Cryo-grids were imaged on a JEOL JEM-2200FS transmission electron microscopy (JEOL, Ltd., Japan) equipped with a field emission gun, Omega energy filter (20 eV slit width), and Direct Electron DE-20 (Direct Electron, LP, San Diego, CA). Tilt series images were acquired at 12 frames per second, 10,000× nominal magnification (6.14 Å/pixel), and -6 μm defocus, over a tilt range of +62° to -62° degrees at 2° increments semi-automatically using the SerialEM package [39]. Total electron dose ranged from 120 to 130 $e^-/Å^2$. Images were motion corrected using scripts from Direct Electron, LP, and tomograms were reconstructed by r-weighted back projection using the IMOD package [40, 41].

Statistical analyses

Graphs were generated using Prism 6 software (GraphPad Software, Inc.) and statistical analyses were performed using one-way ANOVA and Dunnett's multiple comparisons test at 95% confidence interval.

RESULTS

Despite the lack of a retraction ATPase in T4cP, pilus retraction in *C. crescentus* has been directly visualized [23] and it has long been suggested that pilus retraction is responsible for bringing the ϕCbK phage tail to the receptor at the cell pole [36]. To test this hypothesis, we sought to physically block pilus retraction by allowing antibody binding along the pilus filament. We inoculated wild-type *C. crescentus* with dilutions of anti-PilA antibody ranging from 1:500 to 1:10000 to test if motility or the ϕCbK adsorption rate was affected (Figure 1A and 1B). We examined the potential effects of antibody binding on cell motility in a motility assay (Figure 1A). At 24 hours incubation, cells treated with a 1:10000 dilution of antibody showed a slight but significant decrease in colony diameter compared to wild type *C. crescentus* colonies (Figure 1A). The effect was more pronounced for cells treated with a 1:1000 dilution of antibody, which also a showed significant difference from the 1:10000 dilution treated cells. These data suggest that antibody does bind and inhibit pilus retraction as this is required for cell motility in T4P expressing cells [5, 42], however binding does not appear to affect the flagellum, which explains why cells remain motile.

We observed a dose-dependent reduction in the adsorption of ϕCbK phage after antibody treatment (Figure 1B). The K-values for ϕCbK adsorption in the presence of anti-PilA antibody are listed in Table 2. The adsorption K-values were significantly lower for cells treated with anti-PilA antibody at 1:10000, 1:1000, and 1:500 dilutions. This suggests two possibilities: 1) the ϕCbK phage tails bind the pilus filament and antibody along the filament prevents retraction and irreversible binding of the phage to the receptor at the cell pole or 2) antibody binding along the pilus filament blocks the ϕCbK phage tail from binding the pilus filament altogether. Both would require that the ϕCbK phage tail initially binds the extended pilus filament and retraction of the pilus brings the phage to the receptor at the cell surface.

To prevent pilus retraction in *C. crescentus* chemically, we treated cells with carbonyl cyanide m-chlorophenyl hydrazone (CCCP). CCCP is a proton ionophore that dissipates the proton motive force (PMF), uncoupling electron transfer from ATP synthesis. To assess motility in the presence of CCCP, we performed motility assays on semi-solid agar plates containing CCCP at various concentrations. We observed a reduction in motility at 5 and 10 μM CCCP (Figure 2A). This was expected, as flagellar rotation is known to be powered by the PMF [43]. We did not observe any bacterial growth on semi-solid agar plates containing 50 μM CCCP. We similarly observed a dose-dependent reduction in ϕCbK adsorption (Figure 2B). The K-values for ϕCbK adsorption in the presence of CCCP are listed in Table 3. The K-value for adsorption at concentrations of CCCP higher than 1 μM was significantly lower than for untreated cells, indicating that the PMF is involved in the ϕCbK adsorption process.

Because ϕCbK is known to initially bind reversibly to the *C. crescentus* flagellum through its head filament and use flagellar rotation to concentrate at the cell pole [38], we also performed experiments in Δ*motA* and Δ*tipF* mutants. The Δ*motA* strain assembles a flagellum that is incapable of rotating [44, 45] and the Δ*tipF* strain does not assemble a flagellum [44]. In this way we can observe the results of dissipating the PMF without the confounding effects that the flagellum or flagellar rotation contribute to the ϕCbK adsorption process. The ϕCbK adsorption rate is substantially lower in these strains compared to wild type NA1000, as previously reported (Figure 3) [38]. The rate was further reduced by treatment with anti-PilA antibody or CCCP, indicating that the PMF is also involved during the pilus stage of ϕCbK adsorption.

To quantify the effects of antibody and CCCP treatments on pilus dynamics, we used negative stain electron microscopy to count the number of cells with extended pili. Example images are shown in

Figure 4. 52% (55/106) of untreated cells expressed pili, while 65% (53/81) of cells that had been treated with a 1:500 dilution of anti-PilA antibody had extended pili. This increase supports the hypothesis that antibody binding physically blocks pilus retraction. Additionally, we are able to visualize extra density along the pilus filaments in the presence of anti-PilA antibody compared to untreated cells (Figure 4A and 4B). Interestingly, after the addition of 10 μM CCCP, only 15% (21/139) of cells expressed pili. A possible explanation for this reduction could be that the PMF is involved in both pilus assembly and retraction. This would result in fewer pili, and as we observed, a lower ϕCbK adsorption rate (Figure 2B).

To further investigate the effects of anti-PilA antibody binding in *C. crescentus*, we imaged the cells by cryo-electron tomography (cryo-ET) (Figure 5). We observed a similar increase in the number of cells expressing pili when comparing untreated cells to cells in the presence of anti-PilA antibody as we saw by negative stain imaging. Cryo-ET also revealed that on cells expressing pili, the number of pili per cell was greater when treated with antibody than without treatment (Figure 5A and 5B). Untreated cells expressing pili had an average of 1.3 pili per cell while antibody treated cells expressing pili averaged 2.9 pili per cell. To increase the number of infection events available for imaging on the EM grids, we infected cells treated with 1:500 or 1:1000 dilutions of anti-PilA antibody at an MOI of 10 for cryo-ET. ϕCbK phages were resolved with head filaments interacting with the flagellum, with tails binding pilus filaments (data not shown), and with tails bound to the cell pole (Figure 5C2 and 5C3). Similarly to the negative stain images, density corresponding to antibody could be resolved along the pilus filaments, and in some cases several pili bundled together (Figure 5C1). The increase in the number of cells expressing pili and the number of pili on these cells indicates that antibody binding of the pilus filament physically prevents retraction. That we found phages bound to the cell pole despite having blocked retraction is not surprising because the

flagellar mechanism of adsorption was still functional for these cells. This is also reflected in the ϕCbK adsorption data in which not all adsorption is prevented at these dilutions of antibody (Figure 1B). Concentration of the phages at the pole through flagellar rotation could bring the tail into close enough proximity to bind the pole without the use of pilus retraction. We rarely observed phages that had ejected their genomes bound to the cell pole, however, which may indicate that antibody binding affects the irreversible binding step at the cell pole. Future experiments will include cryo-ET imaging of anti-PilA antibody and CCCP treatments of Δ*motA* and Δ*tipF* strains with and without ϕCbK infection to help elucidate pilus specific interactions.

DISCUSSION

Ellison *et al.* recently directly visualized retraction of the T4cP of *C. crescentus* by fluorescently labeling a cysteine knock-in of PilA using maleimide dyes [23]. Retraction was physically blocked by the addition of a large polyethylene glycol maleimide and this tension was shown to provide a surface-sensing signal for the cell. Because ϕCbK is known to use the pilus during the adsorption and attachment process, we sought to understand whether the phage exploited the pilus retraction process to reach the cell receptor for irreversible binding. We physically blocked retraction using an antibody against the major pilin protein, PilA, which led to reduced motility and ϕCbK adsorption, indicating that ϕCbK utilizes pilus dynamics during its adsorption process. Chemically preventing retraction using the proton ionophore CCCP dramatically reduced ϕCbK adsorption, suggesting that the PMF is required for this process, both in wild type and flagellar mutant strains.

Imaging by negative stain electron microscopy after treatment with anti-PilA antibody showed an increase in the number of cells expressing pilus filaments, confirming that pilus retraction was blocked by antibody binding. After treatment with CCCP we observed a decrease in the number of cells expressing pili, suggesting that the pilus assembly process depends on the PMF, as well. Cryo-ET experiments of cells treated with antibody showed similar results. In the context of treatment and phage infection, cells often expressed multiple pili and phages were not observed to eject their genome into the cells, indicating that an essential step in the adsorption process had been blocked.

We propose a model in which the ϕCbK phage initially adsorbs to the flagellum using the phage head filament (Figure 6A), allowing it to use flagellar rotation to concentrate at the *C. crescentus* cell pole (Figure 6B). The phage tail fibers then bind the extended pilus filament (Figure 6C), and retraction of the pilus brings the phage tail to the receptor on the cell surface (Figure 6D).

Pilus retraction in *C. crescentus* has been shown to function in surface sensing [23] and here we show that it is also required for pilus specific phage adsorption. The T4b toxin co-regulated pilus (TCP) of *Vibrio cholerae* similarly lacks a retraction ATPase, but is retractile and TCP retraction is necessary to bring CTXϕ, the lysogenic phage encoding the major virulence factors of *V. cholerae*, to the bacterium [46, 47]. TCP retraction is facilitated mechanically by the minor pilin TcpB. It will be of great interest whether the T4cP of *C. crescentus* uses a similar means for retraction or if its mechanism is unique.

ACKNOWLEDGEMENTS

We thank Ms. Jeannette Taylor and Ms. Hong Yi of the Emory University Robert P. Apkarian Integrated Electron Microscopy Core for assistance. This work was supported in part by Emory University, Children's Healthcare of Atlanta, the Center for AIDS Research at Emory University (P30 AI050409), and the Georgia Research Alliance to E.R.W.; NSF grant 0923395 to E.R.W; Human Frontier Science Program Grant RGP0051 (to P.H.V. and E.R.W.); and public health service grant GM104540 to E.R.W.

REFERENCES

1. Proft, T. and Baker, E. N. Pili in gram-negative and gram-positive bacteria - structure, assembly and their role in disease. *Cell Mol Life Sci*, 2009. **66**(4): p. 613-635.
2. Donnenberg, M. S., Girón, J. A., Nataro, J. P., and Kaper, J. B. A plasmid-encoded type IV fimbrial gene of enteropathogenic *Escherichia coli* associated with localized adherence. *Mol Microbiol*, 1992. **6**: p. 3427-3437.
3. Tacket, C. O., Taylor, R. K., Losonsky, G., Lim, Y., Nataro, J. P., Kaper, J. B., and Levine, M. M. Investigation of the roles of toxin-coregulated pili and mannose-sensitive hemagglutinin pili in the pathogenesis of *Vibrio cholerae* O139 infection. *Infect Immun*, 1998. **66**(2): p. 692-695.
4. Virji, M., Saunders, J. R., Sims, G., Makepeace, K., Maskell, D., and Ferguson, D. J. P. Pilus-facilitated adherence of *Neisseria meningitidis* to human epithelial and endothelial cells: Modulation of adherence phenotype occurs concurrently with changes in primary amino acid sequence and the glycosylation status of pilin. *Mol Microbiol*, 1993. **10**: p. 1013-1028.
5. Bradley, D. E. A function of *Pseudomonas aeruginosa* PAO polar pili: Twitching motility. *Can J Microbiol*, 1980. **26**: p. 146-154.
6. Hu, N. T., Lee, P. F., and Chen, C. H. The type IV pre-pilin leader peptidase of *Xanthomonas campestris* pv. *campestris* is functional without conserved cysteine residues. *Mol Microbiol*, 1995. **18**: p. 769-777.
7. LaPointe, C. F. and Taylor, R. K. The type 4 prepilin peptidases comprise a novel family of aspartic acid proteases. *J.Biol.Chem.*, 2000. **275**(2): p. 1502-1510.
8. Craig, L., Pique, M. E., and Tainer, J. A. Type IV pilus structure and bacterial pathogenicity. *Nat Rev Microbiol.*, 2004. **2**(5): p. 363-378.
9. Pelicic, V. Type IV pili: E pluribus unum? *Mol Microbiol*, 2008. **68**(4): p. 827-837.

10. Roux, N., Spagnolo, J., and de Bentzmann, S. Neglected but amazingly diverse type IVb pili. *Res Microbiol*, 2012. **163**(9): p. 659-673.

11. Tomich, M., Planet, P. J., and Figurski, D. H. The tad locus: Postcards from the widespread colonization island. *Nat Rev Microbiol*, 2007. **5**(5): p. 363-75.

12. Bernard, C. S., Bordi, C., Termine, E., Filloux, A., and de Bentzmann, S. Organization and PprB-dependent control of the *Pseudomonas aeruginosa* tad locus, involved in Flp pilus biology. *J Bacteriol*, 2009. **191**(6): p. 1961-73.

13. Clock, S. A., Planet, P. J., Perez, B. A., and Figurski, D. H. Outer membrane components of the tad (tight adherence) secreton of *Aggregatibacter actinomycetemcomitans*. *J Bacteriol*, 2008. **190**(3): p. 980-90.

14. Janowicz, D. M., Cooney, S. A., Walsh, J., Baker, B., Katz, B. P., Fortney, K. R., Zwickl, B. W., Ellinger, S., and Munson, R. S., Jr. Expression of the Flp proteins by *Haemophilus ducreyi* is necessary for virulence in human volunteers. *BMC Microbiol*, 2011. **11**: p. 208.

15. Wang, Y. and Chen, C. Mutation analysis of the flp operon in *Actinobacillus actinomycetemcomitans*. *Gene*, 2005. **351**: p. 61-71.

16. Laub, M. T., Shapiro, L., and McAdams, H. H. Systems biology of *Caulobacter*. *Annu Rev Genet*, 2007. **41**: p. 429-41.

17. Thanbichler, M. Spatial regulation in *Caulobacter crescentus*. *Curr Opin Microbiol*, 2009. **12**(6): p. 715-21.

18. Ely, B., Ely, T. W., Crymes, W. B. Jr., Minnich, S. A. A family of six flagelling genes contributies to the *Caulobacter crescentus* flagellar filament. *J Bacteriol*, 2000. **182**(17): p. 5001-5004.

19. Briegel, A., Dias, D. P., Li, Z., Jensen, R. B., Frangakis, A. S., and Jensen, G. J. Multiple large filament bundles observed in *Caulobacter crescentus* by electron cryotomography. *Mol Microbiol*, 2006. **62**(1): p. 5-14.

20. Faulds-Pain, A., Birchall, C., Aldridge, C., Smith, W. D., Grimaldi, G., Nakamura, S., Miyata, T., Gray, J., Li, G., Tang, J. X., Namba, K., Minamino, T., and Aldridge, P. D. Flagellin redundancy in *Caulobacter crescentus* and its implications for flagellar filament assembly. *J Bacteriol*, 2011. **193**(11): p. 2695-707.

21. Lagenaur, C., Agabian, N. *Caulobacter crescentus* pili: Structure and stage-specific expression. *J Bacteriol*, 1977. **131**(1): p. 340-346.

22. Skerker, J. M., Shapiro, L. Identification and cell cycle control of a novel pilus system in *Caulobacter crescentus. EMBO*, 2000. **19**(13): p. 3223-3234.

23. Ellison, C. K., Kan, J., Dillard, R. S., Kysela, D. T., Ducret, A., Berne, C., Hampton, C. M., Ke, Z., Wright, E. R., Biais, N., Dalia, A. B., and Brun, Y. V. Obstruction of pilus retraction stimulates bacterial surface sensing. *Science*, 2017. **358**(6362): p. 535.

24. Tsokos, C. G. and Laub, M. T. Polarity and cell fate asymmetry in *Caulobacter crescentus. Curr Opin Microbiol*, 2012. **15**(6): p. 744-50.

25. Viollier, P. H., Sternheim N., Shapiro L. A dynamically localized histidine kinase controls the asymmetric distribution of polar pili proteins. *EMBO*, 2002. **21**(17): p. 4420-4428.

26. Viollier, P. H. and Shapiro, L. A lytic transglycosylase homologue, PleA, is required for the assembly of pili and the flagellum at the *Caulobacter crescentus* cell pole. *Mol Microbiol*, 2003. **49**(2): p. 331-345.

27. Tan, M. H., Kozdon, J. B., Shen, X., Shapiro, L., and McAdams, H. H. An essential transcription factor, SciP, enhances robustness of *Caulobacter* cell cycle regulation. *Proc Natl Acad Sci U S A*, 2010. **107**(44): p. 18985-90.

28. Curtis, P. D., Quardokus, E. M., Lawler, M. L., Guo, X., Klein, D., Chen, J. C., Arnold, R. J., and Brun, Y. V. The scaffolding and signalling functions of a localization factor impact polar development. *Mol Microbiol*, 2012. **84**(4): p. 712-35.

29. Davis, N. J. and Viollier, P. H. Probing flagellar promoter occupancy in wild-type and mutant *Caulobacter crescentus* by chromatin immunoprecipitation. *FEMS Microbiol Lett*, 2011. **319**(2): p. 146-52.

30. Purucker, M., Bryan, R., Amemiya, K., Ely, B., and Shapiro, L. Isolation of a *Caulobacter* gene cluster specifying flagellum production by using nonmotile Tn5 insertion mutants. *Proc Natl Acad Sci U S A*, 1982. **79**(22): p. 6797-801.

31. Huguenel, E. D. and Newton, A. Evidence that subcellular flagellin pools in *Caulobacter crescentus* are precursors in flagellum assembly. *J Bacteriol*, 1984. **157**(3): p. 727-32.

32. Li, G., Brown, P. J. B., Tang, J. X., Xu, J., Quardokus, E. M., Fuqua, C., and Brun, Y. V. Surface contact stimulates the just-in-time deployment of bacterial adhesins. *Mol Microbiol*, 2012. **83**(1): p. 41-51.

33. Entcheva-Dimitrov, P. and Spormann, A. M. Dynamics and control of biofilms of the oligotrophic bacterium *Caulobacter crescentus*. *J Bacteriol*, 2004. **186**(24): p. 8254-66.

34. Christen, M., Beusch, C., Bösch, Y., Cerletti, D., Flores-Tinoco, C. E., Del Medico, L., Tschan, F., and Christen, B. Quantitative selection analysis of bacteriophage ϕCbK susceptibility in *Caulobacter crescentus*. *J Mol Biol*, 2016. **428**(2, Part B): p. 419-430.

35. Lagenaur, C., Farmer, S., Agabian, N. Adsorption properties of stage-specific *Caulobacteri* phage ϕCbK. *J Virol*, 1977. **77**: p. 401-407.

36. Skerker, J. M. and Shapiro, L. Identification and cell cycle control of a novel pilus system in *Caulobacter crescentus*. *EMBO J*, 2000. **19**(13): p. 3223-3234.

37. Kropinski, A. M. M., A.; Waddell, T. E.; Lingohr, E.; and Johnson, R. P. Enumeration of bacteriophages by double agar overlay plaque assay, in *Bacteriophages: Methods and Protocols*. 2009, Humana Press. p. 69-76.

38. Guerrero-Ferreira, R. C., Viollier, P. H., Ely, B., Poindexter, J. S., Georgieva, M., Jensen, G. J., and Wright, E. R. Alternative mechanism for bacteriophage adsorption to the motile bacterium *Caulobacter crescentus*. *Proc Natl Acad Sci U S A*, 2011. **108**(24): p. 9963-8.

39. Mastronarde, D. N. Automated electron microscope tomography using robust prediction of specimen movements. *J Struct Biol*, 2005. **152**(1): p. 36-51.

40. Mastronarde, D. N. Dual-axis tomography: An approach with alignment methods that preserve resolution. *J Struct Biol*, 1997. **120**(3): p. 343-352.

41. Kremer, J. R., Mastronarde, D. N., and McIntosh, J. R. Computer visualization of three-dimensional image data using IMOD. *J Struct Biol*, 1996. **116**(1): p. 71-76.

42. Merz, A. J., So, M., and Sheetz, M. P. Pilus retraction powers bacterial twitching motility. *Nature*, 2000. **407**(6800): p. 98-102.

43. Manson, M. D., Tedesco, P., Berg, H. C., Harold, F. M., and Van der Drift, C. A proton motive force drives bacterial flagella. *Proc Natl Acad Sci U S A*, 1977. **74**(7): p. 3060-3064.

44. Huitema, E., Pritchard, S., Matteson, D., Radhakrishnan, S. K., and Viollier, P. H. Bacterial birth scar proteins mark future flagellum assembly site. *Cell*, 2006. **124**(5): p. 1025-1037.

45. Radhakrishnan, S. K., Thanbichler, M., and Viollier, P. H. The dynamic interplay between a cell fate determinant and a lysozyme homolog drives the asymmetric division cycle of *Caulobacter crescentus*. *Genes Dev*, 2008. **22**(2): p. 212-225.

46. Ng, D., Harn, T., Altindal, T., Kolappan, S., Marles, J. M., Lala, R., Spielman, I., Gao, Y., Hauke, C. A., Kovacikova, G., Verjee, Z., Taylor, R. K., Biais, N., and Craig, L. The *Vibrio*

cholerae minor pilin TcpB initiates assembly and retraction of the toxin-coregulated pilus. *PLoS Pathog*, 2016. **12**(12): p. e1006109.

47. Faruque, S. M. and Mekalanos, J. J. Phage-bacterial interactions in the evolution of toxigenic *Vibrio cholerae*. *Virulence*, 2012. **3**(7): p. 556-565.

FIGURE LEGENDS

Figure 1. Effects of pretreating NA1000 cells with dilutions of anti-PilA antibody. (A) Motility of NA1000 cells treated with anti-PilA antibody. Columns represent mean diameters of colonies grown for 24 hours on semi-solid agar relative to the untreated control. Treatment is noted on the x-axis. Mean colony diameter of both antibody treated groups are significantly lower than untreated cells at 24 hours of growth. Error bars represent standard deviation. $^{**}P = 0.0068$, $^{****}P < 0.0001$, $^{***}P = 0.0001$. (B) Phage adsorption assays of cells treated with varying dilutions of antibody. Data represent the mean percentage of the natural log of plaque forming units (PFU) over time from three independent experiments.

Figure 2. Effects of pretreating NA1000 with CCCP. (A) Motility of NA1000 cells treated with CCCP. Columns represent mean diameters of colonies grown for 24 hours on semi-solid agar relative to the untreated control. CCCP concentration is noted on the x-axis. Mean colony diameters of groups treated with CCCP at 5 μM or higher are significantly lower than untreated cells at 24 hours of growth. Interestingly, treatment with 1 μM CCCP resulted in a significant increase in mean colony diameter. Error bars represent standard deviation. $^{****}P < 0.0001$. (B) Phage adsorption assays of cells treated with CCCP. Data represent the mean percentage of the natural log of plaque forming units (PFU) over time from three independent experiments.

Figure 3. Effects of antibody and CCCP treatment on strains lacking flagellar rotation or flagellar filaments. Anti-PilA antibody and CCCP treatments reduce the rate of ϕCbK adsorption in both (A) Δ*motA* and (B) Δ*tipF* strains, indicating that the treatments are not acting solely on the flagellum.

Figure 4. Negative stain electron microscopy of (A) untreated, (B) 1:500 anti-PilA antibody treated, and (C) 10 μM CCCP treated NA1000 cells allows quantification of the number of cells expressing pili. Antibody is observed as additional density coating the pilus filaments in (B). Scale bars, 200 nm.

Figure 5. Cryo-ET slices of NA1000 cells (A) untreated, (B) 1:500 anti-PilA antibody treated, and (C) 1:500 anti-PilA antibody treated and infected with ϕCbK at an MOI of 10. (A1, A2, B1, and B2) the number of extended pilus filaments increases upon addition of anti-PilA antibody. (A3 and B3) Flagella of untreated and antibody treated cells. (C1) A bundle of pilus filaments observed after antibody treatment and ϕCbK infection. (C2) A ϕCbK phage with a full capsid attached to the *C. crescentus* cell pole. (C3) The ϕCbK tail attached to the cell pole. White arrowheads indicate pilus filaments, black arrows indicate flagella, black arrowheads indicate a bundle of pili, the white asterisk indicates a full ϕCbK capsid, and the white arrowhead indicates the ϕCbK tail attached to the cell. and Scale bars, 100 nm.

Figure 6. Model of ϕCbK adsorption *to C. crescentus*. (A) the ϕCbK head filament wraps the flagellum. (B) Flagellar rotation concentrates phages at the cell pole. (C) the ϕCbK tail fiber adsorbs to the extended pilus filament. (D) pilus retraction brings the ϕCbK tail to the receptor at the cell pole. Green, ϕCbK; Blue, pilus; magenta, flagellum; yellow, S-layer; orange, outer membrane; red, inner membrane.

Supplementary Figure 1. ϕCbK adsorption assay of cells treated with 10 μM CCCP 15 minutes after the addition of ϕCbK phages. CCCP treatment immediately reduces the rate of ϕCbK adsorption.

Figure 1

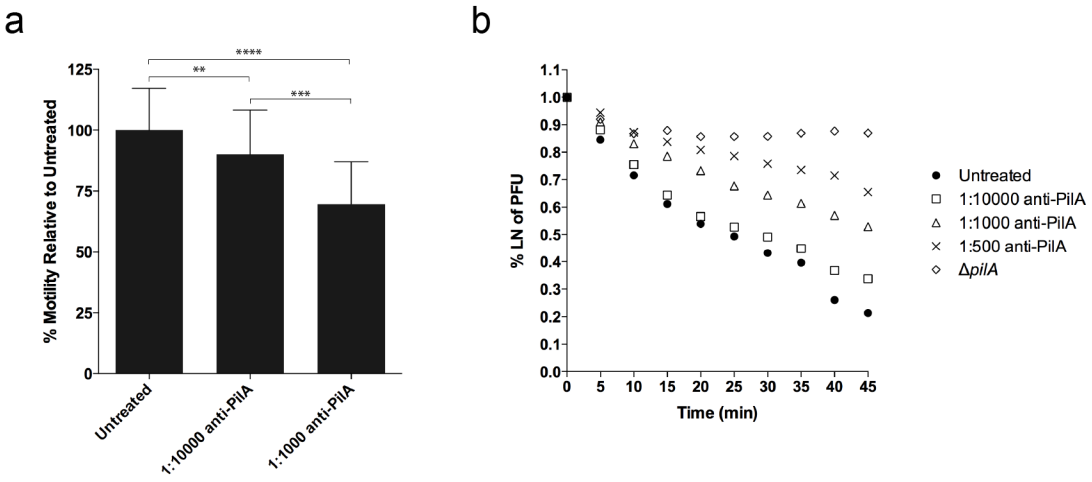
a
b
% Motility Relative to Untreated
125
100
75
50
25
0
****
**
***
Untreated
1:10000 anti-PilA
1:1000 anti-PilA
% LN of PFU
1.1
1.0
0.9
0.8
0.7
0.6
0.5
0.4
0.3
0.2
0.1
0.0
0
5
10
15
20
25
30
35
40
45
Time (min)
Untreated
1:10000 anti-PilA
1:1000 anti-PilA
1:500 anti-PilA
ΔpilA

Figure 2

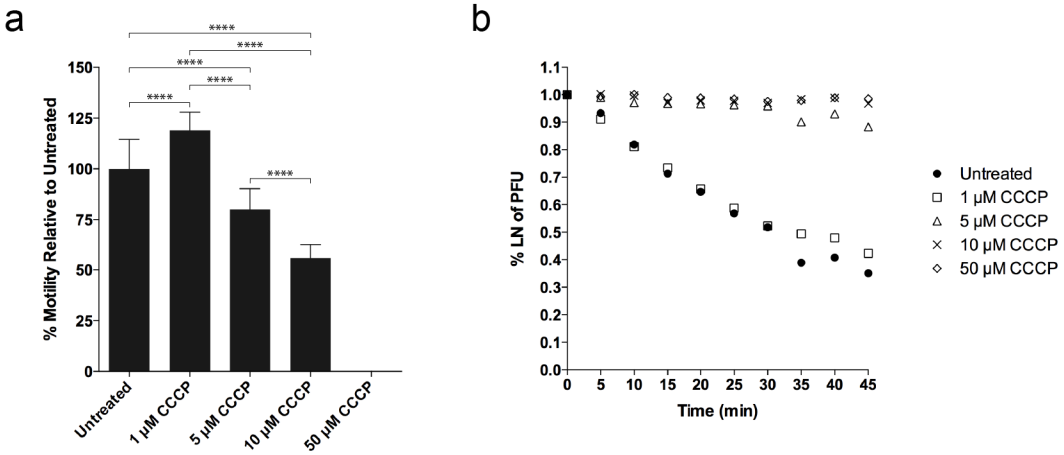
a
b
% Motility Relative to Untreated
Untreated
1 μM CCCP
5 μM CCCP
10 μM CCCP
50 μM CCCP
****
% LN of PFU
Time (min)
Untreated
1 μM CCCP
5 μM CCCP
10 μM CCCP
50 μM CCCP

Figure 3

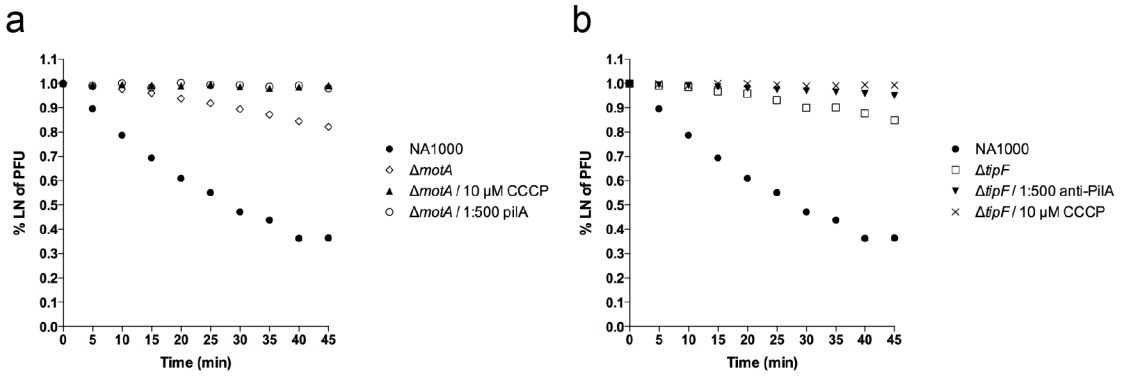
a
% LN of PFU
Time (min)
NA1000
ΔmotA
ΔmotA / 10 μM CCCP
ΔmotA / 1:500 pilA
b
% LN of PFU
Time (min)
NA1000
ΔtipF
ΔtipF / 1:500 anti-PilA
ΔtipF / 10 μM CCCP

Figure 4

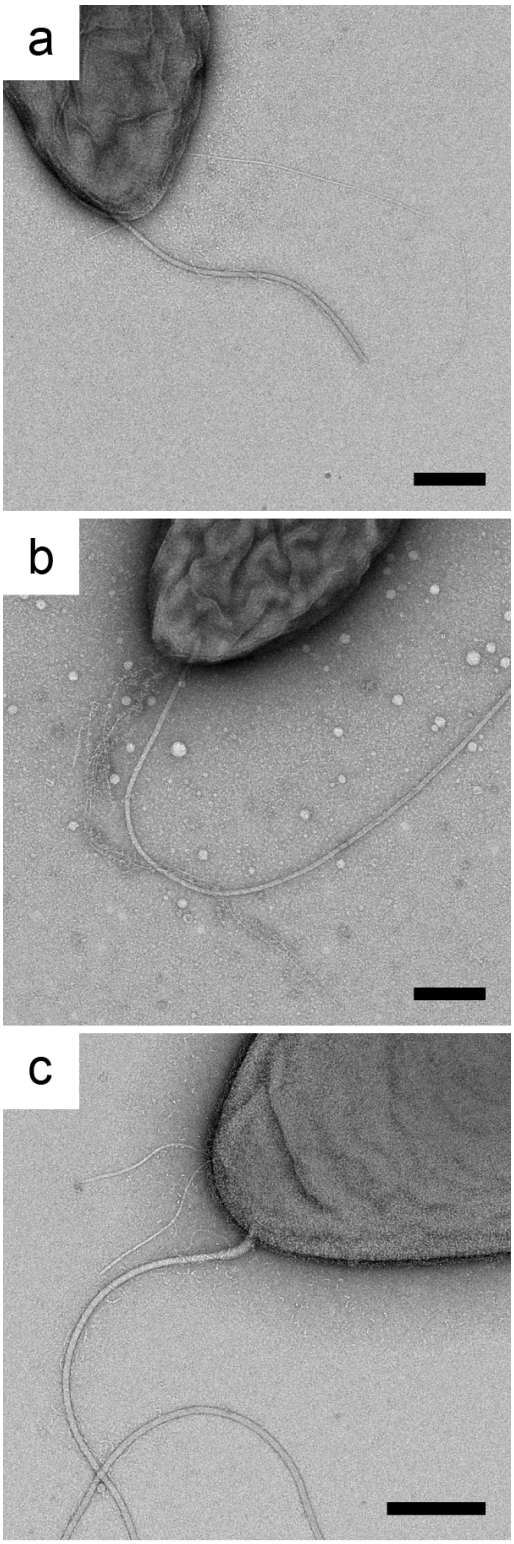

Figure 5

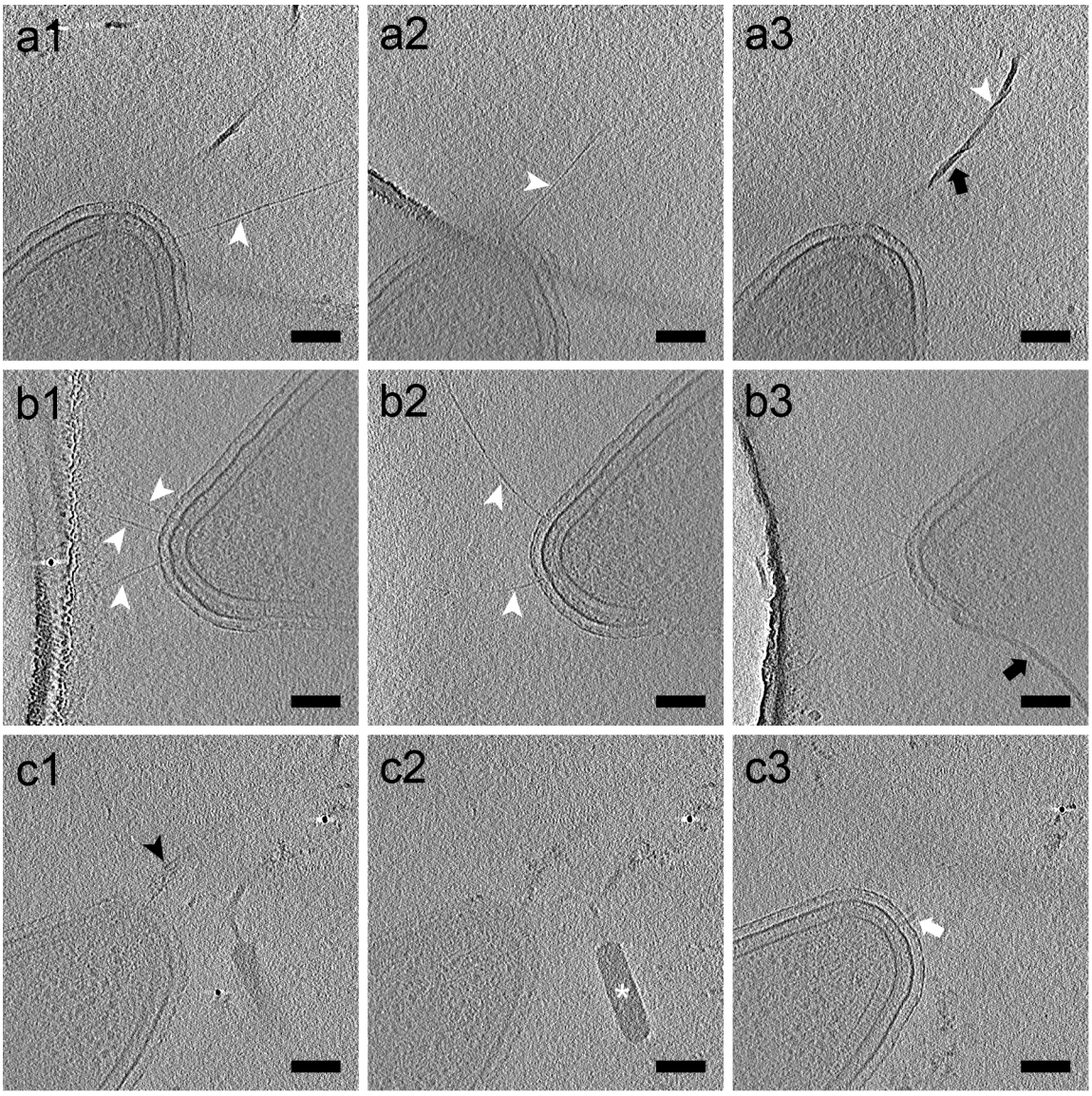

Figure 6

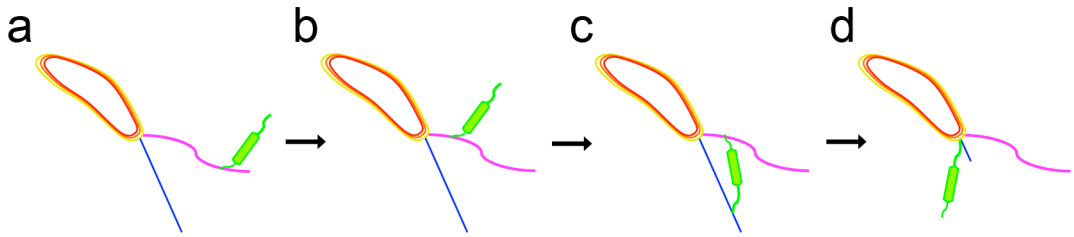

Supplementary Figure 1

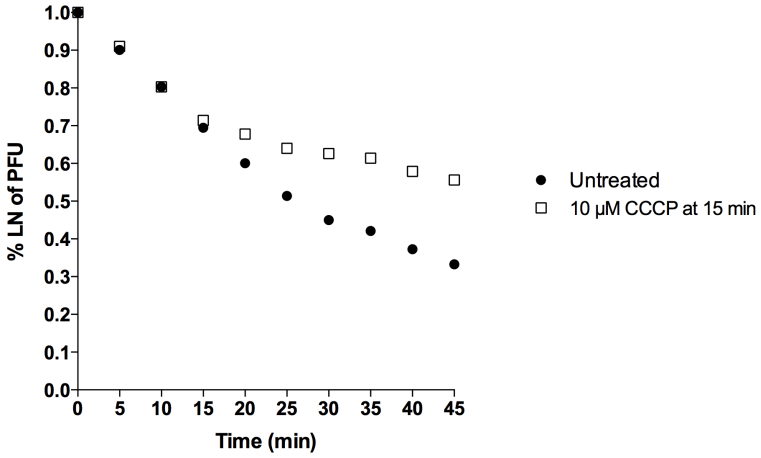

Table 1. Bacterial strains used in this study

Strain	**Phenotype**	**Source**
C. crescentus NA1000	Synchronizable derivative of CB15	Marks *et al.*
C. crescentus Δ*motA*	Deficient flagellar stator	Huitema *et al.*, Radhakrishnan *et al.*
C. crescentus Δ*tipF*	No flagellum	Huitema *et al.*

Table 2. Rate of phage adsorption to anti-PilA antibody treated *C. crescentus*

Strain	**Mean K Value Relative to NA1000 (untreated) +/- Standard Error**	**P-value (Compared to NA1000 untreated)**	**R^2 of Mean of Regression Lines for % LN of PFU**
NA1000 (untreated)	100	1	0.97
NA1000 1:10000 anti-PilA Antibody	66.5 +/- 1.7	0.0071	0.95
NA1000 1:1000 anti-PilA Antibody	61.4 +/- 7.5	0.0027	0.95
NA1000 1:500 anti-PilA Antibody	33.1 +/- 16.1	<0.0001	0.96
Δ*pilA*	8.9 +/- 6.3	<0.0001	0.93

Table 3. Rate of phage adsorption to CCCP treated *C. crescentus*

Strain	**Mean K-Value Relative to NA1000 (untreated) +/- Standard Error**	**P-value (Compared to NA1000 untreated)**	**R^2 of Mean of Regression Lines for % LN of PFU**
NA1000 (untreated)	100	1	0.97
NA1000 1 μM CCCP	97.5 +/- 21.3	0.9998	0.96
NA1000 5 μM CCCP	23.9 +/- 21.4	0.0027	0.823
NA1000 10 μM CCCP	9.4 +/- 11.6	0.0006	0.430
NA1000 50 μM CCCP	2.4 +/- 0.2	0.0003	0.55

Chapter 5: Structural specificity of the bacteriophage ϕCbK head filament to the *Caulobacter crescentus* flagellum

Rebecca S. Dillard[1], Conrad W. Shebelut[2], Ricardo C. Guerrero-Ferreira[1], Zunlong Ke[3], Chris Birchall[4,5], Phillip D. Aldridge[4,5], Elizabeth R. Wright[1,6]

[1]Division of Pediatric Infectious Diseases, Emory University School of Medicine, Children's Healthcare of Atlanta, Atlanta, GA 30322

[2]School of Medicine, University of Virginia, Charlottesville, VA 22908, USA

[3]School of Biology, Georgia Institute of Technology, Atlanta, GA 30332

[4]Centre for Bacterial Cell Biology, Newcastle University, Framlington Place, Newcastle upon Tyne, United Kingdom NE2 4HH

[5]Institute for Cell and Molecular Biosciences, Newcastle University, Framlington Place, Newcastle upon Tyne, United Kingdom NE2 4HH2

[6]Robert P. Apkarian Integrated Electron Microscopy Core, Emory University, Atlanta, GA

This manuscript was written by R.S.D. and E.R.W.

Experiments were performed by R.S.D., C.W.S., R.G.F., and Z.K.

ABSTRACT

Caulobacter crescentus is a small, free-living, Gram-negative alpha-proteobacterium that commonly lives in oligotrophic fresh and salt-water environments. *C. crescentus* is host to many bacteriophages, including bacteriophage ϕCbK, which first adsorbs to cells by interactions with the bacterial flagellum. In this study we established that, in addition to their impact on flagellar structure and motility, the presence of specific flagellins in the assembled flagellar filament directly influenced the adsorption efficiency of the flagellotropic bacteriophage φCbK to *C. crescentus*. To investigate the relationship between *C. crescentus* flagellum composition and φCbK predation, we used a number of approaches, including motility and bacteriophage adsorption assays, negative stain transmission electron microscopy (TEM), cryo-electron microscopy (cryo-EM), and cryo-electron tomography (cryo-ET). We have now generated straight flagellum mutants and are optimizing imaging conditions for the determination of a detailed structural model to provide understanding about *C. crescentus* flagellum assembly and ϕCbK interactions with the flagellar filament.

INTRODUCTION

Bacterial flagella are necessary for the initial interactions that occur between flagellotropic bacteriophages and their hosts [1-17]. In most cases, phage tail fibers wrap directly around the flagellum as the bacteria swim, efficiently facilitating the consequential irreversible attachment of the phages to their hosts. An alternative strategy has evolved for ϕCbK and the other ϕCbK -like phages of *Caulobacter crescentus* (ϕCb13 and others), in which a headfirst mechanism is exploited to establish the initial contact with the flagellar filament [4, 18]. While both the headfirst and tailfirst approaches increase the phages' chances of infecting the host cell, the method used by ϕCbK and ϕCbK -like phages proves to be more advantageous in several ways. Firstly, the head filament – flagellum connection efficiently increases the local concentration of phages around the cell pole where the cell surface receptors to the phage are located. Secondly, headfirst contact simultaneously leaves the ϕCbK tails unconstrained and available to detect and bind the pilus portal for irreversible attachment. The molecular mechanisms and structural contacts that regulate the interfaces between phage ϕCbK and the *Caulobacter* flagellum, however, are not well defined.

The bacterial flagellum is composed of three major structures: the motor (basal body), the hook, and the filament. The basal body, which drives the complex, is located within the cell wall; the hook attaches to the basal body and extends beyond the bacterial outer membrane; and the flagellar filament assembles at the end of the hook. Bacterial flagellar filaments are long tubular structures that arise from the assembly of multiple secreted subunits of flagellin [19, 20]. An examination of the bacterial flagellar filament genes shows that there is a high degree of sequence conservation in C-terminal and N-terminal D0 and D1 regions of most flagellins. D0 and D1 are associated with flagellin polymerization and form the lumen of the flagellar filament [21] and specific regions of D1 are known recognition sites for the innate immune systems of mammals and plants [22-24].

Conversely, the two surface-exposed domains, D2 and D3, are present on the outer lobes of the flagellum and are highly variable [21]. Analogous to an antibody response, both molecular and structural specificities may be present between bacteriophage and the bacterial flagellum as a whole, or more specifically to parts within domains of the flagellin protein.

The number of flagellin genes present in bacterial genomes is highly variable. For example, some bacteria have a single flagellin gene, such as *Escherichia coli* and *Bacillus subtilis,* whereas others maintain multiple flagellin genes, including *Helicobacter pylori*, *Rhizobium meliloti*, *Salmonella enterica* serovar Typhimurium, and the *Vibrionaceae* [25]. In addition to bacterial phase variation orchestrating the expression of a single flagellin to produce an active flagellum in species such as *Campylobacter jejuni* and *Salmonella*, almost 50% of bacterial species, including *C. crescentus*, assemble flagella composed of several flagellin proteins [26]. That said, the rationale behind the need for a bacterial species to actively retain multiple flagellin genes is not understood. It is possible that seamless flagellar filament assembly may necessitate the inclusion of multiple flagellins. Alternatively, the inclusion of multiple flagellins may provide the organism with an ability to combat environmental pressures such as survival in a particular environment, improved pathogenicity, or resistance to bacteriophage predation. The likelihood of the latter has been highlighted in studies to determine the factors that regulate phage infection specificity in *C. jejuni*, a species known to exhibit phase variation in the expression of flagellum proteins and capsular polysaccharide (CPS) [27, 28]. Similarly, *Salmonella* also expresses its two flagellins, *fliC* and *fljB*, in a phase variable manner [29, 30]. As with the *C. jejuni* phage, the success of flagellotropic *Salmonella* phage infection of the host is highly dependent on the flagellins present in the *Salmonella* flagellar filament [31].

The *C. crescentus* flagellum has been a model for understanding the composition, handedness, and structure of bacterial flagella [32-34]. The *C. crescentus* flagellar filament is composed of six independent flagellin subunits [35]. The flagellins are expressed from six genes that are located on two separate loci in the *C. crescentus* genome. The alpha locus contains the *fljJ* (29 kDa flagellin), *fljK* (25 kDa flagellin) and *fljL* (27 kDa flagellin) genes as well as the two flagellin translation regulators, *flaF* and *flbT*. The beta locus includes the *fljM*, *fljN* and *fljO* genes, all of which encode 25 kDa flagellins [26, 35]. Previously, it was determined that alterations to the inclusion of the six flagellins into the *C. crescentus* flagellum did not improve motility or speed profiles, but caused either maintenance of or a reduction to wild type motility patterns [26]. It is possible that the selection of specified flagellins in the flagellum may regulate other structure-function relationships, such as bacteria-bacteriophage interactions.

In this study we established that, in addition to their impact on flagellar structure and motility, the presence of specific flagellins in the formed flagellar filament directly influenced the adsorption efficiency of the flagellotropic bacteriophage ϕCbK to *C. crescentus*. By combining motility and bacteriophage adsorption assays with negative stain transmission electron microscopy (TEM), cryo-electron microscopy (cryo-EM), and cryo-electron tomography (cryo-ET) of *C. crescentus* mutants infected with ϕCbK, we propose that multiple flagellins are structurally required for proper assembly and function and that the ϕCbK adsorption mechanism has adapted to the multi-flagellin flagellum.

MATERIALS AND METHODS

Bacterial strains and growth conditions

Bacterial strains used in this study are noted in Table 1. All *C. crescentus* strains were grown in peptone yeast extract (PYE; 0.2% peptone, 0.1% yeast extract, 1 mM $MgSO_4$, and 0.5 mM $CaCl_2$) modified from Schmidt and Stanier [36, 37]. For phage adsorption assays, PYE contained 4 mM instead of 1 mM of MgSO4. Plating medium contained 1.5% (wt/vol) Bacto agar.

Motility assays

In order to confirm the motility phenotypes of the flagellin mutants we carried out motility assays as previously described [4]. Briefly, PYE soft-agar plates containing 0.3% (wt/vol) agar were stab-inoculated with colony forming units (CFUs) from plates that had been incubated overnight. Motility zone diameters were measured on three separate plates after 72 hours of incubation at 30°C, and are presented as percentage motility with respect to the wild type strain NA1000.

Evaluation of adsorption kinetics

Phage adsorption to the *C. crescentus* flagellum was measured as previously described [4, 36, 38] after the systematic removal of one or more flagellins. Briefly, overnight cultures of *C. crescentus* were infected with ϕCbK at a multiplicity of infection (MOI) of 0.001 in PYE adsorption media (4 mM $MgSO_4$). A parallel control flask contained only phages. Adsorption proceeded with slow shaking (60 rpm) at 30 °C for 45 minutes. Aliquots of 100 μl were mixed in ice-cold tubes containing 900 μL of PYE medium and 30 μL of chloroform to disrupt bacterial cells; after 45 minutes, samples were centrifuged (5 minutes at 12000 x *g*, 4 °C) to precipitate bacterial debris. The supernatant containing unabsorbed phages was used to infect an indicator strain (*C. crescentus* bNY30A; OD_{600}=0.3) and overlaid on PYE agar. Plates were incubated at 30 °C overnight for PFU enumeration. The

adsorption rate constant (K) was calculated by plotting relative plaque-forming units over time and dividing the slope of the regression line by the viable bacterial count.

Electron microscopy of *C. crescentus* and φCbK adsorption to *C. crescentus* cells

Samples were prepared for TEM by first glow discharging 400-mesh copper, carbon-coated, formvar grids (EM Sciences) for 40 seconds. Five μl of overnight cultures of *C. crescentus* were applied to the grids and allowed to adsorb for one minute before being washed three times with fresh PYE and stained with 1% phosphotungstic acid (PTA; pH 6.8) for 1 minute.

Negatively stained *C. crescentus* cells were imaged on a JEOL JEM-1400 transmission electron microscope (TEM; JEOL, Ltd., Japan) equipped with a LaB_6 filament and operated at an accelerating voltage of 120 kV. In order to capture the total length of the bacterial flagellum, images at a low magnification of 2,000× were digitally captured on a Gatan Ultrascan US1000 (2k × 2k) CCD camera (Gatan, Pleasanton, CA). Images were imported into ImageJ and flagellar length was quantified using the measure analysis option [39]. The average flagellum length for each *C. crescentus* strain was determined from at least 25 (except strain FljJ) flagella that were intact and attached to the cell. The presence or absence of flagella and the ability of φCbK to infect the *C. crescentus* strains was also investigated.

To characterize ϕCbK adsorption to *C. crescentus* strains by cryo-ET, bacterial overnight cultures were grown to an OD_{600} of 0.6, infected at an MOI of 10 and incubated without shaking for 15 minutes at 30°C. Four μL aliquots were plunge frozen onto glow-discharged, 200 mesh, copper Quantifoil grids (Quantifoil, Germany) in liquid ethane using a Vitrobot Mark III (FEI, Hillsboro,

Oregon). BSA-treated 10 nm colloidal gold was either previously applied onto the grids and air dried or mixed with the sample for homogeneous gold distribution in the ice.

Cryo-EM and cryo-ET data collection was carried out using a JEOL JEM-2200FS 200 kV FEG-TEM with an in-column Omega energy filter (slit width 20 eV). Images were collected at 12 frames per second with a Direct Electron, LP DE-20 direct electron detector (San Diego, CA) and motion corrected using scripts from the vendor. A cumulative electron dose between 120 e-/Å^2 and 140 e-/Å^2 was used for tilt series acquisition from -62° to +62° and images were acquired at 10,000× nominal magnification (6.14 Å/pixel) and -6.0 μm defocus. Tilt series images were automatically collected with 2° angular increments using SerialEM [40]. Tomograms were reconstructed from the aligned images using the IMOD package [41]. 2D projection images were acquired at 40,000× nominal magnification (1.38 Å/pixel) with a total electron dose of 20 e$^-$/Å^2.

fljK mutagenesis

To produce straight flagellum mutants composed of FljK, *fljK*^{T103C} was PCR amplified from a *C. crescentus* Δ*fljJLMNO* strain with a cysteine knock-in the *fljK* gene (YB6528) using primers fljK-F-BamHI and fljK-R-HindIII and the GeneMorph II random mutagenesis kit. The products were digested with BamHI and HindIII and ligated with similarly digested pMR10 for 12 hours at 16°C. The digested insert and vector were treated with recombinant shrimp alkaline phosphatase prior to ligation to prevent re-ligation of the vector. The ligation was dialyzed for 30-60 minutes using Millipore membrane filters with 0.025 μm pore size floating on MilliQ water then used to transform *C. crescentus* Δ*fljJKLMNO* (TPA2357) by electroporation. *fljK*^{T103C} amplified using Phusion High-Fidelity DNA Polymerase was used as a control. Strains were screened for loss of motility using motility assays as described above. Non-motile mutants were labeled using Alexa Fluor 594 C5

Maleimide dye and imaged by fluorescence microscopy to determine if they expressed straight flagellar filaments.

Fluorescence microscopy

To assess the flagellar morphology of the motility defective strains, 1 μl of stained cells was spotted onto the glass portion of a MatTek dish (P35G-1.0-14-C). A 2x2x1 mm pad consisting of 1% agarose in M2 (1X) salts was placed on top of the spotted cells, trapping the cells between the glass coverslip and agarose pad. Up to four individual strains were simultaneously imaged on each MatTek plate. Imaging was performed on a Nikon Eclipse Ti microscope with a 100×, 1.49 NA oil immersion objective using a spinning disk confocal head (CSU-22, Yokagawa) and an EMCCD camera (Clara; Andor).

Flagellar filament purification

Straight flagellar filaments purification was based on filament preparations as described previously by Faulds-Pain *et al.* [26]. Briefly, an overnight culture was diluted 1:10 in 250 ml of PYE and grown until mid-exponential phase. Cells were removed from the culture by centrifugation at 10,000 × g for 15 min. The supernatant was then ultracentrifuged using an SW-32 Ti rotor at 27,000 rpm for 30 min. The pellet was resuspended in 20 ml of PBS and centrifuged at 17,500 × g for 15 min to remove remaining cells. The supernatant was ultracentrifuged again at 27,000 rpm for 30 min. The pellet was resuspended in 50 μl of PBS. Filaments were stored at 4°C until grid preparation.

RESULTS

C. crescentus flagellum structure

The length of the flagellum for the *C. crescentus* strains examined ranged from 0.1 μm to 10 μm with a mean of 3.4 μm (Figure 1, Figure 2, and Table 2), which is in good agreement with previous measurements of isolated flagellar filaments [26, 42]. Driks *et al.* [43] proposed that the largest (29 kDa) flagellin subunit (FljJ) is used to initiate the assembly of flagellin subunits in *C. crescentus* by forming a short flagellar segment to which other flagellins assemble. Our negative stain EM and cryo-ET results of the Δ*fljKLMNO* mutant agree with this model as we resolved the combined length of the flagellar filament and flagellar hook to be between 120 nm and 160 nm, respectively (Figure 2B and Figure 3B). The only other mutant strain that presented extremely short flagella was the Δ*fljJKLM* mutant (Figure 1 and Figure 2H). Similar to Δ*fljKLMNO*, the flagella of Δ*fljJKLM* cells were limited in length and extended only several hundred nm, or less, from the cell pole. The results illustrated that the Δ*fljJKLM* mutant was unable to produce a full-length flagellum and further substantiated the requirement for another flagellin for proper filament assembly. The impact of the incorporation of an additional flagellin with FljN and FljO for the synthesis of a flagellum of average length was confirmed with the Δ*fljJKL* strain. The mean length of the flagellum for Δ*fljJKL* was 4.3 μm (Figure 1 and Figure 2J). Of great interest was that with the addition of the fourth 25 kDa flagellin, FljK, the average length of the flagellum decreased to 3.6 μm (Figure 1 and Figure 2L). This may be evidence to support that structural nuances associated with the individual flagellins promote or inhibit formation, strength, and ultimate structure of the filament.

The results of Driks *et al.* also indicate that the intermediate size (27 KDa) flagellin (FljL) may serve as an adapter between FljJ and the subsequent assembly of the smaller (25 KDa) flagellin subunits (FljK, FljM, FljN and FljO). Similar work by Minnich *et al.* [44] supported this hypothesis by

illustrating that deletion mutants of *fljJ* and *fljL* assemble a shortened flagellum. We observed an increase in filament length upon the addition of FljL to FljJ and close to wild type filament lengths when FljJ and FljL were combined with one or more 25 kDa flagellin (Figure 1 and Figure 2), providing additional support for this model.

Examining the collection of 15 strains expressing various combinations of flagellins, we found that flagellum length, although highly variable, generally correlated with motility (Figure 1). The strains exhibiting motility closest to wild type levels were Δ*fljMNO,* Δ*fljK,* and Δ*fljM*. This suggests that the combination of FljJ with FljL and one or more of the 25 kDa flagellins is required for wild type motility. Motility was slightly reduced in mutants expressing one or more 25 kDa flagellin but lacking FljJ or FljL, and it was further reduced in mutants expressing one or more 25 kDa flagellin but lacking both FljJ and FljL (**Figure 1**). Low levels of motility were seen for mutants only expressing FljJ, FljL, or FljJ and FljL, which corresponds to the truncated filament lengths observed for these strains.

Kinetics of phage adsorption.

Reduced motility results in decreased phage ϕCbK adsorption to *C. crescentus* [4], a result that extends to phage Chi [2], *B. subtilis* phage PBS1 [45], and *Agrobacterium tumefaciens* phages GS2 and GS6 [46]. In the case of φCbK, we wanted to determine whether in addition to motility *per se*, the composition of a flagellum also affected adsorption rates. Similar to our previous study which included *C. crescentus* strain Δ*tipF* (no flagellum) [4], we determined that *C. crescentus* strains Δ*fliF* (non-flagellated) and Δ*fljJKLMNO* (no flagellins), examined in this study, had significantly reduced motility levels and greatly reduced ϕCbK adsorption rates (Figure 1).

Examining a collection of 15 strains expressing various combinations of flagellins, we found that three strains had ϕCbK adsorption rates close to that of wild type: Δ*fljLMNO* (FljJ and FljK only), Δ*fljL and* Δ*fljM*, indicating the FljJ and FljK flagellins are important for ϕCbK adsorption (Figure 1). Deletion of either *fljJ* or *fljK* leads to ϕCbK adsorption rates that are half that of wild type rates, suggesting that FljJ and FljK are equally necessary for wild type levels of adsorption. The Δ*fljKLMNO* and Δ*fljJLMNO* strains had adsorption rates of 14% and 37% of the wild type rate, respectively, indicating that FljJ and FljK must be present together (Figure 1 and Table 2).

The addition of FljL to FljJ or FljK increased the rate of ϕCbK adsorption from 14% for Δ*fljKLMNO* to 34% for Δ*fljKMNO* and 37% for Δ*fljJLMNO* to 47% for Δ*fljJMNO*, but comparison of adsorption rates of Δ*fljLMNO* (99%) with Δ*fljMNO* (45%) and Δ*fljMNO* (45%) with Δ*fljM* (101%) indicates that FljL counteracts the combination of FljJ and FljK, unless FljN and FljO are present. The addition of FljN and FljO also counteracts the adsorption rates provided by FljJ and FljK unless FljL or FljM is present. This can be seen by comparing Δ*fljLM* adsorption (65%) with Δ*fljM* adsorption (101%) or Δ*fljL* adsorption (93%). Expression of the 25 kDa flagellins in any combination examined did not achieve wild type levels of ϕCbK adsorption, although the addition of FljK to the β-flagellins increased the adsorption rate from 23% to 65% (Δ*fljJKL* compared to Δ*fljJL)*, further implicating an important role for FljK in the adsorption process. The compositional requirements for ϕCbK adsorption are therefore fairly complex. While the presence of FljJ and FljK is sufficient, FljL must be offset by the addition of FljN and FljO and FljN and FljO must be offset by the addition of FljL or FljM in order for ϕCbK to achieve rates of adsorption similar to wild type.

Cryo-electron tomography of ϕCbK adsorption

The adsorption of ϕCbK phage along the flagella of the flagellin deletion strains was examined by cryo-electron tomography. It was noted that ϕCbK phage were adsorbed along the length of the flagella of flagellin mutant strains and that the overall structure of the flagella was comparable to the flagella of wild type cells (Figure 3A, 3C, and 3D). We resolved intact flagella for all flagellin deletion strains, except for Δ*fljKLMNO* (Figure 3B) and Δ*fljJKLM*, which had flagella stubs and no ϕCbK phage adsorbed headfirst along the truncated flagellum length. Cryo-ET investigations of the ϕCbK -infected Δ*fljKLMNO* mutant established that ϕCbK was able to attach to the pole of the Δ*fljKLMNO* mutant in spite of limited adsorption due to the truncated flagellar filament (data not shown). Interestingly, the Δ*fljKLMNO* mutant supports ϕCbK infection, albeit at a greatly reduced level when compared with the other strains (Figure 1). Cryo-ET imaging of the ϕCbK-infected Δ*fljJLMNO* and Δ*fljK* strains revealed that the head filament of ϕCbK interacted with the flagella to support the adsorption process despite reduced rates of adsorption (Figure 1, Figure 3C and 3D). Thus, ϕCbK head filament interactions with the flagellum at the ultrastructural level appear to be unaffected by the flagellin composition of the flagellar filament.

Cryo-EM structures of the flagellar filament

We would now like to develop a detailed structural model of the flagellar filament by cryo-EM, to provide an understanding of multi-flagellin filament assembly and the potential implications this has on phage adsorption to the flagellum. The determination of high-resolution cryo-EM structures of helical assemblies generally requires that the filaments be straight. Flagellar filaments can be locked into L- and R-state straight conformations by mutation of the residues involved in L to R switching [47].

Using random mutagenesis, we have generated a number of straight filaments composed of the FljK flagellin. A strain with a cysteine knock-in within the *fljK* gene was used so that the filaments could be fluorescently labeled with a maleimide dye for screening purposes [48]. Three single amino acid changes conferring straight flagella have been identified so far: T198I, L201Q, and N130S and imaged by negative stain EM (Figure 4 and Figure 5). Filaments from the FljK N130S mutant have been prepared and imaged by cryo-EM (Figure 6). The current preparation is at low concentration and cryo-EM shows densities corresponding to debris, so further purification will be required.

The next steps will include the generation and structural determination of straight filaments composed of FljM and of both FljK and FljM. No structures of multi-flagellin flagella have yet been solved to high resolution, so comparison of these structures is poised to provide a great contribution to the understanding of flagellar filament structure and assembly.

DISCUSSION

It has been well established that bacterial flagellins adopt a hairpin-like structure with the extended D2 and D3 regions forming the area exposed at the flagellar filament surface. In light of this structural characteristic common to flagellin proteins, amino acid substitutions present in this area are likely to generate antigenic diversity, as has been reported in other bacterial species [49]. In contrast, the C-terminus and N-terminus of the flagellin structure are conserved due to their contribution to flagellum shape [50] and their role in the formation of the flagellar filament core [51, 52]. Taking into consideration these characteristics and our findings, we hypothesize that flagellin redundancy in *C. crescentus* contributes to flagellum assembly and function and that flagellotropic phages, such as ϕCbK, interact preferentially with specific combinations of flagellins.

Although there appeared to be some correlation between length and adsorption and between motility and adsorption, there were exceptions in both cases. ϕCbK adsorbed poorly to all strains with short flagella, but adsorption was variable in strains producing longer filaments, indicating that the composition of the flagellum is important to this process. Previous research by Yen *et al.* [53] on *Agrobacterium* spp. illustrated that deletions of secondary flagellin genes brought about increased infectivity by phages. For the *Agrobacterium* system, it has been suggested that a specific, primary flagellin subunit, namely FlaA, is the site for phage tail docking and that the absence of the secondary flagellin genes increased the density of FlaA along the filament, hence increasing the efficiency of infection. In the *C. crescentus* – ϕCbK system, the interactions seem to be more complex. Our study illustrates that FljJ and FljK are important for ϕCbK adsorption and removal of the 27 kDa flagellin FljL increases the efficiency of ϕCbK adsorption, but only in the absence of FljN and FljO. The removal of FljN and FljO also increases adsorption efficiency unless FljL or FljM is

present. Only three combinations of flagellins were capable of supporting wild type levels of ϕCbK adsorption and no mutants produced adsorption rates superior to wild type.

Our previous research has shown that ϕCbK adsorption to the flagellar filament and the rotation of the flagellum allow for an increase in the local concentration of viral particles around the pilus portals of *C. crescentus*, which are the sites of irreversible attachment and genome injection [4]. Our results complement this unusual adsorption mechanism by providing evidence that the initial adsorption of ϕCbK is affected by the composition of flagellins in the flagellar filament and specifically favored by the presence of 25 kDa flagellins.

The consequence of flagellin redundancy could also be alterations to flagellum surface structure that would ultimately regulate phage susceptibility. This hypothesis has led us to study high-resolution structures of the *C. crescentus* flagellum and how alterations to flagellin composition impact the structure.

ACKNOWLEDGEMENTS

We would like to thank Ms. Rachel Storms for her assistance with φCbK adsorption assays. We would also like to thank the Robert P. Apkarian Integrated Electron Microscopy Core of Emory University for microscopy services and support.

FUNDING

This work was supported in part by Emory University, Children's Healthcare of Atlanta, and the Georgia Research Alliance to E.R.W.; the Center for AIDS Research at Emory University (P30 AI050409); the James B. Pendleton Charitable Trust to E.R.W.; HFSP grant RGP0051 to E.R.W.; public health service grant GM104540 to E.R.W. from the NIH/NIGMS, and NSF grant 0923395 to E.R.W. The funders had no role in study design, data collection and interpretation, or the decision to submit the work for publication.

REFERENCES

1. Raimondo, L. M., Lundh, N. P., and Martinez, R. J. Primary adsorption site of phage pbs1: The flagellum of *Bacillus subtilis*. *J Virol*, 1968. **2**(3): p. 256-64.
2. Schade, S. Z., Adler, J., and Ris, H. How bacteriophage chi attacks motile bacteria. *J Virol*, 1967. **1**(3): p. 599-609.
3. Zhilenkov, E. L., Popova, V. M., Popov, D. V., Zavalsky, L. Y., Svetoch, E. A., Stern, N. J., and Seal, B. S. The ability of flagellum-specific *Proteus vulgaris* bacteriophage PV22 to interact with *Campylobacter jejuni* flagella in culture. *Virol J*, 2006. **3**: p. 50.
4. Guerrero-Ferreira, R. C., Viollier, P. H., Ely, B., Poindexter, J. S., Georgieva, M., Jensen, G. J., and Wright, E. R. Alternative mechanism for bacteriophage adsorption to the motile bacterium *Caulobacter crescentus*. *Proc Natl Acad Sci U S A*, 2011. **108**(24): p. 9963-8.
5. Pate, J. L., Petzold, S. J., and Umbreit, T. H. Two flagellotropic phages and one pilus-specific phage active against *Asticcacaulis biprosthecum*. *Virology*, 1979. **94**(1): p. 24-37.
6. Edwards, S. and Meynell, G. G. The widespred occurrence of enteric flagellar phages. *J Gen Virol*, 1968. **2**(3): p. 443-4.
7. Baldvinsson, S. B., Sorensen, M. C., Vegge, C. S., Clokie, M. R., and Brondsted, L. *Campylobacter jejuni* motility is required for infection of the flagellotropic bacteriophage f341. *Appl Environ Microbiol*, 2014. **80**(22): p. 7096-106.
8. Choi, Y., Shin, H., Lee, J. H., and Ryu, S. Identification and characterization of a novel flagellum-dependent Salmonella-infecting bacteriophage, iEPS5. *Appl Environ Microbiol*, 2013. **79**(16): p. 4829-37.
9. Fukuda, A., Miyakawa, K., Iida, H., and Okada, Y. Regulation of polar surface structures in *Caulobacter crescentus*: Pleiotropic mutations affect the coordinate morphogenesis of flagella, pili and phage receptors. *Mol Gen Genet*, 1976. **149**(2): p. 167-73.

10. Lee, H. S., Choi, S., Shin, H., Lee, J. H., and Choi, S. H. *Vibrio vulnificus* bacteriophage SSP002 as a possible biocontrol agent. *Appl Environ Microbiol*, 2014. **80**(2): p. 515-24.

11. Lotz, W., Acker, G., and Schmitt, R. Bacteriophage 7-7-1 adsorbs to the complex flagella of *Rhizobium lupini* H13-3. *J Gen Virol*, 1977. **34**(1): p. 9-17.

12. Lovett, P. S. Pbp1: A flagella specific bacteriophage mediating transduction in *Bacillus pumilus*. *Virology*, 1972. **47**(3): p. 743-752.

13. Shea, T. B. and Seaman, E. Sp3: A flagellotropic bacteriophage of *Bacillus subtilis*. *J Gen Virol*, 1984. **65 (Pt 11)**: p. 2073-6.

14. Joys, T. M. Correlation between susceptibility to bacteriophage PBS1 and motility in *Bacillus subtilis*. *J Bacteriol*, 1965. **90**(6): p. 1575-7.

15. Meynell, E. W. A phage, phi chi, which attacks motile bacteria. *J Gen Microbiol*, 1961. **25**: p. 253-90.

16. Meynell, E. W. A bacteriophage for motile bacteria. *Nature*, 1961. **190**: p. 564.

17. Frankel, R. W. and Joys, T. M. Adsorption specificity of bacteriophage PBS1. *J Bacteriol*, 1966. **92**(2): p. 388-9.

18. Gill, J. J., Berry, J. D., Russell, W. K., Lessor, L., Escobar-Garcia, D. A., Hernandez, D., Kane, A., Keene, J., Maddox, M., Martin, R., Mohan, S., Thorn, A. M., Russell, D. H., and Young, R. The *Caulobacter crescentus* phage phiCbK: Genomics of a canonical phage. *BMC Genomics*, 2012. **13**: p. 542.

19. Beatson, S. A., Minamino, T., and Pallen, M. J. Variation in bacterial flagellins: From sequence to structure. *Trends Microbiol.*, 2006. **14**(4): p. 151-155.

20. White, D., *The physiology and biochemistry of prokaryotes*. 3rd ed. 2007, New York: Oxford University Press. xix, 628 p.

21. Yonekura, K., Maki-Yonekura, S., and Namba, K. Complete atomic model of the bacterial flagellar filament by electron cryomicroscopy. *Nature*, 2003. **424**(6949): p. 643-50.

22. Smith, K. D., Andersen-Nissen, E., Hayashi, F., Strobe, K., Bergman, M. A., Barrett, S. L., Cookson, B. T., and Aderem, A. Toll-like receptor 5 recognizes a conserved site on flagellin required for protofilament formation and bacterial motility. *Nat Immunol*, 2003. **4**(12): p. 1247-53.

23. Gomez-Gomez, L., Bauer, Z., and Boller, T. Both the extracellular leucine-rich repeat domain and the kinase activity of FSL2 are required for flagellin binding and signaling in Arabidopsis. *Plant Cell*, 2001. **13**(5): p. 1155-63.

24. Gomez-Gomez, L. and Boller, T. FLS2: An LRR receptor-like kinase involved in the perception of the bacterial elicitor flagellin in Arabidopsis. *Mol Cell*, 2000. **5**(6): p. 1003-11.

25. Wilson, D. R. and Beveridge, T. J. Bacterial flagellar filaments and their component flagellins. *Canadian Journal of Microbiology*, 1993. **39**(5): p. 451-72.

26. Faulds-Pain, A., Birchall, C., Aldridge, C., Smith, W. D., Grimaldi, G., Nakamura, S., Miyata, T., Gray, J., Li, G., Tang, J. X., Namba, K., Minamino, T., and Aldridge, P. D. Flagellin redundancy in *Caulobacter crescentus* and its implications for flagellar filament assembly. *J Bacteriol*, 2011. **193**(11): p. 2695-2707.

27. Coward, C., Grant, A. J., Swift, C., Philp, J., Towler, R., Heydarian, M., Frost, J. A., and Maskell, D. J. Phase-variable surface structures are required for infection of *Campylobacter jejuni* by bacteriophages. *Appl Environ Microbiol*, 2006. **72**(7): p. 4638-47.

28. Frost, J. A., Kramer, J. M., and Gillanders, S. A. Phage typing of *Campylobacter jejuni* and *Campylobacter coli* and its use as an adjunct to serotyping. *Epidemiol and Infect*, 1999. **123**(1): p. 47-55.

29. Namba, K. Roles of partly unfolded conformations in macromolecular self-assembly. *Genes to Cells: Devoted to Molecular & Cellular Mechanisms*, 2001. **6**(1): p. 1-12.

30. Gillen, K. L. and Hughes, K. T. Molecular characterization of *flgM*, a gene encoding a negative regulator of flagellin synthesis in *Salmonella typhimurium*. *J Bacteriol*, 1991. **173**(20): p. 6453-9.

31. Shin, H., Lee, J. H., Kim, H., Choi, Y., Heu, S., and Ryu, S. Receptor diversity and host interaction of bacteriophages infecting *Salmonella enterica* serovar Typhimurium. *PLoS One*, 2012. **7**(8): p. e43392.

32. Koyasu, S., Asada, M., Fukuda, A., and Okada, Y. Sequential polymerization of flagellin A and flagellin B into *Caulobacter* flagella. *J Mol Biol*, 1981. **153**(2): p. 471-5.

33. Koyasu, S. and Shirakihara, Y. *Caulobacter crescentus* flagellar filament has a right-handed helical form. *Journal of Molecular Biology*, 1984. **173**(1): p. 125-130.

34. Trachtenberg, S. and DeRosier, D. J. Three-dimensional reconstruction of the flagellar filament of *Caulobacter crescentus*. A flagellin lacking the outer domain and its amino acid sequence lacking an internal segment. *J Mol Biol*, 1988. **202**(4): p. 787-808.

35. Ely, B., Ely, T. W., Crymes, W. B., Jr., and Minnich, S. A. A family of six flagellin genes contributes to the *Caulobacter crescentus* flagellar filament. *J Bacteriol*, 2000. **182**(17): p. 5001-4.

36. Schmidt, J. M. and Stanier, R. Y. Isolation and characterization of bacteriophages active against stalked bacteria. *J Gen Microbiol*, 1965. **39**: p. 95-107.

37. Johnson, R. C. and Ely, B. Isolation of spontaneously derived mutants of *Caulobacter crescentus*. *Genetics*, 1977. **86**(1): p. 25-32.

38. Bender, R. A., Refson, C. M., and O'Neill, E. A. Role of the flagellum in cell-cycle-dependent expression of bacteriophage receptor activity in *Caulobacter crescentus*. *J. Bacteriol.*, 1989. **171**(2): p. 1035-1040.

39. Schneider, C. A., Rasband, W. S., and Eliceiri, K. W. NIH image to ImageJ: 25 years of image analysis. *Nat Methods*, 2012. **9**(7): p. 671-5.

40. Mastronarde, D. N. Automated electron microscope tomography using robust prediction of specimen movements. *J Struct Biol*, 2005. **152**(1): p. 36-51.

41. Kremer, J. R., Mastronarde, D. N., and McIntosh, J. R. Computer visualization of three-dimensional image data using IMOD. *J Struct Biol*, 1996. **116**(1): p. 71-6.

42. Li, G. and Tang, J. X. Low flagellar motor torque and high swimming efficiency of *Caulobacter crescentus* swarmer cells. *Biophys J*, 2006. **91**(7): p. 2726-34.

43. Driks, A., Bryan, R., Shapiro, L., and DeRosier, D. J. The organization of the *Caulobacter crescentus* flagellar filament. *J Mol Biol*, 1989. **206**(4): p. 627-636.

44. Minnich, S. A., Ohta, N., Taylor, N., and Newton, A. Role of the 25-, 27-, and 29-kilodalton flagellins in *Caulobacter crescentus* cell motility: Method for construction of deletion and Tn5 insertion mutants by gene replacement. *J Bacteriol*, 1988. **170**(9): p. 3953-60.

45. Wilson, J. J. and Takahashi, I. Adsorption of *Bacillus subtilis* bacteriophage pbs 1. *Can J Microbiol*, 1978. **24**(1): p. 1-8.

46. Bradley, D. E., Douglas, C. J., and Peschon, J. Flagella-specific bacteriophages of agrobacterium tumefaciens: Demonstration of virulence of nonmotile mutants. *Canadian Journal of Microbiology*, 1984. **30**(5): p. 676-81.

47. Wang, F., Burrage, A. M., Postel, S., Clark, R. E., Orlova, A., Sundberg, E. J., Kearns, D. B., and Egelman, E. H. A structural model of flagellar filament switching across multiple bacterial species. *Nat Commun*, 2017. **8**(1): p. 960.

48. Blair, K. M., Turner, L., Winkelman, J. T., Berg, H. C., and Kearns, D. B. A molecular clutch disables flagella in the bacillus subtilis biofilm. *Science*, 2008. **320**(5883): p. 1636-1638.

49. Mortimer, C. K., Gharbia, S. E., Logan, J. M., Peters, T. M., and Arnold, C. Flagellin gene sequence evolution in salmonella. *Infect Genet Evol*, 2007. **7**(4): p. 411-5.

50. Kanto, S., Okino, H., Aizawa, S., and Yamaguchi, S. Amino acids responsible for flagellar shape are distributed in terminal regions of flagellin. *J. Mol. Biol.*, 1991. **219**(3): p. 471-80.

51. Mimori-Kiyosue, Y., Yamashita, I., Fujiyoshi, Y., Yamaguchi, S., and Namba, K. Role of the outermost subdomain of salmonella flagellin in the filament structure revealed by electron cryomicroscopy. *Journal of molecular biology*, 1998. **284**(2): p. 521-30.

52. Mimori-Kiyosue, Y., Vonderviszt, F., and Namba, K. Locations of terminal segments of flagellin in the filament structure and their roles in polymerization and polymorphism. *J. Mol. Biol.*, 1997. **270**(2): p. 222-37.

53. Yen, J. Y., Broadway, K. M., and Scharf, B. E. Minimum requirements of flagellation and motility for infection of agrobacterium sp. Strain h13-3 by flagellotropic bacteriophage 7-7-1. *Appl Environ Microbiol*, 2012. **78**(20): p. 7216-22.

FIGURE LEGENDS

Figure 1. Flagellin deletion strain flagellum length measurements, cell motility, and ϕCbK adsorption kinetics. The distribution of flagellum lengths is shown with the black points indicating individual measurements of each flagellum. Error bars indicate standard deviation. The central bar represents the average length measurement for each strain. Strain motility (dark grey bars) and adsorption of phage ϕCbK (grey bars) to each strain were measured in triplicate and are presented as the percent difference from the wild type *C. crescentus* strain (NA1000). The black boxes indicate the presence of the corresponding flagellin.

Figure 2. Transmission electron microscopy images of negatively stained *C. crescentus* flagellin gene deletion strains examined. The images depict that most strains examined maintained near-to-wild type length flagella. Only Δ*fljKLMNO* (B) and Δ*fljJKLM* (H) presented a severely truncated flagellum that lacked an appreciable flagellar filament (Figure 1). Scale bars, 1 μm; inset scale bar in 3B is 200 nm.

Figure 3. Averaged slices merged with segmentations through three-dimensional tomographic reconstructions of representative ϕCbK -infected *C. crescentus* cells selected from all strains examined. (A, C and D) Phages were observed either adsorbed along the length of the flagellum or attached to the cell poles of strains investigated. (B) *C. crescentus* Δ*fljKLMNO* assembles a short flagellum. Insets highlight the ϕCbK head filament wrapped around the *C. crescentus* flagellum. Scale bars, 200 nm.

Figure 4. Fluorescence light microscopy of single amino acid change motility defective strains. (A) Positive control expressing unmutagenized $FljK^{T103C}$. (B-D) Strains forming straight flagella with the

mutations T198I (B), L201Q (C), and N130S (D). We observed ejected flagella and flagella attached to the distal end of the stalk of some cells. Scale bars, 2 μm.

Figure 5. Negative stain electron microscopy of single amino acid change motility defective strains. (A) Positive control expressing unmutagenized FljK^{T103C}. (B-D) Strains forming straight flagella with the mutations T198I (B), L201Q (C), and N130S (D). We observed ejected flagella and flagella attached to the distal end of the stalk of some cells. Scale bars, 1 μm.

Figure 6. Cryo-EM of purified FljK^{N130S} flagellar filaments. (A and B) Representative cryo-EM images of filaments purified from the strain containing an N130S mutation in FljK. The filaments are straight and the lumen of the filaments can be resolved. Black arrows indicate flagellar filaments, the black arrowhead indicates a flagellar hook, and white arrowheads indicate debris remaining after the filament preparation process. Scale bars, 100 nm.

Figure 1

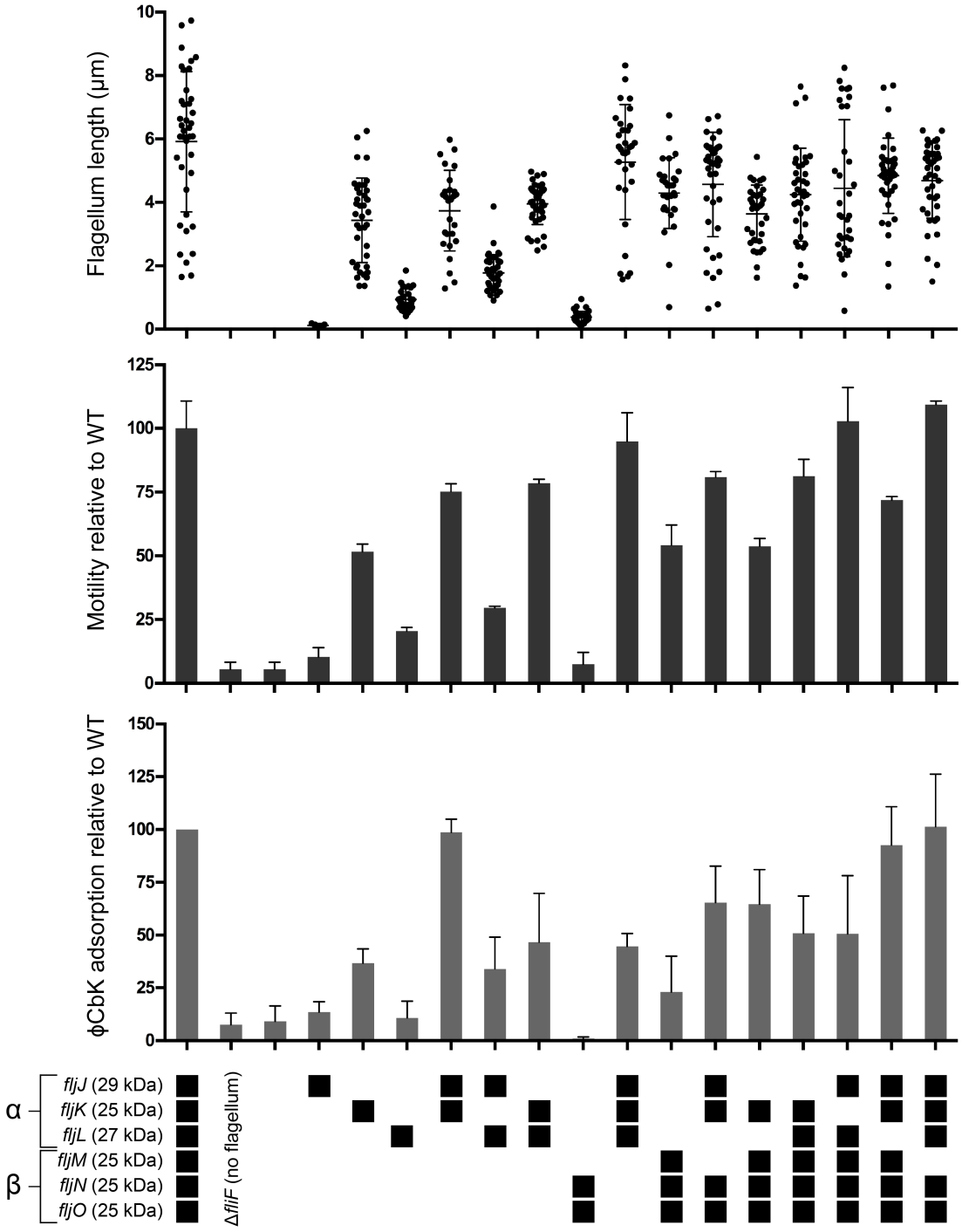
Flagellum length (μm)
Motility relative to WT
ϕCbK adsorption relative to WT
α
β
fljJ (29 kDa)
fljK (25 kDa)
fljL (27 kDa)
fljM (25 kDa)
fljN (25 kDa)
fljO (25 kDa)
ΔflgF (no flagellum)

Figure 2

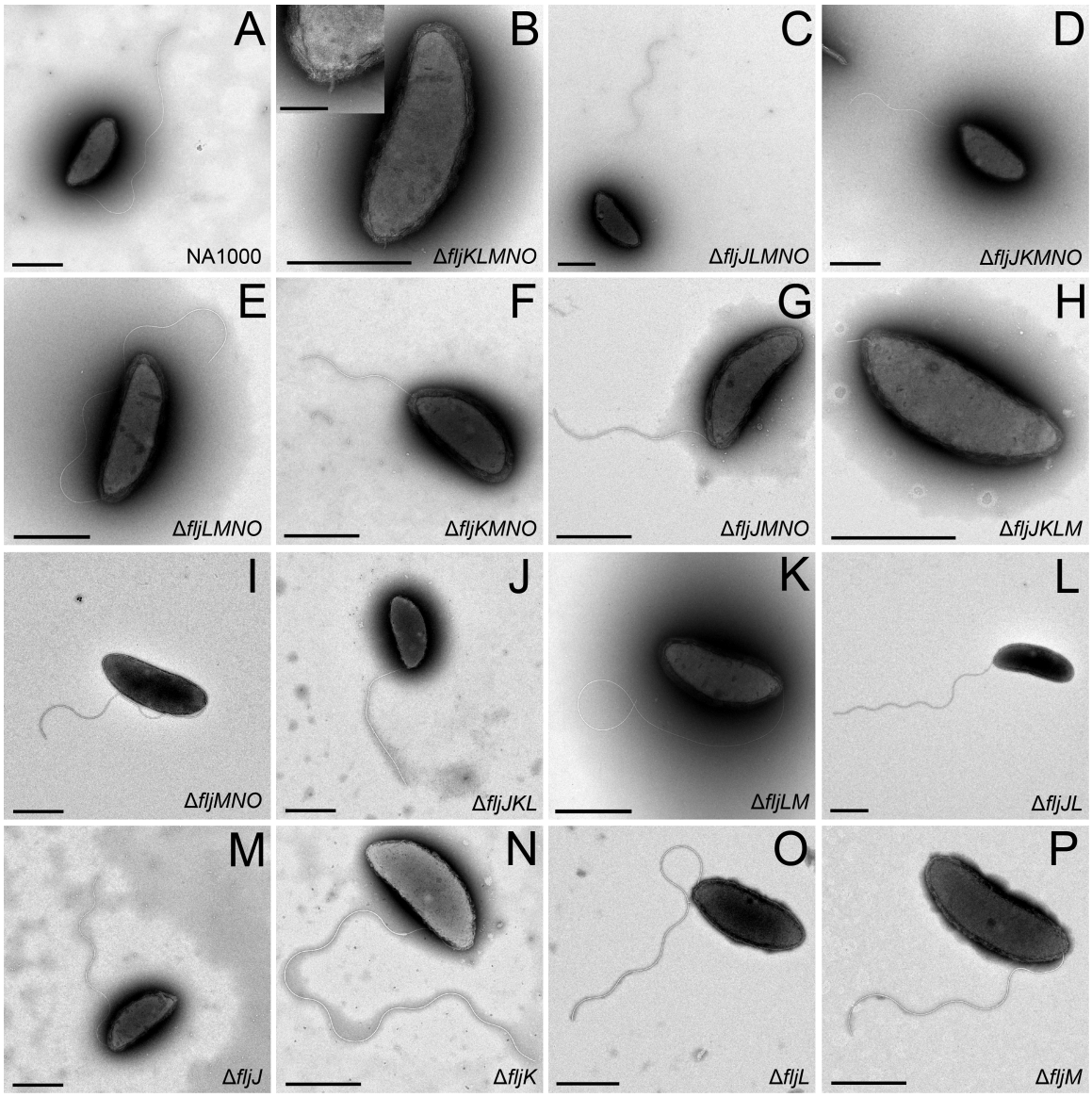
A
NA1000
B
ΔfljKLMNO
C
ΔfljJLMNO
D
ΔfljJKMNO
E
ΔfljLMNO
F
ΔfljKMNO
G
ΔfljJMNO
H
ΔfljJKLM
I
ΔfljMNO
J
ΔfljJKL
K
ΔfljLM
L
ΔfljJL
M
ΔfljJ
N
ΔfljK
O
ΔfljL
P
ΔfljM

Figure 3

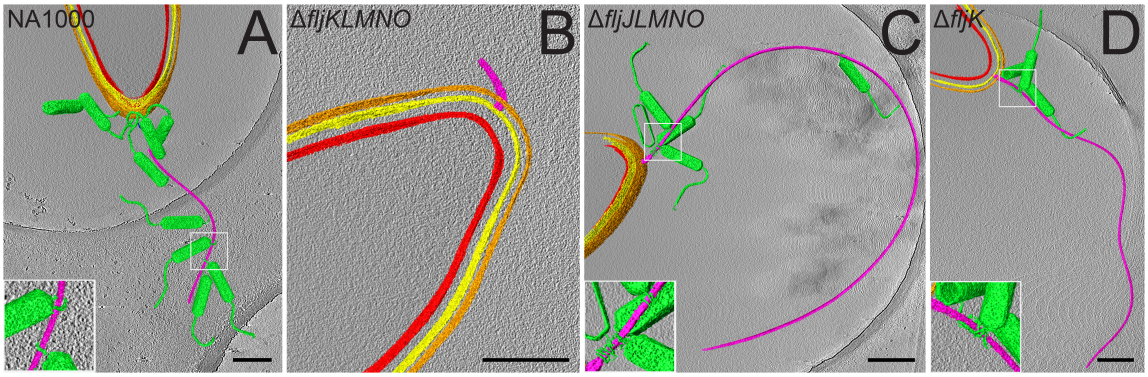

Figure 4

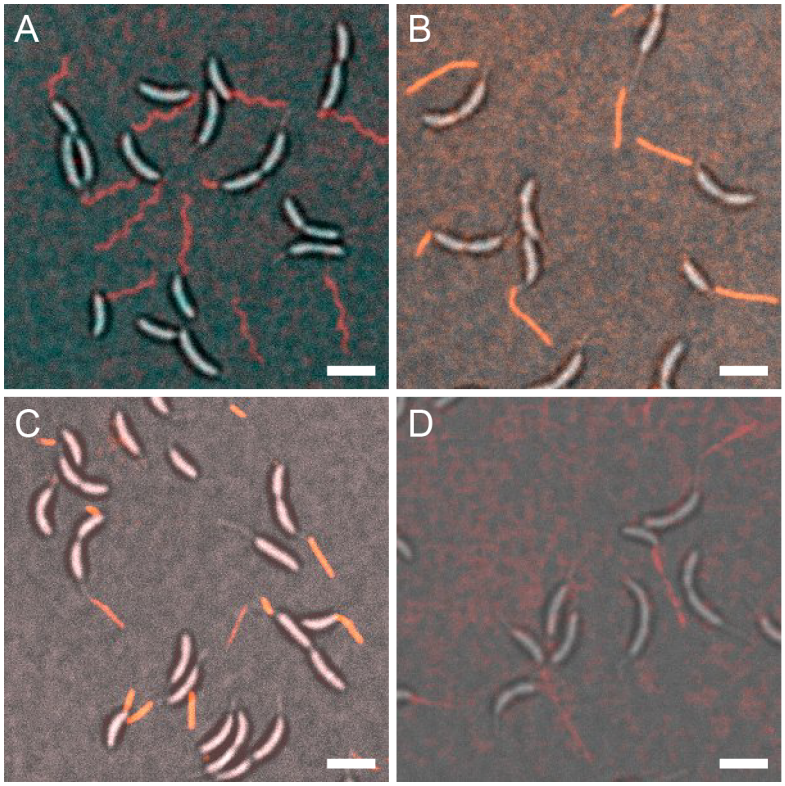

Figure 5

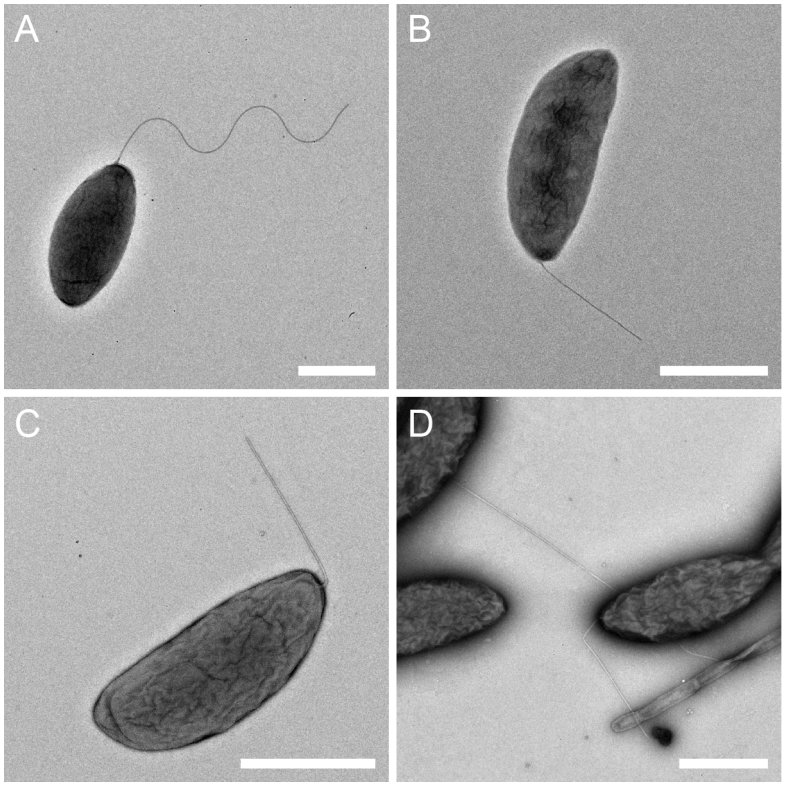

Figure 6

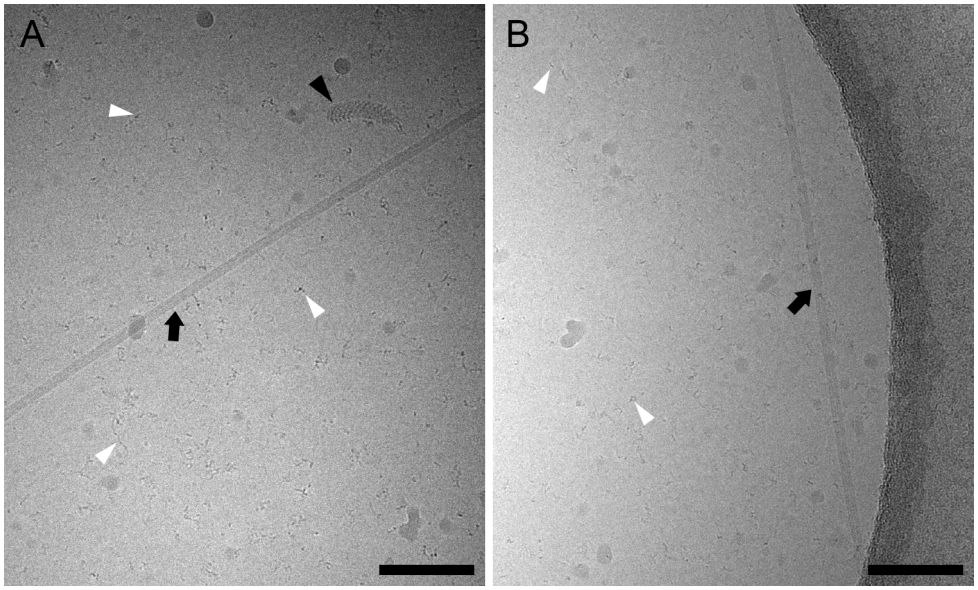

Table 1. *C. crescentus* flagellar mutants used in this study.

Mutation	Strain	Genotype
Wild type	NA1000	syn-1000, synchronizable derivative of a *C. crescentus* wild type strain
Δ*fliF*	LS1218	Δ*fliF*
Δ*fljJKLMNO*	TPA2357	Δ*fljJ* Δ*fljK* Δ*fljL* Δ*fljM*-Δ*fljO*
Δ*fljKLMNO*	TPA2354	Δ*fljK* Δ*fljL* Δ*fljM*-Δ*fljO*
Δ*fljJLMNO*	TPA2353	Δ*fljJ* Δ*fljL* Δ*fljM*-Δ*fljO*
Δ*fljJKMNO*	TPA2346	Δ*fljJ* Δ*fljK* Δ*fljM*-Δ*fljO*
Δ*fljLMNO*	TPA2356	Δ*fljL* Δ*fljM*-Δ*fljO*
Δ*fljKMNO*	TPA2352	Δ*fljK* Δ*fljM*-Δ*fljO*
Δ*fljJMNO*	TPA2344	Δ*fljJ* Δ*fljM*-Δ*fljO*
Δ*fljJKLM*	TPA1140	Δ*fljJ* Δ*fljK* Δ*fljL* Δ*fljM*
Δ*fljMNO*	TPA1299	Δ*fljM-fljO*
Δ*fljJKL*	TPA970	Δ*fljJ* Δ*fljK* Δ*fljL*
Δ*fljLM*	TPA1300	Δ*fljL* Δ*fljM*
Δ*fljJL*	TPA934	Δ*fljJ* Δ*fljL*
Δ*fljJ*	TPA663	Δ*fljJ*
Δ*fljK*	TPA2234	Δ*fljK*
Δ*fljL*	TPA916	Δ*fljL*
Δ*fljM*	TPA541	Δ*fljM*

Deletion mutants are from Faulds-Pain *et al.* [26].

Table 2. Tabulated assays performed to determine flagellum length, motility rate, and rate of ϕCbK adsorption.

Strain	Flagellum length (μm)	Motility (Percentage of NA1000)	ϕCbK Adsorption (Percentage of NA 1000)
Wild type	5.9	100	100
Δ*fliF*	0	6	8
Δ*fljJKLMNO*	0	6	9
Δ*fljKLMNO*	0.1	10	14
Δ*fljJLMNO*	3.4	52	37
Δ*fljJKMNO*	0.9	20	11
Δ*fljLMNO*	3.7	75	99
Δ*fljKMNO*	1.8	30	34
Δ*fljJMNO*	4	78	47
Δ*fljJKLM*	0.4	8	1
Δ*fljMNO*	5.3	95	45
Δ*fljJKL*	4.3	54	23
Δ*fljLM*	4.6	85	65
Δ*fljJL*	3.6	54	65
Δ*fljJ*	4.2	81	51
Δ*fljK*	4.4	103	51
Δ*fljL*	4.8	72	93
Δ*fljM*	4.7	109	101

Chapter 6: Discussion

Cryo-EM portions adapted from:

Biological applications at the cutting edge of cryo-electron microscopy

Rebecca S. Dillard[1,], Cheri M. Hampton[1,], Joshua D. Strauss[1,], Zunlong Ke[1,2,], Deanna Altomara[1], Ricardo C. Guerrero-Ferreira[1], Gabriella Kiss[1], and Elizabeth R. Wright[1,3]

[1]Division of Pediatric Infectious Diseases, Emory University School of Medicine, Children's Healthcare of Atlanta, Atlanta, GA

[2]School of Biology, Georgia Institute of Technology, Atlanta, GA

[3]Robert P. Apkarian Integrated Electron Microscopy Core, Emory University, Atlanta, GA

Submitted to *Microscopy and Microanalysis*

CRYO-ELECTRON MICROSCOPY

Since its development, cryo-electron microscopy (cryo-EM) has played an important role in structural biology and is contributing more and more with recent advances. New developments are broadening the cryo-EM spectrum from whole cells to peptides, allowing more biological questions of greater complexity to be answered and there is still room for improvement.

The timing and capturing of rare and specific events on the macromolecular and cellular levels is now possible using microsprayers and CLEM, respectively, for time-resolved imaging. Reproducibility in the sample preparation and grid preparation processes should continue to improve as grid-based purification methods and the development of vitrification devices such as the Spotiton and cryoWriter mature and expand. Beam-induced motion is being addressed both by the grid substrate and through the use of correction algorithms that utilize the high-frame rate of direct electron detectors.

Advances in electron detection over the past several years have provided remarkable improvements for cryo-EM data collection and quality. Further increasing frame rates, the use of counting mode on all systems, and increased pixel sizes will provide even higher DQEs and super resolution mode should allow direct electron detectors to be used beyond Nyquist frequency [1].

While phase plates have shown extraordinary promise for cryo-EM, there are still improvements that can be made. Usage is generally limited to those with expertise [2-4] and takes a considerable amount of time, so workflow development will be incredibly important for more widespread implementation. Higher reproducibility in the manufacture of phase plates and methods for evaluating phase plate quality during use will also prove to be useful. Phase plates should allow

increasingly higher resolution structural work, particularly for small samples, and for entire datasets to be collected more quickly since fewer images will be required.

As CLEM continues to develop, labeling strategies that are retained between live cell and cryo-EM imaging will allow more complex biological questions to be addressed and simultaneously fluorescent and electron-dense markers will aid in more precise correlation between light and electron microscopy. Combining cryo-FIB milling of cryo-samples with cryo-CLEM will provide a method for thicker specimens to be investigated and improvements to sample stability between steps of the workflow will help the process become more user-friendly.

The recent developments in cryo-EM imaging, along with improvements in image processing, have allowed tremendous growth in the field over the last few years. We expect this expansion to continue, with cryo-EM providing structures to higher resolutions and answers to increasingly intricate biological questions.

CRYO-CLEM APPLICATIONS

In Hampton *et al.* (Chapter 2), we developed a workflow for the investigation of viral entry, assembly, and release in the context of mammalian cells by cryo-correlative light and electron microscopy [5]. This opens a variety of opportunities for the study of interactions between viruses and host cells. In the context of RSV assembly, many questions remain concerning glycoprotein arrangements, glycoprotein interactions with matrix, and the association between matrix and the ribonucleoprotein (RNP) complexes. Fluorescent labeling of these components would allow us to track their trafficking within the cell, cryo-preserve the sample, and locate specific events by cryo-CLEM. This technique will also be useful in understanding host factor contributions to RSV

assembly. We are particularly interested in the role of the cytoskeleton, as we have often observed microtubules and actin at assembly sites (Figure 1A and 1B), as well as actin within released viral filaments by cryo-electron tomography (cryo-ET) (Figure 1C and 1D). Cryo-CLEM will also be utilized for the continued study of the HIV-1 fusion process. Combined with live-cell imaging, cryo-CLEM will allow us to identify HIV-1 cores at various stages of uncoating and, with the additional use of cryo-focused ion beam (cryo-FIB) milling, could provide higher resolution information about nuclear import of the pre-initiation complexes (PICs).

Cryo-CLEM also has applications outside of mammalian virus studies. The development of a *Caulobacter crescentus* strain with a cysteine knock-in the major pilin protein, PilA, has allowed us to fluorescently label the Cpa pili with maleimide dyes [6]. We have begun using cryo-CLEM to investigate pilus dynamics in *C. crescentus*. Figure 2 illustrates this process using pili labeled with Alexa Fluor 594 C_5 maleimide (red) and blocked with a large polyethylene glycol maleimide conjugate (PEG5000-mal, ~5000 Da). *C. crescentus* cells autofluoresce at an excitation wavelength of 488 nm (green), allowing us to easily locate cells. The cryo-light microscopy map (Figure 2A) was correlated to the cryo-EM map (Figure 2B) and a tomogram was collected where red signal corresponding to labeled pili was present at a cell pole (Figure 2C and 3D segmentation in 2D). Cryo-ET revealed that additional density coats the pili in the presense of PEG5000-mal.

VIBRIO CHOLERAE OUTER-MEMBRANE VESICLES PREVENT BACTIOPHAGE INFECTION

The work described in Chapter 3 revealed that *Vibrio cholerae* is able to defend itself against bacteriophage infection by secreting outer membrane vesicles (OMVs), which act as a decoy. Cryo-ET studies revealed ICP phages directly interacting with OMVs, but suggested that the phages do

not eject their genomes into the OMVs. To investigate this further, we collected large montages of phages incubated with OMVs preserved on cryo-EM grids and quantified the number of full or empty phages that were associated or not with OMVs. We found that 81% of ICP1 phages associated with OMVs were full and 92% of ICP3 phages associated with OMVs were full, further supporting that these phages do not eject their genomes into the OMVs (Figure 3). Only 57% of ICP2 phages associated with OMVs were full, however, indicating the possibility that these phages are capable of ejecting their genomes into the OMVs (Figure 3). To further investigate genome ejection, it will be important to quantify the number of empty and full phages outside of the context of OMV interactions for comparison.

One hypothesis for the lack of genome ejection for ICP1 and ICP3 is that the phages are able to sense the curvature of the membrane to which they are attaching. Since the membrane curvature is much greater for OMVs than for a bacterial cells, perhaps the phages don't initiate a necessary step in the genome ejection process. Whether or not the phages can detach from the OMVs would also be of interest. If the phages do not eject their genomes into the OMVs and are capable of detaching, they may remain infectious. OMV inhibition of the phages would therefore be only temporary.

The results of the study indicate that OMVs could play an important role in bacterial defense against bacteriophages. With growing interest in phage therapy, this will be a consideration that could affect the treatment outcomes. While it is unknown in what quantities OMVs are produced and present during bacterial infections, they have the potential to neutralize phage and could therefore be a confounding factor.

PILUS RETRACTION IN *CAULOBACTER CRESCENTUS* IS REQUIRED FOR ϕCbK INFECTION

Further study of type IVc pilus (T4cP) retraction in *C. crescentus* will require elucidation of the mechanism of retraction. The Cpa pilus may utilize minor pilins, as was shown for the *Vibrio cholerae* toxin-coregulated pilus (TCP) [7], it may use an ATPase that is unrelated to the T4aP retraction ATPases, or the T4cP may have an entirely unique mechanism. The structures of two T4aP machines have been solved by cryo-ET and sub-tomogram averaging [8, 9]. Gold *et al.* revealed major conformational changes between the open and closed state of the *Thermus thermophilus* T4aP machinery and Chang *et al.* developed a pseudo-atomic model of the *Myxococcus xanthus* T4aP machine, mapping all of the known components [8, 9]. Such structural analysis of the *C. crescentus* pilus would provide an understanding of the Cpa complex and allow identification of the proteins involved in the assembly and retraction processes. This could also be done in the context of phage infection to provide information about receptor binding and genome translocation into the cell.

STRUCTURAL SPECIFICITY OF THE BACTERIOPHAGE ϕCbK HEAD FILAMENT TO THE *CAULOBACTER CRESCENTUS* FLAGELLUM

Determining the structural changes associated with different flagellins as well as with multiple flagellins will help us to understand why almost 50% of flagellated species encode more than one flagellin. Comparison of the mutations that lock the *C. crescentus* flagellum into the L- or R-states with those that lock that flagella of other species into straight conformations could provide broader information about flagellum assembly and how related the process is among species.

Our data supports a model of *C. crescentus* flagellum assembly in which FljJ initiates filament formation, followed by FljL as an adaptor, and the 25 kDa flagellins as the extended filament. It will

be interesting to examine whether this relates to other species, such as *Vibrio cholerae*. *V. cholerae* encodes five flagellins, *flaACEDB,* on two loci and assembles a sheathed flagellum [10]. In a collection of *V. cholerae* flagellin mutants, we found that filament length varies greatly depending on composition and in some strains, the diameter of the flagellar sheath is much more variable (Figure 4). We hypothesize that the different flagellins are required for proper assembly and that interactions with the sheath vary between flagellins. As flagella are important virulence factors for *V. cholerae*, future studies should examine the effects that flagellar composition has on *V. cholerae* infection.

OVERALL CONCLUSIONS

Cryo-EM preserves biological specimens in a close-to-native state and allows us to directly visualize the electron density of the sample without artifact-inducing fixation or staining. We have used cryo-EM to study the interactions between viruses and their hosts in two systems: 1) Mammalian viruses infecting cells cultured on EM grids, providing novel insights into RSV morphology and assembly mechanisms and HIV-1 entry and fusion events (Chapter 1, Chapter 2, Appendix A, and Appendix C); and 2) Bacteriophage interactions with bacterial cells and their components, offering new understanding of bacterial defense mechanisms (Chapter 3), T4cP function (Chapter 4), the role of multiple flagellins in flagellar assembly and phage adsorption (Chapter 5), and phage-induced bacterial lysis (Appendix E). Cryo-EM has proven to be a valuable tool for the study of host-microbe interactions.

REFERENCES

1. McMullan, G., Faruqi, A. R., and Henderson, R. Direct electron detectors. *Methods Enzymol*, 2016. **579**: p. 1-17.
2. Danev, R. and Nagayama, K. Single particle analysis based on Zernike phase contrast transmission electron microscopy. *J Struct Biol*, 2008. **161**(2): p. 211-8.
3. Glaeser, R. M., Sassolini, S., Cambie, R., Jin, J., Cabrini, S., Schmid, A. K., Danev, R., Buijsse, B., Csencsits, R., Downing, K. H., Larson, D. M., Typke, D., and Han, B. G. Minimizing electrostatic charging of an aperture used to produce in-focus phase contrast in the tem. *Ultramicroscopy*, 2013. **135**: p. 6-15.
4. Subramaniam, S., Kuhlbrandt, W., and Henderson, R. Cryoem at iucrj: A new era. *IUCrJ*, 2016. **3**(Pt 1): p. 3-7.
5. Hampton, C. M., Strauss, J. D., Ke, Z., Dillard, R. S., Hammonds, J. E., Alonas, E., Desai, T. M., Marin, M., Storms, R. E., Leon, F., Melikyan, G. B., Santangelo, P. J., Spearman, P. W., and Wright, E. R. Correlated fluorescence microscopy and cryo-electron tomography of virus-infected or transfected mammalian cells. *Nat Protoc*, 2017. **12**(1): p. 150-167.
6. Ellison, C. K., Kan, J., Dillard, R. S., Kysela, D. T., Ducret, A., Berne, C., Hampton, C. M., Ke, Z., Wright, E. R., Biais, N., Dalia, A. B., and Brun, Y. V. Obstruction of pilus retraction stimulates bacterial surface sensing. *Science*, 2017. **358**(6362): p. 535.
7. Ng, D., Harn, T., Altindal, T., Kolappan, S., Marles, J. M., Lala, R., Spielman, I., Gao, Y., Hauke, C. A., Kovacikova, G., Verjee, Z., Taylor, R. K., Biais, N., and Craig, L. The *Vibrio cholerae* minor pilin TcpB initiates assembly and retraction of the toxin-coregulated pilus. *PLoS Pathog*, 2016. **12**(12): p. e1006109.
8. Gold, V. A. M., Salzer, R., Averhoff, B., and Kühlbrandt, W. Structure of a type IV pilus machinery in the open and closed state. *eLife*, 2015. **4**: p. e07380.

9. Chang, Y. W., Rettberg, L. A., Treuner-Lange, A., Iwasa, J., Sogaard-Andersen, L., and Jensen, G. J. Architecture of the type IVa pilus machine. *Science*, 2016. **351**(6278): p. aad2001.

10. Klose, K. E. and Mekalanos, J. J. Differential regulation of multiple flagellins in *Vibrio cholerae*. *J Bacteriol*, 1998. **180**(2): p. 303-316.

FIGURE LEGENDS

Figure 1. Actin filament involvement in RSV assembly and morphology. HeLa cells infected with RSV contain actin filaments near and inside a filamentous RSV particle: (A) tomographic slice and corresponding segmented view (B) (cyan: membrane; yellow: glycoproteins; red: RNP; cyan green: actin in the budding viral filament; green: actin filament inside cell). (C) Tomographic slice of RSV infected BEAS-2B cells. (D) Tomographic slice of RSV infected Niemann-Pick Type C (NPC) cells showing actin filaments in released filamentous RSV. Note the RSV viral proteins are resolved in both assembling and released viral filaments. Scale bars, 200 nm.

Figure 2. Cryo-correlative light and electron microscopy of *Caulobacter crescentus* pili labeled with Alexa Fluor 594 C_5 maleimide (red) and blocked with a large polyethylene glycol maleimide conjugate (PEG5000-mal; ~5000 Da). (A) Cryo-light microscopy map allowing the identification of cells expressing pili. The green signal results from autofluorescence of the cells. (B) Cryo-EM map showing densities corresponding to the cell fluorescence shown in (A). (C and D) Tomographic slice and segmentation of the cell pole of the C. crescentus cell indicated in (A) and (B) with a white box. The red fluorescence in (A) correlates to the three extended pili shown in (C) and (D). Scale bars, (B), 10 μm and (C), 200 nm.

Figure 3. Quantification of phages with full or empty capsids and their association with *V. cholerae* OMVs. Phages were incubated for 1 hour with *V. cholerae* OMVs before application to an EM grid and plunge-freezing. Large montages of the grid were collected on a JEOL JEM-2200FS transmission electron microscope. Phages within the holes of the Quantifoil carbon film were counted and classified based on whether the capsid contained the phage genome and whether they were associated with OMVs.

Figure 4. Flagellum length and diameter measurements of *V. cholerae* flagellin deletion strains. *V. cholerae* cultures were applied to EM grids and plunge-frozen and cells were imaged on a JEOL JEM-2200FS transmission electron microscope. Measurements of flagella were made from images of filaments attached to intact cells. The black points indicate individual measurements of each flagellum and the error bars indicate standard deviation. The central bar represents the average length or diameter for each strain.

Figure 1

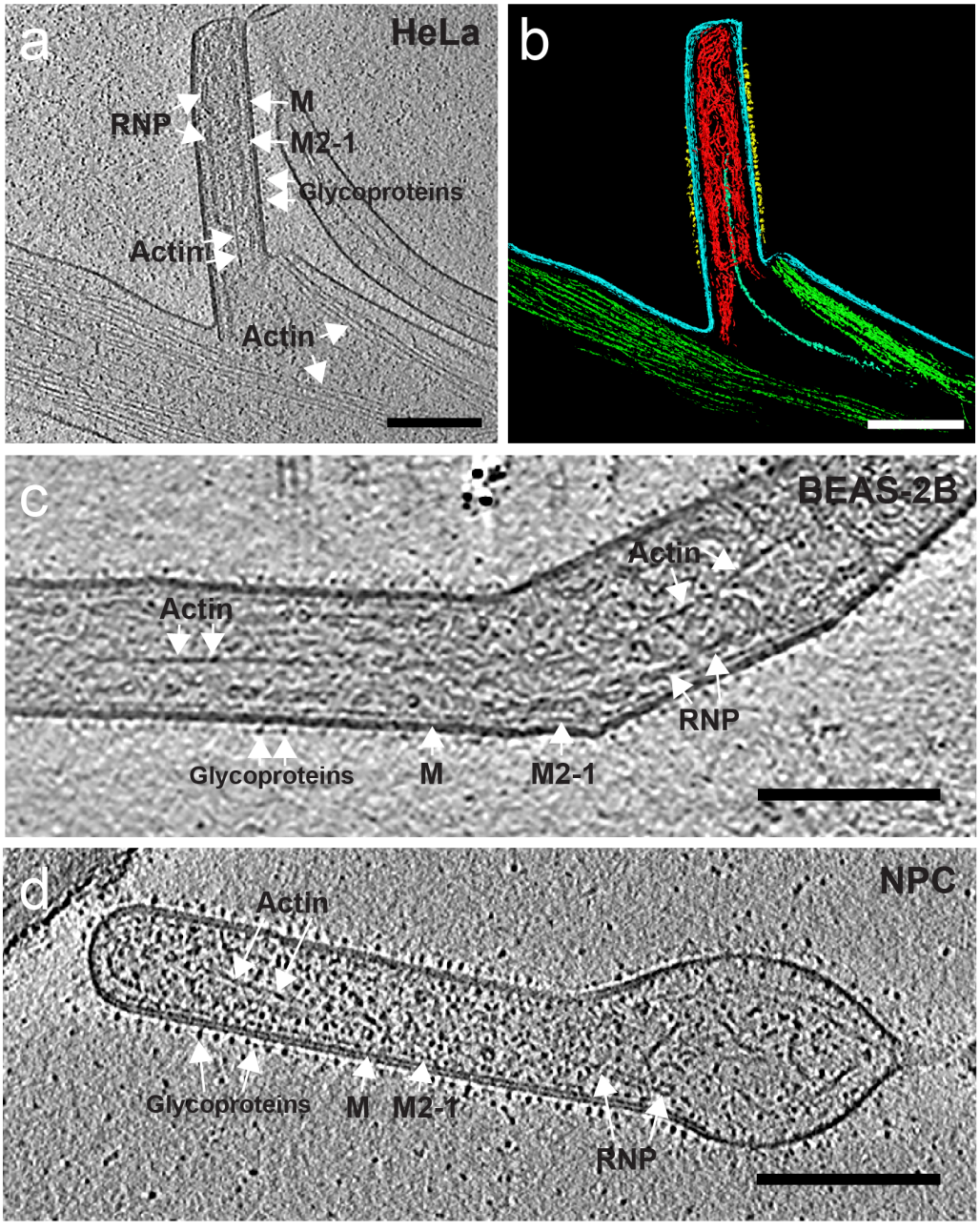
a
HeLa
RNP
M
M2-1
Glycoproteins
Actin
Actin
b
c
BEAS-2B
Actin
Actin
RNP
Glycoproteins
M
M2-1
d
NPC
Actin
Glycoproteins
M
M2-1
RNP

Figure 2

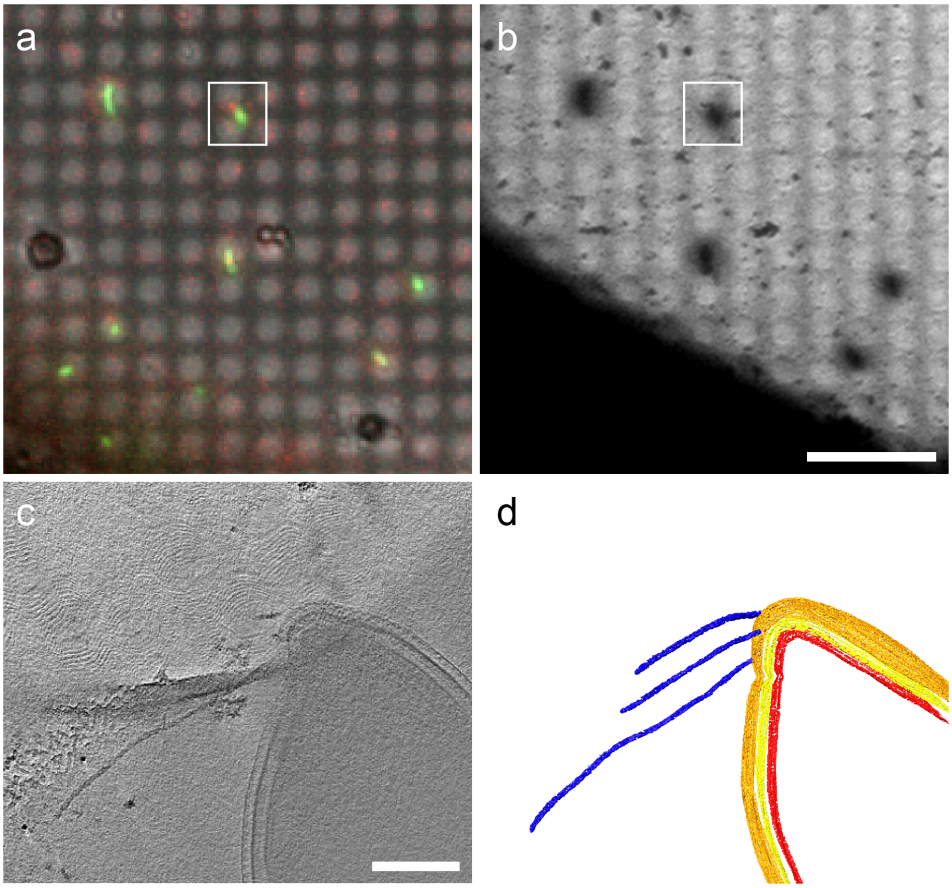

Figure 3

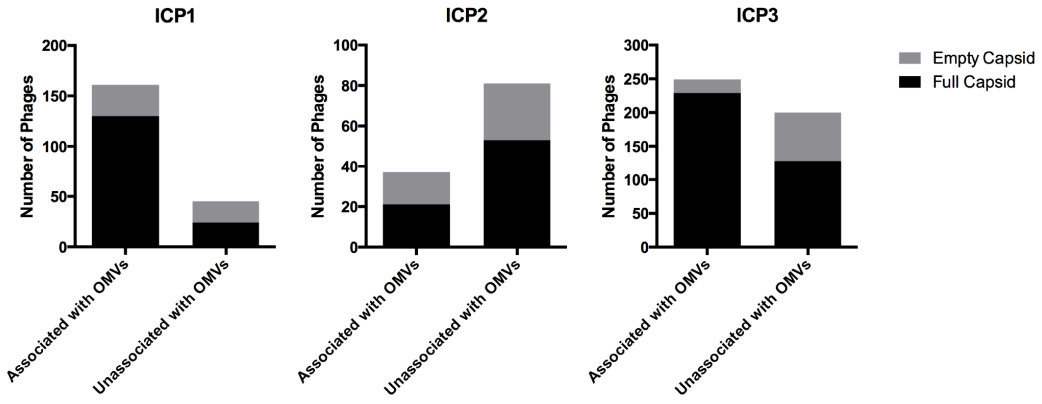
ICP1
ICP2
ICP3
Number of Phages
200
150
100
50
0
100
80
60
40
20
0
300
250
200
150
100
50
0
Associated with OMVs
Unassociated with OMVs
Empty Capsid
Full Capsid

Figure 4

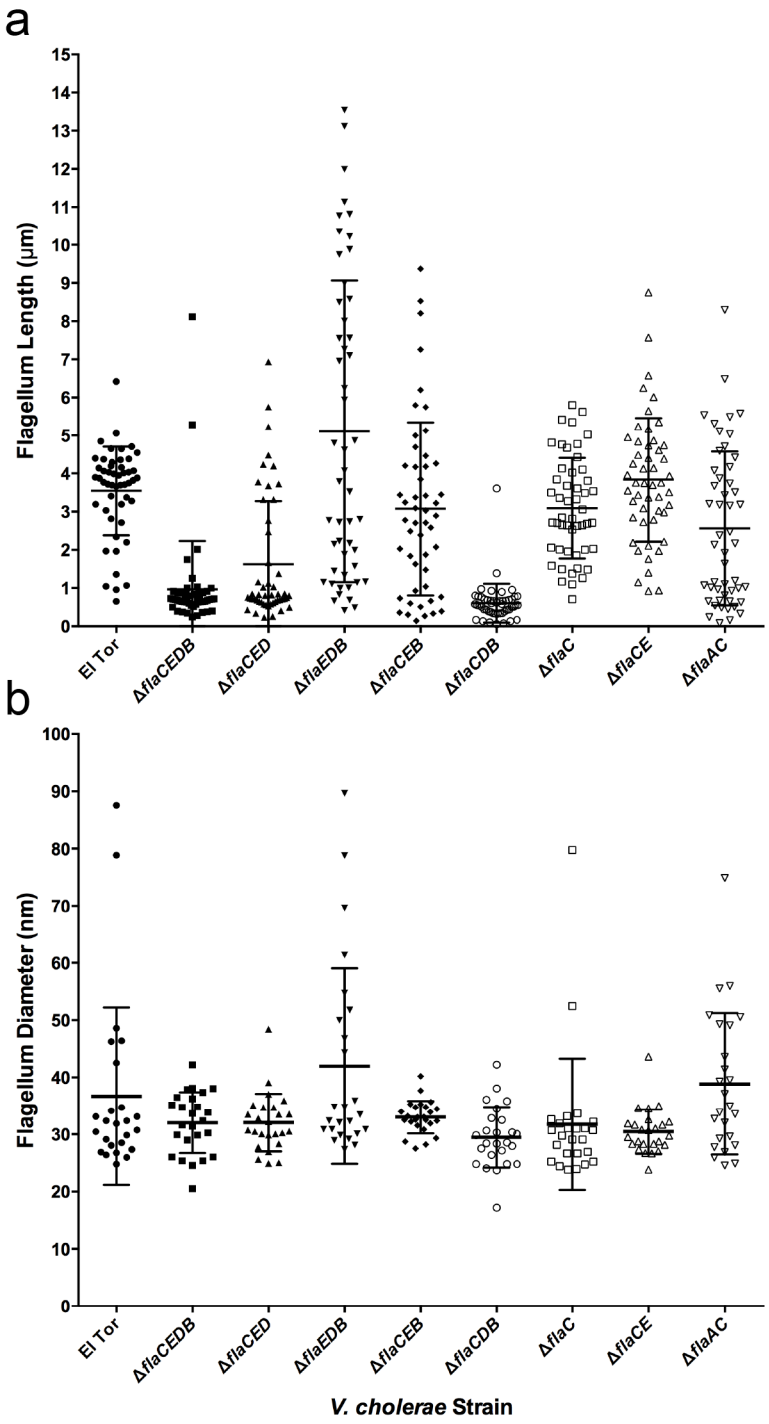
a
Flagellum Length (μm)
0
1
2
3
4
5
6
7
8
9
10
11
12
13
14
15
El Tor
ΔflaCEDB
ΔflaCED
ΔflaEDB
ΔflaCEB
ΔflaCDB
ΔflaC
ΔflaCE
ΔflaAC
b
Flagellum Diameter (nm)
0
10
20
30
40
50
60
70
80
90
100
El Tor
ΔflaCEDB
ΔflaCED
ΔflaEDB
ΔflaCEB
ΔflaCDB
ΔflaC
ΔflaCE
ΔflaAC
V. cholerae Strain

Appendix A: Native immunogold labeling of cell surface proteins and viral glycoproteins for cryo-electron microscopy and cryo-electron tomography applications

Hong Yi[1,5], Joshua D. Strauss[2,5], Zunlong Ke[3], Eric Alonas[4], Rebecca S. Dillard[2], Cheri M. Hampton[2], Kristen M. Lamb[2], Jason E. Hammonds[2], Philip J. Santangelo[4], Paul W. Spearman[2], and Elizabeth R. Wright[1,2]

[1]Robert P. Apkarian Integrated Electron Microscopy Core, Emory University, Atlanta, GA

[2]Division of Pediatric Infectious Diseases, Emory University School of Medicine, Children's Healthcare of Atlanta, Atlanta, GA

[3]School of Biology, Georgia Institute of Technology, Atlanta, GA

[4]Wallace H. Coulter Department of Biomedical Engineering, Georgia Institute of Technology and Emory University, Atlanta, GA

[5]These authors contributed equally to this work.

Published in:

Journal of Histochemistry & Cytochemistry, 2015

Vol. 63, No. 10

p. 780-792

H.Y. and E.R.W. conceived and designed the experiments; H.Y., J.D.S., Z.K., E.A., R.S.D., C.M.H., K.M.L., and J.E.H. performed the experiments; P.J.S. and P.W.S. provided reagents and materials; H.Y., J.D.S., Z.K., E.A., C.M.H., and E.R.W. wrote the paper.

ABSTRACT

Numerous methods have been developed for immunogold labeling of thick, cryo-preserved biological specimens. However, most of the methods are permutations of chemical fixation and sample sectioning, which select and isolate the immunolabeled region of interest. We describe a method for combining immunogold labeling with cryo-electron microscopy (cryo-EM) and cryo-electron tomography (cryo-ET) of the surface proteins of intact mammalian cells or the surface glycoproteins of assembling and budding viruses in the context of virus-infected mammalian cells cultured on EM grids. In this method, the cells were maintained in culture media at physiologically relevant temperatures while sequentially incubated with the primary and secondary antibodies. Subsequently, the immunogold-labeled specimens were vitrified and observed under cryo-conditions in the transmission electron microscope. Cryo-EM and cryo-ET examination of the immunogold-labeled cells revealed the association of immunogold particles with the target antigens. Additionally, the cellular structure was unaltered by pre-immunolabeling chemical fixation and retained well-preserved plasma membranes, cytoskeletal elements, and macromolecular complexes. We think this technique will be of interest to cell biologists for cryo-EM and conventional studies of native cells and pathogen-infected cells.

INTRODUCTION

Cryo-electron microscopy (cryo-EM) technologies and techniques were established in order to retain specimen hydration during direct-image and diffraction data acquisition with the transmission electron microscope (TEM) [1]. Much of the early work in the late 1970s and early 1980s focused on improving cryo-fixation approaches [2, 3] cryo-holders for specimen introduction into the TEM [4-6], and low-dose data acquisition schemes for viruses, macromolecules, and small cells [7-10]. Later, as microscopes became more automated and intermediate voltage microscopes were more accessible, cryo-electron tomography (cryo-ET) emerged as the leading approach for determining the three-dimensional (3D) structures of pleomorphic objects, such as asymmetric viruses and bacteria [11-15]. Cryo-EM imaging, combined with single particle analysis and cryo-ET united with sub-volume averaging, is a major branch of the structural biology continuum, and over the past forty years have matured to the level where many biological structures are now determined at sub-nanometer to atomic-level resolutions [16-19].

Of great interest to those who employ cryo-EM methods to investigate cellular ultrastructure and the localization patterns of complexes within and surrounding cells, as is the development and application of target-specific labeling strategies [20]. Already, the feasibility of antibody labeling for purified macromolecules, viruses, and isolated organelles has been demonstrated [21, 22]. These studies have enabled investigators to determine the 3D structures of low molecular weight proteins by single particle cryo-EM [23], where proteins localize on specific regions of a virus [22], and the structural rearrangements that occur when a neutralizing antibody binds with the target antigen [24-28]. However, similar procedures have not been widely applied to studies of whole, intact mammalian cells because of the concerns associated with retaining cell viability during immunolabeling; the thicknesses of cells and the impact this has on cryo-preservation and cryo-EM

imaging; and early reports of antibody-induced membrane protein 'capping' on live cells [29, 30]. Therefore, techniques were developed that combined the benefits of initial cryo-preservation of cells by high-pressure freezing with chemical fixation through freeze substitution, embedding in hydrophilic resins, sectioning, and immunolabeling. Although these more traditional approaches have been used for countless immunolocalization studies for conventional electron microscopy [31, 32], there are a number of intrinsic issues associated with methods that include chemical fixation [33]. Most notably, fixation is required to prevent specimen degradation during subsequent steps of the procedure. However, fixation, dehydration, and embedding not only alter the antigen conformation, and thus hinder antibody binding, but also severely obscure or even remove ultrastructural detail. In addition, residual aldehydes from the fixative can potentially cross-link immuno-reagents to the cell or tissue and therefore lead to potential negative background immunolabeling. These additive negative effects limit the ability to resolve localization patterns at the molecular level via both conventional immuno-EM and hybrid cryo-immuno EM approaches.

In this study, we describe the procedures used for the immunogold labeling of live mammalian cells cultured on carbon-coated gold EM-support grids. Here, we performed native-state immunogold labeling of a cell-derived protein and of a viral glycoprotein. The first target protein labeled was tetherin (BST-2), a cellular restriction factor that inhibits the release of enveloped viruses from the plasma membrane of infected cells [34, 35]. We demonstrated site-specific labeling of tetherin and tetherin microdomains during the restriction of HIV-1 virus and virus-like particle (VLP) release from the plasma membrane of HT1080 cells. The second protein labeled was the fusion (F) glycoprotein of human respiratory syncytial virus (hRSV) in the context of an active infection of HEp-2 and HeLa cells. In this case, the hRSV F glycoprotein was labeled with a monoclonal antibody, palivizumab [36, 37], at sites of virus assembly, on assembling and budding virus particles,

and on released virus particles. We also describe some of the challenges associated with the immunolabeling method and provide detailed approaches for optimum labeling and specimen preservation for both cryo-EM and conventional EM applications.

MATERIALS AND METHODS

Antibodies and Reagents

Rabbit anti-tetherin antisera [38] was provided by Dr. Paul W. Spearman (Department of Pediatrics, Emory University, Atlanta, GA). Dr. Philip J. Santangelo (Department of Biomedical Engineering, Georgia Institute of Technology and Emory University, Atlanta, GA) supplied the palivizumab, a humanized monoclonal antibody that targets the antigenic site II of the hRSV fusion (F) glycoprotein [36, 37]. MedImmune, LLC, commercially manufactures palivizumab under the brand name Synagis for the prevention of hRSV infections in high-risk infants. The secondary antibodies, which included the 6-nm gold-conjugated goat anti-human IgG, F(ab')2 fragment of goat anti-rabbit IgG, and protein G, were purchased from Electron Microscopy Sciences (Hatfield, PA).

Cell culture, Transfection, and Immunolabeling for Tetherin

HT1080 cells, obtained from the American Type Culture Collection (Manassas, VA), were maintained in high-glucose pyruvate DMEM (GIBCO; Grand Island, NY) supplemented with 10% fetal bovine serum (FBS), 5 mM penicillin-streptomycin, and 5 mM l-Glutamate. Cells were grown in an incubator at 37°C with 5% CO_2. HT1080 cells (20,000-30,000) for tetherin immunogold labeling were seeded on pre-sterilized, 0.2% collagen coated Aclar disks or gold R2/1 Quantifoil TEM grids (Quantifoil, Germany) 24 hr before transfection.

HT1080 cells were co-transfected with either mCherry Gag (1:3 ratio codon optimized Gag) or with an HIV-1 Vpu- and Env-deficient provirus cDNA [39] (kindly provided by Klaus Strebel, NIAID, Bethesda, MA) and eGFP-tetherin, using jetPRIME (Polyplus-Transfection Inc.; New York, NY), according to the manufacturer's instructions.

Immunogold labeling of tetherin on HIV-1 transfected HT1080 cells was carried out 16 hr post-transfection. Transfected cells on Aclar disks or gold Quantifoil TEM grids were maintained in growth medium in a 37°C incubator before immunogold labeling. Rabbit anti-tetherin antiserum [38] was added directly into the medium at a 1:200 dilution of the original stock solution (endpoint titer of 1×10^8/ml). Primary antibody incubation proceeded for 1.5 hr at 37°C, during which time the dishes were gently shaken periodically to facilitate antibody binding. After primary antibody incubation, cells were gently washed with medium four times for 30 sec each. The secondary antibodies, either the 6-nm gold-conjugated F(ab')2 fragment of goat anti-rabbit IgG or protein G, were then added to the medium directly at a 1:20 dilution of the original stock solutions (10–20 μg/ml) and allowed to incubate for 1.5 hr at 37°C. The cells were washed after secondary antibody incubation as described above. Cells cultured on the Aclar disks were washed twice with phosphate-buffered saline (PBS) and then fixed with 2.5% glutaraldehyde in 0.1 M phosphate buffer (pH 7.4) for conventional electron microscopy examination. Cells grown on the gold Quantifoil TEM grids were plunge-frozen immediately after the final wash with culture medium.

hRSV Purification

HEp-2 cells cultured in T75 flasks at 60% to 80% confluence were inoculated with RSV at a multiplicity of infection (MOI) of 0.01 in 3 ml serum-free medium for 1 hr, after which 12 ml of complete growth medium was added. The infection continued for approximately four days (>80% cytopathic effect, CPE), with 5 ml of complete media added each day. The flasks were then frozen at -80°C before purification. After thawing in a 37°C water bath, the contents of each flask were clarified at 1,902 × g for 7 min at 4°C. The supernatant was centrifuged using a 20% sucrose cushion at 90,353 × g (SW41 Ti, Beckman) for 3 hr at 4°C. The virus-containing pellet was resuspended in 100 μl Hanks Balanced Salt Solution (HBSS) after a brief wash and stored at -80°C.

The final titer of the virus was ~2–5×10^8 plaque forming units per ml (PFU/ml). The purified virus was then used to infect the HeLa or HEp-2 cells [40].

Cell Culture, RSV Infection, and Immunolabeling for hRSV F Glycoprotein

HeLa and HEp-2 cells (ATCC CCL-2 and CCL-23, respectively) were maintained in DMEM growth medium with 4.5 g/L d-glucose (Lonza), 4 mM l-glutamine (BioWhittaker), 10% fetal bovine serum (Sigma-Aldrich), and 1% penicillin-streptomycin (Sigma-Aldrich). Cells were grown in an incubator at 37°C with 5% CO_2. For hRSV F glycoprotein immunogold labeling, 100,000–150,000 HEp-2 cells or HeLa cells were seeded on pre-sterilized, pre-incubated (with complete medium) Aclar disks or gold R2/1 Quantifoil TEM grids in MatTek dishes (MatTek Corp., MA) 4–8 hr prior to infection.

Cells for immunogold labeling were inoculated with an MOI of 10 with hRSV in serum-free media. Complete growth media was added after 1 hr. Infected cells were incubated at 37°C for 24 hr. Palivizumab was then added directly into the medium at 5 μg/ml and the cells were allowed to incubate for 1.5 hr at 37°C, during which time the culture plates and MatTek dishes were shaken gently to facilitate antibody binding. After primary antibody incubation, the cells were gently washed with complete medium 4 times for 30 sec each time. The secondary antibodies, 6-nm gold-conjugated goat anti-human IgG or protein G, were then added to the medium directly at 1:20 dilution of the original stock solutions (10–20 μg/ml) and allowed to incubate for 1.5 hr. Washes were repeated as described above after secondary antibody incubation. Cells on Aclar disks were washed twice with PBS and then fixed with 2.5% glutaraldehyde in 0.1 M phosphate buffer (pH 7.4) for conventional transmission electron microscopy examination. Cells on the gold Quantifoil TEM grids were plunge-frozen immediately after the final wash with culture medium.

Immunogold Labeling Controls

Primary Antibody Specificity Control

HT1080 cells transfected with only HIV-1 Gag were incubated with anti-tetherin antiserum and 6-nm gold particles conjugated with secondary antibodies, as described above. Following immunogold labeling, cells were fixed for conventional electron microscopy examination. The HT1080 cell line does not constitutively express tetherin [34]; therefore, one would not expect to see immunogold labeling in the absence of exogenous tetherin.

Capping and Patching Control

To test whether capping and patching occurred during the labeling process, we performed immunogold labeling of tetherin on transfected, chemically fixed HT1080 cells. The labeling was done following standard pre-embedding immunogold protocols [41].

Conventional TEM Sample Preparation and Imaging

Fixed cells on Aclar disks were washed twice with 0.1 M phosphate buffer (pH 7.4) after overnight fixation with 2.5% glutaraldehyde in the same buffer. Cells were then post-fixed with 1% osmium tetroxide in 0.1 M phosphate buffer (pH 7.4) for 1 hr. Following graded ethanol dehydration, cells were infiltrated, embedded, and then polymerized in Eponate 12 resin (Ted Pella Inc., Redding, CA).

Ultrathin sections were cut using a Leica Ultracut S ultramicrotome at a thickness of 70 nm. Sections were then stained with 5% uranyl acetate and 2% lead citrate and imaged on a Hitachi H-7500 transmission electron microscope (TEM, Hitachi High-Technologies, Japan) equipped with a SIA L12C 16-megapixel CCD camera (SIA, Duluth, GA) or a JEOL JEM-1400 TEM (JEOL Ltd., Japan) equipped with a Gatan US1000 2k×2k CCD camera (Gatan, Pleasanton, CA).

Cryo-TEM Sample Preparation, Imaging, and Image Processing

Prior to sample vitrification, a 4-µl aliquot of 10- or 20-nm gold nanoparticles (Sigma-Aldrich) was applied to the surface of the TEM grid. These gold nanoparticles were used for image alignment in the 3D tomographic reconstruction process [42, 43]. Cells cultured on the gold Quantifoil TEM grids were vitrified by rapid immersion in liquid ethane using a Gatan CryoPlunger3 (Cp3) apparatus. Cryo-grids were transferred to a Gatan 914 high-tilt holder maintained at -178°C. Cryo-specimens were imaged with JEOL JEM-2200FS 200-kV field emission gun transmission electron microscope equipped with an in-column Omega energy filter (slit width 20 eV) and a Gatan US4000 4k×4k CCD camera. Polygon montages and tilt series were acquired using SerialEM software [44]. A single-axis tilt series was collected over an angular range of -62° to 62°, with a 2° tilt increment. The total electron dose applied to the specimens did not exceed 120–150 $e^-/Å^2$. Tilt series images were acquired at 30,000× nominal magnification (calibrated pixel size of 0.737 or 0.764 nm) with -4 to -8-µm defocus applied. Tomographic reconstructions were generated with IMOD using the r-weighted back-projection algorithm [42, 43].

RESULTS AND DISCUSSION

The rationale for this study was to develop a strategy for the improved identification of the 3D localization patterns of membrane-bound proteins associated with enveloped virus-infected cells while retaining structural information at a macromolecular resolution (2–10 nm). First, we examined tetherin placement at sites of HIV-1 VLP and HIV-1 virus assembly and release using HT1080 cells. Second, we studied hRSV F glycoprotein location and order using hRSV-infected HEp-2 and HeLa cells. In order to achieve our aims, we used a native immunolabeling process followed by rapid sample vitrification methods or chemical fixation and conventional TEM specimen processing that allowed for the proteins, viral particles, and cells to remain whole and well preserved.

In the protocol, each protein-specific primary antibody was applied to the cultured cells and allowed to incubate for 1.5 hr while the cells were maintained at 37°C with 5% CO_2. The specimens were gently washed and then incubated with a 6-nm gold-conjugated secondary antibody for 1.5 hr at 37°C with 5% CO_2. As with the studies of vaccinia virus assembly by Roos *et al.* (1996) [22], it was necessary to use gold-conjugated secondary antibodies as an electron-dense marker in order to resolve the locations of the primary antibodies and target proteins along the cell and viral surfaces.

Targeted Labeling of Cellular and Viral Proteins

We sought to determine whether a native-immunolabeling approach would be specific to the protein targets of interest. We therefore examined the method as applied to the immunolabeling of tetherin on HIV-1 and tetherin co-transfected HT1080 cells. It has been well established that tetherin, an interferon-induced protein, when expressed, functions to inhibit the release of HIV-1 and other enveloped viruses [45-49]. In addition, multiple immunofluorescence microscopy studies as well as conventional and immuno-TEM experiments have shown that tetherin and budding HIV-1 VLPs

and HIV-1 viruses localize in specific domains along the plasma membrane [38, 41, 50-52]. However, many of the previous imaging experiments incorporated chemical fixation, which subsequently may have altered or compromised the ultrastructure of the cells and viruses, as well as the structure of the labeled target protein complexes. Cryo-EM imaging of the unfixed tetherin immunolabeled HT1080 cells highlighted the presence of 6-nm gold clusters at HIV-1 VLP and HIV-1 virus assembly and budding sites along the cellular plasma membrane (Figures 1, 2). A similar distribution profile of immunolabeled tetherin was present on HT1080 cells that were native-immunolabeled and subsequently chemically fixed and processed for conventional TEM (Figure 3). The black arrowheads in Figures 1-3 and Supplementary Figure 1A and 1B indicate a subset of the 6-nm gold clusters in the image field that are associated with immunolabeled tetherin. All of the 6-nm gold clusters are linked with tetherin on the cell plasma membrane, between the cell plasma membrane and HIV-1 VLPs and virions, or between extended networks of HIV-1 VLPs and virions.

Capping and patching was reported in late 1970s for some membrane proteins when bivalent binding molecules, such as immunoglobulin, were applied to the live cells [29, 30]. It was speculated that the cross-linking effect of immunoglobulin caused the proteins to redistribute within the plasma membrane and form either multiple patches or a single cap. This rearrangement of the proteins could potentially inhibit the determination of native membrane protein distribution patterns. We therefore examined whether aggregates of antibodies noted by unusual gold particle localization patterns, i.e., patches or caps, were present on the cell surfaces of the native-immunolabeled specimens, as compared with conventionally processed samples. If this phenomenon were present, it would obscure the identification of tetherin-rich regions along the plasma membrane and at sites of virus assembly and budding. We determined that antibody-induced capping and patching did not

occur, because, in images of both the native-immunolabeled and conventionally processed specimens, the distribution of antibody immunolabeling was equivalent (Supplementary Figure 1A, 1B). We also assessed the level of immunolabeling specificity; here, we did not transfect the cells with tetherin but followed with the native-immunolabeling procedure and standard processing steps. The absence of tetherin in the cells resulted in the complete loss of tetherin labeling (Supplementary Figure 1C).

We then examined another distinct biological system to validate the performance of the native-immunolabeling protocols. Here, we wished to resolve the presence and arrangement of the hRSV F glycoprotein on virus particle assembly and budding from HeLa and HEp-2 cells. HRSV presents three surface glycoproteins: the fusion (F) and the attachment (G) glycoproteins, and the small hydrophobic (SH) protein, which is significantly smaller in size [53]. The two major glycoproteins (F and G) work in concert to establish and maintain an active infection in host cells; explicitly, the epithelial cells of the lower respiratory tract. HRSV is a major viral pathogen that causes acute lower respiratory tract infections mainly in infants, young children, and immunosuppressed adults [54]. To combat the virus, a series of neutralizing antibodies have been, and continue to be, developed against both glycoproteins. Currently, only one that targets the F glycoprotein is used in the prevention of hRSV infections in high-risk cases, palivizumab [36, 37]; it is this antibody that we used for our analyses. Cryo-EM and cryo-ET imaging of hRSV particles revealed both unlabeled and immunolabeled glycoproteins along the entire length of viral filaments and at sites of virus assembly at the cell plasma membrane (Figures 4, 5; Supplementary Figure 2). The immunolabeling of the hRSV F glycoprotein was consistent with that which has been previously reported. The hRSV F glycoprotein, when labeled for direct stochastic optical reconstruction microscopy (dSTORM) imaging, was present along the length of viral filaments [40], which is consistent with our results.

However, at EM-level resolution, where we are able to resolve the individual glycoproteins [55, 56], we expected to find the distribution of the immunolabeled F glycoproteins to be impacted by: (1) the ratio and organization of the F and G glycoproteins on the virus, and (2) the steric hindrance/accessibility associated with the primary and 6-nm gold-conjugated secondary antibody with the F glycoprotein antigenic site II [57]. The native immunolabeling of the hRSV F glycoprotein underscores this level of glycoprotein organization (Figures 4, 5; Supplementary Figure 2). We examined whether employing different secondary antibodies would alter immunolabeling efficiency and the distribution of the gold particles. No variability in label distribution was noted when either the 6-nm gold-conjugated goat anti-human IgG or protein G was applied (Supplementary Figure 2). Conventional TEM processing and imaging of samples post-immunolabeling disclosed comparable labeling efficiencies and arrangements of the 6-nm gold clusters along hRSV viral filaments and at the hRSV assembly sites along the plasma membrane (Figure 6).

Preservation of Cellular Ultrastructure

One significant compromise researchers make when immunolabeling a specimen for EM is with respect to ultrastructure preservation. Most protocols require chemical fixation using either paraformaldehyde or a combination of paraformaldehyde and glutaraldehyde and, in some cases, post-fixation with osmium tetroxide, in order to stop biological activity and stabilize cell architecture. However, chemical fixation might disrupt antigenicity of the target macromolecules and may alter the cellular ultrastructure. Therefore, we examined the 2D projection images and 3D reconstructions of the cells and viruses to address whether the native immunolabeling technique would inadvertently deteriorate the stability of known cellular and viral structures. In all cryo-preserved samples of the HIV-1 cDNA and tetherin co-transfected HT1080 cells, cellular structures,

such as membranes, the cytoskeleton, intracellular vesicles, and macromolecular complexes were intact and well preserved (Figures 1, 2). The morphology and architecture of the native-immunolabeled cryo-preserved cells was comparable to unlabeled cells also preserved by vitrification [data not shown and [58]]. In particular, long tracts and extended networks of actin filaments were well resolved in the areas associated with HIV-1 virus assembly, budding, and restriction (Figure 2). We also studied the images and 3D volumes of the cryo-preserved hRSV-infected HeLa cells and determined that cellular structures were intact and consistent with those of unlabeled cells (Figure 5). As with the HT1080 cells, HeLa cells also contained extensive actin networks and distinct cell membranes, a hallmark of well-preserved cellular structure.

Three-Dimensional Structure and Localization Information

The main rationales behind the development and application of this native-immunolabeling approach for cells and virus-infected cells were to: 1) rapidly identify regions of interest on a cell, 2) determine the 3D spatial relationships between the immunolabeled entity and other macromolecular complexes, and 3) retain cellular and viral ultrastructural integrity. We used 2D cryo-EM imaging to quickly pinpoint regions of importance and cryo-ET to generate 3D volumes of released viruses and the virus-transfected or virus-infected cells. The gold labels were critical for locating sections of the grids with labeled virus, in the case of hRSV (Figure 4), or regions of the cells where viral particles were assembling (Figures 4, 5) or for HIV-1 association with tetherin (Figures 1, 2). The 6-nm gold particle conjugates used for immunolabeling the target proteins could be clearly differentiated from the 10-nm or 20-nm gold particles used for cryo-ET image alignment (Figures 2, 5; Supplementary Figure 2).

In our analysis of the 3D volumes of the tetherin-labeled HIV-1 cDNA and tetherin co-transfected HT1080 cells, we were able to identify and assess the nature of tetherin along the plasma membrane. As has been reported previously, we show that tetherin-enriched regions resided as discrete areas, or microdomains, on the plasma membrane [41, 50]. The tetherin-containing regions were also closely associated with regions of HIV-1 VLP and virus assembly and budding. Immunolabeled tetherin macromolecules were resolved as small fibrous extensions on the cell membrane, between the cell membrane and viral particles, and between viral particles (Figure 2). Characteristic HIV-1 VLP and virus particle structures were preserved in all samples examined [59-63]. HIV-1 VLPs ranged from 78 nm to 182 nm in diameter (mean ± SD, 115 nm ± 20; n=178) and contained highly ordered regions of the Gag lattice (Figure 1). Both immature Gag-containing and mature, cored HIV-1 virus particles were observed bound to the plasma membrane of the HT1080 cells by filamentous extensions (Figure 2).

We examined the 3D volumes of the hRSV viral filaments and hRSV-infected cells immunolabeled for the F glycoprotein to determine: 1) the location and organization of the F glycoprotein on the viral filaments, 2) the relationship between the F glycoprotein and other hRSV structural proteins located in the interior of the viral filaments, and 3) discrete sites of virus assembly on the cell surface. The placement of the immunolabeled hRSV F glycoproteins was easily determined both along extending viral filaments (Figure 4) and at sites of assembly (Figure 5). The arrangement of the hRSV F glycoprotein along viral filaments was consistent with that which has been reported previously [55, 56]. The matrix protein and ribonucleoprotein (RNP) complex were also resolved along the viral membrane in close proximity to the glycoproteins (Figure 4) [55, 56]. Native immunolabeling of the hRSV F glycoprotein also proved useful for identifying the location of an early stage of virus assembly (Figure 5). Studies of this early event will play a significant role in our

understanding of the coordination of hRSV viral proteins during assembly and subsequent budding at the plasma membrane. 2D cryo-EM imaging allowed us to locate a small patch of 6-nm gold particles on the plasma membrane of an hRSV-infected HeLa cell (Figure 5A). The 3D tomographic reconstruction revealed the hRSV glycoproteins on the membrane surface and the matrix protein and the RNP complex coalescing under the membrane. Actin filaments were also visualized in the cell cytoplasm beneath areas containing the viral proteins. Results from the hRSV experiments highlight that native immunolabeling of surface proteins provides guidance for cryo-ET data collection; in this case, assistance for locating the early stages of hRSV assembly.

In summary, we have demonstrated the practicality of a native-immunolabeling approach for cells and virus-infected or virus-transfected cells that can be used for both cryo-EM and conventional EM strategies. This methodology provides a rapid means for immunolabeling proteins and protein complexes present on the membranes of cells and viruses. The ultrastructure of the immunolabeled cells was retained to high fidelity, contrary to conventional immunolabeling strategies. When the cryo-preserved labeled specimens were imaged by cryo-EM, the regions of interest were readily identified and the 3D spatial relationships between specific complexes were determined at macromolecular resolution. Immunolabeled specimens that were processed for conventional TEM also retained plasma membrane integrity, cytoplasm and cytoskeleton organization, and virus architecture.

In this study, we used 'indirect' immunolabeling, whereby a gold particle-conjugated secondary antibody was applied. To further expand the utility of native immunolabeling for correlative imaging from light microscopy to electron microscopy, fluorescently labeled secondary antibodies conjugated with gold particles could be employed. This strategy would facilitate the light microscopic

identification of specific cells grown on a substrate prior to sample preservation for cryo-TEM or scanning electron microscopy (SEM) imaging. In addition, future investigations to improve the method will include employing gold-conjugated primary antibodies to 'directly' immunolabel the target and the use of smaller gold particles to minimize size-associated steric hindrances.

The focus of this study was to investigate the localization patterns of proteins and complexes present on the membrane surfaces of cells and virus-infected or virus-transfected cells. Further improvements and advancements are required for the targeted native-state, electron-dense labeling of macromolecules within the interior of cells and viruses. Current conventional, pre-embedding immunolabeling methods of whole cells generally necessitate the permeabilization of the plasma membrane for the introduction of antibodies and marker-conjugated antibodies into the cell cytoplasm [64]. However, the process of permeabilizing the plasma membrane may alter membrane integrity or cell ultrastructure, neither of which is ideal for cryo-EM structural studies. Consequently, several approaches are under development and incorporate the use of ferritin [65], quantum dots [66], or metallothionein [67-69] fusion constructs for the targeted labeling of macromolecules. However, even though each technique has shown promise in specific biological instances, none have been widely used in cryo-EM analyses due to incompatibilities with cell types, inability of the target protein to assemble properly, or cytotoxicity associated with the reagents. Concurrent with the exploration of electron-dense probes for cryo-EM, high-precision correlative light and electron microscopy (CLEM) approaches have been realized [70-72]. These advances may have eliminated some of the need for using an electron-dense marker to determine the placement of complexes within a cell. However, immunolabeling with electron-dense markers will remain an essential tool for all areas of electron microscopy because it permits the assessment of interactions between complexes at resolutions not readily achievable by fluorescence microscopy.

Finally, we did not computationally 'remove' gold particles from the 2D images or 3D reconstructions [42]. This approach, combined with the use of smaller gold particles may be advantageous for improved 3D structure interpretation. Due to the utility and easy implementation of the method we have described for labeling thicker biological specimens, such as whole mammalian cells, for cryo-EM investigations, we believe it will be an advantageous technique for ultrastructural analyses of many cellular systems.

ACKNOWLEDGEMENTS

We thank Ms. Jeannette Taylor of the Emory University Robert P. Apkarian Integrated Electron Microscopy Core for assistance.

FUNDING

The authors disclosed receipt of the following financial support for the research, authorship, and/or publication of this article: This work was supported in part by Emory University, Children's Healthcare of Atlanta, the Center for AIDS Research at Emory University (P30 AI050409), and the Georgia Research Alliance to E.R.W.; NSF grant 0923395 to E.R.W; the James B. Pendleton Charitable Trust to P.W.S. and E.R.W.; and public health service grants F32GM112517 to J.D.S, AI101775 to E.R.W., and AI058828 and S10 RR025679 to P.W.S.

REFERENCES

1. Taylor, K. A. and Glaeser, R. M. Electron-diffraction of frozen, hydrated protein crystals. *Science*, 1974. **186**(4168): p. 1036-1037.
2. Lepault, J., Booy, F. P., and Dubochet, J. Electron-microscopy of frozen biological suspensions. *J Microsc*, 1983. **129**(JAN): p. 89-102.
3. Dubochet, J., Adrian, M., Chang, J. J., Homo, J. C., Lepault, J., McDowall, A. W., and Schultz, P. Cryo-electron microscopy of vitrified specimens. *Q Rev Biophys*, 1988. **21**(2): p. 129-228.
4. Heide, H. G. and Grund, S. Deep-cooled chain for transfer of hydrated biological-material in electron-microscope. *J Ultrastruct Res*, 1974. **48**(2): p. 259-268.
5. Jeng, T. W. and Chiu, W. High-resolution cryo system designed for JEM 100CX electron-microscope. *Ultramicroscopy*, 1987. **23**(1): p. 61-66.
6. Taylor, K. A., Milligan, R. A., Raeburn, C., and Unwin, P. N. T. A cold stage for the Philips EM300 electron-microscope. *Ultramicroscopy*, 1984. **13**(3): p. 185-189.
7. McDowall, A. W., Smith, J. M., and Dubochet, J. Cryoelectron microscopy of vitrified chromosomes *in situ*. *EMBO J*, 1986. **5**(6): p. 1395-1402.
8. Frank, J., Radermacher, M., Wagenknecht, T., and Verschoor, A. A new method for 3-dimensional reconstruction of single macromolecules using low-dose electron-micrographs. *Ann N Y Acad Sci*, 1986. **483**: p. 77-87.
9. Adrian, M., Dubochet, J., Lepault, J., and McDowall, A. W. Cryo-electron microscopy of viruses. *Nature*, 1984. **308**(5954): p. 32-36.
10. Milne, J. L. S. and Subramaniam, S. Cryo-electron tomography of bacteria: Progress, challenges and future prospects. *Nat Rev Microbiol*, 2009. **7**(9): p. 666-675.

11. Dierksen, K., Typke, D., Hegerl, R., Walz, J., Sackmann, E., and Baumeister, W. 3-dimensional structure of lipid vesicles embedded in vitreous ice and investigated by automated electron tomography. *Biophys J*, 1995. **68**(4): p. 1416-1422.

12. Guerrero-Ferreira, R. C. and Wright, E. R. Cryo-electron tomography of bacterial viruses. *Virology*, 2013. **435**(1): p. 179-186.

13. Koning, R. I. and Koster, A. J. Cryo-electron tomography in biology and medicine. *Ann Anat*, 2009. **191**(5): p. 427-445.

14. Koster, A. J., Chen, H., Sedat, J. W., and Agard, D. A. Automated microscopy for electron tomography. *Ultramicroscopy*, 1992. **46**(1-4): p. 207-227.

15. Subramaniam, S., Bartesaghi, A., Liu, J., Bennett, A. E., and Sougrat, R. Electron tomography of viruses. *Curr Opin Struct Biol*, 2007. **17**(5): p. 596-602.

16. Briggs, J. A. G. Structural biology *in situ* - the potential of subtomogram averaging. *Curr Opin Struct Biol*, 2013. **23**(2): p. 261-267.

17. Campbell, M. G., Veesler, D., Cheng, A., Potter, C. S., and Carragher, B. 2.8 angstrom resolution reconstruction of the *Thermoplasma acidophilum* 20S proteasome using cryo-electron microscopy. *eLife*, 2015. **4**.

18. Jiang, J., Pentelute, B. L., Collier, R. J., and Zhou, Z. H. Atomic structure of anthrax protective antigen pore elucidates toxin translocation. *Nature*, 2015. **521**(7553): p. 545-U323.

19. Schur, F. K. M., Hagen, W. J. H., Rumlova, M., Ruml, T., Mueller, B., Kraeusslich, H.-G., and Briggs, J. A. G. Structure of the immature HIV-1 capsid in intact virus particles at 8.8 angstrom resolution. *Nature*, 2015. **517**(7535): p. 505-508.

20. Lucic, V., Rigort, A., and Baumeister, W. Cryo-electron tomography: The challenge of doing structural biology *in situ*. *J Cell Biol*, 2013. **202**(3): p. 407-419.

21. Beck, M., Lucic, V., Foerster, F., Baumeister, W., and Medalia, O. Snapshots of nuclear pore complexes in action captured by cryo-electron tomography. *Nature*, 2007. **449**(7162): p. 611-615.

22. Roos, N., Cyrklaff, M., Cudmore, S., Blasco, R., KrijnseLocker, J., and Griffiths, G. A novel immunogold cryoelectron microscopic approach to investigate the structure of the intracellular and extracellular forms of vaccinia virus. *EMBO J*, 1996. **15**(10): p. 2343-2355.

23. Wu, S., Avila-Sakar, A., Kim, J., Booth, D. S., Greenberg, C. H., Rossi, A., Liao, M., Li, X., Alian, A., Griner, S. L., Juge, N., Yu, Y., Mergel, C. M., Chaparro-Riggers, J., Strop, P., Tampe, R., Edwards, R. H., Stroud, R. M., Craik, C. S., and Cheng, Y. Fabs enable single particle cryoem studies of small proteins. *Structure*, 2012. **20**(4): p. 582-592.

24. Bartesaghi, A., Merk, A., Banerjee, S., Matthies, D., Wu, X., Milne, J. L., and Subramaniam, S. 2.2 Å resolution cryo-em structure of beta-galactosidase in complex with a cell-permeant inhibitor. *Science*, 2015. **348**(6239): p. 1147-51.

25. Dutta, M., Liu, J., Roux, K. H., and Taylor, K. A. Visualization of retroviral envelope spikes in complex with the V3 loop antibody 447-52D on intact viruses by cryo-electron tomography. *J Virol*, 2014. **88**(21): p. 12265-12275.

26. Harris, A. K., Bartesaghi, A., Milne, J. L. S., and Subramaniam, S. HIV-1 envelope glycoprotein trimers display open quaternary conformation when bound to the gp41 membrane-proximal external-region-directed broadly neutralizing antibody Z13e1. *J Virol*, 2013. **87**(12): p. 7191-7196.

27. Lin, J., Cheng, N., Hogle, J. M., Steven, A. C., and Belnap, D. M. Conformational shift of a major poliovirus antigen confirmed by immuno-cryogenic electron microscopy. *J Immunol*, 2013. **191**(2): p. 884-891.

28. Tran, E. E. H., Borgnia, M. J., Kuybeda, O., Schauder, D. M., Bartesaghi, A., Frank, G. A., Sapiro, G., Milne, J. L. S., and Subramaniam, S. Structural mechanism of trimeric HIV-1 envelope glycoprotein activation. *PLoS Pathog*, 2012. **8**(7).

29. Ash, J. F., Louvard, D., and Singer, S. J. Antibody-induced linkages of plasma-membrane proteins to intracellular actomyosin-containing filaments in cultured fibroblasts. *Proc Natl Acad Sci U S A*, 1977. **74**(12): p. 5584-5588.

30. Ferrante, A. and Thong, Y. H. Antibody induced capping and endocytosis of surface-antigens in *naegleria fowleri*. *Int J Parasitol*, 1979. **9**(6): p. 599-601.

31. McDonald, K. High-pressure freezing for preservation of high resolution fine structure and antigenicity for immunolabeling. *Methods Mol Biol*, 1999. **117**: p. 77-97.

32. Sawaguchi, A., McDonald, K. L., and Forte, J. G. High-pressure freezing of isolated gastric glands provides new insight into the fine structure and subcellular localization of H^+/K^+-ATPase in gastric parietal cells. *J Histochem Cytochem*, 2004. **52**(1): p. 77-86.

33. Schnell, U., Dijk, F., Sjollema, K. A., and Giepmans, B. N. G. Immunolabeling artifacts and the need for live-cell imaging. *Nat Methods*, 2012. **9**(2): p. 152-158.

34. Neil, S. J., Zang, T., and Bieniasz, P. D. Tetherin inhibits retrovirus release and is antagonized by HIV-1 Vpu. *Nature*, 2008. **451**(7177): p. 425-30.

35. Van Damme, N., Goff, D., Katsura, C., Jorgenson, R. L., Mitchell, R., Johnson, M. C., Stephens, E. B., and Guatelli, J. The interferon-induced protein BST-2 restricts HIV-1 release and is downregulated from the cell surface by the viral vpu protein. *Cell Host Microbe*, 2008. **3**(4): p. 245-252.

36. Group, T. I.-R. S. Palivizumab, a humanized respiratory syncytial virus monoclonal antibody, reduces hospitalization from respiratory syncytial virus infection in high-risk infants. *Pediatrics*, 1998. **102**(3): p. 531-537.

37. Johnson, S., Oliver, C., Prince, G. A., Hemming, V. G., Pfarr, D. S., Wang, S. C., Dormitzer, M., Ogrady, J., Koenig, S., Tamura, J. K., Woods, R., Bansal, G., Couchenour, D., Tsao, E., Hall, W. C., and Young, J. F. Development of a humanized monoclonal antibody (MEDI-493) with potent in vitro and in vivo activity against respiratory syncytial virus. *J Infect Dis*, 1997. **176**(5): p. 1215-1224.

38. Hammonds, J., Wang, J.-J., Yi, H., and Spearman, P. Immunoelectron microscopic evidence for tetherin/BST2 as the physical bridge between HIV-1 virions and the plasma membrane. *PLoS Pathog*, 2010. **6**(2).

39. Khan, M. A., Aberham, C., Kao, S., Akari, H., Gorelick, R., Bour, S., and Strebel, K. Human immunodeficiency virus type I Vif protein is packaged into the nucleoprotein complex through an interaction with viral genomic rna. *J Virol*, 2001. **75**(16): p. 7252-7265.

40. Alonas, E., Lifland, A. W., Gudheti, M., Vanover, D., Jung, J., Zurla, C., Kirschman, J., Fiore, V. F., Douglas, A., Barker, T. H., Yi, H., Wright, E. R., Crowe, J. E., Jr., and Santangelo, P. J. Combining single RNA sensitive probes with subdiffraction-limited and live-cell imaging enables the characterization of virus dynamics in cells. *ACS Nano*, 2014. **8**(1): p. 302-315.

41. Hammonds, J., Ding, L., Chu, H., Geller, K., Robbins, A., Wang, J.-J., Yi, H., and Spearman, P. The tetherin/BST-2 coiled-coil ectodomain mediates plasma membrane microdomain localization and restriction of particle release. *J Virol*, 2012. **86**(4): p. 2259-2272.

42. Kremer, J. R., Mastronarde, D. N., and McIntosh, J. R. Computer visualization of three-dimensional image data using IMOD. *J Struct Biol*, 1996. **116**(1): p. 71-76.

43. Mastronarde, D. N. Dual-axis tomography: An approach with alignment methods that preserve resolution. *J Struct Biol*, 1997. **120**(3): p. 343-352.

44. Mastronarde, D. N. Automated electron microscope tomography using robust prediction of specimen movements. *J Struct Biol*, 2005. **152**(1): p. 36-51.

45. Jouvenet, N., Neil, S. J. D., Zhadina, M., Zang, T., Kratovac, Z., Lee, Y., McNatt, M., Hatziioannou, T., and Bieniasz, P. D. Broad-spectrum inhibition of retroviral and filoviral particle release by tetherin. *J Virol*, 2009. **83**(4): p. 1837-1844.

46. Le Tortorec, A. and Neil, S. J. D. Antagonism to and intracellular sequestration of human tetherin by the human immunodeficiency virus type 2 envelope glycoprotein. *J Virol*, 2009. **83**(22): p. 11966-11978.

47. Mansouri, M., Viswanathan, K., Douglas, J. L., Hines, J., Gustin, J., Moses, A. V., and Frueh, K. Molecular mechanism of BST2/tetherin downregulation by K5/MIR2 of Kaposi's sarcoma-associated herpesvirus. *J Virol*, 2009. **83**(19): p. 9672-9681.

48. Radoshitzky, S. R., Dong, L., Chi, X., Clester, J. C., Retterer, C., Spurgers, K., Kuhn, J. H., Sandwick, S., Ruthel, G., Kota, K., Boltz, D., Warren, T., Kranzusch, P. J., Whelan, S. P. J., and Bavari, S. Infectious lassa virus, but not filoviruses, is restricted by BST-2/tetherin. *J Virol*, 2010. **84**(20): p. 10569-10580.

49. Sakuma, T., Noda, T., Urata, S., Kawaoka, Y., and Yasuda, J. Inhibition of lassa and marburg virus production by tetherin. *J Virol*, 2009. **83**(5): p. 2382-2385.

50. Billcliff, P. G., Rollason, R., Prior, I., Owen, D. M., Gaus, K., and Banting, G. CD317/tetherin is an organiser of membrane microdomains. *J Cell Sci*, 2013. **126**(7): p. 1553-1564.

51. Fitzpatrick, K., Skasko, M., Deerinck, T. J., Crum, J., Ellisman, M. H., and Guatelli, J. Direct restriction of virus release and incorporation of the interferon-induced protein BST-2 into HIV-1 particles. *PLoS Pathog*, 2010. **6**(3).

52. Lehmann, M., Rocha, S., Mangeat, B., Blanchet, F., Uji-i, H., Hofkens, J., and Piguet, V. Quantitative multicolor super-resolution microscopy reveals tetherin HIV-1 interaction. *PLoS Pathog*, 2011. **7**(12).

53. McLellan, J. S., Ray, W. C., and Peeples, M. E. Structure and function of respiratory syncytial virus surface glycoproteins, in *Challenges and opportunities for respiratory syncytial virus vaccines*, L.J. Anderson and B.S. Graham, Editors. 2013. p. 83-104.

54. Nair, H., Nokes, D. J., Gessner, B. D., Dherani, M., Madhi, S. A., Singleton, R. J., O'Brien, K. L., Roca, A., Wright, P. F., Bruce, N., Chandran, A., Theodoratou, E., Sutanto, A., Sedyaningsih, E. R., Ngama, M., Munywoki, P. K., Kartasasmita, C., Simoes, E. A. F., Rudan, I., Weber, M. W., and Campbell, H. Global burden of acute lower respiratory infections due to respiratory syncytial virus in young children: A systematic review and meta-analysis. *Lancet*, 2010. **375**(9725): p. 1545-1555.

55. Kiss, G., Holl, J. M., Williams, G. M., Alonas, E., Vanover, D., Lifland, A. W., Gudheti, M., Guerrero-Ferreira, R. C., Nair, V., Yi, H., Graham, B. S., Santangelo, P. J., and Wright, E. R. Structural analysis of respiratory syncytial virus reveals the position of M2-1 between the matrix protein and the ribonucleoprotein complex. *J Virol*, 2014. **88**(13): p. 7602-7617.

56. Liljeroos, L., Krzyzaniak, M. A., Helenius, A., and Butcher, S. J. Architecture of respiratory syncytial virus revealed by electron cryotomography. *Proc Natl Acad Sci U S A*, 2013. **110**(27): p. 11133-11138.

57. McLellan, J. S., Yang, Y., Graham, B. S., and Kwong, P. D. Structure of respiratory syncytial virus fusion glycoprotein in the postfusion conformation reveals preservation of neutralizing epitopes. *J Virol*, 2011. **85**(15): p. 7788-7796.

58. Strauss, J. D., Hammonds, J. E., Spearman, P. W., and Wright, E. R. Structural characterization of tethered HIV-1 VLPs by light microscopy and cryo-electron tomography. *Microsc Microanal*, 2014. **20**(S3): p. 1256-1257.

59. Benjamin, J., Ganser-Pornillos, B. K., Tivol, W. F., Sundquist, W. I., and Jensen, G. J. Three-dimensional structure of HIV-1 virus-like particles by electron cryotomography. *J Mol Biol*, 2005. **346**(2): p. 577-588.

60. Briggs, J. A. G., Gruenewald, K., Glass, B., Foerster, F., Kraeusslich, H. G., and Fuller, S. D. The mechanism of HIV-1 core assembly: Insights from three-dimensional reconstructions of authentic virions. *Structure*, 2006. **14**(1): p. 15-20.

61. Briggs, J. A. G., Riches, J. D., Glass, B., Bartonova, V., Zanetti, G., and Kraeusslich, H. G. Structure and assembly of immature HIV. *Proc Natl Acad Sci U S A*, 2009. **106**(27): p. 11090-11095.

62. Carlson, L.-A., Briggs, J. A. G., Glass, B., Riches, J. D., Simon, M. N., Johnson, M. C., Mueller, B., Gruenewald, K., and Kraeusslich, H.-G. Three-dimensional analysis of budding sites and released virus suggests a revised model for HIV-1 morphogenesis. *Cell Host Microbe*, 2008. **4**(6): p. 592-599.

63. Wright, E. R., Schooler, J. B., Ding, H. J., Kieffer, C., Fillmore, C., Sundquist, W. I., and Jensen, G. J. Electron cryotomography of immature HIV-1 virions reveals the structure of the CA and SP1 Gag shells. *EMBO J*, 2007. **26**(8): p. 2218-2226.

64. Hayat, M. A., *Immunogold-silver staining: Principles, methods, and applications*. 1995: CRC Press.

65. Wang, Q., Mercogliano, C. P., and Loewe, J. A ferritin-based label for cellular electron cryotomography. *Structure*, 2011. **19**(2): p. 147-154.

66. Gold, V. A. M., Ieva, R., Walter, A., Pfanner, N., van der Laan, M., and Kuehlbrandt, W. Visualizing active membrane protein complexes by electron cryotomography. *Nat Commun*, 2014. **5**.

67. Diestra, E., Fontana, J., Guichard, P., Marco, S., and Risco, C. Visualization of proteins in intact cells with a clonable tag for electron microscopy. *J Struct Biol*, 2009. **165**(3): p. 157-168.

68. Fernandez de Castro, I., Sanz-Sanchez, L., and Risco, C. Metallothioneins for correlative light and electron microscopy, in *Correlative Light and Electron Microscopy II*, T. MullerReichert and P. Verkade, Editors. 2014. p. 55-70.

69. Mercogliano, C. P. and DeRosier, D. J. Concatenated metallothionein as a clonable gold label for electron microscopy. *J Struct Biol*, 2007. **160**(1): p. 70-82.

70. Briegel, A., Chen, S., Koster, A. J., Plitzko, J. M., Schwartz, C. L., and Jensen, G. J. Correlated light and electron cryo-microscopy, in *Methods Enzymol*, G.J. Jensen, Editor. 2010. p. 317-341.

71. Jun, S., Ke, D., Debiec, K., Zhao, G., Meng, X., Ambrose, Z., Gibson, G. A., Watkins, S. C., and Zhang, P. Direct visualization of HIV-1 with correlative live-cell microscopy and cryo-electron tomography. *Structure*, 2011. **19**(11): p. 1573-1581.

72. Schorb, M. and Briggs, J. A. Correlated cryo-fluorescence and cryo-electron microscopy with high spatial precision and improved sensitivity. *Ultramicroscopy*, 2014. **143**: p. 24-32.

73. Schneider, C. A., Rasband, W. S., and Eliceiri, K. W. NIH image to ImageJ: 25 years of image analysis. *Nat Methods*, 2012. **9**(7): p. 671-5.

FIGURE LEGENDS

Figure 1. Cryo-electron tomography of immunolabeled-tetherin and HIV-1 virus-like particles (VLPs) attached to an HT1080 cell. (A) The central projection image from a tilt series of HIV-1 VLPs tethered to the edge of an HT1080 cell. Image was low-pass filtered using ImageJ (Gaussian blur, [73]). (B–D) Slices (7.64 nm) near the bottom (B), through the middle (C), and at the top (D) of the 3D reconstruction, showing a visible, ordered Gag lattice in the HIV-1 VLPs and immunogold-labeled tetherin located on the plasma membrane (D) and on HIV-1 VLPs (B–D), as indicated by black arrowheads. Cytoskeletal elements are visible, as indicated by white arrowheads in a 3D tomographic slice (D). Insets in (B–D) (black boxes) are 2× magnification. White asterisks indicate the immature HIV-1 Gag lattice in insets for panels (B) and (C). Gold fiducial markers, 20 nm in diameter, were added to the sample and used as image alignment aids during the 3D tomographic reconstruction process. Scale, 50 nm.

Figure 2. Cryo-electron tomography (Cryo-ET) of immunolabeled tetherin and HIV-1 virions attached to an HT1080 cell microspike. (A) Cryo-TEM 2D image montage of HIV-1 tethered to a thin HT1080 cell extension. The dashed white box highlights the area of enlargement in (B). (C and D) Slices (8.84 nm) through the 3D reconstruction; black arrowheads indicate immunogold-labeled tetherin located between HIV-1 virions and the plasma membrane. Preserved cytoskeletal elements are visible in the 2D images and the 3D tomographic slices, as indicated by white arrowheads. White asterisk was placed over typical mature HIV-1 conical cores in panel (C) and the inset for panel (D). Insets in (B–D) (black boxes) are 2× magnification. Gold fiducial markers, 20-nm in diameter, were added to the sample and used as image alignment aids during the 3D tomographic reconstruction process. Scale (A) 500 nm; (A) and (B–D) 100 nm.

Figure 3. Conventional transmission electron microscopy of native immunolabeled tetherin on HIV-1 VLPs and HIV-1 virions attached to HT1080 cells. (A and B) Low and high magnification images, respectively, of native immunolabeled tetherin on the plasma membrane of an HT1080 cell and HIV-1 VLPs. Black arrowheads point to immunogold labeling. (A and C) Actin filaments extend through the cell, as indicated by white arrowheads. (C and D) Low and intermediate magnification images, respectively, of native immunolabeled tetherin on the plasma membrane of an HT1080 cell and HIV-1 virions. Black arrowheads point to immunogold labeling. White asterisks are placed over the immature HIV-1 Gag lattice in the inset of panel (B). Black asterisks cover the mature HIV-1 conical core in the inset of panel (D). Insets in (A–D) (black boxes) are 2× magnification. Scale (A, C) 500 nm; (B, D) 200 nm.

Figure 4. Cryo-transmission electron microscopy and cryo-electron tomography of hRSV-infected HeLa cells with the hRSV F glycoprotein immunolabeled. (A) Low magnification montage of released, filamentous hRSV particles and a HeLa cell extension (white asterisk). (B and C) Higher magnification views of the montage in (A) highlighting immunolabeling of hRSV F along the viral filaments. (B–C) Dashed box (B) and solid box (C) are indicated in (A). (D) Slice (7.64 nm) from the 3D reconstruction of the area in (B) illustrating hRSV filaments with surface glycoproteins and immunogold (black arrowheads). Note the presence of ribonucleoprotein (RNP) in some of the viral filaments (white arrowheads). Insets in (C) and (D) (black boxes) are 2× magnification. Gold fiducial markers, 20 nm in diameter, were added to the sample and used as image alignment aids during the 3D tomographic reconstruction process. Scale (A) 2 μm; (B, C) 500 nm; (D) 200 nm.

Figure 5. Early hRSV assembly site detected by native immunolabeling. (A) 2D cryo-electron microscopy image of an hRSV assembly site; the 6-nm gold particles indicate the location of the

hRSV F glycoprotein (black arrowheads) at the upper surface of the plasma membrane. (B and C) Segmented 3D volume of the hRSV and cellular macromolecules. (B) Top view. (C) Cut-away and side view of (B) with 90° rotation applied. The cell membrane is presented in cyan. The filamentous actin network is noted in green. The matrix protein is depicted in blue. The glycoprotein densities are highlighted in magenta. Red tubular densities correspond to ribonucleoprotein (RNP). Gold densities are the 6-nm gold particles conjugated to the secondary antibody. (D–F) Slices (7.64 nm) through the reconstructed 3D volume showing the gold on the top (D, black arrowheads), a quarter-plane slice noting the hRSV viral proteins (E, white asterisk), and a bottom slice highlighting the actin filaments (F, white arrowheads). Inset in A is 2× magnification, insets in D-F are 1.5× magnification. Gold fiducial markers, 20 nm in diameter, were added to the sample and used as image alignment aids during the 3D tomographic reconstruction process. Scale (A, B, D–F) 200 nm; (C) 50 nm.

Figure 6. Conventional transmission electron microscopy (TEM) of hRSV with the native F glycoprotein immunolabeled. (A–C) Black arrowheads point to immunogold labeling along viral filaments both at assembly sites and of released hRSV filaments. (A) White arrowheads note actin filaments and the white asterisk points to a mitochondrion. (B) Assembling viral filament extended from the plasma membrane. (C) Intermediate magnification image of filamentous hRSV virion with immunogold labeling of the F glycoproteins. Inset in (A) is 3× magnification, insets in (B) and (C) are 2× magnification. Scale (A) 500 nm and (B and C) 200 nm.

Supplementary Figure 1. Conventional TEM of immunolabeling controls for tetherin. (A) Native immunolabeled HT1080 cells, transfected with eGFP-tetherin and mCherry-Gag. (B) Capping control of immunolabeled HT1080 cells transfected with eGFP-tetherin and mCherry-Gag. Cells

were fixed prior to incubation with antibodies. (C) Tetherin antibody control, immunolabeled HT1080 cells transfected only with mCherry-Gag. Note the absence of tetherin immunolabeling. (A-C) Black arrowheads note 6 nm gold particles. Insets in A, B and C (black boxes) are 2X. Scale bars 200 nm.

Supplementary Figure 2. HRSV F glycoprotein secondary antibody labeling control. Comparison of 2D cryo-TEM images (A and C) and slices (B: 7.37 nm and D: 7.64 nm) through the 3D reconstructions (B and D) of native immunolabeled hRSV F glycoproteins. (A and B) The secondary antibody was a 6 nm gold-conjugated protein G and (C and D) was 6 nm gold-conjugated goat anti-human IgG. Arrowheads indicate immunogold labeling of the hRSV F glycoprotein. Insets are 2X. Gold fiducial markers 10 nm (A and B) or 20 nm (C and D) in diameter were added to the sample and used as image alignment aids during the 3D tomographic reconstruction process. Scale bars 200 nm.

Figure 1

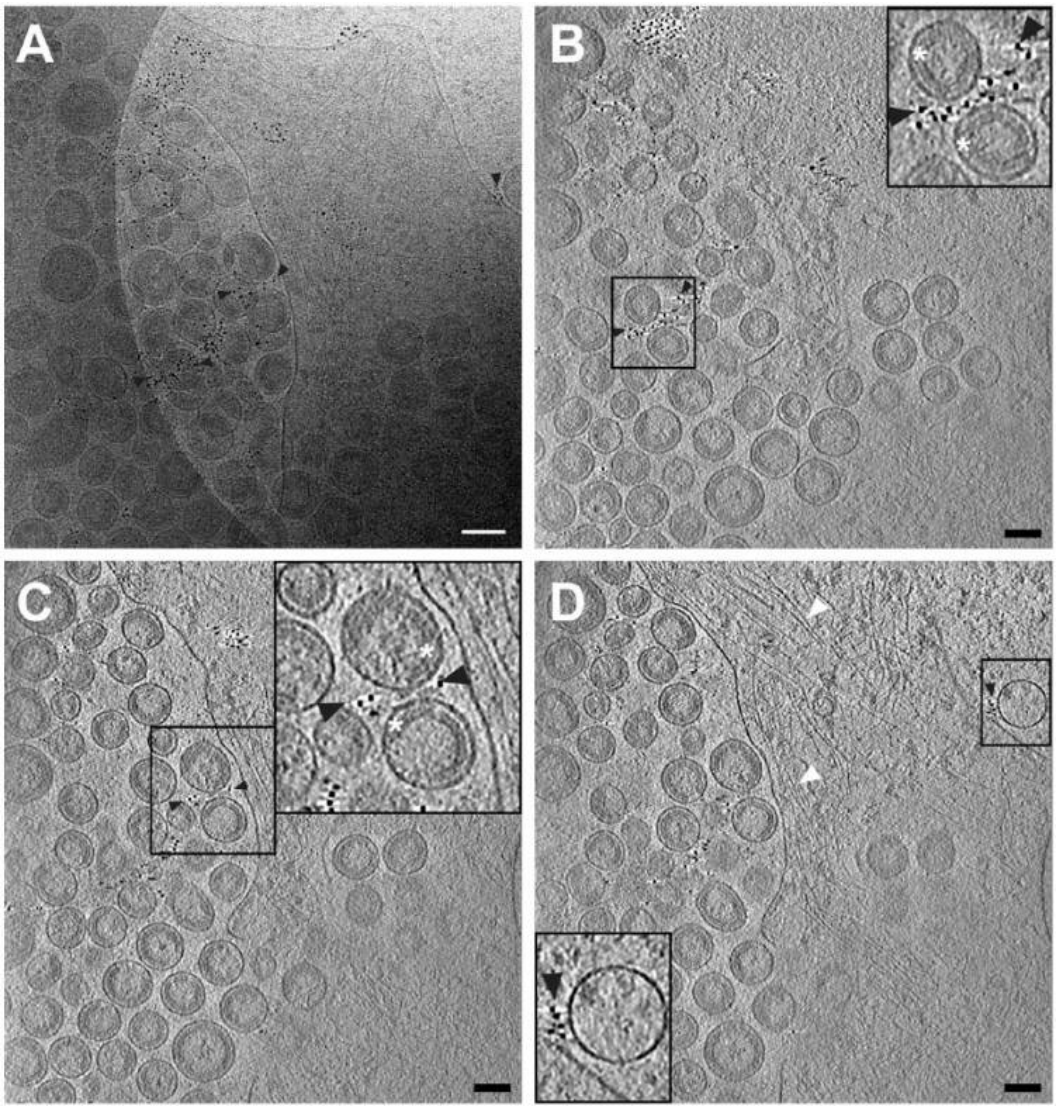

Figure 2

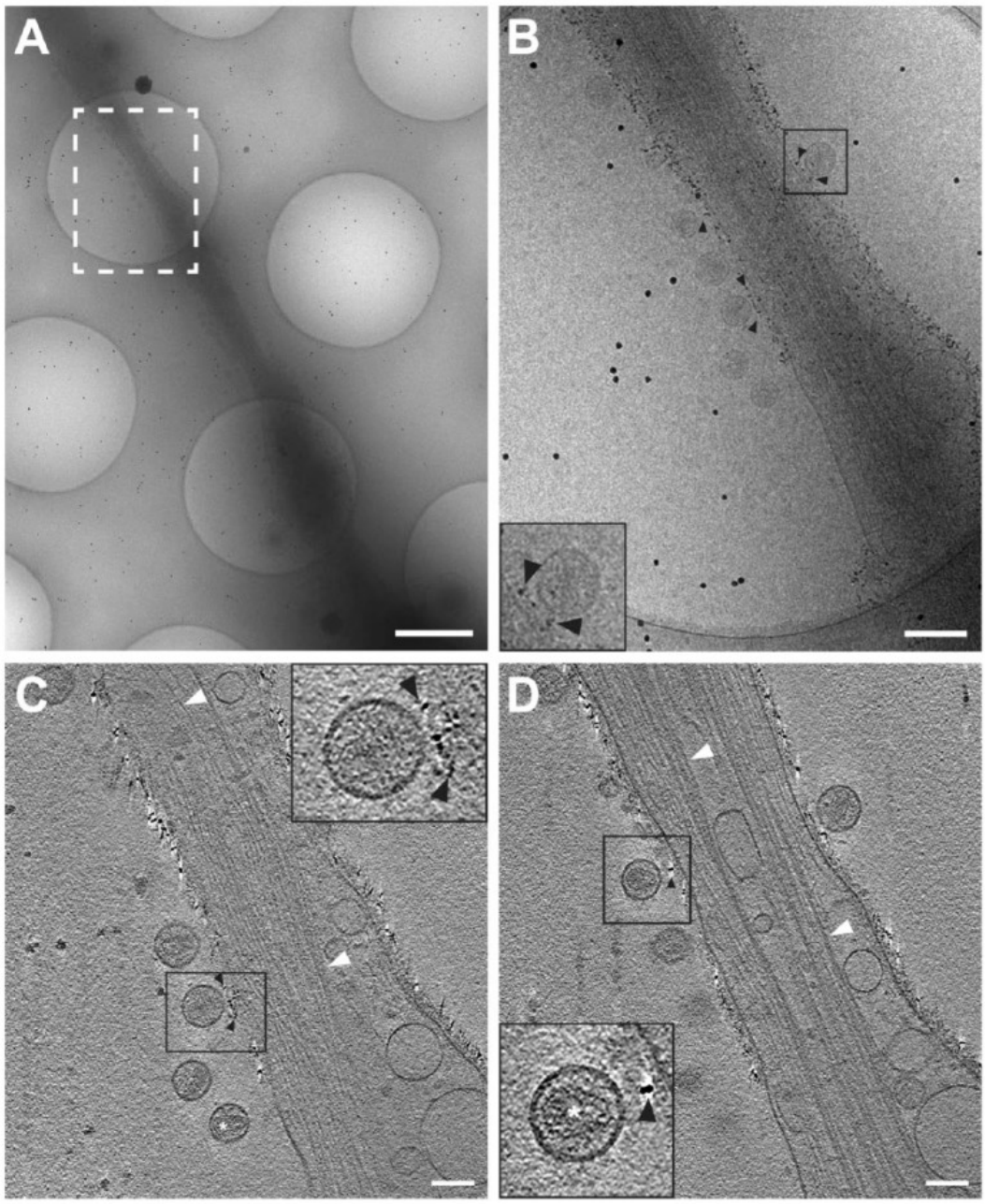

Figure 3

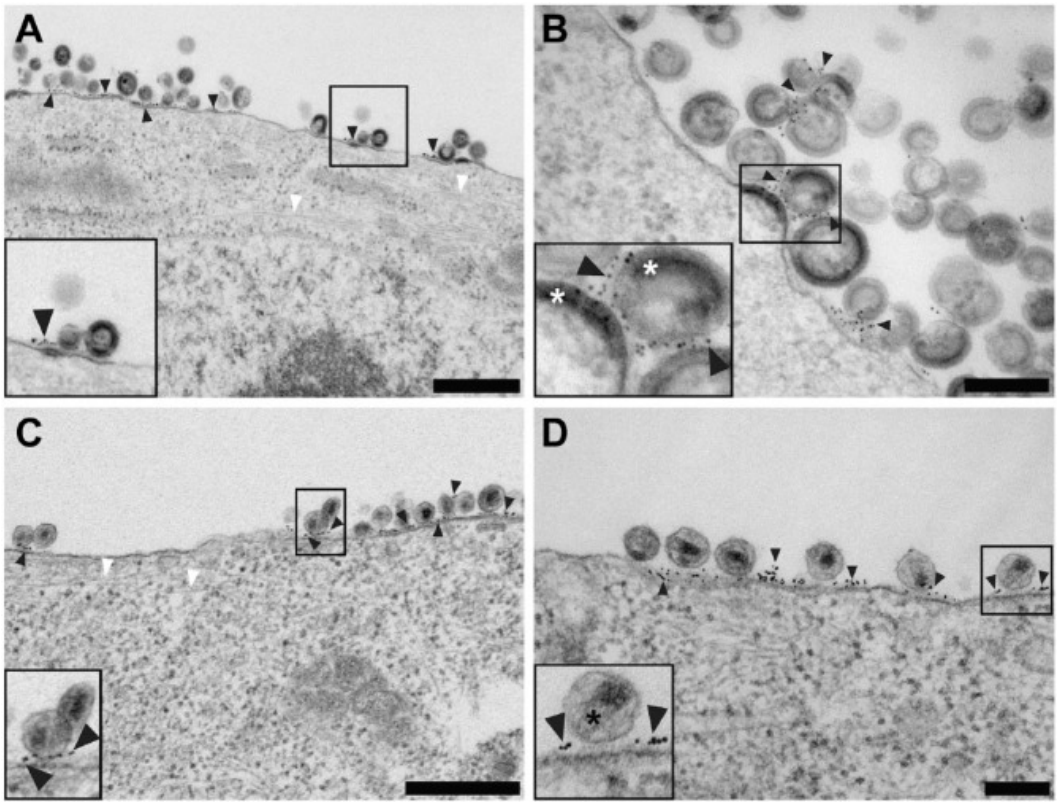

Figure 4

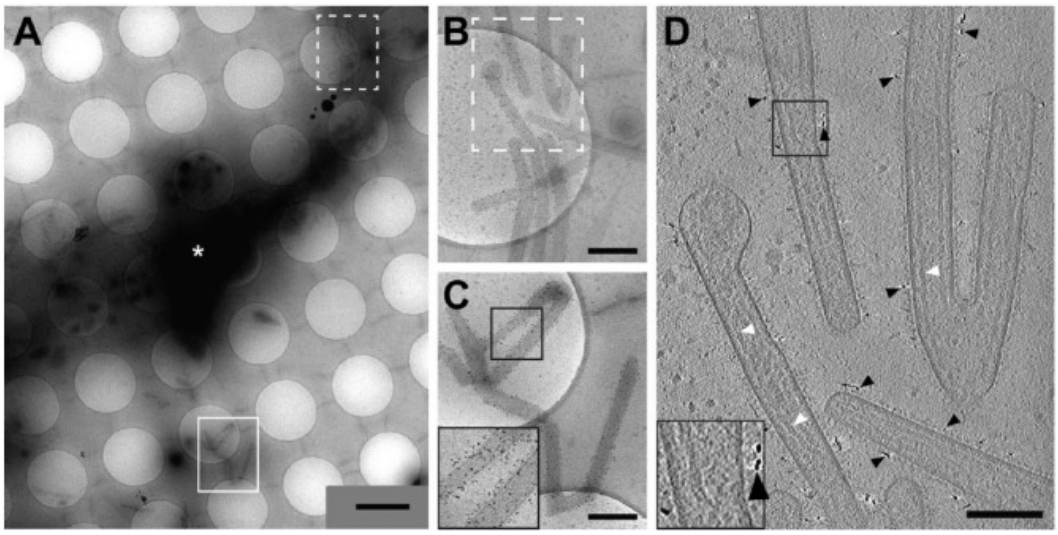

Figure 5

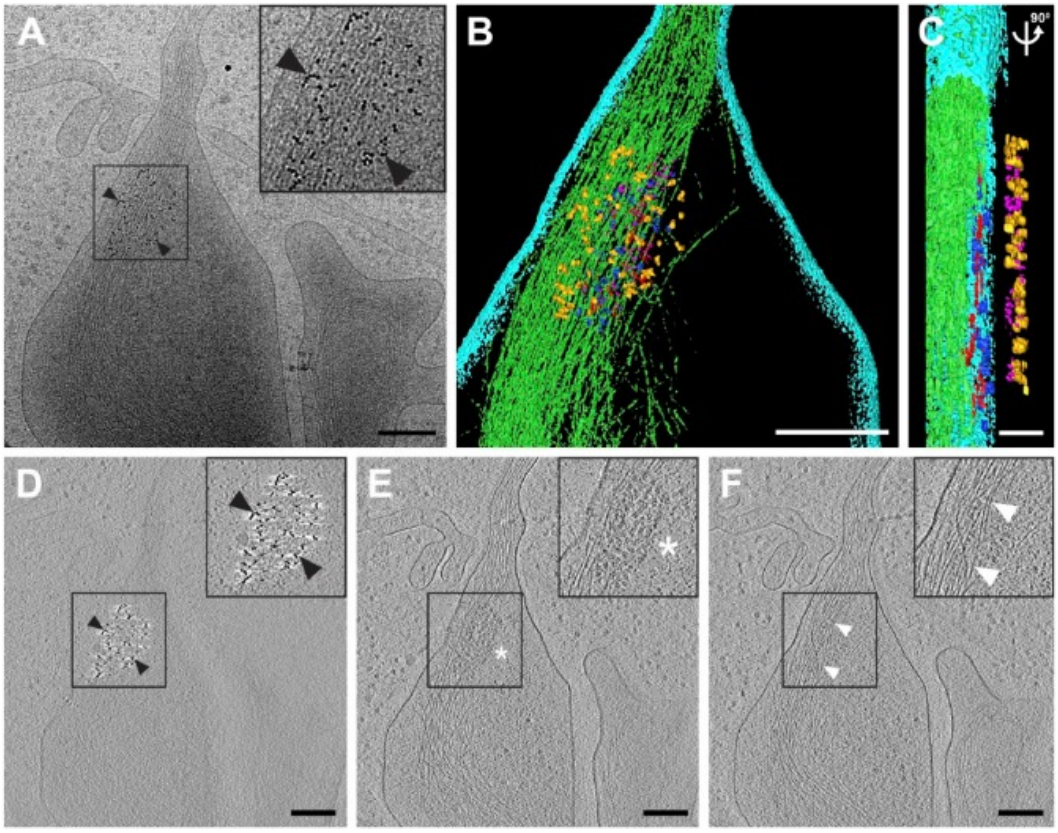

Figure 6

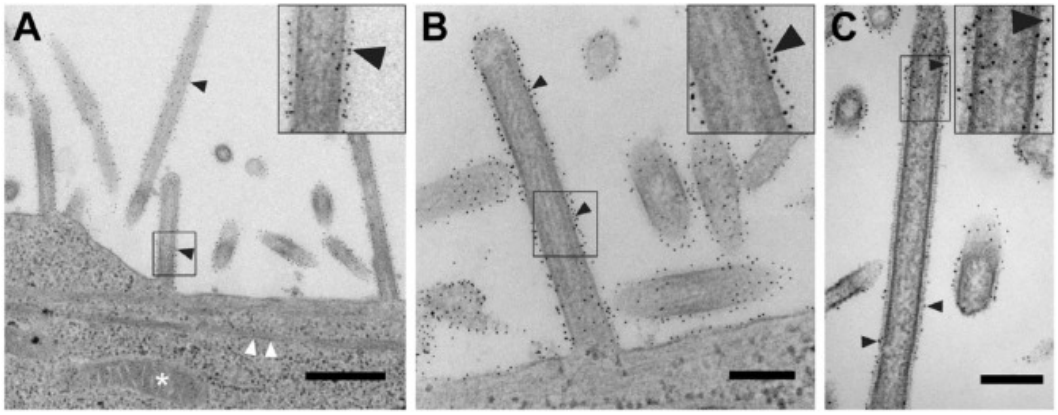

Supplementary Figure 1

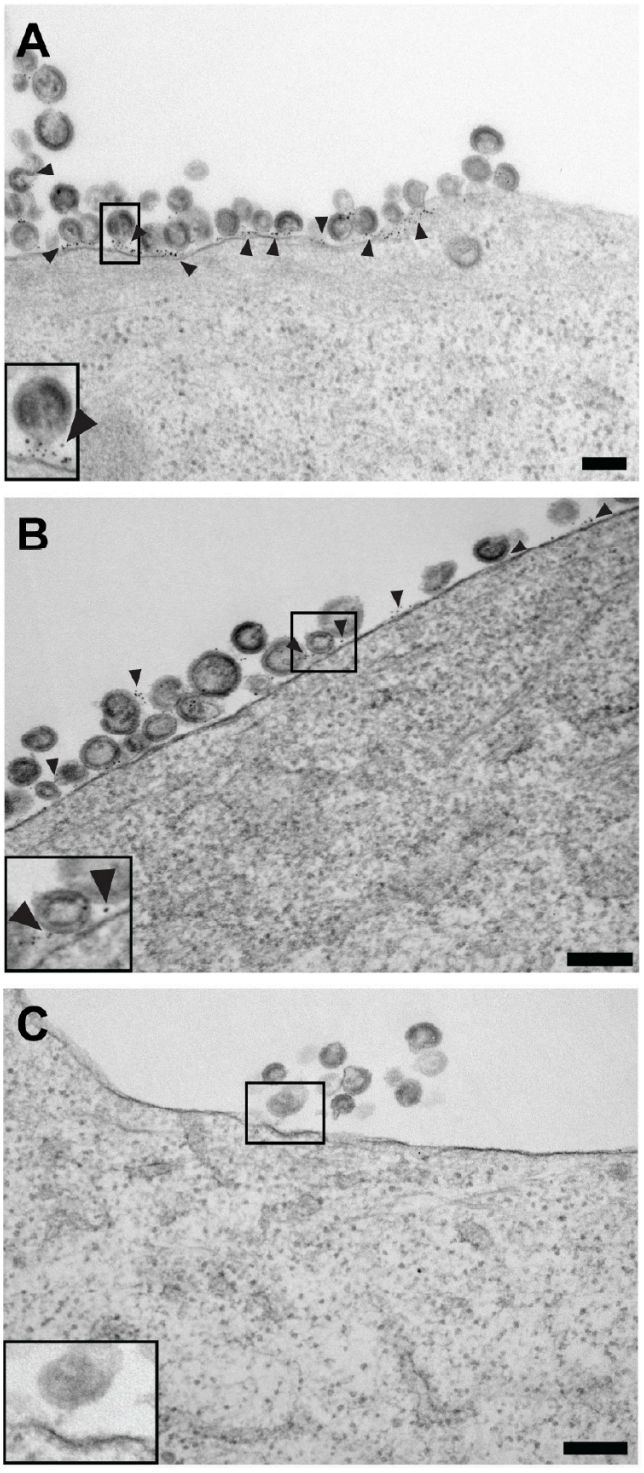

Supplementary Figure 2

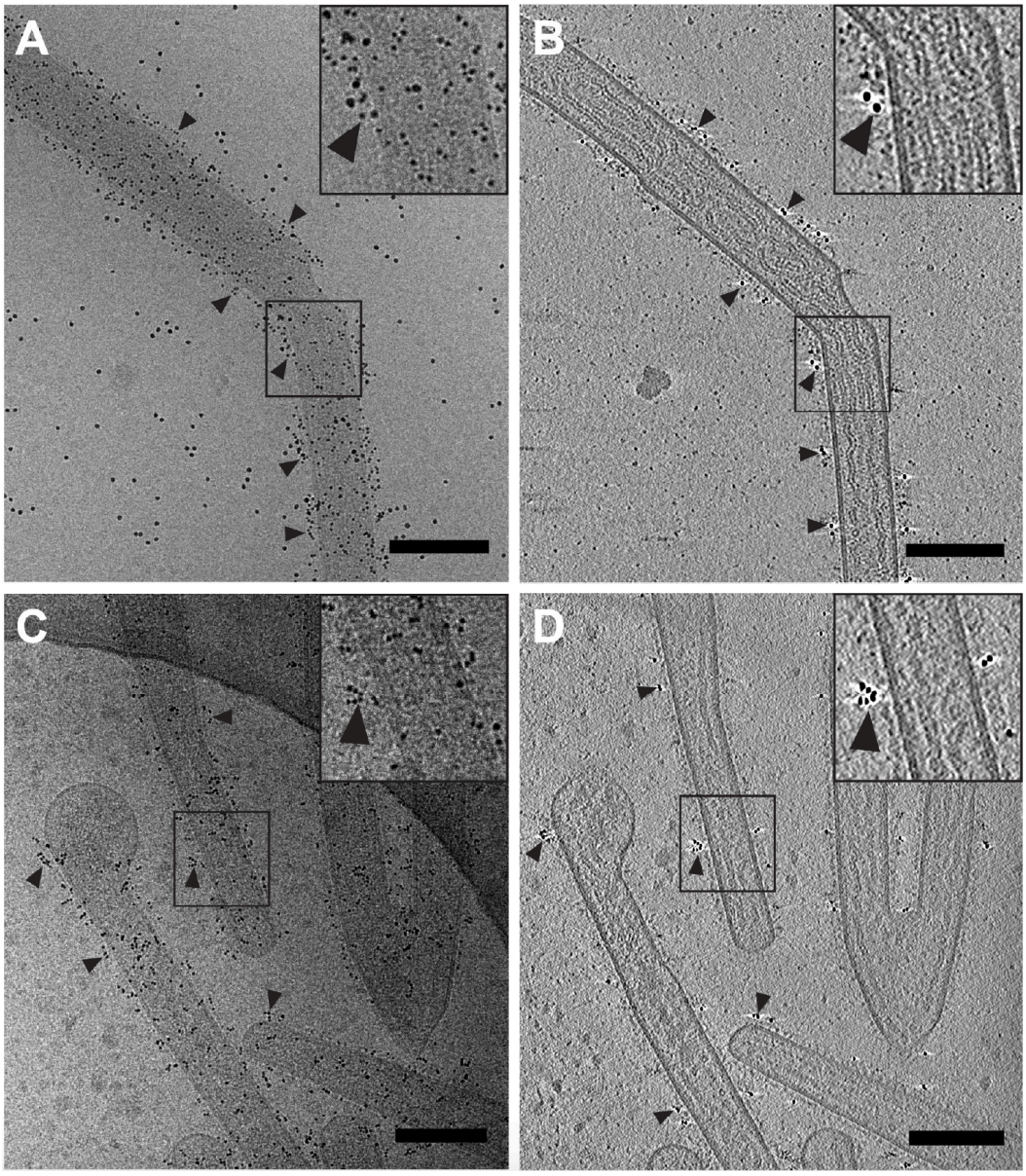

Appendix B: Pleomorphic structures in human blood are red blood cell-derived microparticles, not bacteria

Adam J. Mitchell,[1] Warren D. Gray,[1] Max Schroeder,[2] Hong Yi,[3] Jeannette V. Taylor,[3] Rebecca S. Dillard,[4] Zunlong Ke,[5] Elizabeth R. Wright,[3,4] David Stephens,[2] John D. Roback,[6] and Charles D. Searles[1,7,*]

[1]Division of Cardiology, Department of Medicine, Emory University, Atlanta, GA

[2]Division of Infectious Disease, Department of Medicine, Emory University, Atlanta, GA

[3]Robert P. Apkarian Integrated Electron Microscopy Core, Emory University, Atlanta, GA

[4]Division of Infectious Disease, Department of Pediatrics, Emory University, Atlanta, GA

[5]School of Biology, Georgia Institute of Technology, Atlanta, GA

[6]Center for Transfusion and Cellular Therapy, Department of Pathology and Laboratory Medicine, Emory University, Atlanta, GA

[7]Section of Cardiology, Atlanta VA Medical Center, Decatur, GA

Published in:

PLoS One, 2016

Vol. 11, No. 10

e0163582

A.J.M., W.D.J., M.S., H.Y., E.R.W., D.S., J.D.R., and C.D.S. conceived and designed the experiments. A.J.M., W.D.G., M.S., H.Y., J.T., R.S.D., and Z.K. performed the experiments. A.J.M. W.D.G. M.S. H.Y. E.R.W. D.S. J.D.R. C.D.S. R.S.D., and Z.K. analyzed the data. E.R.W., D.S., J.D.R., and C.D.S. contributed reagents/materials/analysis tools. A.J.M., W.D.G., M.S., E.R.W., D.S., J.D.R., C.D.S., and R.S.D. wrote the paper.

ABSTRACT

Background

Red blood cell (RBC) transfusions are a common, life-saving therapy for many patients, but they have also been associated with poor clinical outcomes. We identified unusual, pleomorphic structures in human RBC transfusion units by negative-stain electron microscopy that appeared identical to those previously reported to be bacteria in healthy human blood samples. The presence of viable, replicating bacteria in stored blood could explain poor outcomes in transfusion recipients and have major implications for transfusion medicine. Here, we investigated the possibility that these structures were bacteria.

Results

Flow cytometry, miRNA analysis, protein analysis, and additional electron microscopy studies strongly indicated that the pleomorphic structures in the supernatant of stored RBCs were RBC-derived microparticles (RMPs). Bacterial 16S rDNA PCR amplified from these samples were sequenced and was found to be highly similar to species that are known to commonly contaminate laboratory reagents.

Conclusions

These studies suggest that pleomorphic structures identified in human blood are RMPs and not bacteria, and they provide an example in which laboratory contaminants may can mislead investigators.

BACKGROUND

Red blood cell (RBC) transfusions are a common and often life-saving therapy, but have been associated with significant morbidity and mortality [1]. The mechanisms responsible for this association remain unclear. During the course of studying RBC-derived microparticles (RMPs), which originate from RBC membrane blebbing and accumulate over time in stored human RBC units, we detected submicron, pleomorphic structures by negative-stain electron microscopy (EM). A review of the literature revealed previous reports of identical, submicron, pleomorphic structures in human blood that were characterized as bacteria [2, 3]. McLaughlin *et al.* concluded that the pleomorphic structures were bacteria based on bacterial 16S rDNA sequencing, flow cytometry-based fluorescent *in situ* hybridization studies, the apparent ability of the structures to replicate, and their sensitivity to antibiotics [2]. However, bacteria could not be cultured by standard techniques. Intrigued by the possibility of viable nanobacteria in RBC transfusion units as a possible etiology of poor clinical outcomes after transfusion, we examined the pleomorphic structures isolated from RBC storage units further, and conclude that these structures are not bacteria, but rather RMPs.

METHODS

The Emory University IRB approved all studies and study participants gave written consent prior study participation.

Isolation of RBC-derived vesicles

Leukocyte-depleted RBC transfusion units were obtained from the blood bank at Emory University Hospital and stored from 0–42 days under standard conditions at 4°C. Blood product samples were obtained through a syringe port using a sterile 18-gauge needle under aseptic conditions. Samples were then prepared using a protocol developed to isolate microparticles (MPs). RBCs were centrifuged at 1900 x g for 1 minute to pellet cells, the supernatant was transferred to a sterile tube, and centrifuged a second time at 800 x g for 10 minutes to pellet any residual RBCs. The supernatant was then centrifuged at 16,100 x g for 20 minutes to pellet MPs. The MP pellet was re-suspended in molecular grade PBS and either studied immediately or frozen in aliquots at minus 80°C.

Electron microscopy

Negative staining

The Robert P. Apkarian Integrated Electron Microscopy Core, Emory University performed transmission electron microscopy of the RBC vesicles using a standard negative staining protocol. Briefly, 400-mesh carbon coated copper grids were made hydrophilic by glow discharging. A 5 µl droplet of the vesicle isolate, either unfixed or fixed with 2.5% glutaraldehyde, was placed on the grid, after 5 minutes, the grid with the suspension was rinsed by briefly touching the sample side to three drops of distilled water. The excess water on the grid was then removed by blotting the side of the grid on a piece of filter paper. For negative staining, 5 µl of 1% phosphotungstic acid (PTA) was

applied onto the grid immediately after water removal, and then removed as described above after 30 seconds. The grid was allowed to completely dry before viewing in the microscope.

TEM

For thin-section TEM examination of embedded RBC vesicles, the samples were fixed with 2.5% glutaraldehyde in 0.1 M sodium cacodylate (pH 7.4). Samples were then washed with the same buffer twice and post-fixed with 1% osmium tetroxide and 1.5% potassium ferrocyanide in the same buffer, dehydrated through a graded ethanol series to 100%, and embedded in Eponate 12 resin (Ted Pella Inc., Redding, CA). Ultrathin sections were cut on a Leica UltraCut S ultramicrotome (Leica Microsystems Inc., Buffalo Grove, IL) at 70 nm, and counter-stained with 4% aqueous uranyl acetate and 2% lead citrate. Sections were examined using a 120 kV JEOL JEM-1400 LaB_6 transmission electron microscope (JEOL, Ltd., Japan) equipped with a Gatan 2k x 2k US1000 CCD camera (Gatan, Inc., Pleasanton, CA).

SEM

For SEM examination of RBC vesicles, the samples were fixed with 2.5% glutaraldehyde in 0.1 M sodium cacodylate buffer (pH 7.4). The samples were then placed onto poly-L-lysine coated silicon chips and washed with the same buffer twice before post-fixation with 1% osmium tetroxide in the same buffer and dehydration through a graded ethanol series to 100%. Silicon chips with vesicles were then loaded into a Polaron E3000 critical point drying apparatus to exchange 100% ethanol for liquid CO_2. Once liquid CO_2 was brought to its critical point, it was vented slowly. The samples on the silicon chips were coated with 8 nm chromium in a Denton DV-602 Turbo Magnetron Sputter Coater (Denton Vacuum, LLC, Moorestown, NJ) before imaging on the upper-stage of a Topcon DS-150 field emission-scanning electron microscope (FE-SEM).

Cryo-electron microscopy and cryo-electron tomography

Purified RBC microparticles (4 μl) were applied to Quantifoil R 2/1 TEM grids and plunge frozen using an FEI Vitrobot Mark III system (FEI, Hillsboro, OR). 10 nm BSA-treated colloidal gold fiducial markers were mixed with the sample prior to freezing. Images were acquired using a JEOL JEM-2200FS field-emission TEM (JEOL Ltd., Japan) operated at 200 kV and equipped with an in-column Omega energy filter (slit width: 20 eV). Montages were collected on a Gatan US4000 4k × 4k CCD camera (Gatan) at 10,000× nominal magnification. Montages were stitched together prior to particle counting and diameter measurements. Diameters were measured using the *imodinfo* command by placing open model points at two ends of the particles. Tilt series were collected using the SerialEM software package [4] from -62° to 62° at 2° increments, with a defocus of -6 μm and a total dose of ~135 $e^-/Å^2$. Tilt series were recorded on a Direct Electron DE-20 (Direct Electron, LP, CA) at 12 frames per second and a nominal magnification of 10,000× (pixel size 6.14 Å) [5]. Frames were motion corrected using scripts provided by the vendor (DE). The images were CTF-corrected by phase inversion and the three-dimensional reconstructions were calculated via the weighted-back projection algorithm using IMOD software [6]. The reconstructed volumes (binned by 2) were further denoised using nonlinear anisotropic diffusion as implemented in IMOD.

Microbial DNA analysis

DNA was isolated from microparticle pellets, molecular grade water, and a colony of *Streptococcus pneumoniae* using a QIAamp DNA Mini Kit according to the manufacturer's specified protocol for bacteria (Qiagen). As an alternative, DNA was extracted using a conventional phenol-chlorophorm extraction protocol [7]. Standard agarose gel electrophoresis was carried out on a 1% agarose accompanied by a 1kb DNA ladder (NEB). The same universal 16S PCR primers used by McLaughlin *et al.* were utilized to amplify 16S rDNA: BSF8/20 (5′-

AGAGTTTGATCCTGGCTCAG-3′) and the reverse primer BSR1541/20 (5′-AAGGAGGTGATCCAGCCGCA-3′) [2]. PCRs were performed in 20 µl reaction volumes with 1X Q5 High Fidelity Master Mix (New England Biolabs), 1 µM forward and reverse primer, and 6 ul of DNA template. Reactions were carried out on a Biorad C1000 Touch Thermocycler with the following conditions: 98°C x 10 minutes, (98°C x 10 seconds, 70°C x 30 seconds, 72°C x 30 seconds) x 38 cycles, 72°C x 2 minutes. PCR products were purified using a Qiaquick PCR Purification Kit per the manufacturer's protocol and sent for commercial first pass sequencing (Beckman Coulter) using the BSF8/20 and BSR1541/20 primers.

16S rDNA qPCR of human serum

Under aseptic conditions, blood was collected into serum vacutainers (BD) from 3 healthy donors (no medications). Cells were removed by centrifugation (3,000 x g for 7 minutes) and serum was incubated for 0, 5, or 10 days at 30°C. DNA was extracted from 100 ul of serum as described above and used as a template for qPCR. Universal 16S primers developed previously for 16S rDNA qPCR were utilized: EUBAC-F (5′-TCCTACGGGAGGCAGCAGT-3′) and EUBAC-R (5′-GGACTACCAGGGTATCTAATCCTGTT-3′) [8]. These primers were selected for qPCR because the amplicon size was more appropriate for qPCR studies than the primers used by McLaughlin et al. Reactions were performed in 20 µl volumes with 1X Quantitect SYBR Green Master Mix, 300nM forward and reverse primers, and 8.8 µl DNA. Thermocycler conditions were: 95C x 10 minutes, (95°C x 15 seconds, 60°C x 1 minute) x 40 cycles. All reactions were performed in triplicate. Relative expression was calculated as 2^{-dCt} and converted to fold-change by normalizing to the mean expression at day 0. Data was analyzed using a one-way ANOVA with the assistance of Prism (Graphpad).

Flow cytometry

Isolated particles were stained with 10 μM calcein-AM (Life Technologies) and anti-CD235a (GPA) fluorescently labeled antibody (PE/Cy7; BioLegend), incubated at room temperature for 20 minutes, and analyzed on a BD LSR flow cytometer (BD Biosciences). The concentration of RMPs in a sample was calculated by ratiometric comparison after adding a known concentration of Flow-Check Fluoroshperes (Beckman).

miRNA analysis

Total RNA was isolated using a miRNeasy Mini Kit according to the manufacturer's protocol (Qiagen) and analyzed on an Agilent Bioanalyzer with the RNA 6000 Pico Kit by standard protocol. qRT-PCR analysis of miR-451 was performed using Qiagen products (miScript II RT Kit, miScript Primer assay) and analyzer on a StepOne Real-Time PCR System (ThermoFisher).

Western blot

Particles were lysed in RIPA buffer, exposed to brief sonication, and protein was quantified using the BCA assay. 0.3 μg of protein was separated by gel electrophoresis, transferred to a nitrocellulose membrane, and probed using an anti-hemoglobin-alpha antibody (Santa Cruz Biotechnology; sc-21005).

RESULTS

Electron microscopy of RMPs

Several groups have published electron micrographs of RMPs, thus we expected to find a mostly spherical morphology [9, 10]. However, negative-stain EM images (Figure 1A and 1B) of the unfixed pellet obtained from the supernatant of stored RBC units appeared identical to images published by McLaughlin *et al.* and Szymanski *et al.* [2, 3]. In both of these latter cases, the pleomorphic structures were reported to be bacteria. We consistently identified similar pleomorphic structures in RBC units obtained from >6 healthy donors; these structures were present immediately after donation (day 0) as well as after several weeks of storage at 4°C, under standard blood bank conditions. We reasoned that these pleomorphic structures were either RMPs with unusual morphology (possibly due to artifact), or they were in fact microbial in nature. We systematically ruled out possible sources of artifact, including: RBC centrifugation, washing of the carbon grid with water, a lack of albumin in the isolated pellet. We also performed TEM and SEM of fixed pellets (Figure 1C–1F). Regardless of how the unfixed samples were prepared, negative-stain EM reliably produced images represented in Figure 1A and 1B. However, detailed analysis of fixed material by TEM and SEM revealed that, whereas some of the vesicles were pleomorphic and rod-like in shape, many retained the expected ellipsoidal shape (Figure 1C–1F) [9, 10]. Further, comparison of fixed and unfixed samples by negative-stain EM showed mostly ellipsoidal versus mostly pleomorphic, rod-like shaped vesicles respectively (Figure 1G and 1H). To definitely determine the native structure of the vesicles, two-dimensional (2D) cryo-electron microscopy (cryo-EM) images were acquired and three-dimensional (3D) cryo-electron tomography (cryo-ET) data sets were recorded and processed. 2D Cryo-EM micrographs and 3D cryo-ET reconstructions revealed predominantly round (77%) rather the pleomorphic vesicles (23%) and the presence of a single lipid bilayer (Figure 2) instead of the complex cell wall of a bacterial species. Average vesicle diameter was 190–288 nanometers.

Interestingly, while most vesicles appeared to be filled with a dense granular substance, a significant fraction (23%) did not, appearing "empty" (Figure 2A and 2B).

Microbial DNA analysis of vesicles identifies common contaminants

To further assess whether bacterial DNA is present in the supernatant of stored RBC units, a large microparticle pellet was isolated by sequential centrifugation of RBCs (100mL) that had been stored for 42 days under standard blood bank conditions. The pellet contained ~3 billion submicron, calcein-positive vesicles, as determined by flow cytometric analysis. DNA was extracted from the pelleted material and analyzed by standard gel electrophoresis. *S. pneumoniae* was used as a positive control, and molecular grade water or molecular grade water passed through the Qiagen DNA extraction protocol were negative controls. Despite the isolation of very large numbers of these vesicles, no genomic DNA was observed by gel electrophoresis (Figure 3A). Similar results were obtained using a phenol-chloroform based DNA extraction protocol. Subsequently, PCR was performed on the pelleted material using the same universal 16S rDNA primers as described by McLaughlin et al. PCR product was observed in pelleted vesicles and both positive and negative controls (Figure 3B). The PCR product from each sample was purified and sequenced by single pass sequencing (Beckman Coulter Genomics) using the same 16S rDNA primers (S1 File). BLAST analysis revealed that 16S sequences in the pelleted material were highly similar to *Pelomonas* spp. Sequences from molecular grade water and water passed through the Qiagen extraction protocol were related to *Bradyrhizobium* spp. and *Propionibacterium* spp., respectively. All three species are known to be common contaminants in laboratory reagents [11]. Of note, both species identified by McLaughlin et al. are also now known to be typical contaminants (*Stenotrophomonas* spp., *Pseudomonas* spp.). As expected, 16S rDNA amplified from *S. pneumonia* DNA was identified as *S. pneumonia* (raw sequences available in supplemental material).

16S rDNA levels are unchanged in human serum incubated for up to 10 days

To further rule out the possibility of viable bacteria in the blood of healthy humans, serum from 3 donors was subjected to 16S rDNA qPCR analysis after incubation for 0, 5, and 10 days. The abundance of 16S rDNA would be expected to increase over time if viable, replicating bacteria were present. Here, we did not find any change in the amount of 16S rDNA over time (ANOVA, $p = 0.53$) (Figure 3C).

Flow cytometry, miRNA, and protein analysis indicate isolated structures are RMPs

Flow cytometric analysis demonstrated that all vesicles in the pelleted material from RBC storage units were positive for glycophorin-A (GPA), a RBC specific surface antigen, and calcein-AM (Figure 4A), suggesting that they were membrane-bound and intact [12]. Calcein-AM is a non-fluorescent, membrane permeable dye that becomes fluorescent and membrane impermeant after it is cleaved by esterases. RNA isolated from the vesicles was characterized using an Agilent Bioanalyzer and revealed that it contained only small RNA (Figure 4B). miR-451, a miRNA known to be highly enriched in RBCs was highly abundant in both RBC and in RMP fractions, as compared to RNA isolated from cultured human aortic endothelial cells (HAECs), which have low levels of miR-451 and were used as a negative control (Figure 4C). High levels of hemoglobin-alpha were detected in protein lysate of the vesicles and RBCs (Figure 4D). Since the RMP pellet was washed extensively with PBS prior to RNA or protein isolation, it is not expected that the miR-451 or hemoglobin-alpha was derived from lysed RBCs in the stored unit.

DISCUSSION

In summary, unfixed negative-stain EM of material in the extracellular fluid of RBC storage units identified pleomorphic structures that appeared identical to those previously reported to be circulating bacteria. Our results suggest that these pleomorphic structures are RMPs, not viable bacteria. First, genomic DNA was undetectable in the extracellular material, even when very large numbers of vesicles were used for DNA isolation. Second, incubation of serum samples from healthy humans at 30°C for up to 10 days failed to show any increase in bacterial 16S rDNA content. Third, bacterial 16S rDNA sequences amplified by PCR, both in this study and in previous studies, are known to be common contaminants in laboratory reagents [11]. Lastly, isolated vesicles had intact membranes, RBC specific antigen on their surface, and relatively abundant amounts of hemoglobin alpha and miR-451, a miRNA highly expressed in RBCs [13].

The unusual, pleomorphic nature of the vesicles present in unfixed negative-stain EM appeared to largely be due to the vesicles remaining flexible and deformable just prior to grid preparation. Whereas, most vesicles were observed to be ellipsoidal when fixed for negative-stain EM, thin-section TEM, or SEM. However, a small fraction of particles seemed to have a rod-shaped morphology. Why RBC-derived vesicles would assume this seemingly energetically unfavorable morphology is not clear, though it may be related to the unique structural proteins or lipid content responsible for the biconcave shape of RBCs. The cryo-EM studies revealed the presence of "full" and "empty" MPs. We suspect the granular material in the full MPs is hemoglobin, and that the empty MPs are ghost MPs, which others have observed in stored RBC units [14].

While it is accepted that bacteria transiently transmigrate into healthy human circulation, the concept that naturally occurring, viable nanobacteria routinely circulate in blood is not well supported. In

general, the existence of nanobacteria is controversial [15], and, whereas multiple groups have provided evidence that nanobacteria-like structures can form spontaneously in human serum, the consensus opinion is that these structures are likely mineraloprotein complexes rather than microbes [16, 17].

CONCLUSIONS

The existence of pleomorphic nanobacteria in healthy human blood has been described elsewhere; however, our study suggests that pleomorphic structures observed in negative-stain electron micrographs of human RBC storage units are RMPs and that 16S rDNA PCR products associated with these RMPs are contaminants, commonly known to be present in laboratory reagents.

FUNDING

This work was supported by the National Institutes of Health (R01HL109559, R01HL124879, R01HL095476, S10RR025679), and a VA Merit Award (I01 BX000704). Research reported in this publication was also supported by the National Heart, Lung, and Blood Institute of the National Institutes of Health under Award Number T32HL007745. The JEOL JEM-1400 transmission electron microscope was acquired with an NIH S10 grant (S10RR025679). The JEOL JEM-2200FS transmission electron microscope was acquired with an NSF-MRI grant (0923395). The content is solely the responsibility of the authors and does not necessarily represent the official views of the National Institutes of Health.

REFERENCES

1. Hopewell, S., Omar, O., Hyde, C., Yu, L.-M., Doree, C., and Murphy, M. F. A systematic review of the effect of red blood cell transfusion on mortality: Evidence from large-scale observational studies published between 2006 and 2010. *BMJ Open*, 2013. **3**(5).
2. McLaughlin, R. W., Vali, H., Lau, P. C. K., Palfree, R. G. E., De Ciccio, A., Sirois, M., Ahmad, D., Villemur, R., Desrosiers, M., and Chan, E. C. S. Are there naturally occurring pleomorphic bacteria in the blood of healthy humans? *J Clin Microbiol*, 2002. **40**(12): p. 4771-4775.
3. Szymanski, M., Petric, M., Saunders, F. E., and Tellier, R. *Mycoplasma pneumoniae* pericarditis demonstrated by polymerase chain reaction and electron microscopy. *Clin Infect Dis*, 2002. **34**(1): p. E16-E17.
4. Mastronarde, D. N. Automated electron microscope tomography using robust prediction of specimen movements. *J Struct Biol*, 2005. **152**(1): p. 36-51.
5. Yi, H., Strauss, J. D., Ke, Z., Alonas, E., Dillard, R. S., Hampton, C. M., Lamb, K. M., Hammonds, J. E., Santangelo, P. J., Spearman, P. W., and Wright, E. R. Native immunogold labeling of cell surface proteins and viral glycoproteins for cryo-electron microscopy and cryo-electron tomography applications. *J Histochem Cytochem*, 2015. **63**(10): p. 780-792.
6. Kremer, J. R., Mastronarde, D. N., and McIntosh, J. R. Computer visualization of three-dimensional image data using IMOD. *J Struct Biol*, 1996. **116**(1): p. 71-76.
7. Bergallo, M., Costa, C., Gribaudo, G., Tarallo, S., Baro, S., Ponzi, A. N., and Cavallo, R. Evaluation of six methods for extraction and purification of viral DNA from urine and serum samples. *New Microbiol*, 2006. **29**(2): p. 111-119.

8. Dinakaran, V., Rathinavel, A., Pushpanathan, M., Sivakumar, R., Gunasekaran, P., and Rajendhran, J. Elevated levels of circulating DNA in cardiovascular disease patients: Metagenomic profiling of microbiome in the circulation. *PLoS One*, 2014. **9**(8).

9. Rubin, O., Canellini, G., Delobel, J., Lion, N., and Tissot, J.-D. Red blood cell microparticles: Clinical relevance. *Transfus Med Hemother*, 2012. **39**(5): p. 342-347.

10. Dinkla, S., Brock, R., Joosten, I., and Bosman, G. J. C. G. M. Gateway to understanding microparticles: Standardized isolation and identification of plasma membrane-derived vesicles. *Nanomedicine*, 2013. **8**(10): p. 1657-1668.

11. Salter, S. J., Cox, M. J., Turek, E. M., Calus, S. T., Cookson, W. O., Moffatt, M. F., Turner, P., Parkhill, J., Loman, N. J., and Walker, A. W. Reagent and laboratory contamination can critically impact sequence-based microbiome analyses. *BMC Biol*, 2014. **12**.

12. Gray, W. D., Mitchell, A. J., and Searles, C. D. An accurate, precise method for general labeling of extracellular vesicles. *MethodsX*, 2015. **2**: p. 360-367.

13. Azzouzi, I., Moest, H., Wollscheid, B., Schmugge, M., Eekels, J. J. M., and Speer, O. Deep sequencing and proteomic analysis of the microRNA-induced silencing complex in human red blood cells. *Exp Hematol*, 2015. **43**(5): p. 382-392.

14. Salzer, U., Zhu, R., Luten, M., Isobe, H., Pastushenko, V., Perkmann, T., Hinterdorfer, P., and Bosman, G. J. C. G. M. Vesicles generated during storage of red cells are rich in the lipid raft marker stomatin. *Transfusion*, 2008. **48**(3): p. 451-462.

15. Young, J. D. and Martel, J. The rise and fait of nanobacteria. *Sci Am*, 2010. **302**(1): p. 52-59.

16. Martel, J. and Young, J. D.-E. Purported nanobacteria in human blood as calcium carbonate nanoparticles. *Proc Natl Acad Sci U S A*, 2008. **105**(14): p. 5549-5554.

17. Raoult, D., Drancourt, M., Azza, S., Nappez, C., Guieu, R., Rolain, J.-M., Fourquet, P., Campagna, B., La Scola, B., Mege, J.-L., Mansuelle, P., Lechevalier, E., Berland, Y., Gorvel, J.-P., and Renesto, P. Nanobacteria are mineralo fetuin complexes. *PLoS Pathog*, 2008. **4**(2).

FIGURE LEGENDS

Figure 1. Representative electron micrographs of pelleted material from supernatant of RBC storage units. (A and B) Negative-stain EM images of the unfixed material, showing pleomorphic structures. (C and D) Thin-section TEM images, showing membrane encapsulate vesicles. (E and F) SEM images. (G and H) Negative-stain EM of fixed (G) versus unfixed (H) structures. Vesicles were isolated and imaged as described in Methods section.

Figure 2. Representative 3D cryo-electron tomograpahy data and visual characterization of RBC-derived microparticles (RMPs). (A) Slices through 3D volumes of RMPs. (B) RMPs were measured and were characterized as either round or pleiomorphic, and as either full or empty. The number of each particle type, percent of the total, mean diameter, and standard deviation are presented in the table.

Figure 3. Analysis of bacterial DNA in pelleted material from RBC storage units and serum. RMPs were isolated from ~100 mL of RBCs stored under standard conditions for 42 days. (A) Genomic DNA was isolated and analyzed by gel electrophoresis. Molecular grade water and DNA from *S. Pneumoniae* served as negative and positive controls, respectively. Band reflective of genomic DNA was only observed in positive control lane. (B) Isolated DNA was also subjected to 16S rDNA PCR analysis, using universal primers. PCR product was observed for all samples assessed. **C**, Serum from 3 healthy donors was incubated at 30°C for 5 and 10 days, and then analyzed using a 16S rDNA qPCR assay. No significant difference in 16S rDNA was observed between the different time points.

Figure 4. Vesicles isolated from supernatant of RBC storage units are membrane-bound, intact, and contain RBC surface antigen and RBC-specific miRNA. (A) Unstained vesicles (red, bottom left) or vesicles co-stained with calcein-AM and fluorescent anti-GPA (blue, top right) were analyzed by flow cytometry. >99% of the vesicles were positive for calcein-AM and anti-GPA. (B)RNA from vesicles was analyzed by Agilent Bioanalyzer. Peak on electropherogram at 25 nt is internal standard and small peak to the right reflects small RNA. This electropherogram is representative of Bioanlyzer data from six different RBC storage units. (C) Levels (Ct values) of miR-451 were assessed by qRT-PCR in stored RBCs, the RMP pellet, and in human aortic endothelial cells (HAECs, negative control). (D) Hemoglobin-alpha content of RMP pellet and stored RBCs, as assessed by Western blot. Blot is representative of six different RBC storage units.

Figure 1

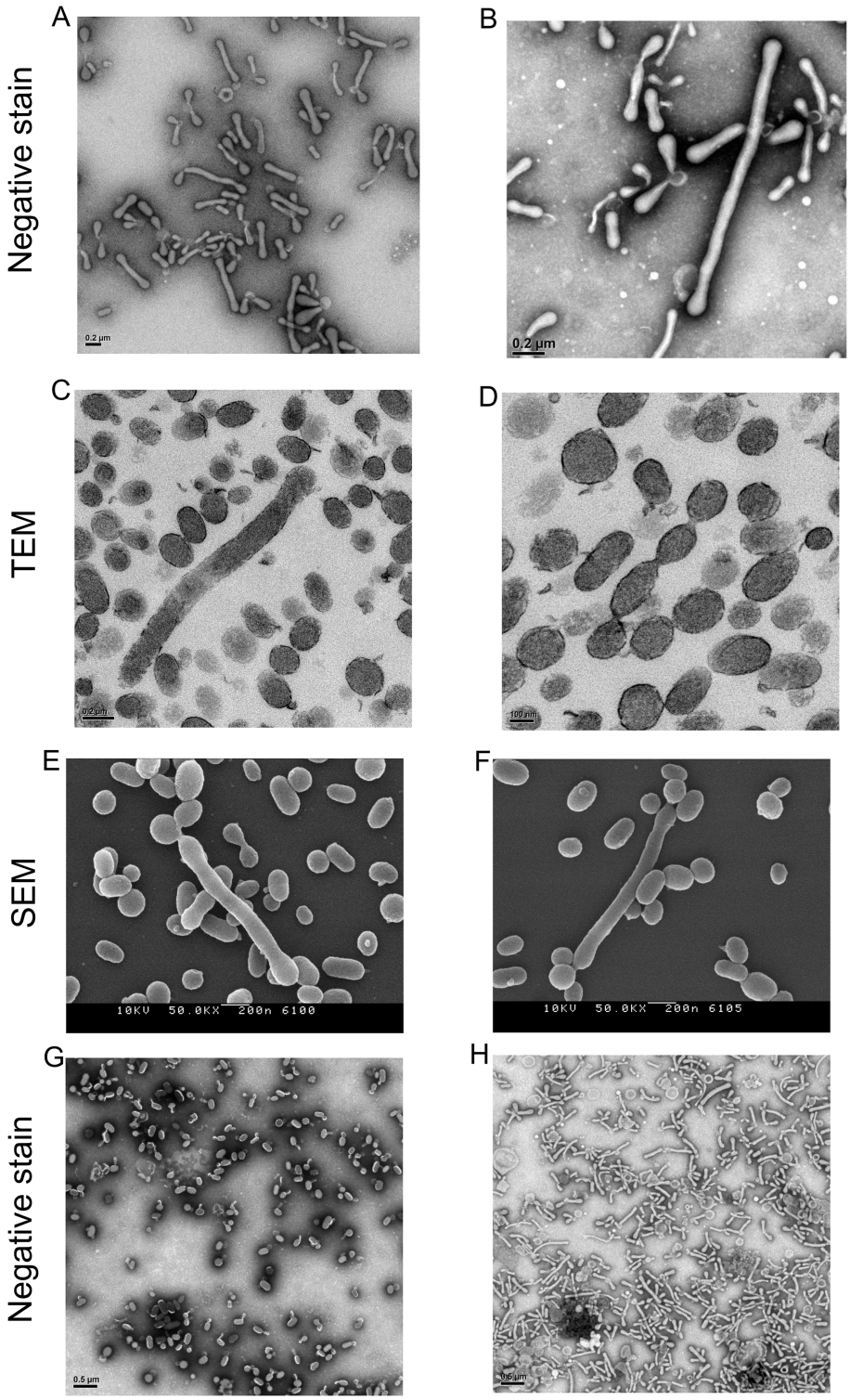
A
B
Negative stain
0.2 µm
0.2 µm
C
D
TEM
0.2 µm
100 nm
E
F
SEM
10KV 50.0KX 200n 6100
10KV 50.0KX 200n 6105
G
H
Negative stain
0.5 µm
0.5 µm

Figure 2

A

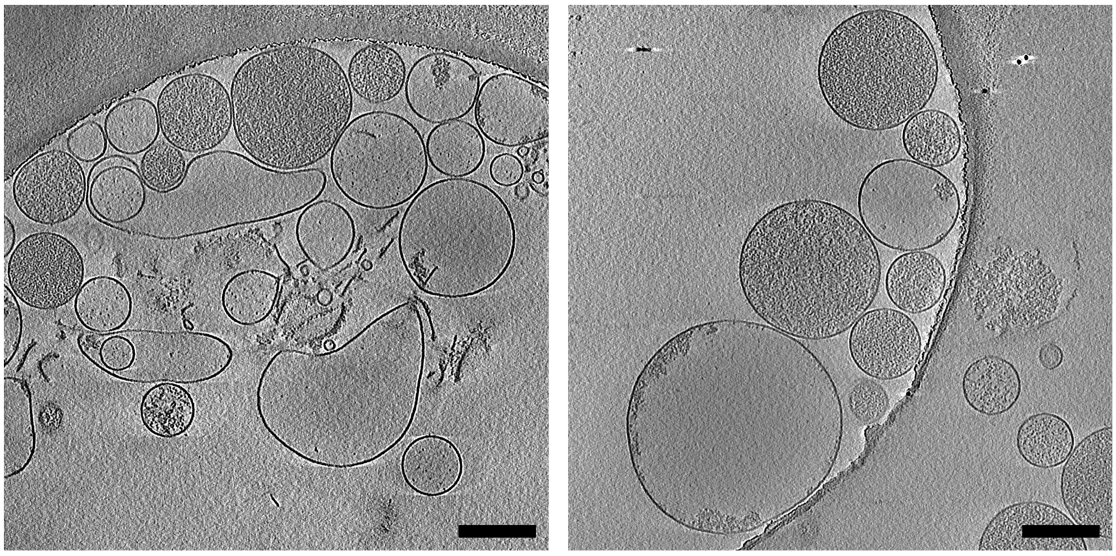

B

	Round, Full	Round, Empty	Pleomorphic, Full	Pleomorphic, Empty
Number of Particles (%)	608 (66)	148 (16)	104 (11)	65 (7)
Average Diameter (nm)	189.48	203.42	246.80	288.98
Standard Deviation	62.74	88.32	68.86	111.46

Figure 3

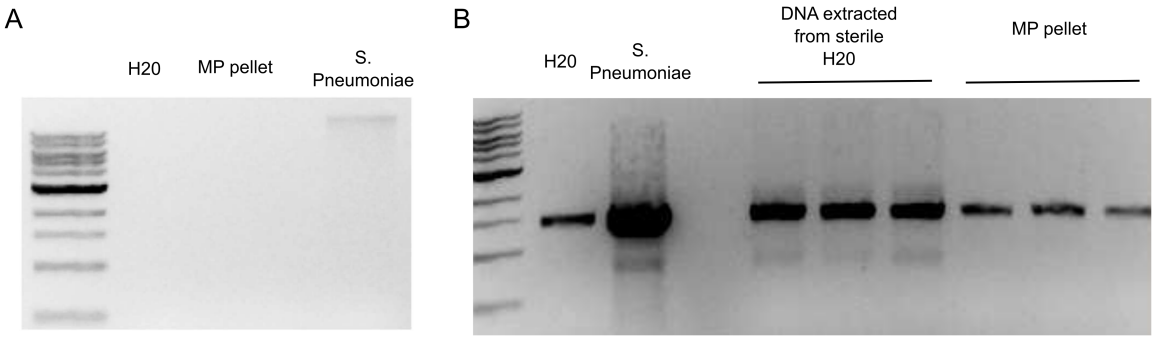
A
H20
MP pellet
S. Pneumoniae
B
H20
S. Pneumoniae
DNA extracted from sterile H20
MP pellet

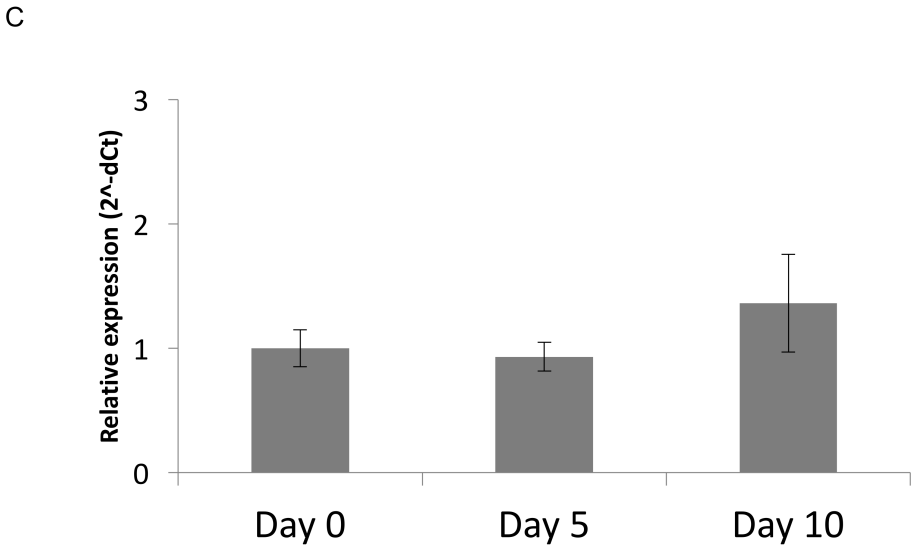
C
Relative expression (2^-dCt)
3
2
1
0
Day 0
Day 5
Day 10

Figure 4

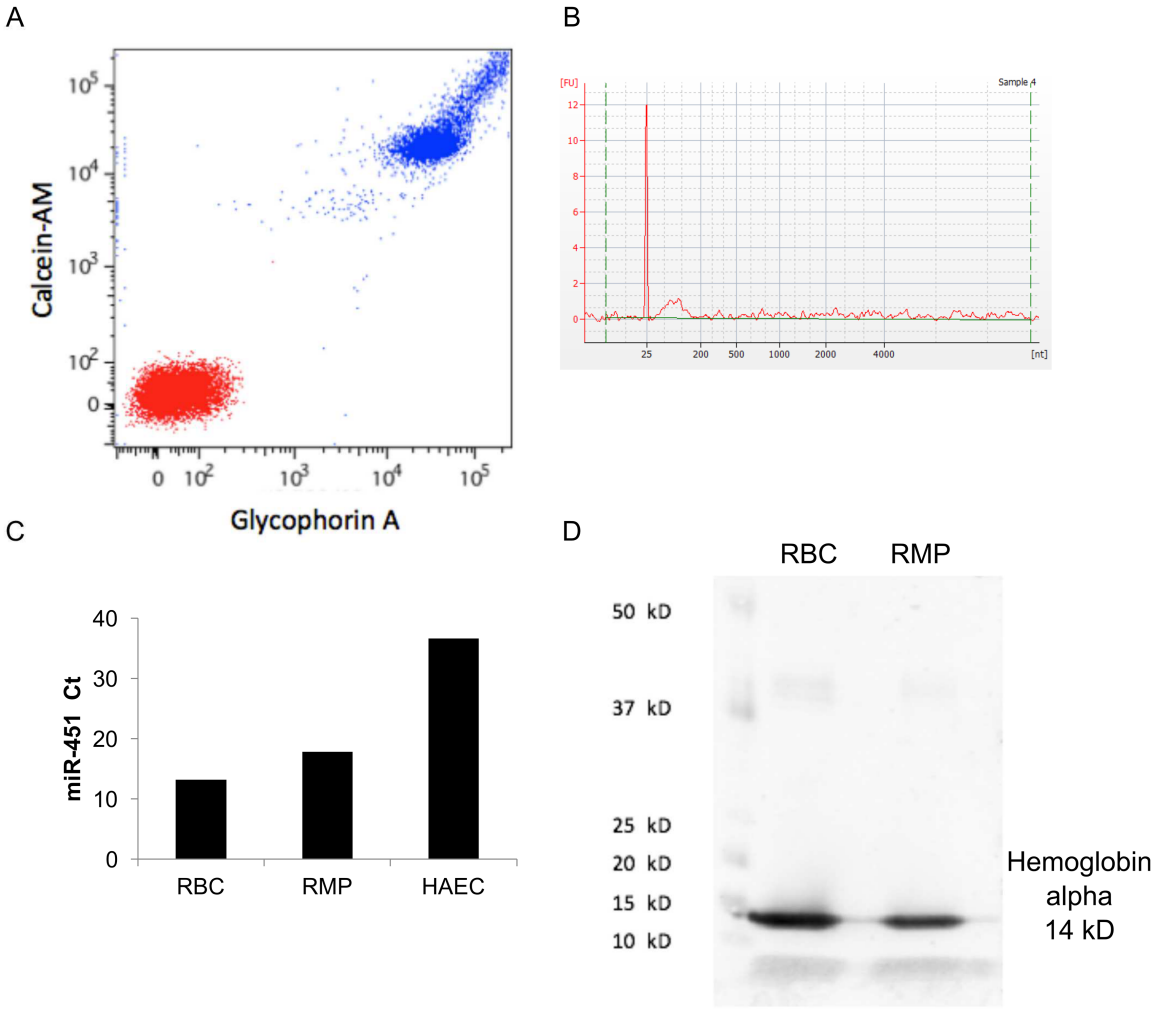
A
B
C
D
Calcein-AM
Glycophorin A
[FU]
Sample 4
[nt]
miR-451 Ct
RBC
RMP
HAEC
RBC
RMP
50 kD
37 kD
25 kD
20 kD
15 kD
10 kD
Hemoglobin
alpha
14 kD

Appendix C: A live RSV vaccine with engineered thermostability is immunogenic in cotton rates despite high attenuation

Christopher C. Stobart,[1,2,*] Christina A. Rostad,[1,2,*] Zunlong Ke,[3] Rebecca S. Dillard,[1,2] Cheri M. Hampton,[1,2] Joshua D. Strauss,[1,2] Hong Yi,[4] Anne L. Hotard,[1,2,‡] Jia Meng,[1,2,§] Raymond J. Pickles,[5] Kaori Sakamoto,[6] Sujin Lee,[1,2] Michael G. Currier,[1,2] Syed M. Moin,[7] Barney S. Graham,[7] Marina S. Boukhvalova,[8] Brian E. Gilbert,[9] Jorge C. G. Blanco,[8] Pedro A. Piedra,[9,10] Elizabeth R. Wright,[1,2,4] and Martin L. Moore[1,2]

[1]Department of Pediatrics, Emory University School of Medicine, Atlanta, GA

[2]Children's Healthcare of Atlanta, Atlanta, GA

[3]School of Biology, Georgia Institute of Technology, Atlanta, GA

[4]Robert P Apkarian Integrated Electron Microscopy Core, Emory University, Atlanta, GA

[5]Department of Microbiology and Immunology, University of North Carolina, Chapel Hill, NC

[6]Department of Pathology, College of Veterinary Medicine, University of Georgia, Athens, GA

[7]Vaccine Research Center, National Institute of Allergy and Infectious Diseases, National Institutes of Health, Bethesda, MD

[8]Sigmovir Biosystems Inc., Rockville, MD

[9]Department of Molecular Virology and Microbiology, Baylor College of Medicine, Houston, TX

[10]Department of Pediatrics, Baylor College of Medicine, Houston,TX

[*]These authors contributed equally to this work

Published in:

Nature Communications, 2016

Vol. 7

p. 13916

C.C.S., C.A.R., Z.K., R.S.D., H.Y., A.L.H., J.M., R.J.P., K.S., S.L., M.G.C., M.S.B., J.C.G.B. and M.L.M. performed experiments. S.M.M. and B.S.G. provided reagents and advice. C.C.S., C.A.R., Z.K., J.C.G.B., P.A.P., E.R.W. and M.L.M. designed the experiments and analysed data. C.C.S., C.A.R., E.R.W. and M.L.M. wrote the paper.

ABSTRACT

Respiratory syncytial virus (RSV) is a leading cause of infant hospitalization and there remains no pediatric vaccine. RSV live-attenuated vaccines (LAVs) have a history of safe testing in infants; however, achieving an effective balance of attenuation and immunogenicity has proven challenging. Here we seek to engineer an RSV LAV with enhanced immunogenicity. Genetic mapping identifies strain line 19 fusion (F) protein residues that correlate with pre-fusion antigen maintenance by ELISA and thermal stability of infectivity in live RSV. We generate a LAV candidate named OE4 which expresses line 19F and is attenuated by codon-deoptimization of non-structural (NS1 and NS2) genes, deletion of the small hydrophobic (SH) gene, codon-deoptimization of the attachment (G) gene and ablation of the secreted form of G. OE4 (RSV-A2-dNS1-dNS2-ΔSH-dG_m-Gs_{null}-line19F) exhibits elevated pre-fusion antigen levels, thermal stability, immunogenicity, and efficacy despite heavy attenuation in the upper and lower airways of cotton rats.

INTRODUCTION

In the 1960s, a formalin-inactivated RSV (FI-RSV) vaccine primed for enhanced illness in infants on natural infection [1]. This phenomenon was replicable in animal models and considered dependent on RSV naive status [2]. Subsequent studies using subunit-based vaccines also primed for immunopathology in animals [3, 4]. These early RSV vaccines encouraged development of LAVs, which do not prime for enhanced disease in animals or seronegative infants [2, 5]. However, development of pediatric RSV LAV strains with sufficient attenuation and immunogenicity has been difficult [6]. To address these dual challenges, newer RSV LAVs have incorporated genetic modifications rationally designed to retain or enhance immunogenicity compared with wild type virus [7-9] because natural infection may be suboptimally immunogenic for LAVs derived by classic attenuation methods.

Recent elucidation of the structure of the pre-fusion conformation of RSV F protein (pre-F [10]) and discovery of its importance as a natural immunogen [11] has had implications for RSV vaccine development. The high capacity of pre-F to elicit neutralizing antibody titres has been demonstrated in multiple vaccine platforms, including purified proteins [12-14], virus-like particles [15], and recombinant parainfluenza viruses [16]. Use of pre-F in passive immunization, either by anti-pre-F monoclonal antibody (mAb) prophylaxis or by boosting RSV neutralizing antibody (nAb) titres in pregnant mothers with pre-F protein-based vaccines, holds promise for reducing RSV disease in the youngest infants [14]. Nevertheless, active immunization of infants with a replicating RSV vaccine could potentially have a large child health benefit if protection spanned beyond the persistence of passively acquired maternal Ab. Since natural RSV infection induces anti-pre-F nAb [11], we hypothesized that RSV with enhanced pre-F expression would have increased LAV immunogenicity.

Here we first identified a chimeric RSV strain A2-line19F with enhanced pre-fusion antigen levels, thermostability and immunogenicity compared with parental strain A2. We then incorporated line19F into an RSV LAV candidate 'OE4' with the genotype RSV-A2-dNS1- dNS2-ΔSH-dG_m-Gs_{null}-line19F. We found that OE4 exhibited elevated pre-fusion antigen levels, thermal stability, immunogenicity, and efficacy despite heavy attenuation in the upper and lower airways of cotton rats.

METHODS

Cells and animals

HEp-2 (ATCC CCL-23) and Vero (ATCC CCL-81) were cultured in minimal essential medium (MEM) containing 10% fetal bovine serum (FBS) and 1 $\mu g\,ml^{-1}$ penicillin, streptomycin and amphotericin B (PSA) [8]. BSR-T7/5 (a gift from Ursula Buchholz, National Institutes of Health, Bethesda, MD) were cultured in Glasgow's minimal essential medium (GMEM) containing 10% FBS and 1 $\mu g\,ml^{-1}$ PSA supplemented with 1 $mg\,ml^{-1}$ Geneticin with every other passage [8]. BEAS-2B cells (ATCC CRL-9609) were cultured in RMPI containing 10% FBA and 1 $\mu g\,ml^{-1}$ PSA [17]. The cell lines were not authenticated, and they were negative for mycoplasma using the LookOut Mycoplasma detection kit (Sigma). Normal human bronchial epithelial (NHBE) cells were purchased from Lonza and differentiated 4–6 weeks at air–liquid interface (ALI) as described [8]. Prior to infection, NHBE-ALI cultures exhibited trans-epithelial resistance. Human airway epithelial (HAE) cells from airway specimens of patients without defined lung disease were isolated by the University of North Carolina (UNC) Marsico Lung Institute Tissue Culture Core [18]. Patients provided informed consent under UNC at Chapel Hill Institutional Review Board-approved protocols from the National Disease Research Interchange (NDRI, Philadelphia, PA). Primary cells were cultured initially in a cell culture-treated flask before being seeded at a density of 3×10^5 cells per Transwell disk. Similar to NHBE cells, HAE cells were cultured at ALI for 4–6 weeks forming differentiated polarized cultures [18].

Six- to eight-week-old female BALB/c mice (The Jackson Laboratory or Charles River) were maintained under pathogen-free conditions until the time of use. The Emory University Institutional Animal Care and Use Committee (IACUC) approved the mouse studies. Male and female *Sigmodon hispidus* cotton rats were bred and housed in the vivarium in Baylor College of Medicine. These

cotton rats were ~75 to 150 g of body weight at the start of the experiments, and all experimental protocols were approved by the Baylor College of Medicine's IACUC. Inbred *Sigmodon hispidus* cotton rats at Sigmovir Biosystems, Inc. (Rockville, MD) were utilized in a challenge study approved by the Sigmovir IACUC. All mouse and cotton rat experiments were conducted in accordance with the Guide for Care and Use of Laboratory Animals of the National Institutes of Health, as well as local, state and federal laws. Mice and cotton rats were randomly assigned to groups based on sequential selection from an inventory, and investigators were not blinded to outcome assessment.

Assembly and rescue of recombinant RSV viruses

The following recombinant viruses were previously described: A2, A2-line19F, A2-line19F(M79I), A2-line19F(R191K), A2-line19F(K357T), A2-line19F(Y371N), A2-line19F(I557V), A2-line19F(K357T/Y371N) and A2-mKate2-2-20F/G [19-21]. The bacterial artificial chromosome (BAC) construct for OE4 was generated through modification of the published BAC containing A2-mKate2-line19F(I557V) [20]. The gene for monomeric Katushka 2 (mKate2, K), a far-red fluorescent reporter, is in the first gene position of the RSV antigenomic cDNA. Inclusion of mKate2 in this position did not attenuate RSV *in vitro* or in mice [20]. Deletion of SH (ΔSH) was performed by recombination-mediated mutagenesis (recombineering) [20]. The following oligonucleotides (Integrated DNA Technologies/IDT) were used to PCR-amplify the *galK* cassette such that the amplicon termini are homologous to the target site to replace SH with galK: dSH50f (5′-AGATCTAGTACTCAAATAAGTTAATAAAAAATATACACATGGACGTCCATCCTGTTGACAATTAATCATCGGCA-3′), where the underlined portions represent the 50 nt immediately upstream of the SH gene start in the BAC, and dSH50r (5′-GTCTTAGCGGTGCGTTGGTCCTTGTTTTTGGACATGTTTGCATTTGCCCCTCAGCACT

GTCCTGCTCCTT-3′), where the underlined portion represents the complement of 50 nt beginning with the G gene start in the BAC. The non-underlined portions of the primers are specific to the *galK* cassette, as described[41]. Recombination in *E coli* resulted in replacing SH, from the beginning of the gene start to the end of the SH-G intergenic region, with the *galK* cassette. The following complementary oligonucleotides were annealed and used for removing the *galK* cassette in the second step of recombineering: dSH100f (5′-AGATCTAGTACTCAAATAAGTTAATAAAAAATATACACATGGACGTCCATGGGGCAAATGCAAACATGTCCAAAAACAAGGACCAACGCACCGCTAAGAC-3′) and dSH100r (5′-GTCTTAGCGGTGCGTTGGTCCTTGTTTTTGGACATGTTTGCATTTGCCCCATGGACGTCCATGTGTATATTTTTTATTAACTTATTTGAGTACTAGATCT-3′). Precise deletion of SH was confirmed by sequencing, yielding A2-K-ΔSH-line19F(I557V) BAC. The human codon-deoptimized NS1 (Supplementary Figure 5) and NS2 (Supplementary Figure 6) coding regions were digested from the BAC used for recovery of A2-dNSh previously described and ligated into the A2-K-ΔSH-line19F(I557V) BAC yielding an A2-K-dNSh-ΔSH-line19F(I557V) [8]. This construct was used for recovery of OE4+wild type A2 G (termed OE4+wtG). Codon deoptimization of G was performed through substitution *in silico* of all codons least frequently used based on human codon usage bias into the RSV G sequence of A2. A point mutation (M48I) was introduced to ablate the secreted form of G (Supplementary Figure 7). The coding region of codon-deoptimized G (dG) was synthesized by GenScript and cloned by restriction digestion and ligation into the A2-K-dNSh-ΔSH-line19F(I557V) BAC yielding A2-K-dNSh-ΔSH-dG-line19F(I557V) yielding the recovery BAC for OE4. The rescue of DB1 was previously described [9]. DB1–357/371 was generated through introduction of the line 19F residues K357 and Y371 into the DB1 coding sequence. The BAC for rescue of A2-del-M2-2 was generated by recombineering. We deleted 234 nt (from the seventh codon to the stop codon) of M2-2, as had been done previously for RSV ΔM2-2 [22]. The following

oligonucleotides were used to PRC-amplify the *galK* cassette for the first step of recombineering, delM2-1-f (5′-TTAGTGATACAAATGACCATGCCAAAAATAATGATACTACCTGACAAATACCTGTTGACAATTAATCATCGGCA-3′) and delM2-2-r (5′-ATTGTTTGAATTAATAATGTAACGATGTGGTGAGTGTTAGAATTGAGTGTTCAGCACTGTCCTGCTCCTT-3′). The following complementary oligonucleotides were annealed and used for the second recombineering step, M22_100f (5′-TTAGTGATACAAATGACCATGCCAAAAATAATGATACTACCTGACAAATAACACTCAATTCTAACACTCACCACATCGTTACATTATTAATTCAAACAAT-3′), and M22_100r (5′-ATTGTTTGAATTAATAATGTAACGATGTGGTGAGTGTTAGAATTGAGTGTTATTTGTCAGGTAGTATCATTATTTTTGGCATGGTCATTTGTATCACTAA-3′). Precise deletion of the targeted 234 nt was confirmed by sequencing. A version of OE4 without the mKate2 gene was also generated from pSynkRSV-dNS1-dNS2-ΔSH-line19F by excising the coding region containing the mKate2 gene with KpnI and AvrII. The resultant fragment containing mKate2 flanked by identical BlpI sites was then excised using BlpI, and the flanking fragments were ligated to generate pSynkRSV-dNS1-dNS2-ΔSH-line19F without mKate2. Recombinant viruses described in this paragraph were rescued in BSR-T7/5 cells [20], and virus stocks were propagated in Vero cells.

The panel of RSV strains used for quantification of RSV nAb titres in cotton rat anti-sera were generated by first having cDNAs of F and G genes of the following A and B strains synthesized (GeneArt, Invitrogen): RSVA/1998/12-21 (JX069802), Riyadh A/91/2009 (JF714706/JF714710); and RSV B strains NH1276 (JQ680988/JQ736678), 9320 (AY353550), and TX11-56 (JQ680989JQ736679). The G and F gene segments were cloned into the A2-K BAC by restriction

digestion and ligation, and the reporter viruses were recovered by transfection into BSR-T7/5 cells, followed by propagation of stocks in HEp-2 cells as was previously described [9].

RSV thermal stability

Virus aliquots were thawed at room temperature, pooled in 15 ml conical tubes, and mixed 1:1 with serum-free MEM before vortexing for 30 s. After vortexing, 1.5 ml of each virus suspension was transferred to replicate tubes to be incubated at either 4 or 37 °C in water baths. At designated time points, the tubes containing virus suspensions were removed, vortexed for 30 s each, and 300 µl was transferred to tubes then frozen in liquid nitrogen and stored at −80 °C. Quantification of titre was either determined by counting fluorescent focus units (FFU), if the virus was mKate2-expressing, or by plaque assay. For quantification by FFU titre, after all time points had been collected, samples were thawed on ice, vortexed 30 s, and serially diluted by 10-fold reductions in serum-free MEM in a 96 well plate. Once serially diluted, 50 µl of each dilution in triplicate was transferred to a 96-well plate containing confluent Vero cells. The virus was spinoculated onto the cells at 2,900*g* for 30 min at 4 °C before being overlaid with a 0.75% methylcellulose suspension in complete MEM. The plates were incubated at 37 °C for 2 days before FFU were counted. The methods for plaque assay have been previously described [19]. Plates of Vero cells infected for immunoplaque assay were incubated at 37 °C for 6 days prior to processing.

Pre-F antigen ELISAs

Virus aliquots were thawed and diluted in MEM to yield high-titre stock suspensions. Then 100 µl of each virus stock suspension was added in triplicate to wells in a 96-well Costar Assay Plate, High Binding (Corning). The plates were covered and incubated at room temperature overnight. The next

day, the virus suspension was dumped from the plate, and the plate was washed once with 150 μl per well of PBS-Tween (PBST, 0.05% Tween20 in PBS) followed by addition of 150 μl of 5% BSA (in PBS) per well for blocking. The plate was incubated at room temperature for 2 h. Pre-F-specific mAb MPE8 [23] was generated in HEK293-X2FreeStyle cells (U-Protein Express, BV) using human codon-optimized V_H and V_L sequences. Motavizumab mAb which binds pre-F and post-F was kindly provided by Nancy Ulbrandt (MedImmune/AZ). MPE8 and motavizumab antibodies were prepared by diluting the antibodies to 1 $\mu g\,ml^{-1}$ in PBS before further dilution of 1:10,000 to 1:320,000 by serial dilutions in 1% BSA. Following blocking, the plate was washed once again with 150 μl per well of PBST before 100 μl of the serially diluted primary antibodies were applied to the wells. The plate was incubated for 2 h at room temperature before being dumped and washed three times with 150 μl per well of PBST. After washing, 100 μl of a 1:10,000 dilution of anti-human-HRP antibody in 1% BSA was applied and the plate incubated for 1 h at room temperature. Then the plate was dumped and washed three times with 150 μl of PBST before 100 μl of a pre-mixed reactive substrate reagent mixture (R&D Systems) was applied to catalyse a colorimetric reaction. The plate was covered and incubated for ~10 min before the reaction was quenched by the addition of 100 μl of 0.2 N sulfuric acid. The plate was read at 450 nm on an ELISA plate reader. Background absorbance levels were subtracted from the test sample absorbance readings and plotted to a curve. The ratio of the area under the curve for MPE8 (pre-F) to the area under the curve for motavizumab (pre-F and post-F, total F) was calculated to determine pre-F level normalized to total F. The identical ELISA procedure was replicated using D25 instead of MPE8 as an additional measure of pre-F antigen levels.

To determine the stability of pre-F in OE4 compared with A2 at 4 °C over time, we incubated vials of virus for 0, 3 or 7 days and similarly applied 100 µl of each virus stock suspension in triplicate to wells in a 96-well Costar plate. We incubated the plates at 4 °C overnight, such that the final time points at time of measurement were 1, 4 and 8 days, respectively. We then performed ELISAs using MPE8 and motavizumab as above, but kept the plates and substrates at 4 °C or on ice for the remainder of the experiment.

Western blotting

Western blots were performed on infected Vero cell lysates harvested in RIPA buffer as described [8] using polyclonal rabbit antisera specific to NS1 (1:5,000) and NS2 (1:400; gifts from Michael Teng, USF Health), D14 (1:5,000; anti-RSV N; gift from Edward Walsh, University of Rochester), 131-2G (1:2,000; anti-RSV G, MAB858-2-5; Millipore), motavizumab (1:5,000; anti-F; gift from Nancy Ulbrant) or GAPDH (1:5,000), followed by peroxidase-conjugated anti-rabbit, anti-mouse or anti-human secondary antibodies (1:10,000; Jackson ImmunoResearch) (Figure 3 and Supplementary Figure 8). Densitometry analyses were performed using Image Lab software (Bio-Rad).

Viral replication in immortalized and primary cell cultures

The media from 70% confluent Vero or BEAS-2B cells in six-well plates was aspirated, and 0.5 ml of virus at a multiplicity of infection (MOI) of 0.01 was added to replicate wells for each of the time points to be acquired for each virus strain. The plates were rocked at room temperature for 1 h. Following infection, the virus was carefully aspirated and the monolayers washed twice with 1 ml of PBS before 2 ml of pre-warmed complete E-MEM (Vero) or RPMI (BEAS-2B) was added. The plates were incubated at 37 °C and 5% CO_2 for the duration of the time courses. Time points were acquired at 1, 12, 24, 36, 48, 72 and 96 h post infection. At each time point, the monolayers were

scrapped into the supernatant, vortexed briefly and flash frozen in liquid nitrogen before storage at −80 °C. NHBE cells from two donors were differentiated at ALI and the monolayers washed with PBS before being infected apically with 100 µl of virus at an MOI of 2.6. The virus was left to incubate for 2 h at 37 °C before removal and three subsequent washes with PBS. At designated time points, 150 µl of differentiated medium without inducer was incubated on the apical surface for 10 min at 37 °C before harvesting and transfer into microcentrifuge tubes. The process was repeated to yield a total of 300 µl of pooled apical wash, which was frozen in liquid nitrogen and stored at −80 °C for later titration. Similar to the NHBE infection, HAE cells from two donors were differentiated at ALI, the apical surface washed with PBS, and infected with an initial MOI of 6.7. Following 2 h incubation at 37 °C, the virus inoculum was aspirated, the apical layer washed three times with PBS and the culture incubated at 37 °C. For each designated time point, the apical layers were washed with 425 µl of media for 30 min at 37 °C and the supernatant stored at −80 °C. FFU titration was performed for all analyses as described above on either HEp-2 or Vero cells.

Attenuation and efficacy in mice

For determination of viral load, 7-week-old female BALB/c mice (Charles River) were infected i.n. under sedation with 100 µl of virus in serum-free MEM. On days 2, 4, 6 and 8, the mice were euthanized and the left lung harvested and homogenized for viral FFU titre assay. Titres below the limit of detection were assigned a value equal to half of the limit of detection. To assess the genetic stability of OE4 NS1, NS2, F and G genes *in vivo*, we also used the lung homogenate from day 6 post infection to sequence the genes of interest after passage in mice. We first isolated viral RNA directly from lung homogenate using Nucleospin RNA purification kit (Macherey-Nagel) and performed reverse transcription using SuperScript III reverse transcriptase (Thermo-Fisher). We

then amplified regions of interest using PfuTurbo DNA polymerase (Agilent) and obtained sequences via GenHunter Corp.

For determination of serum nAb titres and challenge studies, 7-week-old female BALB/c mice (Jackson) were infected i.n. with 100 µl of virus in serum-free MEM. On days 35, 70 and 100, the mice were sedated and serum samples obtained via submandibular vein bleeding. Sera were stored at −80 °C until quantification by a FFU microneutralization assay [8]. Neutralization titres were determined by co-incubating heat-inactivated (56 °C, 30 min) sera, which had been two-fold serially diluted with 50–100 FFU of virus for 1 h at 37 °C. The serum-virus mixtures were then spinoculated onto HEp-2 monolayers in 96-well plates at 2,900*g* for 30 min at 4 °C before being overlaid with 0.75% methylcellulose in complete MEM. FFU per well were counted 2 days later, and EC50 titres were determined by nonlinear regression analysis (GraphPad Prism). To challenge the mice after vaccination, the mice were sedated on day 102 post inoculation and infected i.n. with 10^5 PFU A2-line19F. After 4 days, the viral load was determined on the left lung by plaque assay on HEp-2 cells.

Histopathology in mice

Female 8-week-old BALB/c mice (Jackson) were sedated and infected intranasally with either mock solution or 10^5 FFU of A2, A2-line19F, OE4 or A2-del-M2-2. After 8 days, the lungs were harvested, fixed, sectioned and stained with Periodic acid-Schiff (PAS). Morphometric quantification of airway PAS positivity was performed on digitized slides using a Mirax digital pathology system (Zeiss) and Histoquant software as previously described [19]. All airways in the sections were analysed.

Attenuation and efficacy in cotton rats

For determination of viral load in naive animals, 8- to 10-week-old male and female cotton rats were sedated and inoculated i.n. with 10^5 FFU of virus in 100 μl in serum-free MEM at Baylor College of Medicine. On day 4 post infection, the cotton rats were killed. For acquisition of lung lavage washes, the left lobe of the lung was excised and transpleurally lavaged with 3 ml of Iscove's media with 15% glycerin mixed with 2% FBS-MEM (1:1). For acquisition of nasal wash, the jaws were first disarticulated and the head was removed. A solution of 1 ml of Iscove's media with 15% glycerin mixed with 2% FBS-MEM (1:1) was washed through each nare for a total of 2 ml of volume. Titration was performed by plaque assay on HEp-2 cell monolayers. For determination of nAb titres, 8- to 10-week-old male and female cotton rats at Baylor College of Medicine were sedated and inoculated i.n. with 10^5 FFU of virus in 100 μl of serum-free MEM. On day 42, serum was obtained via the orbital plexus of the cotton rats and stored at −80 °C until analysed as described above. To assess efficacy, cotton rats were challenged on day 42 post infection (following i.n. vaccination with 3×10^5 FFU) with 1×10^6 FFU i.n. of RSV strain A2-line19F at Sigmovir Biosystems Inc. On day 4 post challenge, the nasal turbinates were homogenized in 3 ml of HBSS supplemented with 10% SPG, and the left lung was homogenized in 3 ml of HBSS supplemented with 10% SPG. The nasal and lung tissue titres were determined by plaque assay as described above.

Enhanced disease study in cotton rats

Groups of five 6- to 8-week-old female cotton rats were vaccinated intranasally with either 10^5 FFU of OE4, MEM (mock treatment), or intramuscularly with FI-RSV (lot 100; 1:125) at Sigmovir, Inc. On day 21, FI-RSV-vaccinated rats were boosted with a second identical vaccination. On day 42, all cotton rats were challenged intranasally with 1.35×10^5 PFU of A2-line19F. On day 48 (day 6 post challenge), the cotton rats were killed and the lungs excised, perfused with 10% formalin and

sections of paraffin-embedded inflated lungs were stained with hematoxylin-eosin (H&E). The slides were scored by a pathologist blinded to the groups on a scale of 0 to 4 based on increasing severity of peribronchial mononuclear inflammatory cell infiltration, perivascular mononuclear inflammatory cell infiltration, interstitial pneumonitis and alveolitis.

Cryo-ET

BEAS-2B cells were seeded on gold R2/1 Quantifoil TEM grids in MatTek dishes and were infected when subconfluent (30–40%) at an MOI of 10 using A2 and OE4 strains. Twenty-four hours post infection, infected cells on gold Quantifoil TEM grids were plunge frozen using a Gatan CryoPlunge 3 apparatus (Gatan, Inc., Pleasanton, CA). For the A2 strain that was heat-treated, BEAS-2B cells were seeded on gold R2/1 Quantifoil TEM grids in MatTek dishes and were infected when subconfluent (30–40%) at an MOI of 10 with the A2 strain. Twenty-four hours post infection, the MatTek dishes containing TEM grids were incubated for 30 min at 55 °C [24]. Immediately after heat treatment, infected cells on gold Quantifoil TEM grids were plunge frozen using a CryoPlunge 3 apparatus. In all instances, 4 μl of BSA-conjugated 10 nm gold nanoparticles was applied onto the TEM grid prior to cryoplunging. Cryogrids were stored in liquid nitrogen prior to imaging with a JEOL JEM-2200FS TEM at 200 kV (JEOL Ltd., Japan), which is equipped with a field emission gun, an in-column Omega energy filter with a slit width of 20 eV. Tilt series were recorded semi-automatically using the SerialEM package from −65° to 65° at 2° increment step, −6 μm defocus, with a total dose of ~120 e^{-} $Å^{-2}$ [25-28]. Images were recorded on a Direct Electron DE-20 camera (Direct Electron, LP, San Diego, CA) at 12 frames per second at a nominal magnification of 10,000 resulting in a pixel size of 0.614 nm.

Tilt series frames were motion corrected prior to tomographic reconstruction using python scripts provided by the manufacturer (Direct Electron, LP). Motion corrected frames were used for tomographic reconstruction in the IMOD software package using the weighted back-projection algorithm, and the 10 nm gold nanoparticles were used as fiducials to align frames at the different tilt angles [29]. Reconstructed three-dimensional volumes (unbinned and binned by a factor of 2) were also CTF-corrected by inversing the phase and de-noised by nonlinear anisotropic diffusion.

Subvolume averaging and model fitting

Subvolumes of RSV glycoproteins were manually selected (3,827, 2,567 and 1,313 subvolumes for A2, OE4 and A2-heat, respectively) from tomograms binned by a factor of 2, using EMAN2 *e2spt_boxer.py* script [30]. Initially, two-fold binned data were used in the subvolume averaging process. Alignments and averaging were performed in PEET 1.11.0 Alpha version, and each subvolume was normalized ('flgNormalize=1') prior to alignment and averaging [31]. Initial orientations of the subvolumes were determined using SpikeInit. Particles were considered duplicates if the centre-to-centre distance was <60 Å for A2 and OE4 and 40 Å for A2-heat samples; only the ones with the highest cross-correlation coefficient values were kept. The initial reference was a previously published post-fusion F glycoprotein (EMDB-2393) low-pass filtered to 60 Å. A soft-edged cylinder mask was applied during alignment to eliminate contributions from the neighbouring particles. Using the two-fold binned data, six iterations were run with missing wedge compensation (eight weight groups) and the resulting averages indicated three-fold symmetry, consistent with the crystal structures. Thus, we imposed C3 symmetry by creating a three-fold symmetric data set: the first set are the aligned particles, the second and third sets have all the same tilt angles and positions as the first set, but with either 120° or 240° of twist rotation along the *y* axis applied using *modifyMotiveList* in PEET. The initial subvolume averages were used as references for

refinements with C3 symmetry imposed, and three more iterative refinements were run with smaller transitional and angular search ranges and increasing high-frequency cutoff values. The respective translation information from the two-fold binned data were scaled by a factor of two to match the unbinned tomograms, and were used as input MotiveList for three more iterative refinements on the unbinned data. The final subvolume averages (final pixel size of 6.14 Å, unbinned) with C3 symmetry were reconstructed from 2,268, 1,687 and 823 subvolumes, for A2, OE4 and A2-heat, respectively. The final density maps of F were low-pass filtered to FSC=0.143 cutoff calculated in PEET, and masked using a soft edged cylinder generated using SPIDER [32]. The atomic crystal structures of pre-fusion and post-fusion F glycoprotein (PDB IDs 4JHW and 3RRT, respectively) were manually fitted into the final electron density maps using Chimera [33].

Immuno-TEM

BEAS-2B cells were seeded on Alcar disks in 24-well plates and were infected when subconfluent (50–70%) at an MOI of 10 using A2 and OE4 strains. Twenty-four hours post infection, anti-pre-F (MPE8) [23], anti-post-F (131-2A) [34, 35], anti-F (motavizumab, gift from Nancy Ulbrant) and anti-G (131-2G, MAB858-2-5; Millipore), primary antibodies were added to RPMI-1640 medium at a final concentration of 5 $\mu g\,ml^{-1}$. After primary antibody incubation for 1.5 h at 37 °C, cells were washed four times with RPMI-1640 medium, and then incubated for 1.5 h at 37 °C with goat anti-human (used for MPE8 and motavizumab) or goat anti-mouse (used for 131-2A and 131-2G) secondary antibody conjugated to 6 nm gold particles in RPMI-1640 medium at a final concentration of 10–20 $\mu g\,ml^{-1}$. Following additional medium washes, cells were fixed in 2.5% glutaraldehyde at 4 °C overnight. The next day, fixed cells on Aclar disks were washed with 0.1 M phosphate butter (pH 7.4) followed by pre-fixation with 1% OsO_4 in 0.1 M phosphate buffer for 1 h. The cells were then washed with deionized water before dehydration at 5 min intervals in graded concentrations of

ethanol (25, 50, 75, 95 and 100%). The cells were then treated with a 1:1 resin mixture of 100% ethanol and Eponate 12 for 1 h, followed by polymerization with 100% Eponate 12 resin overnight in the oven. Ultrathin sections were cut between 60 and 80 nm in thickness, and then stained using 5% uranyl acetate and 2% lead citrate. Sections were imaged as montages using SerialEM software on a JEOL JEM-1400 TEM (JEOL Ltd., Japan) equipped with a Gatan US1000 2 k × 2 k CCD camera (Gatan) at × 8,000 nominal magnification [25, 36, 37].

Montages were assembled using sloppyblend.com script, and further measurements and quantification were done using the blended maps. The six groups of data (70 montages, 1,515 viral particles) were randomly blinded among groups prior to quantification. Total membrane length of a viral particle was measured using *imodinfo* command by placing open model points along the viral membrane, where distinct membrane morphology is present. The 6 nm immunogold particles on both sides of viral particle membranes were counted separately. Gold particle intensity per particle was calculated using total gold particles on the viral membrane divided by total viral membrane length (gold particles per μm of membrane length). Representative images for the immuno-TEM were selected based on the average gold particle intensities along the membrane.

Statistical analyses

All statistical analyses were computationally performed using GraphPad Prism. The number of replicates and type of statistical analysis performed are described for all experiments in the figure legends. No statistical methods were used in predetermining sample sizes.

RESULTS

Pre-fusion F ELISAs

Metastable pre-F undergoes a dynamic transition to form a thermodynamically stable six-helix post-fusion bundle that facilitates viral and host membrane fusion [10, 14]. Since both pre-F and post-F are present on RSV virions in prepared virus stocks [25, 36], we evaluated the relative amount of pre-F antigen in RSV stocks using an ELISA-based approach to compare MPE8 with motavizumab antibody binding. MPE8 is a human monoclonal antibody that preferentially binds to two highly conserved anti-parallel β-strands on pre-F, which are rearranged in the post-fusion conformation to render them less accessible to antibody binding [23]. Motavizumab, in contrast, stably binds to both pre- and post-fusion F. We found that strain A2-line19F, which expresses the F protein of strain line 19 in the background of the prototypical A2 strain [19, 38], exhibited significantly higher relative binding to MPE8 than did strain A2 (Figure 1a). We confirmed this finding using the human monoclonal antibody D25, which binds to a distinct antigenic site on pre-F (antigenic site Ø) [10] with even greater specificity than MPE8 [39]. We found that A2-line19F exhibited higher relative binding to D25 than A2, which was similar in magnitude and correlated with MPE8 binding (Figure 1b).

Five unique amino-acid residues distinguish line 19F from A2 F: M79, R191, K357, Y371 and I557 (Supplementary Figure 1) [19]. We generated A2-line19F mutants by substituting A2 residues in place of the unique line 19F residues [19]. To determine the effects of these residues on pre-F antigen levels in virus stocks, we performed MPE8 and motavizumab ELISAs on the recombinant A2-line19F mutant viruses. We found that residues M79, K357 and Y371 contributed to line 19 F pre-F antigen levels (Figure 1a). These results were consistent with previous data showing that the K357/Y371 residues together impeded A2-line19F fusion activity *in vitro [19]*.

Thermal stability assays

We next evaluated the thermal stability of A2-line19F compared with A2. RSV is known to be a heat-labile virus, and elevated temperatures can trigger the transition from pre- to post-fusion F [24]. We therefore hypothesized that RSV with enhanced pre-F levels would be more resistant to temperature inactivation. We analysed thermostability at 4 and 37 °C because thermostability at 4 °C may have implications for retention of vaccine potency in cold chain, whereas thermostability at 37 °C has more relevance for physiological conditions. We found that RSV A2-line19F infectivity was more thermostable over time than A2 at both temperatures (Figure 2a,b), a phenotype that was mediated in part by the residues K357 and Y371 (Figure 2c). We then introduced K357 and Y371 into the F of a genetically divergent vaccine strain DB1, which expresses a consensus F gene of the antigenic subgroup B 'Buenos Aires' (BAF) clade. We previously described the generation of DB1, which also contains codon-deoptimized non-structural protein genes and deleted SH gene, with a genotype RSV-A2-dNS1-dNS2-ΔSH-BAF [9]. DB1 expressed low levels of pre-F antigen and was thermally unstable; however, incorporation of the K357 and Y371 residues to generate DB1–357/371 enhanced MPE8 binding (Figure 1a) and partially restored thermal stability (Figure 2d). These data demonstrated that residues 357 and 371 modulated not only MPE8 binding, a correlate of pre-F antigen levels, but also viral resistance to thermal inactivation in viral stocks.

Generation of RSV live-attenuated vaccine OE4

We next generated a novel RSV LAV called OE4, by incorporating line 19F into a multi-component vaccine designed to achieve attenuation, improved immunogenicity and genetic stability. We previously codon-deoptimized the NS1 and NS2 genes, which encode two nonstructural proteins of RSV that suppress host innate immunity by targeting interferon pathways and suppressing apoptosis [40, 41]. Codon deoptimization of NS1 and NS2 genes was genetically stable and reduced NS1 and

NS2 protein expression, resulting in virus attenuation with slightly enhanced immunogenicity in mice [8]. We subsequently deleted the small hydrophobic (SH) protein gene with the goal of increasing the transcription of downstream viral genes, including F, by altering their proximity to the viral leader [42]. The deletion of SH is also mildly attenuating in mice and chimpanzees, but conferred no apparent attenuation in a vaccine candidate in children [42-44]. Last, we codon-deoptimized the RSV attachment (G) glycoprotein gene and ablated the secreted form of G by a point mutation. RSV expresses a membrane-bound form (G_m) and a secreted form (G_s) of G, which are not required for viral replication in immortalized cell lines [45-48]. RSV G is capable of eliciting protective neutralizing antibodies [34]. However, G is less conserved than F and suppresses the innate immune response through chemokine mimicry [49, 50]. G functions as an antigen decoy and can alter dendritic cell signalling and activation through interactions with C-type lectins [51, 52]. The resulting genotype of the OE4 vaccine candidate was RSV-A2-dNS1-dNS2-ΔSH-dG_m-Gs_{null}-line19F (Figure 3a). Using western blotting, we demonstrated that OE4 had decreased expression levels of NS1, NS2 and G as expected compared with parental A2 (Figure 3b,c). We additionally found that OE4 had higher levels of F expression than A2-line19F, likely attributable to the deletion of SH (Figure 3d,e).

Analysis of OE4 surface glycoproteins

We analysed the MPE8 and D25 binding of OE4 and measured vaccine thermal stability at 4 and 37 °C. Similar to A2-line19F, OE4 exhibited high relative pre-F antigen levels by antibody binding (Figure 1a,b) and thermal stability (Figure 2a,b) consistent with its expression of the line 19F protein. We further explored this relationship by quantifying pre-F stability as measured by MPE8 binding of OE4 and A2 from virus stocks incubated at 4 °C over time. Relative pre-F antigen levels declined in both viruses over a period of 8 days (Supplementary Figure 2a). Therefore, the kinetics of thermal

stability of A2 and OE4 infectivity did not correlate with the decay of pre-F antigen levels. However, OE4 maintained greater than twice the levels of pre-F antigen levels at each time point compared with A2 (Supplementary Figure 2b), and a minimal threshold of pre-F may be sufficient to maintain infectivity.

In order to assess the overall structure of the virions and glycoprotein incorporation into RSV A2 and OE4, we then performed thin-section transmission electron microscopy (TEM), native immuno-TEM, and cryo-electron tomography (cryo-ET) of viruses budded from BEAS-2B cells, an immortalized human bronchial epithelial cell line. In all cases, virus-infected cells and released virions were analysed following minimal sample processing to maximize preservation of the native structure of the virions. First, native immunogold labelling combined with thin-section TEM was performed using mAbs that preferentially bound pre-F (MPE8), post-F (131-2A), total F (motavizumab) or G (131-2G) (Figure 4a) [26]. The density of gold particles per membrane length was quantified for each virus and immunolabel (Figure 4b) [53]. OE4 virus particles exhibited a greater density of incorporated pre-F and total F than A2, potentially due to the deletion of SH. There was no significant difference in the amount of post-F detected on the surfaces of A2 and OE4 particles. G protein density on OE4 particles was significantly reduced, as was expected in the setting of codon-deoptimization of the G gene.

When visualized by cryo-ET, A2 and OE4 virus particles were morphologically similar and formed filaments with abundant glycoprotein spikes on the surface, matrix protein lining the inside of the viral membrane, and ribonucleoprotein complex in the interior of the virions (Figure 5a–c) [25, 26, 36]. To further investigate the conformations of RSV F on the surfaces of A2 and OE4 virions in their native states, we then calculated subvolume averages of F structures from the cryo-ET data.

These studies demonstrated that the majority of F proteins on both viruses in their native states immediately after budding was in the pre-F conformation (Figure 5). The application of heat (55 °C for 30 min) triggered the conformational change from pre- to post-F, providing direct evidence of the relationship between temperature and pre-F stability (Figure 5c,f,i,j).

Characterization of OE4 in cell culture and primary cells

We next characterized the OE4 vaccine candidate *in vitro* by measuring attenuation levels in immortalized cells and in primary human airway epithelial cells (Figure 6). In Vero cells, which were used for virus stock generation, OE4 grew to titres slightly below the parental unattenuated A2-line19F (Figure 6a). OE4 was more attenuated relative to wild type in BEAS-2B cells (Figure 6b). We then evaluated OE4 growth in primary human airway epithelial cells, which are an established system for approximating RSV LAV attenuation in seronegative children [54]. We implemented two models, NHBE-ALI and HAE-ALI, and found that OE4 was significantly attenuated in both models (Figure 6c,d) and exhibited deficiency in spreading through the cultures (Figure 6e). The codon deoptimization of G in OE4 contributed significantly to the level of attenuation compared with OE4 expressing wild type G (OE4+wtG) in NHBE-ALI (Figure 6c), likely due to the previously described attachment role of G in primary cells [46].

Characterization of OE4 in BALB/c mice

To measure relative levels of attenuation *in vivo*, we inoculated mice intranasally (i.n.) and measured lung viral loads on days 2, 4, 6 and 8 post infection. We found that OE4 was moderately attenuated compared with A2 and A2-line19F in this model (Figure 7a). We compared lung viral loads of mice inoculated with OE4 with and without the mKate2 gene and found that reporter had no effect on viral attenuation (Supplementary Figure 3), consistent with previously published results [20]. We

sequenced the NS1, NS2, G and F genes of OE4 from virus recovered from mouse lungs on day 6 post infection, and there were no mutations in these genes. To analyse immunogenicity, we then vaccinated mice and measured nAb titres on days 35, 70 and 100 and found that OE4 elicited nAb titres equivalent to A2-line19F and higher than A2 at each time point post infection (Figure 7b). Following i.n. inoculation, the mice were then challenged on day 102 with A2-line19F, and the OE4-vaccinated mice were completely protected against the challenge (Figure 7c). We next measured OE4 mucus production in the lungs of mice. We previously demonstrated that A2-line19F induces increased airway mucin expression, a measure of pathogenicity in this model [19, 38]. However, OE4, which also expresses line 19F, induced lower levels of airway mucin expression than A2-line19F in mice (Figure 7d and Supplementary Figure 4), indicating that the attenuating genetic modifications in OE4 modulated the mucogenic phenotype. Subsequently, we compared OE4-induced mucin expression with a reconstituted RSV mutant containing a deletion of M2-2 (A2-del-M2-2), the primary genetic modification of a clinically advanced LAV candidate [7]. The deletion of M2-2 results in reduced viral replication and elevated transcription of downstream RSV genes (for example, NS1, NS2, SH, G, F and so on), which represents a different attenuation strategy than OE4. It should be noted that our reconstituted A2-del-M2-2 is not identical to MEDI-ΔM2-2 due to minor genetic differences between the A2 backbones. Because the deletion of M2-2 results in increased levels of non-essential virulence proteins, we hypothesized that A2-del-M2-2 would be mucogenic in mice. Compared with OE4, we found that A2-del-M2-2 induced significantly more airway mucin expression (Figure 7d and Supplementary Figure 4).

Characterization of OE4 in cotton rats

OE4 attenuation and immunogenicity were next evaluated in cotton rats, a more permissive model of RSV infection. In cotton rats, OE4 was highly attenuated in the upper and lower respiratory tracts, and more attenuated than A2-del-M2-2 (Figure 7e,f). Despite significant attenuation, OE4 induced relatively high levels of serum nAb against a panel of RSV strains representing RSV diversity (Figure 7g). OE4-vaccinated cotton rats were completely protected against RSV challenge, not only in lungs (Figure 7h) but also in the upper respiratory tracts (Figure 7i). Thus, OE4 established effective mucosal immunity despite being highly attenuated in cotton rats.

Last, a primary concern highlighted by the failure of the FI-RSV vaccine candidate is the potential for vaccine-enhanced priming for disease on natural RSV infection. Although RSV LAV candidates have not been shown to cause enhanced illness, we evaluated whether the novel vaccination strategy employed by OE4 would prime for enhanced disease upon challenge in cotton rats. Results demonstrated that RSV challenge did not cause enhanced histopathology following infection with OE4 compared with mock (Figure 8). In contrast, FI-RSV did result in enhanced disease associated with elevated peribronchiolar infiltration and alveolitis.

DISCUSSION

We identified a chimeric RSV strain A2-line19F that had increased relative MPE8 binding, increased thermal stability in viral stocks and increased immunogenicity *in vivo* compared with parental strain A2. A2-line19F differs from A2 by only five unique residues within the F protein. Incorporation of two of these residues (357/371) into a heterologous vaccine strain DB1 conferred increased relative MPE8 binding and increased thermal stability at 4 °C. To exploit these properties in an RSV LAV, we incorporated the line 19F protein into a rationally designed vaccine candidate OE4 with the genotype RSV-A2-dNS1-dNS2-ΔSH-dG_m-G_{Snull}-line19F. Like A2-line19F, OE4 had increased relative MPE8 and D25 binding and increased thermal stability compared with RSV A2. OE4 was also immunogenic and highly efficacious in BALB/c mice and cotton rats, despite significant levels of attenuation *in vitro* and *in vivo*. The mutations incorporated into OE4 were genetically stable in virus recovered from BALB/c mice. Furthermore, lung histopathologic staining demonstrated that OE4 was not mucogenic in mice, nor did it cause enhanced histopathology following RSV challenge in cotton rats.

One inherent limitation of our study is that neither mice nor cotton rats fully recapitulate RSV disease in humans. In our study, for example, we observed a difference in the attenuation levels of OE4 in our two animal models. Whereas OE4 was highly attenuated in cotton rats and in human primary airway epithelial cells, it was less attenuated in BALB/c mice. We also found that OE4 was more immunogenic in BALB/c mice than in cotton rats. We suspect these discrepancies were attributable to strain-specific differences in the attachment and infectivity of the line 19F protein and the differential effects of codon-deoptimized G protein in cotton rats compared with mice. For example, Teng *et al.* demonstrated that deletion of G from an RSV clinical stain was completely attenuating in cotton rats [48], whereas Widjojoatmodjo *et al.* [55] found that RSV-ΔG was only

moderately attenuated in mice. Nevertheless, OE4 was significantly attenuated in both animal models and was capable of inducing protective neutralizing antibodies.

A second limitation of our study relates to the utilization of MPE8 and D25 ELISAs to quantify pre-F antigen levels in viral stocks. Both MPE8 and D25 are monoclonal antibodies that preferentially bind to the pre-fusion conformation of F; however, the conformational specificities of these two antibodies have not been fully validated. MPE8, in particular, competes with palivizumab [23] and binds only 10–20 times better to pre- than post-fusion F [39]. D25, in contrast, binds at the apex of the pre-fusion trimer at the antigenic site Ø which undergoes marked structural rearrangement upon transition to post-F [10]. Thus, D25 binds with even greater specificity to pre- than post-F (100-fold) [39]. Nevertheless, limited cross-reactivity with post-F has been observed, and a monomeric form of F has also been identified which retains pre-fusion-specific epitopes [13, 56]. Despite these limitations, both MPE8 and D25 demonstrate relatively high pre-F specificity, and generated consistent results among the viruses analysed in this study.

Native immunogold labelling combined with thin-section TEM also demonstrated increased pre-F and total F on the surface of OE4 compared with A2. We suspect the increased incorporation of total F into OE4 was attributable to the deletion of the SH gene, which shifted the F gene towards the viral promoter. The vast majority of F in both OE4 and A2 was in the pre-fusion conformation, likely because the virions were maintained in their native states and not subjected to viral harvesting and stock preparation. Subvolume averaging of the F structures confirmed that the majority of F was in the pre-fusion conformation. However, application of heat to A2 triggered the conformational change to post-F, clearly demonstrating a relationship between temperature and pre-F stability. Although these results demonstrate that heat triggers the transition from pre- to post-

fusion F, the relationship between temperature and pre-F stability remains incompletely defined. Similarly, the favourable immunogenicity to attenuation profile of OE4 is likely multifactorial and cannot be attributed specifically to the expression of pre-fusion F or to thermostability.

In conclusion, we identified key molecular determinant positions of RSV line 19F which were associated with both thermal stability and the availability of the pre-F antigen. Genetically modifying these residues to thermally stabilize and boost immunogenicity of RSV LAVs represents a promising new approach to next-generation RSV vaccine design. Using reverse genetics, we rationally designed a novel RSV LAV OE4 that incorporated line 19F into the genotype RSV-A2-dNS1-dNS2-ΔSH-dG_m-G_{Snull}-line19F. In addition to being thermally and genetically stable, OE4 was also highly immunogenic and efficacious despite significant attenuation *in vitro* and *in vivo*. These data demonstrate that we fundamentally altered RSV immunogenicity and generated a promising LAV candidate that merits further investigation.

ACKNOWLEDGEMENTS

This work was supported by R01 AI087798 (M.L.M.), U19 AI095227 (M.L.M.), T32 AI074492 (C.C.S.), K12 HD072245 (C.A.R.), and the Emory Children's Center for Childhood Infections and Vaccines (CCIV). This work was also supported in part by Emory University, Children's Healthcare of Atlanta, and the Georgia Research Alliance to E.R.W.; the Center for AIDS Research at Emory University (P30 AI050409); the James B. Pendleton Charitable Trust to E.R.W.; public health service grants R21 AI101775, R01 GM114561, to E.R.W. from the NIH, and NSF grant 0923395 to E.R.W., and S10 RR025679. We thank Ursula Buchholz (National Institute of Allergy and Infectious Diseases, Bethesda, MD) for the BSR-T7/5 cells used for virus recovery; Michael Teng (University of South Florida, Tampa, FL) for the rabbit antisera against NS1 and NS2 used for Western blot analysis; Nancy Ulbrandt (MedImmune, Inc., Gaithersburg, MD) for motavizumab; Jeannette Taylor (Emory University, Atlanta, GA) for her assistance and guidance with the TEM immunolabeling experiments; John Heumann (University of Colorado, Boulder, CO) for his advice using PEET; and the Robert P. Apkarian Integrated Electron Microscopy Core of Emory University for microscopy services. The cotton rat studies performed at Baylor College of Medicine were supported by the Division of Microbiology and Infectious Diseases (DMID) of the National Institute of Allergy and Infectious Diseases (NIAID) (HHSN272201000004I).

REFERENCES

1. Kim, H. W., Canchola, J. G., Brandt, C. D., Pyles, G., Chanock, R. M., Jensen, K., and Parrott, R. H. Respiratory syncytial virus disease in infants despite prior administration of antigenic inactivated vaccine. *Am J Epidemiol*, 1969. **89**(4): p. 422-&.

2. Schickli, J. H., Dubovsky, F., and Tang, R. S. Challenges in developing a pediatric RSV vaccine. *Hum Vaccines*, 2009. **5**(9): p. 582-591.

3. Murphy, B. R., Sotnikov, A. V., Lawrence, L. A., Banks, S. M., and Prince, G. A. Enhanced pulmonary histopathology is observed in cotton rats immunized with formalin-inactivated respiratory syncytial virus (RSV) or purified F-glycoprotein and challenged with RSV 3-6 months after immunization. *Vaccine*, 1990. **8**(5): p. 497-502.

4. Connors, M., Collins, P. L., Firestone, C. Y., Sotnikov, A. V., Waitze, A., Davis, A. R., Hung, P. P., Chanock, R. M., and Murphy, B. R. Cotton rats previously immunized with a chimeric RSV fg glycoprotein develop enhanced pulmonary pathology when infected with RSV, a phenomenon not encountered following immunization with vaccinia RSV recombinants or RSV. *Vaccine*, 1992. **10**(7): p. 475-484.

5. Wright, P. F., Karron, R. A., Belshe, R. B., Shi, J. R., Randolph, V. B., Collins, P. L., O'Shea, A. F., Gruber, W. C., and Murphy, B. R. The absence of enhanced disease with wild type respiratory syncytial virus infection occurring after receipt of live, attenuated, respiratory syncytial virus vaccines. *Vaccine*, 2007. **25**(42): p. 7372-7378.

6. Collins, P. L. and Melero, J. A. Progress in understanding and controlling respiratory syncytial virus: Still crazy after all these years. *Virus Res*, 2011. **162**(1-2): p. 80-99.

7. Karron, R. A., Luongo, C., Thumar, B., Loehr, K. M., Englund, J. A., Collins, P. L., and Buchholz, U. J. A gene deletion that up-regulates viral gene expression yields an attenuated

RSV vaccine with improved antibody responses in children. *Sci Transl Med*, 2015. **7**(312): p. 312ra175.

8. Meng, J., Lee, S., Hotard, A. L., and Moore, M. L. Refining the balance of attenuation and immunogenicity of respiratory syncytial virus by targeted codon deoptimization of virulence genes. *mBio*, 2014. **5**(5): p. e01704-14.
9. Rostad, C. A., Stobart, C. C., Gilbert, B. E., Pickles, R. J., Hotard, A. L., Meng, J., Blanco, J. C. G., Moin, S. M., Graham, B. S., Piedra, P. A., and Moore, M. L. A recombinant respiratory syncytial virus vaccine candidate attenuated by a low-fusion F protein is immunogenic and protective against challenge in cotton rats. *J Virol*, 2016. **90**(16): p. 7508-7518.
10. McLellan, J. S., Chen, M., Leung, S., Graepel, K. W., Du, X., Yang, Y., Zhou, T., Baxa, U., Yasuda, E., Beaumont, T., Kumar, A., Modjarrad, K., Zheng, Z., Zhao, M., Xia, N., Kwong, P. D., and Graham, B. S. Structure of RSV fusion glycoprotein trimer bound to a prefusion-specific neutralizing antibody. *Science*, 2013. **340**(6136): p. 1113-1117.
11. Ngwuta, J. O., Chen, M., Modjarrad, K., Joyce, M. G., Kanekiyo, M., Kumar, A., Yassine, H. M., Moin, S. M., Killikelly, A. M., Chuang, G.-Y., Druz, A., Georgiev, I. S., Rundlet, E. J., Sastry, M., Stewart-Jones, G. B. E., Yang, Y., Zhang, B., Nason, M. C., Capella, C., Peeples, M. E., Ledgerwood, J. E., McLellan, J. S., Kwong, P. D., and Graham, B. S. Prefusion F-specific antibodies determine the magnitude of RSV neutralizing activity in human sera. *Sci Transl Med*, 2015. **7**(309).
12. Krarup, A., Truan, D., Furmanova-Hollenstein, P., Bogaert, L., Bouchier, P., Bisschop, I. J. M., Widjojoatmodjo, M. N., Zahn, R., Schuitemaker, H., McLellan, J. S., and Langedijk, J. P. M. A highly stable prefusion RSV F vaccine derived from structural analysis of the fusion mechanism. *Nat Commun*, 2015. **6**.

13. Palomo, C., Mas, V., Thom, M., Vazquez, M., Cano, O., Terron, M. C., Luque, D., Taylor, G., and Melero, J. A. Influence of respiratory syncytial virus F glycoprotein conformation on induction of protective immune responses. *J Virol*, 2016. **90**(11): p. 5485-5498.

14. McLellan, J. S., Chen, M., Joyce, M. G., Sastry, M., Stewart-Jones, G. B. E., Yang, Y., Zhang, B., Chen, L., Srivatsan, S., Zheng, A., Zhou, T., Graepel, K. W., Kumar, A., Moin, S., Boyington, J. C., Chuang, G.-Y., Soto, C., Baxa, U., Bakker, A. Q., Spits, H., Beaumont, T., Zheng, Z., Xia, N., Ko, S.-Y., Todd, J.-P., Rao, S., Graham, B. S., and Kwong, P. D. Structure-based design of a fusion glycoprotein vaccine for respiratory syncytial virus. *Science*, 2013. **342**(6158): p. 592-598.

15. McGinnes Cullen, L., Schmidt, M. R., Kenward, S. A., Woodland, R. T., and Morrison, T. G. Murine immune responses to virus-like particle-associated pre- and postfusion forms of the respiratory syncytial virus F protein. *J Virol*, 2015. **89**(13): p. 6835-6847.

16. Liang, B., Surman, S., Amaro-Carambot, E., Kabatova, B., Mackow, N., Lingemann, M., Yang, L., McLellan, J. S., Graham, B. S., Kwong, P. D., Schaap-Nutt, A., Collins, P. L., and Munir, S. Enhanced neutralizing antibody response induced by respiratory syncytial virus prefusion F protein expressed by a vaccine candidate. *J Virol*, 2015. **89**(18): p. 9499-9510.

17. Stokes, K. L., Chi, M. H., Sakamoto, K., Newcomb, D. C., Currier, M. G., Huckabee, M. M., Lee, S., Goleniewska, K., Pretto, C., Williams, J. V., Hotard, A., Sherrill, T. P., Peebles, R. S., Jr., and Moore, M. L. Differential pathogenesis of respiratory syncytial virus clinical isolates in BALB/c mice. *J Virol*, 2011. **85**(12): p. 5782-5793.

18. Zhang, L. Q., Peeples, M. E., Boucher, R. C., Collins, P. L., and Pickles, R. J. Respiratory syncytial virus infection of human airway epithelial cells is polarized, specific to ciliated cells, and without obvious cytopathology. *J Virol*, 2002. **76**(11): p. 5654-5666.

19. Hotard, A. L., Lee, S., Currier, M. G., Crowe, J. E., Jr., Sakamoto, K., Newcomb, D. C., Peebles, R. S., Jr., Plemper, R. K., and Moore, M. L. Identification of residues in the human respiratory syncytial virus fusion protein that modulate fusion activity and pathogenesis. *J Virol*, 2015. **89**(1): p. 512-522.

20. Hotard, A. L., Shaikh, F. Y., Lee, S., Yan, D., Teng, M. N., Plemper, R. K., Crowe, J. E., Jr., and Moore, M. L. A stabilized respiratory syncytial virus reverse genetics system amenable to recombination-mediated mutagenesis. *Virology*, 2012. **434**(1): p. 129-136.

21. Zhao, H., Wang, X.-Y., Li, M.-K., Hou, Z., Zhou, Y., Chen, Z., Meng, J.-R., Luo, X.-x., Tang, H.-F., and Xue, X.-Y. A novel pregnane-type alkaloid from *Pachysandra terminalis* inhibits methicillin-resistant staphylococcus aureus *in vitro* and *in vivo*. *Phytother Res*, 2015. **29**(3): p. 373-380.

22. Jin, H., Cheng, X., Zhou, H. Z., Li, S., and Seddiqui, A. Respiratory syncytial virus that lacks open reading frame 2 of the M2 gene (M2-2) has altered growth characteristics and is attenuated in rodents. *J Virol*, 2000. **74**(1): p. 74-82.

23. Corti, D., Bianchi, S., Vanzetta, F., Minola, A., Perez, L., Agatic, G., Guarino, B., Silacci, C., Marcandalli, J., Marsland, B. J., Piralla, A., Percivalle, E., Sallusto, F., Baldanti, F., and Lanzavecchia, A. Cross-neutralization of four paramyxoviruses by a human monoclonal antibody. *Nature*, 2013. **501**(7467): p. 439-+.

24. Yunus, A. S., Jackson, T. P., Crisafi, K., Burimski, I., Kilgore, N. R., Zoumplis, D., Allaway, G. P., Wild, C. T., and Salzwedel, K. Elevated temperature triggers human respiratory syncytial virus f protein six-helix bundle formation. *Virology*, 2010. **396**(2): p. 226-237.

25. Kiss, G., Holl, J. M., Williams, G. M., Alonas, E., Vanover, D., Lifland, A. W., Gudheti, M., Guerrero-Ferreira, R. C., Nair, V., Yi, H., Graham, B. S., Santangelo, P. J., and Wright, E. R.

Structural analysis of respiratory syncytial virus reveals the position of M2-1 between the matrix protein and the ribonucleoprotein complex. *J Virol*, 2014. **88**(13): p. 7602-7617.

26. Yi, H., Strauss, J. D., Ke, Z., Alonas, E., Dillard, R. S., Hampton, C. M., Lamb, K. M., Hammonds, J. E., Santangelo, P. J., Spearman, P. W., and Wright, E. R. Native immunogold labeling of cell surface proteins and viral glycoproteins for cryo-electron microscopy and cryo-electron tomography applications. *J Histochem Cytochem*, 2015. **63**(10): p. 780-792.
27. Mastronarde, D. N. Automated electron microscope tomography using robust prediction of specimen movements. *J Struct Biol*, 2005. **152**(1): p. 36-51.
28. Mastronarde, D. N. Dual-axis tomography: An approach with alignment methods that preserve resolution. *J Struct Biol*, 1997. **120**(3): p. 343-352.
29. Kremer, J. R., Mastronarde, D. N., and McIntosh, J. R. Computer visualization of three-dimensional image data using IMOD. *J Struct Biol*, 1996. **116**(1): p. 71-76.
30. Galaz-Montoya, J. G., Flanagan, J., Schmid, M. F., and Ludtke, S. J. Single particle tomography in EMAN2. *J Struct Biol*, 2015. **190**(3): p. 279-90.
31. Nicastro, D., Schwartz, C., Pierson, J., Gaudette, R., Porter, M. E., and McIntosh, J. R. The molecular architecture of axonemes revealed by cryoelectron tomography. *Science*, 2006. **313**(5789): p. 944-948.
32. Frank, J., Radermacher, M., Penczek, P., Zhu, J., Li, Y., Ladjadj, M., and Leith, A. Spider and web: Processing and visualization of images in 3D electron microscopy and related fields. *J Struct Biol*, 1996. **116**(1): p. 190-9.
33. Pettersen, E. F., Goddard, T. D., Huang, C. C., Couch, G. S., Greenblatt, D. M., Meng, E. C., and Ferrin, T. E. UCSF Chimera - a visualization system for exploratory research and analysis. *J Comput Chem*, 2004. **25**(13): p. 1605-1612.

34. Anderson, L. J., Bingham, P., and Hierholzer, J. C. Neutralization of respiratory syncytial virus by individual and mixtures of F-protein and G-protein monoclonal-antibodies. *J Virol*, 1988. **62**(11): p. 4232-4238.

35. McLellan, J. S., Yang, Y., Graham, B. S., and Kwong, P. D. Structure of respiratory syncytial virus fusion glycoprotein in the postfusion conformation reveals preservation of neutralizing epitopes. *J Virol*, 2011. **85**(15): p. 7788-7796.

36. Liljeroos, L., Krzyzaniak, M. A., Helenius, A., and Butcher, S. J. Architecture of respiratory syncytial virus revealed by electron cryotomography. *Proc Natl Acad Sci U S A*, 2013. **110**(27): p. 11133-11138.

37. Wang, H., Zhang, X., Meng, J., Yin, Z., Liu, X., Zhao, Y., and Zhang, L. Controlled growth of few-layer hexagonal boron nitride on copper foils using ion beam sputtering deposition. *Small*, 2015. **11**(13): p. 1542-1547.

38. Moore, M. L., Chi, M. H., Luongo, C., Lukacs, N. W., Polosukhin, V. V., Huckabee, M. M., Newcomb, D. C., Buchholz, U. J., Crowe, J. E., Jr., Goleniewska, K., Williams, J. V., Collins, P. L., and Peebles, R. S., Jr. A chimeric A2 strain of respiratory syncytial virus (RSV) with the fusion protein of RSV strain line 19 exhibits enhanced viral load, mucus, and airway dysfunction. *J Virol*, 2009. **83**(9): p. 4185-4194.

39. Gilman, M. S. A., Moin, S. M., Mas, V., Chen, M., Patel, N. K., Kramer, K., Zhu, Q., Kabeche, S. C., Kumar, A., Palomo, C., Beaumont, T., Baxa, U., Ulbrandt, N. D., Melero, J. A., Graham, B. S., and McLellan, J. S. Characterization of a prefusion-specific antibody that recognizes a quaternary, cleavage-dependent epitope on the RSV fusion glycoprotein. *PLoS Pathog*, 2015. **11**(7).

40. Spann, K. M., Tran, K. C., and Collins, P. L. Effects of nonstructural proteins NS1 and NS2 of human respiratory syncytial virus on interferon regulatory factor 3, NF-kappa B, and proinflammatory cytokines. *J Virol*, 2005. **79**(9): p. 5353-5362.

41. Ling, Z., Tran, K. C., and Teng, M. N. Human respiratory syncytial virus nonstructural protein NS2 antagonizes the activation of beta interferon transcription by interacting with rig-i. *J Virol*, 2009. **83**(8): p. 3734-3742.

42. Bukreyev, A., Whitehead, S. S., Murphy, B. R., and Collins, P. L. Recombinant respiratory syncytial virus from which the entire SH gene has been deleted grows efficiently in cell culture and exhibits site-specific attenuation in the respiratory tract of the mouse. *J Virol*, 1997. **71**(12): p. 8973-8982.

43. Karron, R. A., Wright, P. F., Belshe, R. B., Thumar, B., Casey, R., Newman, F., Polack, F. P., Randolph, V. B., Deatly, A., Hackell, J., Gruber, W., Murphy, B. R., and Collins, P. L. Identification of a recombinant live attenuated respiratory syncytial virus vaccine candidate that is highly attenuated in infants. *J Infect Dis*, 2005. **191**(7): p. 1093-1104.

44. Whitehead, S. S., Bukreyev, A., Teng, M. N., Firestone, C. Y., St Claire, M., Elkins, W. R., Collins, P. L., and Murphy, B. R. Recombinant respiratory syncytial virus bearing a deletion of either the NS2 or SH gene is attenuated in chimpanzees. *J Virol*, 1999. **73**(4): p. 3438-3442.

45. Karron, R. A., Buonagurio, D. A., Georgiu, A. F., Whitehead, S. S., Adamus, J. E., ClementsMann, M. L., Harris, D. O., Randolph, V. B., Udem, S. A., Murphy, B. R., and Sidhu, M. S. Respiratory syncytial virus (RSV) SH and G proteins are not essential for viral replication in vitro: Clinical evaluation and molecular characterization of a cold-passaged, attenuated RSV subgroup B mutant. *Proc Natl Acad Sci U S A*, 1997. **94**(25): p. 13961-13966.

46. Meng, J., Hotard, A. L., Currier, M. G., Lee, S., Stobart, C. C., and Moore, M. L. Respiratory syncytial virus attachment glycoprotein contribution to infection depends on the specific fusion protein. *J Virol*, 2016. **90**(1): p. 245-253.

47. Techaarpornkul, S., Barretto, N., and Peeples, M. E. Functional analysis of recombinant respiratory syncytial virus deletion mutants lacking the small hydrophobic and/or attachment glycoprotein gene. *J Virol*, 2001. **75**(15): p. 6825-6834.

48. Teng, M. N., Whitehead, S. S., and Collins, P. L. Contribution of the respiratory syncytial virus G glycoprotein and its secreted and membrane-bound forms to virus replication in vitro and in vivo. *Virology*, 2001. **289**(2): p. 283-296.

49. Polack, F. P., Irusta, P. M., Hoffman, S. J., Schiatti, M. P., Melendi, G. A., Delgado, M. F., Laham, F. R., Thumar, B., Hendry, R. M., Melero, J. A., Karron, R. A., Collins, P. L., and Kleeberger, S. R. The cysteine-rich region of respiratory syncytial virus attachment protein inhibits innate immunity elicited by the virus and endotoxin. *Proc Natl Acad Sci U S A*, 2005. **102**(25): p. 8996-9001.

50. Tripp, R. A., Jones, L. P., Haynes, L. M., Zheng, H. Q., Murphy, P. M., and Anderson, L. J. CX3C chemokine mimicry by respiratory syncytial virus G glycoprotein. *Nat Immunol*, 2001. **2**(8): p. 732-738.

51. Johnson, T. R., McLellan, J. S., and Graham, B. S. Respiratory syncytial virus glycoprotein G interacts with DC-SIGN and L-SIGN to activate ERK1 and ERK2. *J Virol*, 2012. **86**(3): p. 1339-1347.

52. Bukreyev, A., Yang, L., Fricke, J., Cheng, L., Ward, J. M., Murphy, B. R., and Collins, P. L. The secreted form of respiratory syncytial virus G glycoprotein helps the virus evade antibody-mediated restriction of replication by acting as an antigen decoy and through effects on Fc receptor-bearing leukocytes. *J Virol*, 2008. **82**(24): p. 12191-12204.

53. Mayhew, T. M. Mapping the distributions and quantifying the labelling intensities of cell compartments by immunoelectron microscopy: Progress towards a coherent set of methods. *J Anat*, 2011. **219**(6): p. 647-660.

54. Wright, P. F., Ikizler, M. R., Gonzales, R. A., Carroll, K. N., Johnson, J. E., and Werkhaven, J. A. Growth of respiratory syncytial virus in primary epithelial cells from the human respiratory tract. *J Virol*, 2005. **79**(13): p. 8651-8654.

55. Widjojoatmodjo, M. N., Boes, J., van Bers, M., van Remmerden, Y., Roholl, P. J. M., and Luytjes, W. A highly attenuated recombinant human respiratory syncytial virus lacking the G protein induces long-lasting protection in cotton rats. *Virol J*, 2010. **7**.

56. Swanson, K. A., Balabanis, K., Xie, Y., Aggarwal, Y., Palomo, C., Mas, V., Metrick, C., Yang, H., Shaw, C. A., Melero, J. A., Dormitzer, P. R., and Carfi, A. A monomeric uncleaved respiratory syncytial virus F antigen retains prefusion-specific neutralizing epitopes. *J Virol*, 2014. **88**(20): p. 11802-11810.

FIGURE LEGENDS

Figure 1. MPE8 and D25 ELISAs. (A) Ratio of direct ELISA using MPE8, a pre-F-specific mAb, to direct ELISA using motavizumab, a total F mAb. Values are normalized to strain A2. For A2-line19F mutants, the asterisks show significant differences compared with A2-line19F. (B) Ratio of direct ELISA using D25, another pre-F-specific mAb, to direct ELISA using motavizumab. All graphs represent the means+s.d.'s of at least two experimental replicates, and data were analysed by one-way ANOVA. When significant, *P* values are shown as a bracket between groups ($P<0.0005$) or by asterisk when compared with A2-line19F (*$P<0.05$; **$P<0.005$; ***$P<0.0005$).

Figure 2. Thermal stability assays. Thermal inactivation was carried out either by incubation of virus at 4 °C (A,C,D) or 37 °C (B). The viruses in **c** labelled 79, 191, 357, 371, 557 and 357/371 represent A2-line19F containing substitutions at these indicated positions with A2 residues. The virus in **c** labelled DB1-357/371 represents DB1 with substitutions of line 19F residues at positions 357 and 371. Viruses were harvested at the indicated time points and titrated by FFU or PFU assays. All graphs represent the means+s.d.'s of at least two experimental replicates combined, and data were analysed by two-way ANOVA (*$P<0.05$; **$P<0.005$; ***$P<0.0005$; ****$P<0.00005$).

Figure 3. Design of live-attenuated vaccine OE4 and expression of viral proteins. (A) Schematic of RSV LAV OE4 genome including codon deoptimization of the NS1, NS2 and G genes, deletion of the SH gene, and incorporation of the line 19F gene. (B) Western blotting of Vero cells infected with A2 (white), OE4 (green) or OE4 expressing wild type G (OE4-wtG, grey) for NS1, NS2, N and G. An A2-G_{null} mutant was included as a control. (C) Western densitometry analyses were normalized to A2 expression levels. (D) Western blotting of Vero cells infected with mock, A2-line19F (white), OE4-wtG (grey) or OE4 (green) for F, N and GAPDH. (E) Densitometry results

were normalized to A2 expression levels. Densitometry results represent the means+s.d.'s of at least two experimental replicates and representative blots are shown. Statistical analyses were performed by one-way ANOVA (***P<0.0005; ****P<0.00005). d, codon-deoptimized; F, fusion protein; G, attachment glycoprotein; L, large polymerase; M, matrix; mK2, monomeric Katushka2; N, nucleoprotein; NS1/NS2, nonstructural proteins 1 and 2; P, phosphoprotein; SH, small hydrophobic protein.

Figure 4. Immunogold labelling of RSV surface glycoproteins F and G. (A) Representative TEM images of BEAS-2B cells infected at an MOI of 10 with A2 (black) or OE4 (green) and labelled with MPE8 (pre-F mAb), 131-2A (post-F mAb), Motavizumab (total F mAb) or 131-2G (G mAb) and probed with gold-labelled secondary antibodies. (B) Quantification of the amount of immunogold particles per measured membrane length per virion. For each labeling condition, more than 100 virions (graph data points) were evaluated for each virus. The red lines represent the mean particle densities along the membrane for each condition. Significant differences are indicated by ***P<0.0005 determined by *t*-test with Welch's correction. Scale bars represent 200 nm.

Figure 5. Cryo-electron tomography of RSV virions and subvolume averaging of the F glycoprotein. (A-C) Tomographic slices (6.14 nm) of A2, OE4 and A2-heat (55 °C for 30 min) virions showing overall virus structure and the organization of surface glycoproteins (insets). Inset in OE4 is rotated 180°. Scale bars are 200 nm for A2 and OE4, and 100 nm for A2-heat. (D-L) Subvolume averages and modelling of RSV F structures in pre- and post-fusion conformations. Central slices (6.14 Å in thickness) of the averaged structures lowpass filtered to 40 Å for A2 (D), OE4 (E) and A2-heat (F). Quasi-atomic models generated by fitting the RSV pre-fusion F (PDB ID 4JHW) and RSV post-fusion F (PDB ID 3RRT) crystal structures into the subvolume averages, with

side views (G-I) and top views (J-L) for A2 (G,J), OE4 (H,K) and A2-heat (I,L). Note the height difference between the ectodomain of A2/OE4 and A2-heat. The measurements were made from the top of the membrane to the top of the head domain. Scale bars, 10 nm (D-F); 5 nm (G-L).

Figure 6. OE4 replication in immortalized and primary cell cultures. Vero (A), BEAS-2B (B), primary normal human bronchial epithelial cells differentiated at air–liquid interface (NHBE) (C), primary human tracheobronchial airway cells differentiated at air–liquid interface (HAE) (D) were infected with A2-line19F (black), OE4 (green) and in HAE, OE4+wtG (green dash) at MOI=0.01 (Vero and BEAS-2B), MOI=2.6 (NHBE), or MOI=6.7 (HAE). Samples were titrated by fluorescent focus unit (FFU) assays on Vero cells. (E) Representative images of infected HAE cultures. Scale bar represents 200 μm. Graphs depict the means±s.e.s of the means combined from three experiments (Vero and BEAS-2B), from two donors in duplicate (NHBE), or from six cultures from a single donor per virus (HAE). When significant, *P* values are shown relative to A2-line19F (*$P<0.05$; by two-way ANOVA).

Figure 7. Attenuation and efficacy of OE4 in mice and cotton rats. (A) Lung viral loads were determined in mice inoculated i.n. with 10^6 FFU of A2, A2-line19F or OE4 at the indicated time points. (B) Serum nAb titres were measured in mice inoculated with 10^6 FFU of A2, A2-line19F or OE4. (C) Mice were inoculated with 10^6 FFU of A2, A2-line19F or OE4 then challenged with 10^5 PFU of A2-line19F on day 102. Lung viral loads were determined day 4 post challenge. (A-C) Graphs represent combined data from two experiments of 5–10 mice per group. (D) Mice (five per group) were inoculated with mock, A2-line19F, OE4 or A2-del-M2-2, and lungs were harvested 8 days post inoculation for histological quantification of airway mucin expression. Each dot represents an airway, and graph shows >300 airways per group in one of two experiments with similar results.

(E,F) Viral load on day 4 in cotton rat lung homogenates (*n*=3) (E) and nasal washes (*n*=3) (F) following i.n. inoculation with 10^5 FFU of A2, OE4 or A2-del-M2-2. (G) Cotton rats (six per group) were inoculated with mock, RSV A (Tracy), OE4 or A2-del-M2-2, and serum nAb titres against representative RSV strains were determined on day 42 post inoculation using pooled sera. EC50 was calculated by non-linear regression, and data represent EC50+upper limit of the 95% confidence interval. (H,I) Cotton rats (five per group) were inoculated with mock, A2, or OE4, challenged on day 42 with 10^6 FFU of RSV A2-line19F, and viral loads on day 46 were measured in nasal washes (I) and lung lavages (H). **P*<0.05; ***P*<0.005; ****P*<0.0005; *****P*<0.00005 by one-way (C-F,H,I) or two-way (A,B) ANOVA.

Figure 8. Histopathology following RSV challenge in cotton rats. To evaluate for vaccine attributable enhanced disease post challenge, groups of five cotton rats were inoculated intramuscularly with FI-RSV or intranasally with either mock or OE4. Animals vaccinated with FI-RSV also received a boost on day 21 p.i. All animals were challenged with A2-line19F on day 42 p.i., lungs were harvested 4 days later and histopathology scores were performed (A). Representative haematoxylin and eosin stains for FI-RSV (B), mock (C) and OE4 (D) vaccinated rats are shown. Scale bars represent 200 μm. Data are represented as mean + s.d. **P*<0.05, ***P*<0.005 by two-way ANOVA.

Supplementary Figure 1. Pre-fusion (pre-F) and post-fusion F (post-F) conformations labeled with four unique residues of line 19 F. The labeled images of pre-F (PDB accession number 4JHW) and post-F (PDB accession number 3RRT) were generated using previously described crystal structures (10).

Supplementary Figure 2. Stability of A2 and OE4 pre-F over time at 4ÆC. (a) Ratio of direct ELISA using MPE8, a pre-F specific mAb, to direct ELISA using motavizumab, a total F mAb., on virus incubated at 4ÆC over 8 days. Ratio values are shown without normalization. (b) Normalized ratios of OE4 to A2 at days 1, 4, and 8. t = number of days at 4ÆC. All data for each time point reflect the means + standard deviations of triplicate series of serial dilutions of virus after incubation. Statistical analyses were performed by one-way ANOVA, (****, $P < 0.00005$).

Supplementary Figure 3. Comparison of mouse lung viral loads of OE4 with and without mKatushka-2 reporter. BALB/c mice (n=5) were infected i.n. with 4 x 105 PFU of virus per mouse. On days 2, 4, 6, and 8, the mice were euthanized and the left lung harvested for viral titration. Titers below the limit of detection were assigned a value equal to half of the limit of detection (dashed line). Means are indicated by red bars. Statistical analyses were performed by two-way ANOVA, (*, $P < 0.05$; **, $P < 0.005$; ***, $P < 0.0005$); ****, $P < 0.00005$).

Supplementary Figure 4. Representative airway mucin expression. Mice (5 per group) were inoculated with mock, A2-line19F, OE4, or A2-del-M2-2, and lungs were harvested 8 days postinoculation for sectioning and staining with periodic acid Schiff (PAS). Representative images are shown. Scale bars are 100 μm.

Supplementary Figure 5. Nucleotide and amino acid sequences of codon-deoptimized non-structural protein NS1.

Supplementary Figure 6. Nucleotide and amino acid sequences of codon-deoptimized non-structural protein NS2.

Supplementary Figure 7. Nucleotide and amino acid sequences for codon-deoptimized attachment G protein.

Supplementary Figure 8. Raw western blot images for Figure 3b. Western blotting of Vero cells infected with A2, A2-G-null, OE4 expressing wild-type G (OE4-wtG), or OE4 were performed for G (A), N (B), NS1 (C), and NS2 (D).

Figure 1

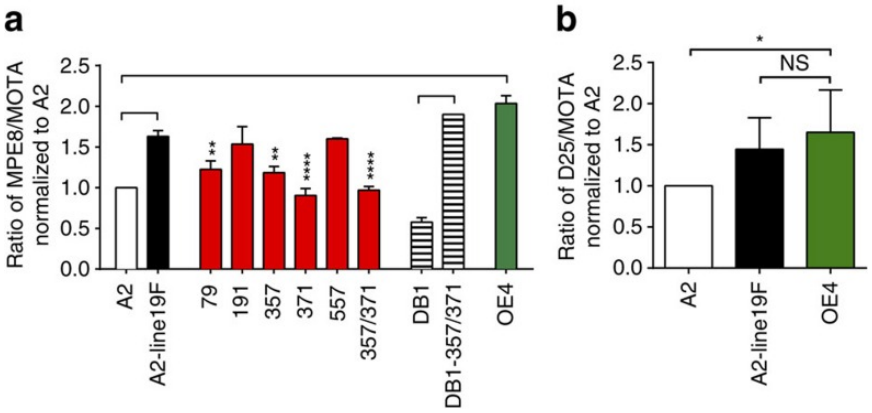
a
Ratio of MPE8/MOTA normalized to A2
2.5
2.0
1.5
1.0
0.5
0.0
**
**
****
****
A2
A2-line19F
79
191
357
371
557
357/371
DB1
DB1-357/371
OE4
b
Ratio of D25/MOTA normalized to A2
2.5
2.0
1.5
1.0
0.5
0.0
*
NS
A2
A2-line19F
OE4

Figure 2

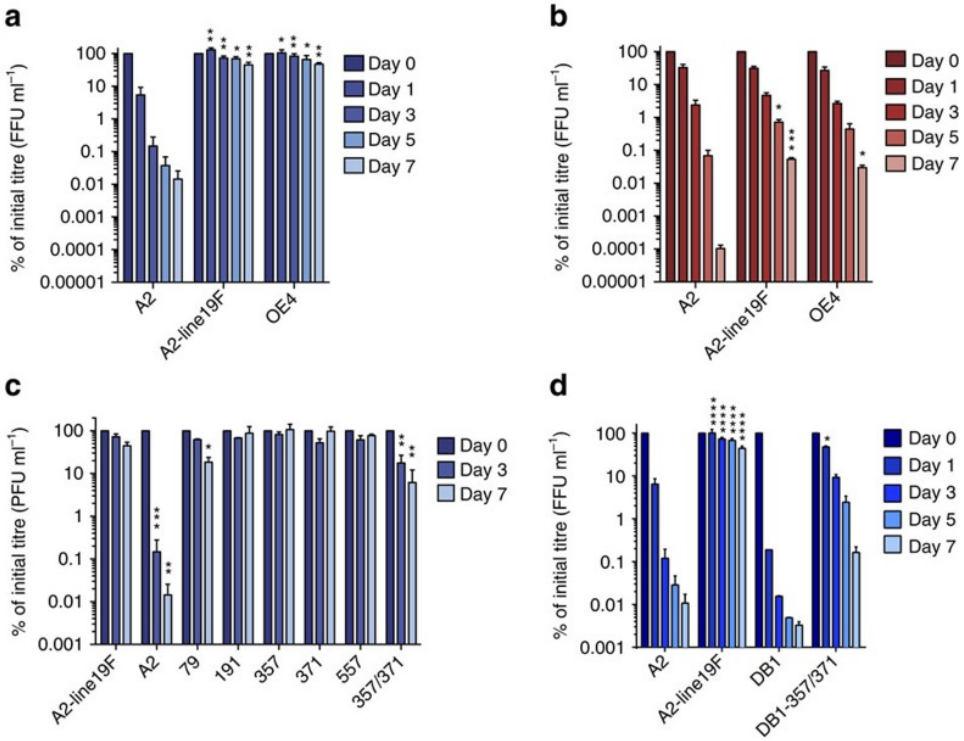
a
% of initial titre (FFU ml−1)
100
10
1
0.1
0.01
0.001
0.0001
0.00001
A2
A2-line19F
OE4
Day 0
Day 1
Day 3
Day 5
Day 7
b
% of initial titre (FFU ml−1)
A2
A2-line19F
OE4
Day 0
Day 1
Day 3
Day 5
Day 7
c
% of initial titre (PFU ml−1)
100
10
1
0.1
0.01
0.001
A2-line19F
A2
79
191
357
371
557
357/371
Day 0
Day 3
Day 7
d
% of initial titre (FFU ml−1)
100
10
1
0.1
0.01
0.001
A2
A2-line19F
DB1
DB1-357/371
Day 0
Day 1
Day 3
Day 5
Day 7

Figure 3

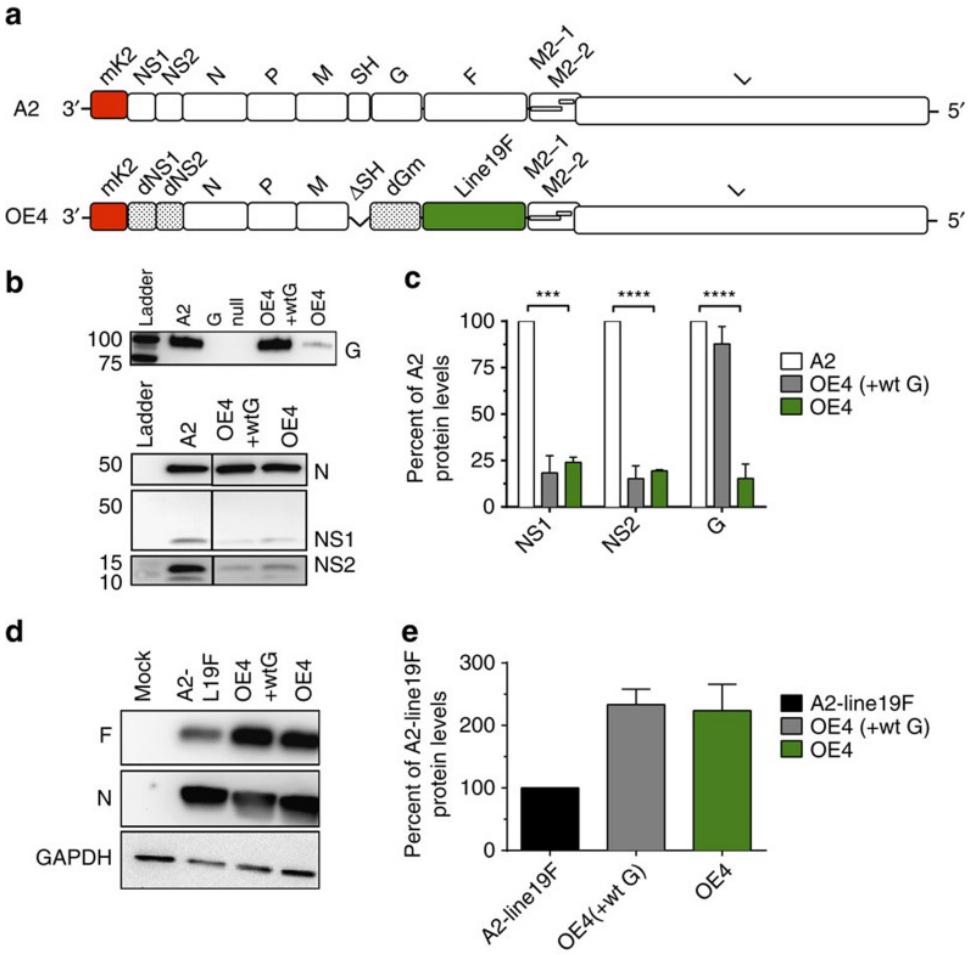
a
A2
3′
mK2
NS1
NS2
N
P
M
SH
G
F
M2–1
M2–2
L
5′
OE4
dNS1
dNS2
ΔSH
dGm
Line19F
b
Ladder
A2
G
null
OE4 +wtG
OE4
100
75
50
15
10
N
NS1
NS2
c
***
****
Percent of A2 protein levels
A2
OE4 (+wt G)
OE4
d
Mock
A2-L19F
F
GAPDH
e
Percent of A2-line19F protein levels
A2-line19F
OE4(+wt G)

Figure 4

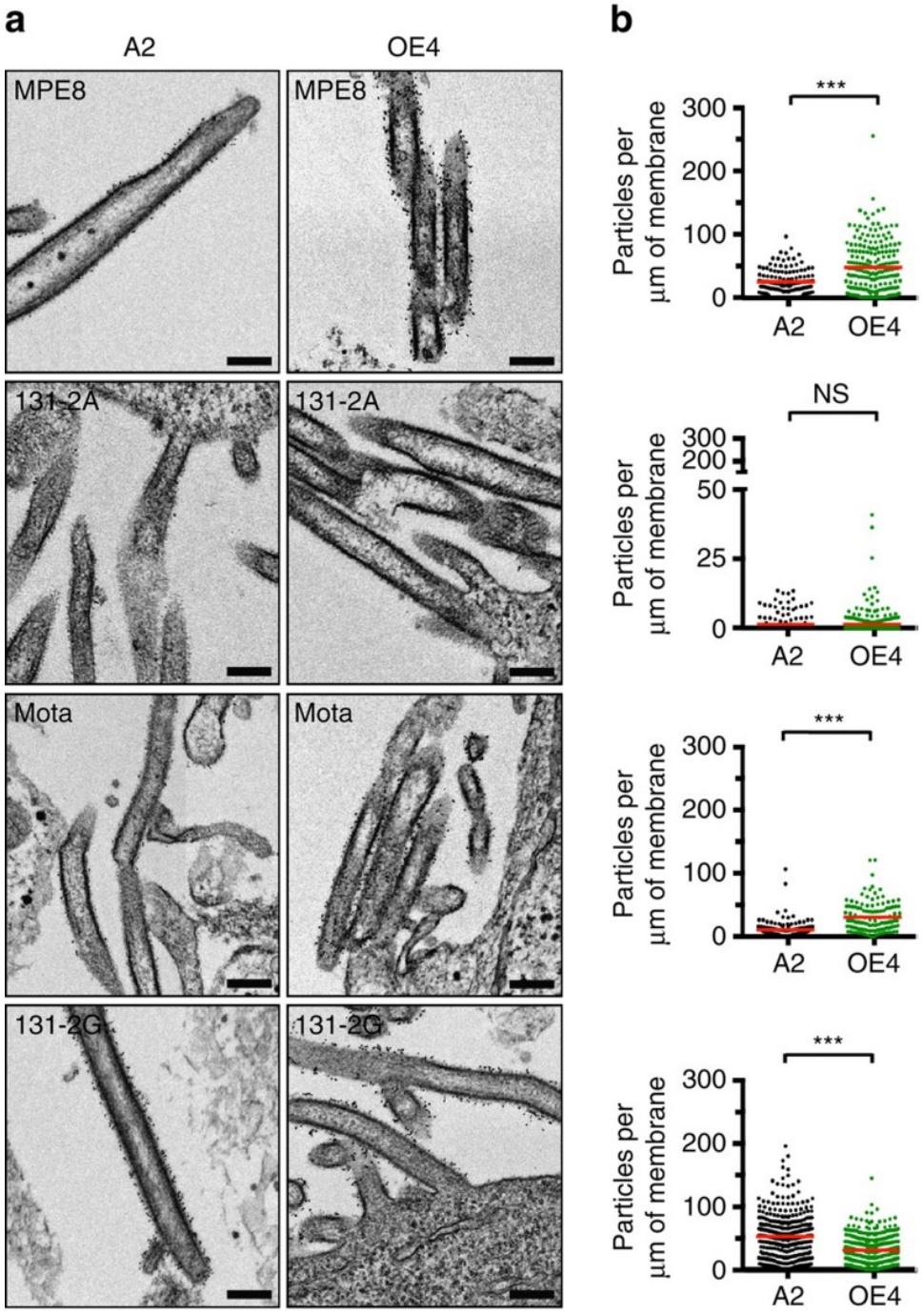
a
A2
OE4
MPE8
MPE8
131-2A
131-2A
Mota
Mota
131-2G
131-2G
b
Particles per µm of membrane
300
200
100
0
***
A2
OE4
Particles per µm of membrane
300
200
50
25
0
NS
A2
OE4
Particles per µm of membrane
300
200
100
0
***
A2
OE4
Particles per µm of membrane
300
200
100
0
***
A2
OE4

Figure 5

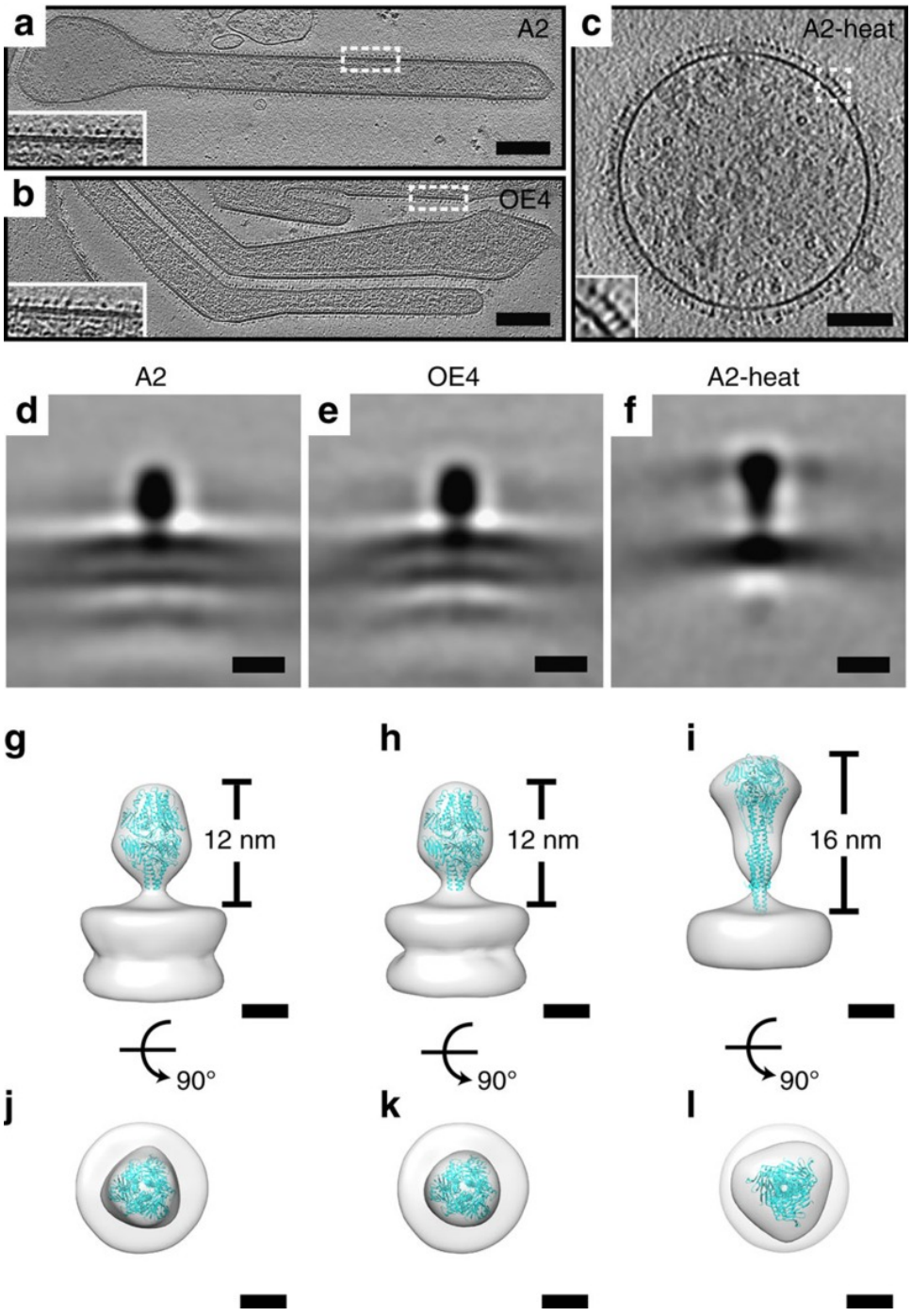
a
A2
b
OE4
c
A2-heat
A2
OE4
A2-heat
d
e
f
g
h
i
12 nm
12 nm
16 nm
90°
90°
90°
j
k
l

Figure 6

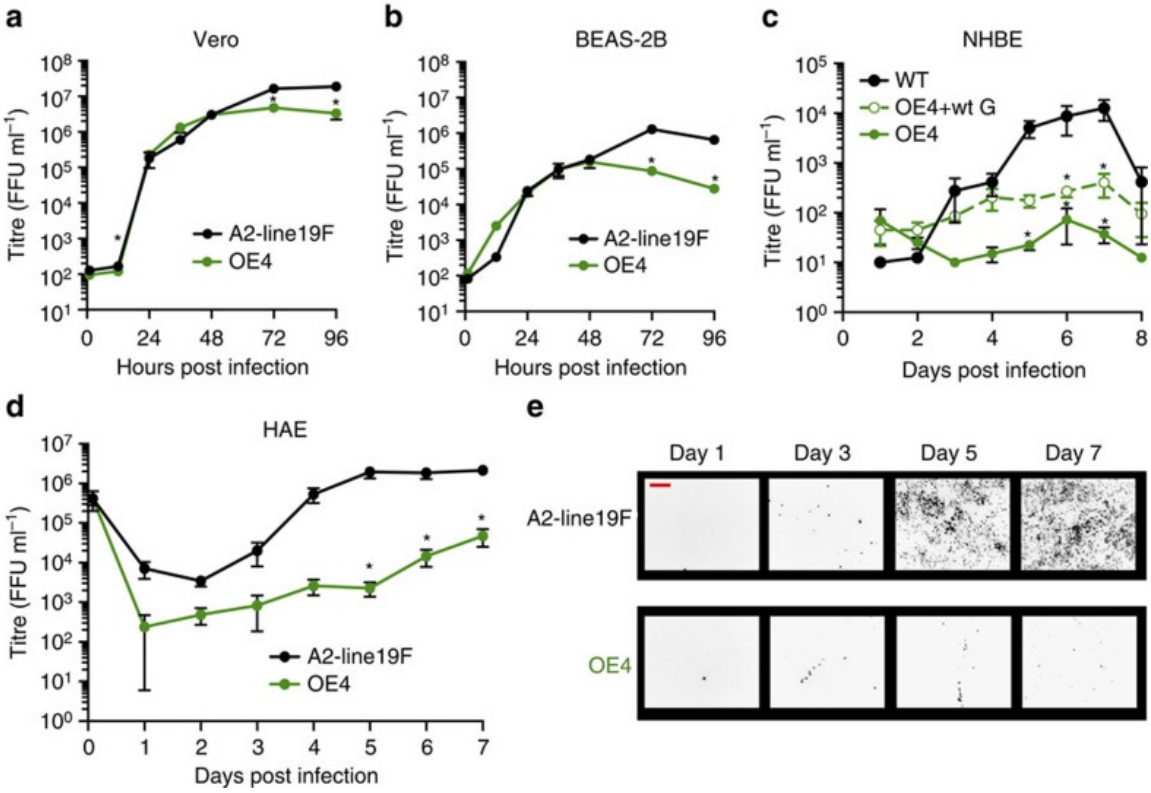
a
Vero
Titre (FFU ml−1)
A2-line19F
OE4
Hours post infection
b
BEAS-2B
Titre (FFU ml−1)
A2-line19F
OE4
Hours post infection
c
NHBE
WT
OE4+wt G
OE4
Titre (FFU ml−1)
Days post infection
d
HAE
Titre (FFU ml−1)
A2-line19F
OE4
Days post infection
e
Day 1
Day 3
Day 5
Day 7
A2-line19F
OE4

Figure 7

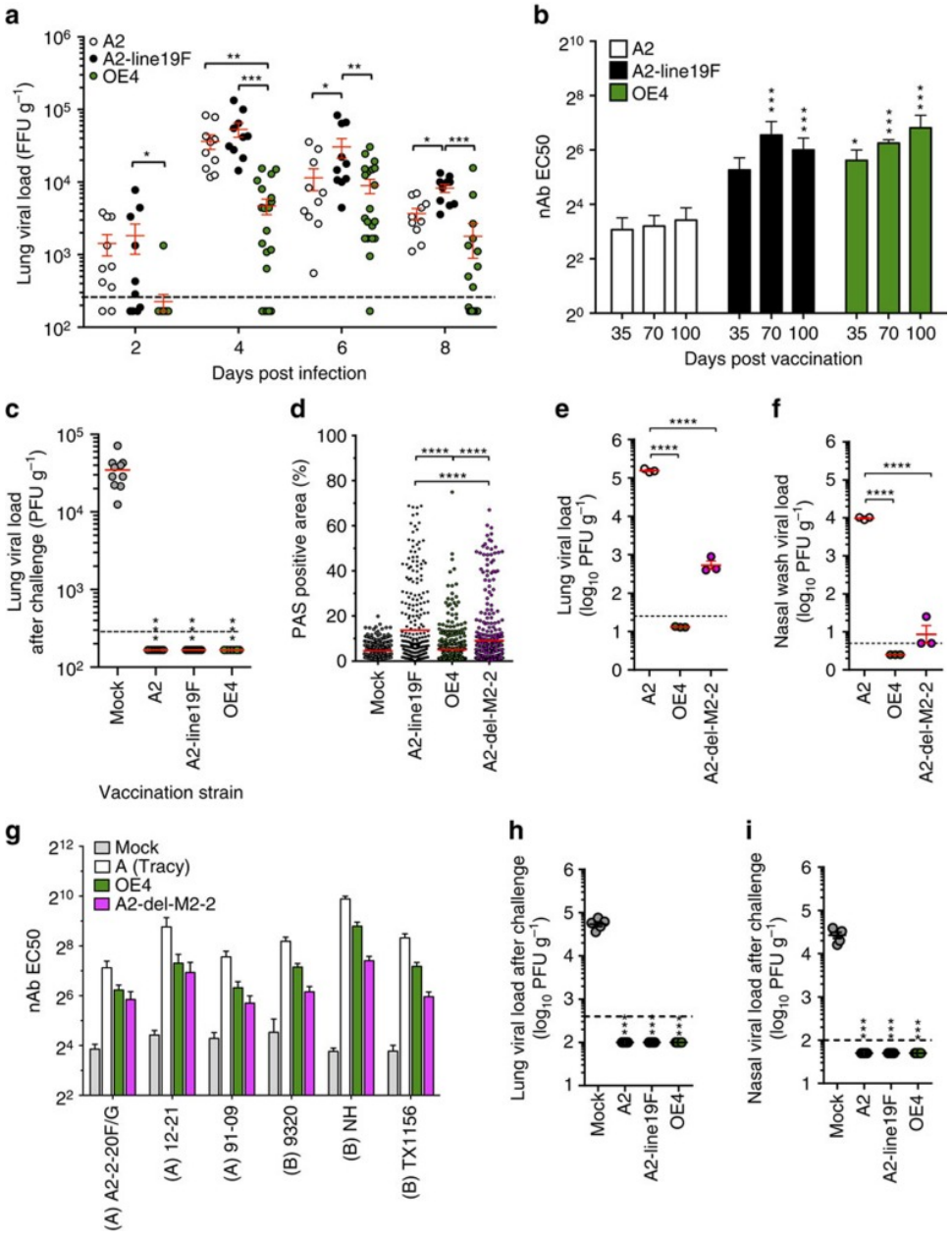
a
A2
A2-line19F
OE4
Lung viral load (FFU g−1)
Days post infection
b
A2
A2-line19F
OE4
nAb EC50
Days post vaccination
c
Lung viral load after challenge (PFU g−1)
Mock
A2
A2-line19F
OE4
Vaccination strain
d
PAS positive area (%)
Mock
A2-line19F
OE4
A2-del-M2-2
e
Lung viral load (log10 PFU g−1)
A2
OE4
A2-del-M2-2
f
Nasal wash viral load (log10 PFU g−1)
A2
OE4
A2-del-M2-2
g
Mock
A (Tracy)
OE4
A2-del-M2-2
nAb EC50
(A) A2-2-20F/G
(A) 12-21
(A) 91-09
(B) 9320
(B) NH
(B) TX1156
h
Lung viral load after challenge (log10 PFU g−1)
Mock
A2
A2-line19F
OE4
i
Nasal viral load after challenge (log10 PFU g−1)
Mock
A2
A2-line19F
OE4

Figure 8

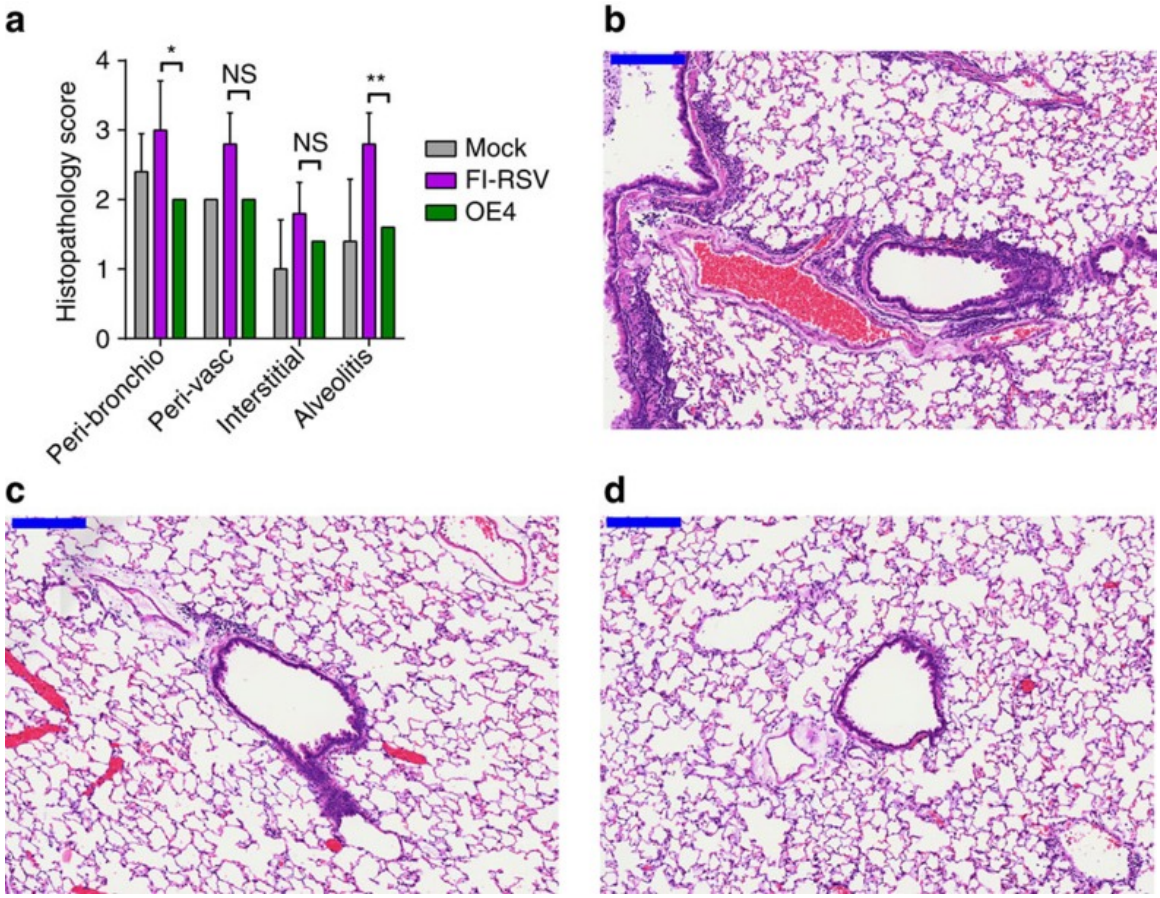
a
b
c
d
Histopathology score
0
1
2
3
4
*
NS
NS
**
Mock
FI-RSV
OE4
Peri-bronchio
Peri-vasc
Interstitial
Alveolitis

Supplementary Figure 1

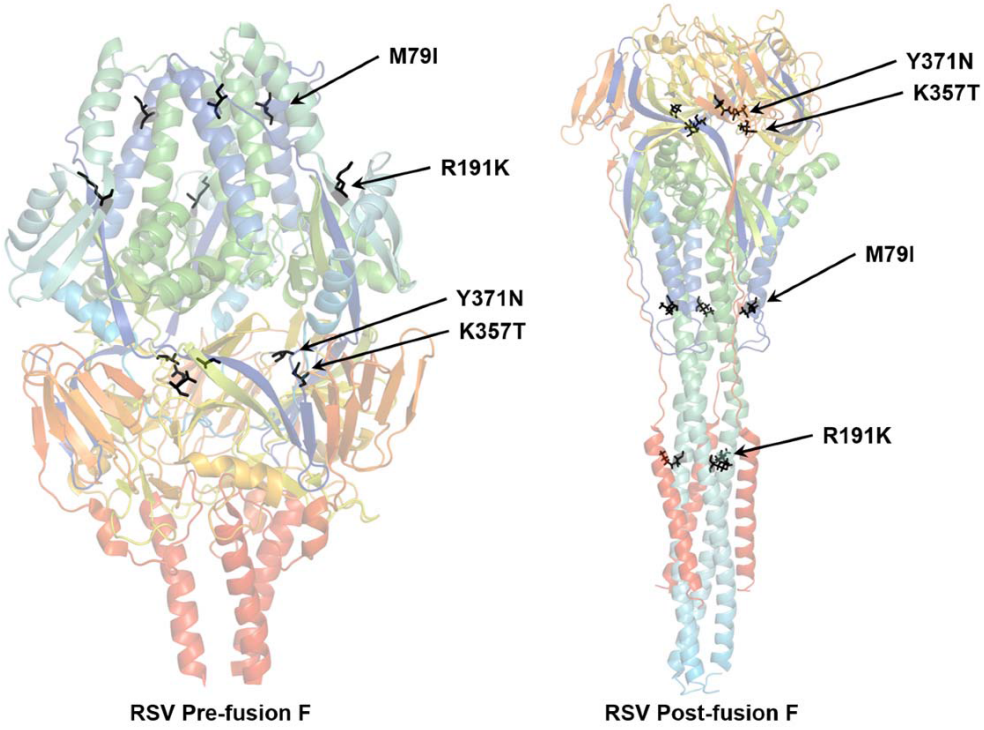

Supplementary Figure 2

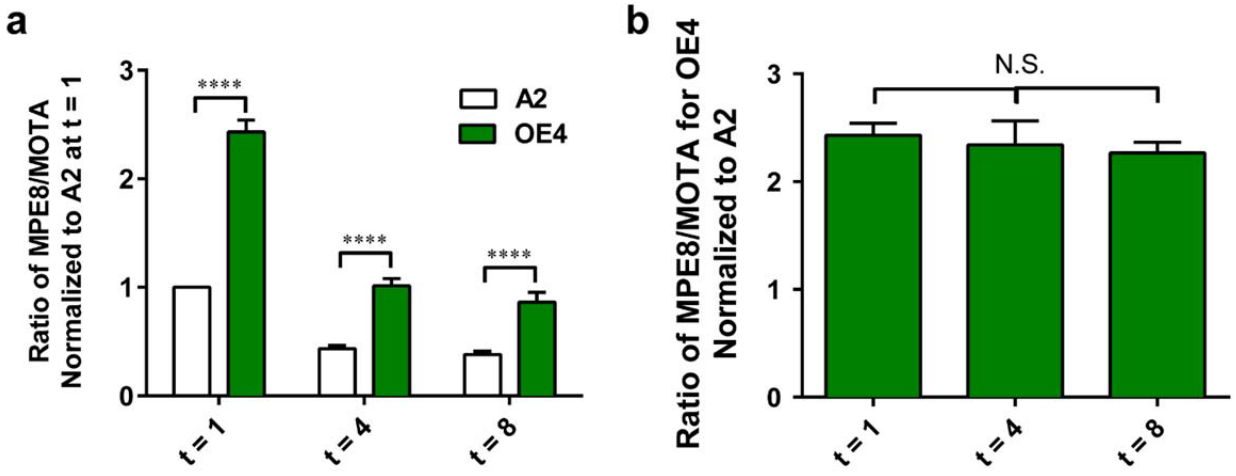

Supplementary Figure 3

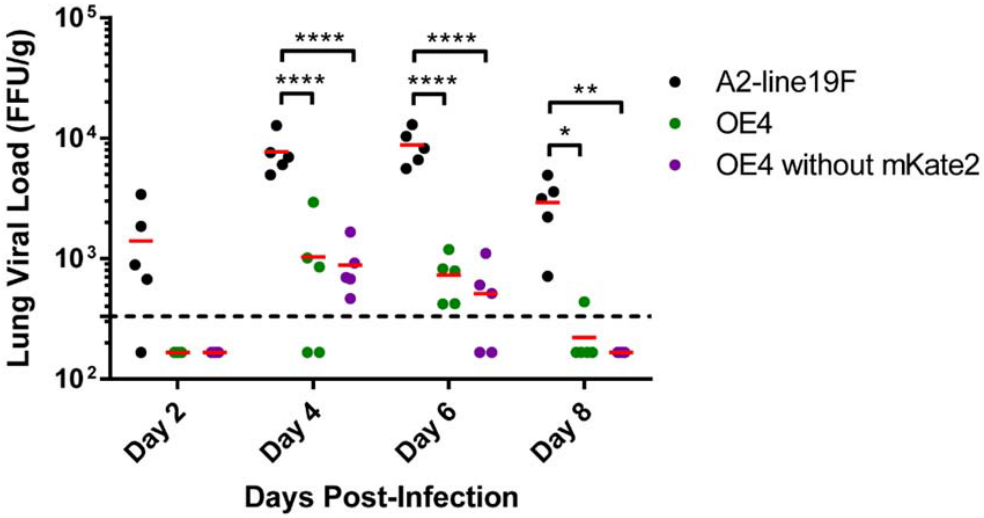

Supplementary Figure 4

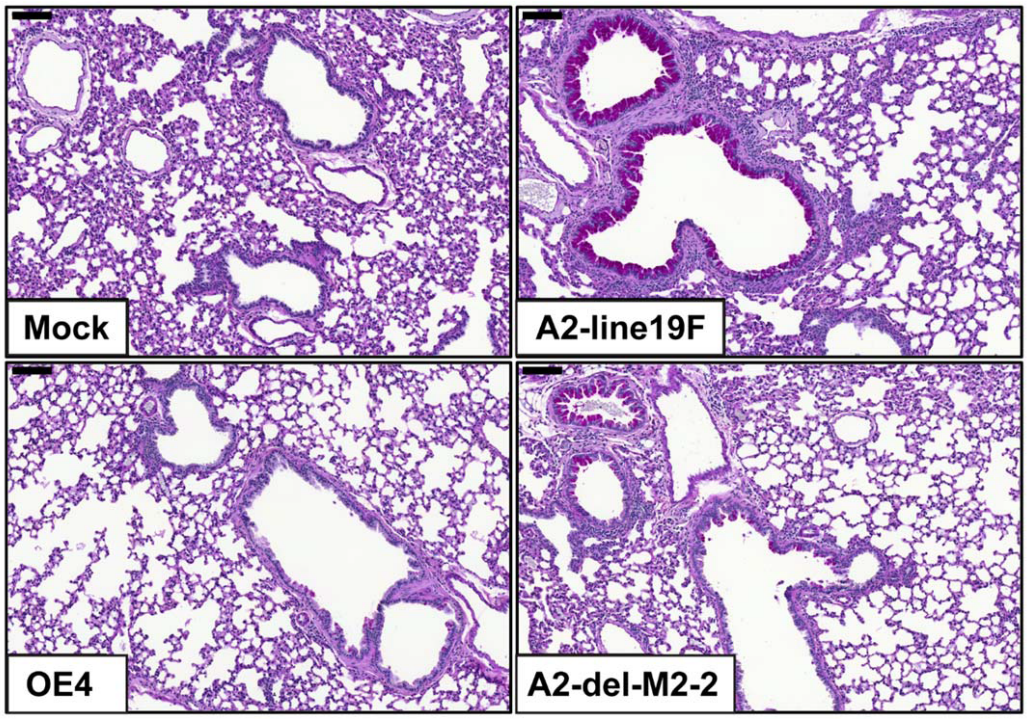

Supplementary Figure 5

Supplementary Figure 6

Supplementary Figure 7

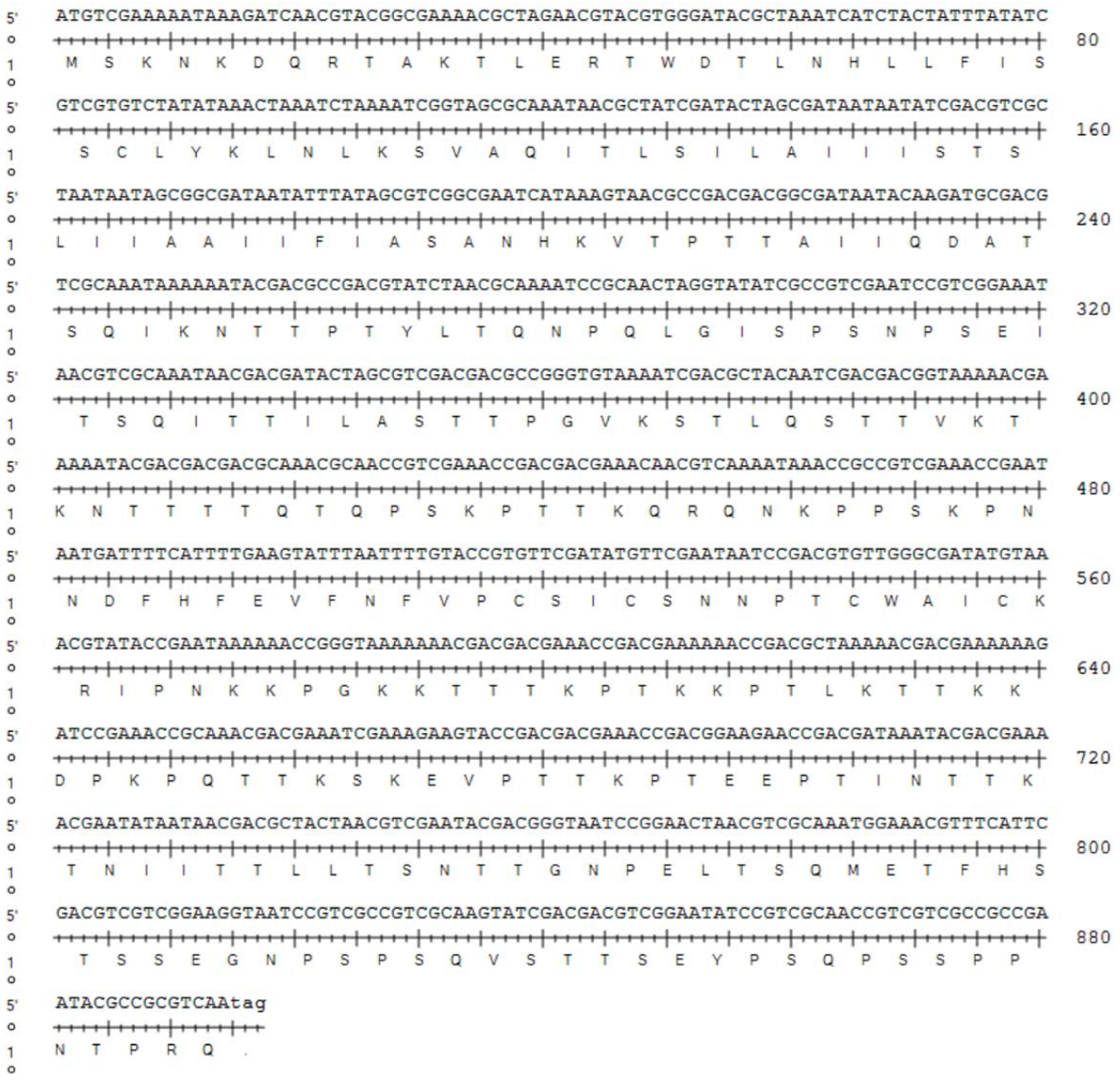

Supplementary Figure 8

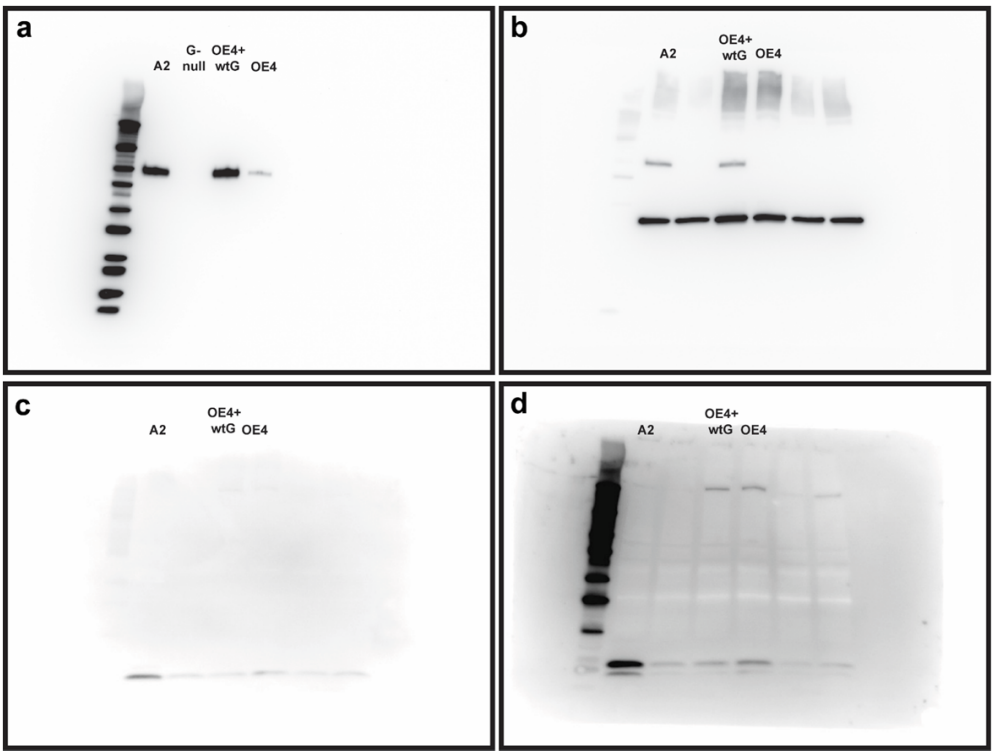

Appendix D: The Ms6 mycolyl-arabinogalactan esterase LysB is essential for an efficient mycobacteriophage-induced lysis

Adriano M. Gigante[1], Cheri M. Hampton[2], Rebecca S. Dillard[2], Filipa Gil[1], Maria João Catalão[1], José Moniz-Pereira[1], Elizabeth R. Wright[2], and Madalena Pimentel[1]

[1]Research Institute for Medicines (iMed.ULisboa), Faculdade de Farmácia, Universidade de Lisboa, Lisbon, Portugal

[2]Division of Pediatric Infectious Diseases, Emory University School of Medicine, Children's Healthcare of Atlanta, Atlanta, GA

Published in:

Viruses, 2017

Vol. 9, No. 11

p. 343

M.P., J.M.P., and E.R.W. conceived and designed the experiments; A.M.G., C.M.H., R.S.D., F.G., and M.J.C. performed the experiments; M.P., A.M.G., E.R.W., C.M.H., and J.M.P. analyzed the data; M.P. wrote and A.M.G., C.M.H. and E.R.W. contributed to the writing of the paper.

ABSTRACT

All dsDNA phages encode two proteins involved in host lysis, an endolysin and a holin that target the peptidoglycan and cytoplasmic membrane, respectively. Bacteriophages that infect Gram-negative bacteria encode additional proteins, the spanins, involved in disruption of the outer membrane. Recently, a gene located in the lytic cassette was identified in the genomes of mycobacteriophages, which encodes a protein (LysB) with mycolyl-arabinogalactan esterase activity. Taking in consideration the complex mycobacterial cell envelope that mycobacteriophages encounter during their life cycle, it is valuable to evaluate the role of these proteins in lysis. In the present work, we constructed an Ms6 mutant defective on *lysB* and showed that Ms6 LysB has an important role in lysis. In the absence of LysB, lysis still occurs but the newly synthesized phage particles are deficiently released to the environment. Using cryo-electron microscopy and tomography to register the changes in the lysis phenotype, we show that at 150 min post-adsorption, mycobacteria cells are incompletely lysed and phage particles are retained inside the cell, while cells infected with Ms6*wt* are completely lysed. Our results confirm that Ms6 LysB is necessary for an efficient lysis of *Mycobacterium smegmatis*, acting, similarly to spanins, in the third step of the lysis process.

INTRODUCTION

Bacteriophages, the viruses of bacteria, are key elements for biosphere equilibrium, playing a fundamental role in bacterial evolution through constant interactions with their hosts [1, 2]. To guarantee their own survival, double-stranded DNA (dsDNA) phages, which represent more than 95% of known bacterial viruses [3], must lyse their hosts. At the end of a lytic cycle, the new phage particles need to be released into the environment, where new host bacteria are potentially available for new infection cycles. The main barrier to phage release is the bacterial cell envelope, and thus, compromising this barrier is the main goal of the lytic process. To accomplish this goal, dsDNA phages synthesize two essential lysis proteins, endolysins and holins. Endolysins are enzymes that disrupt the bacterial cell wall (CW) by cleaving one or more of the five bonds in peptidoglycan (PG). Holins are small proteins that accumulate in the cytoplasmic membrane (CM) and that, at a genetically defined time, form holes in this cell membrane allowing the access of active endolysins to the PG layer or the activation of previously exported endolysins [4, 5]. Phages that infect Gram-positive hosts only require the synthesis of these two proteins to compromise the bacterial envelope and consequently for cell burst. However, phages that infect Gram-negative hosts have to face an additional barrier, the outer membrane (OM). It has been shown recently that disruption of this barrier is also required for cell lysis [6]. This is achieved by a third class of lysis proteins named spanins. The best studied spanins are the λ Rz and Rz1 proteins which are an inner membrane and outer membrane protein, respectively. These two proteins form a complex that spans the entire periplasm mediating the fusion of the CM with the OM. This results in the elimination of the last barrier to phage release and consequently, lysis of the host [7-9]. Spanin genes, which may encode a sole protein (T1 Gp11) or two subunits like the λ Rz and Rz1 proteins, have been identified in nearly all phages infecting Gram-negative hosts [10, 11]. This indicates that, for phages infecting

Gram-negative hosts, lysis is a three-step event where each component of the cell envelope, i.e., CM, CW and OM is sequentially attacked by holins, endolysins and spanins, respectively [9].

Studies of mycobacteriophage Ms6, a phage that infects *Mycobacterium smegmatis*, have shown that the lysis cassette composition reflects the complexity of the cell envelope of its host [12]. Although mycobacteria are classified as Gram-positive bacteria, they have a complex cell envelope composed of a CM, similar to other bacterial CMs [13, 14], surrounded by a peptidoglycan layer covalently linked to arabinogalactan (AG) which is in turn esterified to a mycolic acid (MA), forming the mycolyl arabinogalactan-peptidoglycan (mAGP) complex [15]. The MAs are long fatty acids that constitute the inner leaflet of a true OM. The outermost leaflet is composed of various glycolipids, including trehalose mono and dimycolate, phospholipids and species-specific lipids [16, 17]. Finally, a capsule is composed of proteins, polysaccharides and a few lipids [18, 19]. Thus, phages that infect mycobacteria have to overcome this complex envelope for a successful infective cycle. The Ms6 lysis cassette is composed of five genes [20] (Figure 1). In addition to the holin and the endolysin functions, Ms6 encodes a chaperone-like protein (Gp1) that is involved in the delivery of the endolysin to the PG [21-23] and an additional lysis protein, Lysin B (LysB), identified as a lipolytic enzyme with the ability to cleave ester bonds of both short and long fatty acids [24]. Experiments with components of the mycobacterial cell envelope showed that Ms6 LysB is a mycolyl-arabinogalactan esterase that cleaves the ester bond between the mycolic acids and the arabinogalactan, and this allows the separation of the OM from the CW [25]. Analogies can be made between Ms6 LysB and the spanins, where Ms6 LysB functions to mediate the final step of host cell lysis.

In the present work, we examine the importance of Ms6 LysB in phage lysis and taking advantage of cryo-electron microscopy (cryo-EM) and tomography (cryo-ET), we compare the Ms6 wild type lysis phenotype with that of a Ms6 mutant lacking the *lysB* gene. We present evidence that absence of LysB in the Ms6 infection cycle results in incomplete lysis and suggest that the LysB role in lysis parallels that of spanins.

MATERIALS AND METHODS

Bacterial Strains, Phages, Plasmids and Culture Conditions

Mycobacteria strains, phages, plasmids and oligonucleotides used in this study are listed in Table 1. *M. smegmatis* strains were propagated in 7H9 medium (BD Biosciences, San Jose, CA, USA) with shaking or Middlebrook 7H10 (BD Biosciences), supplemented with 0.5% glucose, at 37 °C. When appropriate, 1 mM $CaCl_2$ or 15 μg/mL kanamycin was also added to the media. For induced conditions, cells were grown in 7H9 supplemented with 0.2% succinate and induced with 0.2% acetamide.

Construction of Ms6 Mutant Phage

Construction of Ms6 mutant phage was performed using Bacteriophage Recombineering of Electroporated DNA (BRED) in *M. smegmatis* as described previously [21, 26]. Briefly, for deletion of gene *lysB* from the Ms6 genome, a 100 bp oligonucleotide (PrΔ*lysB)*, with 50 bp of homology to either flanking region to be deleted was generated. This fragment was extended by PCR to a 200 bp dsDNA substrate using two 75 bp extender primers, PrExtΔ*lysB*Fw and PrExtΔ*lysB*Rv, sharing 25 bp of homology with either end of the 100-mer. After purification, using MinElute PCR Purification Kit (QIAGEN, Hilden, Germany), the 200 bp substrate was co-electroporated with Ms6*wt* DNA into electrocompetent recombineering cells of *M. smegmatis* mc^2155:pJV53. Cells were resuspended in 7H9 supplemented with glucose and $CaCl_2$, incubated at 37 °C for 2 h (prior to lysis) and plated on top agar lawns with *M. smegmatis* mc^2155. Individual plaques were recovered and eluted in 100 μL of phage buffer (10 mM Tris-HCl, pH 7.5, 10 mM $MgSO_4$, 68.5 mM NaCl, 1 mM $CaCl_2$), for two hours at room temperature and analyzed by Deletion Amplification Detection Assay (DADA)-PCR [26] with primers DADA Δ*lysB*-PCRFw/DADA Ms6-PCRRv to detect *lysB* deletion. Mixed primary plaques containing both wild type and mutant alleles were eluted as described above, and serial

dilutions were plated with *M. smegmatis*. Individual secondary plaques were screened by DADA-PCR using the same pair of primers.

Plasmid Construction

To construct plasmid pAG1, a DNA fragment containing the *lysB* gene was obtained by PCR amplification using Ms6 genomic DNA as template, with primers Pr*lysB*Fw/Pr*lysB*Rv and Pfu high-fidelity polymerase (Promega®, Madison, WI, USA). Primers were designed in order to have the restriction sites that allow the correct insertion into the shuttle vector pVVAP (V. Visa and M. McNeil; unpublished). All oligonucleotides used were purchased from Thermo Scientific (Waltham, MA, USA) and are listed in Table 1. DNA amplification, plasmid isolation and electrophoresis were carried out using standard techniques [27]. All constructs used in this study were validated and verified by nucleotide sequencing.

One Step Growth and Single Burst Experiments

One-step growth curves and burst size determination assays [28] were adapted to mycobacteria and carried out in exponential growth phase cell cultures [21]. Briefly, 10^8 *M. smegmatis* cells were suspended in 1 mL of a phage suspension at 10^8 plaque forming units (PFU)/mL. After 50 min of adsorption at 37 °C, nonadsorbed phages were inactivated with 100 μL of 0.4% H_2SO_4 for 5 min followed by neutralization with 100 μL of 0.4% NaOH. The mixture was diluted 1:100 in 7H9 media and aliquots were taken at intervals of 30 min to quantify the number of phage particles [21]. The obtained results are means of three independent experiments.

A similar procedure was used for burst size determination except that 10 μL of infected cells were diluted in supplemented 7H9 in order to obtain one infected cell/mL. Then, 50 mL of the infected

culture was aliquoted into 1 mL volumes and incubated for 3 h at 37 °C. Each sample was plated with 200 µL of *M. smegmatis* cells and top agar (4 mL) on 7H10 medium and incubated at 37 °C for 24 h. Phage plaques were counted, and the Poisson distribution of (P(n)) was applied to determine the burst size (BS): $P(n) = (e^{-c} \times c^{n})/n!$ ($e < 1$), where $P(n)$ is the probability of samples having n infected cells, c is the average number of infected cells per tube, and BS (total plaque count in the 50 plates)/(total number of infected cells) [21]. The obtained results are means of three independent experiments.

Determination of the Number of Phage Particles Released during the Infection Cycle

To determine the number of phage particles released into the supernatant or retained in cells, *M. smegmatis* was grown up to an OD_{600} = 0.5, infected with Ms6*wt* or Ms6Δ*lysB* at a MOI of 1 and incubated at 37 °C for 3 h. Aliquots were taken at 90 min and 180 min post adsorption and separated by centrifugation into supernatant and pellet fractions. The pellets were suspended in ice-cold phage buffer and sonicated twice for 5 s, with a 30 s interval. Each supernatant and the sonicated pellets were serially diluted using phage buffer and plated on a top agar lawn of *M. smegmatis* to determine the number of phage particles. Data represent the mean of three independent experiments.

Cryo-Transmission Electron Microscopy Sample Preparation, Imaging, and Image Processing

To observe the lysis phenotype of Ms6*wt* or Ms6Δ*lysB*, cells were infected as described above for the one step growth experiment except that the phage input was 100-fold higher. At each time point, 200 µL aliquots were mixed with 10-nm gold nanoparticles (Sigma-Aldrich®, St. Louis, MO, USA). The nanoparticles were later used for image alignment in the 3D tomographic reconstruction

process [29, 30]. Four μL of the pre-mixed samples were applied to TEM grids that were vitrified by rapid immersion in liquid ethane using a Gatan CryoPlunger3 (Cp3) apparatus (Gatan, Pleasanton, CA, USA). Cryo-grids were transferred to a Gatan 914 high-tilt holder maintained at −178 °C. Cryo-specimens were imaged with JEOL JEM-2200FS 200-kV field emission gun transmission electron microscope (JEOL Ltd., Tokyo, Japan) equipped with an in-column Omega energy filter (slit width 20 eV), a Gatan US4000 4k × 4k CCD camera, and a Direct Electron DE-20 direct detector (Direct Electron, LP, San Diego, CA, USA). Projection images and tilt series were acquired using SerialEM software (http://bio3d.colorado.edu/SerialEM/) [31]. Single-axis tilt series were collected over an angular range of −62° to 62°, with a 2° tilt increment using the DE-20 direct detector. The total electron dose applied to the specimens did not exceed 120 $e^{-}/Å^{2}$. Tilt series images were acquired at 10,000× nominal magnification (calibrated pixel size of 0.614 nm) with −4 to −8 μm defocus applied. Tomographic reconstructions were generated with IMOD using the r-weighted back-projection algorithm [29, 30].

RESULTS

Ms6 LysB Deletion Decreases Viral Progeny Release

To understand how Ms6 LysB contributes to phage-induced lysis, we took advantage of the Bacteriophage Recombineering of Electroporated DNA (BRED) strategy [26] and constructed an Ms6 derivative mutant lacking gene *lysB*. The Ms6Δ*lysB* was able to form plaques on *M. smegmatis* at equivalent efficiencies to that of the wild type (*wt*); however, a reduction in plaque size produced by the mutant was observed (Figure 2A). In a complementation assay, where LysB production was provided from plasmid pAG1, the wild type phenotype was restored, indicating that plaque size reduction is a consequence of LysB absence.

To test whether this phenotype results from changes in the phage growth parameters, one-step growth and single-burst experiments were performed. *M. smegmatis* cells were infected with Ms6*wt* or Ms6Δ*lysB* at a multiplicity of infection (MOI) of one. The one-step growth curves (Figure 2B) obtained for Ms6*wt* and Ms6Δ*lysB* show that the latent period is similar and that LysB has no effect on the lysis timing; however, the number of infective particles released after Ms6Δ*lysB* infection was lower than in an Ms6*wt* infection. Single-burst experiments performed to compare the viable progeny released from single cells show that a Ms6*wt* infection released an average of 147 ± 27 viable phages per bacterium, while Ms6Δ*lysB* yielded a reduced burst size of approximately 53 ± 14, where the ± values indicate the mean SD of three independent experiments. Again, when LysB was provided in *trans*, the *wt* burst size was restored. These results show that, although Ms6Δ*lysB* can accomplish lysis of the host cell, the overall process seems to be less efficient.

Ms6 Is Trapped in Cell Debris in Absence of LysB

Taking into consideration the observed lysis defect and that: (i) LysB is produced at a late stage of the infection cycle as other lysis proteins, (ii) this protein is a lipolytic enzyme that cleaves the linkage of the mycobacterial OM to the mAGP complex; we hypothesize that the reduced burst size results from a release defect and not from a reduction in the number of synthesized phage particles. To address this question, we performed a time course infection assay with either Ms6*wt* or Ms6Δ*lysB* and at each time point the cell pellet was separated from the supernatant and the number of phage particles in each fraction was determined. As observed in Figure 3, at 90 min post-adsorption the majority of the phage particles are not yet released and the number of PFU in the supernatant is similar for both phage infections. However, at 180 min post-adsorption, for the *wt* phage infection over 90% of phage particles are free in the supernant and only 7% are in the pelleted fraction, while for the Ms6Δ*lysB* infection, a remarkable 47% of total phage progeny is retained in the pellet. These results confirm that the reduced number of phage particles obtained for the mutant phage, in the single burst experiment, results from a deficient cell lysis, where part of the newly synthesized virions are trapped in incompletely lysed cells.

Cryo-EM Shows Incomplete Cell Lysis in Absence of Ms6 LysB

To prove that the unreleased phage particles remained trapped in incompletely lysed cells, we used cryo-electron microscopy (cryo-EM) and cryo-electron tomography (cryo-ET). This method allows us to visualize the host cell lysis and the viral progeny in their native environment and to examine the lysis behavior of *M. smegmatis* infected with Ms6*wt* or Ms6Δ*lysB*. From each infected *M. smegmatis* culture, with either Ms6*wt* or Ms6Δ*lysB*, aliquots were plunge frozen on copper grids for cryo-EM assessment.

Figure 4 shows collected images of infected cells at 90 and 150 min post-adsorption. At 90 min, no lysis is yet observed (Figure 4A,C). At 150 min post-adsorption, cells infected with Ms6*wt* burst and release almost all the phages (Figure 4B), while cells infected with Ms6Δ*lysB* show incomplete lysis and many phages are not released (Figure 4D). Incompletely lysed cells are still captured up to 240 min post-adsorption with the mutant phage, while for the wild type infection only free phage particles and cell debris are observed.

Cryo-ET data collection was performed on Ms6Δ*lysB* infected cells. In Figure 5A, a central slice through the 3D tomogram shows phages inside the incompletely lysed cell and what appears to be lesions throughout the cell envelope. To facilitate the visualization of the phages and to demonstrate they are inside the cell, segmentations of several 3D tomographic volumes was performed. With this method, it is possible to render the structures or regions of interest in the tomogram (Figure 5B). It is clear that many phages are inside the incompletely lysed cell despite the evident deformation of the cell envelope. It is also clear that most of the CM and PG are absent, while the OM still remains as a veil surrounding and holding some of the cell content.

DISCUSSION

It is well known that lysis of the bacterial host is the last event of dsDNA phage lytic cycle, so that the new synthesized phage particles may be released into the environment and infect new available hosts. Compromising the bacterial cell barriers is a sine qua non condition to achieve this final step. Although the role of holins and endolysins has long been well defined, targeting the CM and the CW respectively, the importance of spanins in lysis has only recently been established [9]. The best characterized spanin is that of phage λ, which is composed of two subunits, the Rz and Rz1 proteins, that, once localized to the inner and outer membranes, respectively interact by the C-termini of their periplasmic domains to form a complex that spans the entire periplasm [7, 10]. For many years, *Rz/Rz1* were considered auxiliary genes, because under laboratory conditions λ lysis could be achieved in the absence of these genes, unless the OM was artificially stabilized by the presence of millimolar concentrations of Ca^{2+} [32]. Recently, Berry *et al.* [7, 9] have demonstrated that, in nature, in absence of stabilizing cations, these proteins are required for λ lysis, as induction of λ lysogens in the absence of a spanin function results in lysis failure. The infection cycle terminates leading to spherical cells where the CM and PG have been disrupted, but the OM remains intact, indicating that the latter is an important barrier to lysis. In a λ lytic cycle, the Rz-Rz1 complexes accumulate in the envelope during the morphogenesis phase. It was suggested that, following PG disruption by the endolysins, the spanins function by fusing the inner and outer membrane. This results in outer membrane disruption and consequently cell lysis [7, 9] [7,9].

This spherical phenotype in the absence of spanins has also been observed in infections with phages P2 [33] and PRD1 [11]. The presence of *Rz/Rz1* equivalents in the lysis cassette, of nearly all bacteriophages that infect Gram-negative hosts, strengthens the idea that to accomplish lysis, in

addition to compromising the CM and the CW through the action of holins and endolysins, these phages also need to disrupt the OM [7, 10].

In this work, we show that mycobacteriophage Ms6, a phage that infects the mycobacterial species, *M. smegmatis,* in addition to the holin and endolysin functions also requires an additional lysis protein to overcome the last cell barrier. We provide evidence that Ms6 LysB parallels the function of spanins.

Mycobacteria, which are members of the Corynebacteriales order, are bacteria that, despite being classified as Gram-positive, share a complex cell envelope. In addition to a CM and a CW, they also contain an OM, which is an asymmetrical bilayer where the inner leaflet, composed of long chain mycolic acids, is linked to the CW through an ester bond to AG. This peculiar OM confers to mycobacteria their characteristic impermeability and resistance to therapeutic agents, and as so, is also predicted to be a barrier to mycobacteriophage-induced lysis [13-17]. We have previously shown that Ms6 LysB is a lipolytic enzyme that cuts the linkage between AG and MA on the mycolyl-arabinogalactan-peptidoglycan complex [24, 25].

We have observed that, in contrast with Ms6 LysA [22] and in general with phage endolysins, the Ms6 LysB, under our laboratory conditions, is not essential for the phage life cycle, since the Ms6 derivative mutant lacking gene *lysB* is viable and capable of forming plaques in *M. smegmatis*. We have observed, however, a reduction in the plaque size. In a one-step assay, we could demonstrate that in absence of LysB there is a defective phage release at the end of an infection cycle. Indeed, in the single burst experiment a reduction of 64% in the number of free phage particles per bacterium was observed. This is in agreement with the reduced plaque size of Ms6Δ*lysB*, a phenotype that was

reverted to the wild type when LysB was provided in trans. Since Ms6 LysB is produced during late gene expression, from gene *lysB*, which is part of the lysis cassette, a role in host lysis is obviously expected.

A reduced phage release, together with a reduced plaque size was also reported for the LysB of mycobacteriophage Giles; however, and in contrast to phage Ms6 where absence of LysB did not affect the timing of lysis, the authors observed that lysis induced by GilesΔ*lysB* was delayed in 30 min when compared to the Giles*wt [34]*. It is not clear so far how the absence of Giles LysB affects the timing of lysis.

The observation that, at the end of a Ms6Δ*lysB* infection, 47% of the phages are recovered from the cell pellet against only 7% in a Ms6*wt* infection, indicates that the reduced burst size results from a deficient phage release and not from a reduction in the number of new synthesized phage particles. In the absence of LysB, phage particles are trapped in incompletely lysed cells. Cryo-EM and cryo-ET of infections in the absence of LysB clearly show unreleased phage particles inside cells infected with Ms6Δ*lysB*, while at the same time point (150 min post-adsorption) in a Ms6*wt* infection the cell completely bursts. The 3D tomogram also shows deformations of the cell, indicating that the OM still holds part of the cell content even after disruption of the CM and PG (Figure 5B), following holin and endolysin action.

Our results support the notion that the role of Ms6 LysB in lysis equates to that of spanins, however with different modes of action, since the structure of mycobacteria OM is completely different from that of Gram-negative bacteria. While spanins function either as a complex (λ Rz-Rz1) or as a single protein (T1 Gp11) by fusing the CM and OM [35], Ms6 LysB protein functions as an enzyme that

detaches the OM from the CW by cleaving the bond that links these two structures. As a lipolytic enzyme, Ms6 LysB also acts as an esterase on other lipids containing mycolic acids, such as the trehalose dimycolate (TDM) [25], a glycolipid with an important role in *M. tuberculosis* pathogenesis [36]. However, it is unknown if cleavage of these lipids contributes to lysis.

The fact that the vast majority of mycobacteriophages sequenced so far encode Ms6 LysB homologous proteins suggests that they have an important role in nature. This is also true for other phages that infect members of the mycolata group, a bacterial group that also contain a layer of mycolic acid-containing lipids in their envelope. Examples are the *Rhodococcus equi* phages ReqiDocB7, ReqiPepy6 and ReqiPoco6, which encode Ms6 LysB homologues [12, 37]. A huge number of genome sequences from phages infecting the same bacterial group is available at The Actinobacteriophage Database (http://phagesdb.org/), and here we can also find genes from several phages annotated as coding for Lysin B as exemplified by *gp24* or *gp41* from phages SoilAssassin and Ghobes, respectively, both infecting *Gordonae terrae* [38]. In other cases, although no LysB annotation exists, we could identify the GXSXG motif common to lipolytic enzymes in the deduced amino acid sequence of several genes, such as *gp54* from the TPA4 phage, a lytic phage that infects Tsukamurella species (Figure S1).

Collectively our results lead to the suggestion that mycobacteriophage-induced lysis is also a three-step process where holins subvert the cytoplasmic membrane followed by endolysins targeting the cell wall and LysB proteins disrupting the last barrier to mycobacteriophage release, the outer membrane.

Our present knowledge of the mechanism of bacteriophage lysis suggests that the complexity of phage lytic cassettes depends on their hosts. Hosts with a simpler envelope, like Gram-positive bacteria, require the phage to possess a simple lytic cassette, with genes encoding proteins targeting the CM and the PG. For bacteria with a more complex envelope that also contain an OM, degradation of the cell wall is necessary but not sufficient for lysis and phages need to produce specific proteins to overcome this barrier. Thus, phages that infect Gram-negative hosts or mycobacteria, in addition to holins and endolysins, synthesize spanins or lipolytic enzymes, respectively (Figure 1).

ACKNOWLEDGEMENTS

We would like to thank Varalakshmi Vissa and Michael McNeil (Colorado State University, Fort Collins, CO, USA) for providing pVVAP vector and the Robert P. Apkarian Integrated Electron Microscopy Core, Emory University for microscopy services and support. This work was supported in part by Fundação para a Ciência e Tecnologia (FCT-MCES, Portugal) Grant PTDC/IMI-MIC/0694/2012 to MP; Emory University, Children's Healthcare of Atlanta, and the Georgia Research Alliance to E.R.W.; the Center for AIDS Research at Emory University (P30 AI050409); public health service grant GM104540 to E.R.W. from the NIH/NIGMS, and NSF grant 0923395 to E.R.W. AG (SFRH/BD/87685/2012) is a recipient PhD fellowship from FCT-MCES, Portugal.

REFERENCES

1. Rodriguez-Valera, F., Martin-Cuadrado, A.-B., Rodriguez-Brito, B., Pasic, L., Thingstad, T. F., Rohwer, F., and Mira, A. Opinion explaining microbial population genomics through phage predation. *Nat Rev Microbiol*, 2009. **7**(11): p. 828-836.
2. Hatfull, G. F. and Hendrix, R. W. Bacteriophages and their genomes. *Curr Opin VIrol*, 2011. **1**(4): p. 298-303.
3. Ackermann, H. W. and Prangishvili, D. Prokaryote viruses studied by electron microscopy. *Arch Virol*, 2012. **157**(10): p. 1843-1849.
4. Young, R., Wang, I. N. Phage lysis, in *The Bacteriophages*, R. Calendar, Abedon, S. T., Editor. 2006, Oxford University Press. p. 104-126.
5. Catalao, M. J., Gil, F., Moniz-Pereira, J., Sao-Jose, C., and Pimentel, M. Diversity in bacterial lysis systems: Bacteriophages show the way. *FEMS Microbiol Rev*, 2013. **37**(4): p. 554-571.
6. Rajaure, M., Berry, J., Kongari, R., Cahill, J., and Young, R. Membrane fusion during phage lysis. *Proc Natl Acad Sci U S A*, 2015. **112**(17): p. 5497-5502.
7. Berry, J., Summer, E. J., Struck, D. K., and Young, R. The final step in the phage infection cycle: The Rz and Rz1 lysis proteins link the inner and outer membranes. *Mol Microbiol*, 2008. **70**(2): p. 341-351.
8. Berry, J., Savva, C., Holzenburg, A., and Young, R. The lambda spanin components Rz and Rz1 undergo tertiary and quaternary rearrangements upon complex formation. *Protein Sci*, 2010. **19**(10): p. 1967-1977.
9. Berry, J., Rajaure, M., Pang, T., and Young, R. The spanin complex is essential for lambda lysis. *J Bacteriol*, 2012. **194**(20): p. 5667-5674.

10. Summer, E. J., Berry, J., Tran, T. A. T., Struck, L. N. D. K., and Young, R. RzlRz1 lysis gene equivalents in phages of gram-negative hosts. *J Mol Biol*, 2007. **373**(5): p. 1098-1112.

11. Krupovic, M., Cvirkaite-Krupovic, V., and Bamford, D. H. Identification and functional analysis of the Rz/Rz1-like accessory lysis genes in the membrane-containing bacteriophage PRD1. *Mol Microbiol*, 2008. **68**(2): p. 492-503.

12. Pimentel, M. Genetics of phage lysis. *Microbiol Spectrum*, 2014. **2**(1).

13. Mamadou, D., Marieange, D., and Nicole, G. The cell-envelope of *Mycobacterium smegmatis* - cyto-chemistry and architectural implications. *FEMS Microbiol Lett*, 1989. **61**(1-2): p. 89-93.

14. Daffe, M., The Global Architecture of the Mycobacterial Cell Envelope, in *Mycobacterial Cell Envelope*, ed. M. Daffe and J.M. Reyrat. 2008. 3-11.

15. Brennan, P. J. Structure, function, and biogenesis of the cell wall of *Mycobacterium tuberculosis*. *Tuberculosis*, 2003. **83**(1-3): p. 91-97.

16. Zuber, B., Chami, M., Houssin, C., Dubochet, J., Griffiths, G., and Daffe, M. Direct visualization of the outer membrane of mycobacteria and corynebacteria in their native state. *J Bacteriol*, 2008. **190**(16): p. 5672-5680.

17. Hoffmann, C., Leis, A., Niederweis, M., Plitzko, J. M., and Engelhardt, H. Disclosure of the mycobacterial outer membrane: Cryo-electron tomography and vitreous sections reveal the lipid bilayer structure. *Proc Natl Acad Sci U S A*, 2008. **105**(10): p. 3963-3967.

18. Sani, M., Houben, E. N. G., Geurtsen, J., Pierson, J., de Punder, K., van Zon, M., Wever, B., Piersma, S. R., Jimenez, C. R., Daffe, M., Appelmelk, B. J., Bitter, W., van der Wel, N., and Peters, P. J. Direct visualization by cryo-EM of the mycobacterial capsular layer: A labile structure containing ESX-1-secreted proteins. *PLoS Pathog*, 2010. **6**(3).

19. Lemassu, A., OrtaloMagne, A., Bardou, F., Silve, G., Laneelle, M. A., and Daffe, M. Extracellular and surface-exposed polysaccharides of non-tuberculous mycobacteria. *Microbiology*, 1996. **142**: p. 1513-1520.

20. Garcia, M., Pimentel, M., and Moniz-Pereira, J. Expression of mycobacteriophage Ms6 lysis genes is driven by two sigma(70)-like promoters and is dependent on a transcription termination signal present in the leader RNA. *J Bacteriol*, 2002. **184**(11): p. 3034-3043.

21. Catalao, M. J., Gil, F., Moniz-Pereira, J., and Pimentel, M. The mycobacteriophage Ms6 encodes a chaperone-like protein involved in the endolysin delivery to the peptidoglycan. *Mol Microbiol*, 2010. **77**(3): p. 672-686.

22. Catalao, M. J., Milho, C., Gil, F., Moniz-Pereira, J., and Pimentel, M. A second endolysin gene is fully embedded in-frame with the lysA gene of mycobacteriophage Ms6. *PLoS One*, 2011. **6**(6).

23. Catalao, M. J., Gil, F., Moniz-Pereira, J., and Pimentel, M. The endolysin-binding domain encompasses the N-terminal region of the mycobacteriophage Ms6 Gp1 chaperone. *J Bacteriol*, 2011. **193**(18): p. 5002-5006.

24. Gil, F., Catalao, M. J., Moniz-Pereira, J., Leandro, P., McNeil, M., and Pimentel, M. The lytic cassette of mycobacteriophage Ms6 encodes an enzyme with lipolytic activity. *Microbiology*, 2008. **154**: p. 1364-1371.

25. Gil, F., Grzegorzewicz, A. E., Catalao, M. J., Vital, J., McNeil, M. R., and Pimentel, M. Mycobacteriophage Ms6 LysB specifically targets the outer membrane of *Mycobacterium smegmatis*. *Microbiology*, 2010. **156**: p. 1497-1504.

26. Snapper, S.B.; Melton, R.E.; Mustafa, S.; Kieser, T.; Jacobs, W.R., Jr. Isolation and characterization of efficient plasmid transformation mutants of *Mycobacterium smegmatis*. *Mol. Microbiol,* 1990. **4**: p. 1911–1919.

27. Portugal, I.; Anes, E.; Moniz-Pereira, J. Temperate mycobacteriophage from *M. smegmatis*. *Acta Leprol*, 1989. **1**: 243–244.

28. Van Kessel, J.C.; Hatfull, G.F. Recombineering in *Mycobacterium tuberculosis*. *Nat Methods* 2007. **4**: 147–152.

29. Vissa, V.; McNeil, M.; Department of Microbiology, Immunology and Pathology, Colorado State University, Fort Collins; CO 80523, USA. pVVAp is a mycobacteria shuttle vector, containing the pAL5000 replication origin, the kanamycin resistance gene and the acetamidase promoter region. 2008.

30. Marinelli, L. J., Piuri, M., Swigonova, Z., Balachandran, A., Oldfield, L. M., van Kessel, J. C., and Hatfull, G. F. Bred: A simple and powerful tool for constructing mutant and recombinant bacteriophage genomes. *PLoS One*, 2008. **3**(12).

31. Sambrook, J., Russell, D. W. *Molecular cloning: A laboratory manual*. 3rd ed. 2001, Cold Spring Harbor, NY, USA: Cold Spring Harbor Laboratory Press.

32. Adams, M. H. Methods of study of bacterial viruses, in *Bacteriophages*, M.H. Adams, Editor. 1959, Interscience Publisers, Inc.: New York, NY, USA. p. 443-522.

33. Mastronarde, D. N. Dual-axis tomography: An approach with alignment methods that preserve resolution. *J Struct Biol*, 1997. **120**(3): p. 343-352.

34. Kremer, J. R., Mastronarde, D. N., and McIntosh, J. R. Computer visualization of three-dimensional image data using IMOD. *J Struct Biol*, 1996. **116**(1): p. 71-76.

35. Mastronarde, D. N. Automated electron microscope tomography using robust prediction of specimen movements. *J Struct Biol*, 2005. **152**(1): p. 36-51.

36. Zhang, N. and Young, R. Complementation and characterization of the nested Rz and Rz1 reading frames in the genome of bacteriophage lambda. *Mol Gen Genet*, 1999. **262**(4-5): p. 659-667.

37. Markov, D., Christie, G. E., Sauer, B., Calendar, R., Park, T., Young, R., and Severinov, K. P2 growth restriction on an rpoC mutant is suppressed by alleles of the Rz1 homolog lysC. *J Bacteriol*, 2004. **186**(14): p. 4628-4637.

38. Payne, K., Sun, Q., Sacchettini, J., and Hatfull, G. F. Mycobacteriophage Lysin B is a novel mycolylarabinogalactan esterase. *Mol Microbiol*, 2009. **73**(3): p. 367-381.

39. Berry, J. D., Rajaure, M., and Young, R. Spanin function requires subunit homodimerization through intermolecular disulfide bonds. *Mol Microbiol*, 2013. **88**(1): p. 35-47.

40. Jackson, M. The mycobacterial cell envelope-lipids. *Cold Spring Harbor Perspect Med*, 2014. **4**(10).

41. Summer, E. J., Liu, M., Gill, J. J., Grant, M., Chan-Cortes, T. N., Ferguson, L., Janes, C., Lange, K., Bertoli, M., Moore, C., Orchard, R. C., Cohen, N. D., and Young, R. Genomic and functional analyses of *Rhodococcus equi* phages ReqiPepy6, ReqiPoco6, ReqiPine5, and ReqiDocB7. *Appl Environ Microbiol*, 2011. **77**(2): p. 669-683.

42. Pope, W. H., Mavrich, T. N., Garlena, R. A., Guerrero-Bustamante, C. A., Jacobs-Sera, D., Montgomery, M. T., Russell, D. A., Warner, M. H., Hatfull, G. F., and Sea, P. Bacteriophages of *Gordonia* spp. Display a spectrum of diversity and genetic relationships. *mBio*, 2017. **8**(4).

FIGURE LEGENDS

Figure 1. Cell envelopes of bacteria (left) and representative lysis cassettes of their infecting phages (right). (A) Gram-positive bacteria; (B) Gram-negative bacteria; (**C**) Mycobacteria. The white segments in holin-like genes indicate the number and position of transmembrane domain coding sequences. Abbreviations: CapGlu, capsular glucan CM, cytoplasmic membrane; LA, lypoteichoic acid; LAM, lipoarabinomannan; LP, lipoprotein; LPS, lipopolysaccharide; P, protein; PG, peptidoglycan; PIMs, phosphatidylinositol mannosides; PLs, phospholipids; PO, porin; Pp, periplasm; TDM, trehalose dimycolate; TMM, trehalose monomycolate. Adapted from reference [5] with permission.

Figure 2. (A) Phage plaques formed by Ms6 (top) or Ms6Δ*lysB* (bottom) on a lawn of *M. smegmatis*. The plaques formed by Ms6Δ*lysB* phage are smaller than the ones formed by the wild type Ms6; (B) one-step growth curves of Ms6*wt* (circles) or Ms6Δ*lysB* (squares) on *M. smegmatis* mc^2155 show a lower number of plaque-forming units (PFU) released from Ms6Δ*lysB* infection. Both curves show similar progression up to 90 min post-adsorption showing no differences in the timing of lysis. T0 marks the end of the adsorption and start of the one-step experiment. The PFU/mL at t = 0 was used to normalize PFU/mL of each time point. For each time point, the mean ± SD of four independent assays is indicated.

Figure 3. Distribution of phage particles in the supernatant and pellet of *M. smegmatis* infected with Ms6*wt* or Ms6Δ*lysB*. Ms6 is trapped in cell debris in absence of LysB. At the indicated time points, the distribution of phage particles in the pellet and in the supernatant was determined as a percentage of the total amount of PFU counted in both fractions. The values indicate the mean ± SD of three independent experiments.

Figure 4. Cryo-EM images of *M. smegmatis* infected with Ms6*wt* or Ms6Δ*lysB*. At 90 min post-adsorption, cells infected with Ms6*wt* (A) or Ms6Δ*lysB* (C) are still intact and no difference is observed. At 150 min post-adsorption, the abrupt burst of a cell infected with Ms6*wt* is clear (B) while cells infected with Ms6Δ*lysB* (D) do not lyse abruptly and deformations in the cell envelope are clearly visible. Scale bar (200 nm).

Figure 5. Cryo-electron tomography of *M. smegmatis* infected with Ms6Δ*lysB* at 150 min post-adsorption. (A) Slice through the tomogram of an infected cell; (B) segmented volume of the phage capsids (purple), cell membrane and PG (magenta) and the outer membrane (green). Scale bar (200 nm).

Supplementary Figure 1. Comparison of *lysB* genes from phages infecting members of the Mycolatagroup. (A) Illustrated are representatives of mycobacteriophages and phages infecting *Rhodococcus equi, Gordoniae terrae and Tsukamurella* spp. The genes marked with a white segment indicate genes not previously assigned as holins, but having predicted transmembrane segments. (B) Alignment of Ms6 LysB and putative LysB protein homologues. The conserved pentapeptide (G/A-X-S-X-G) is highlighted on a grey background. Numbers refer to the amino acid positions.

Figure 1

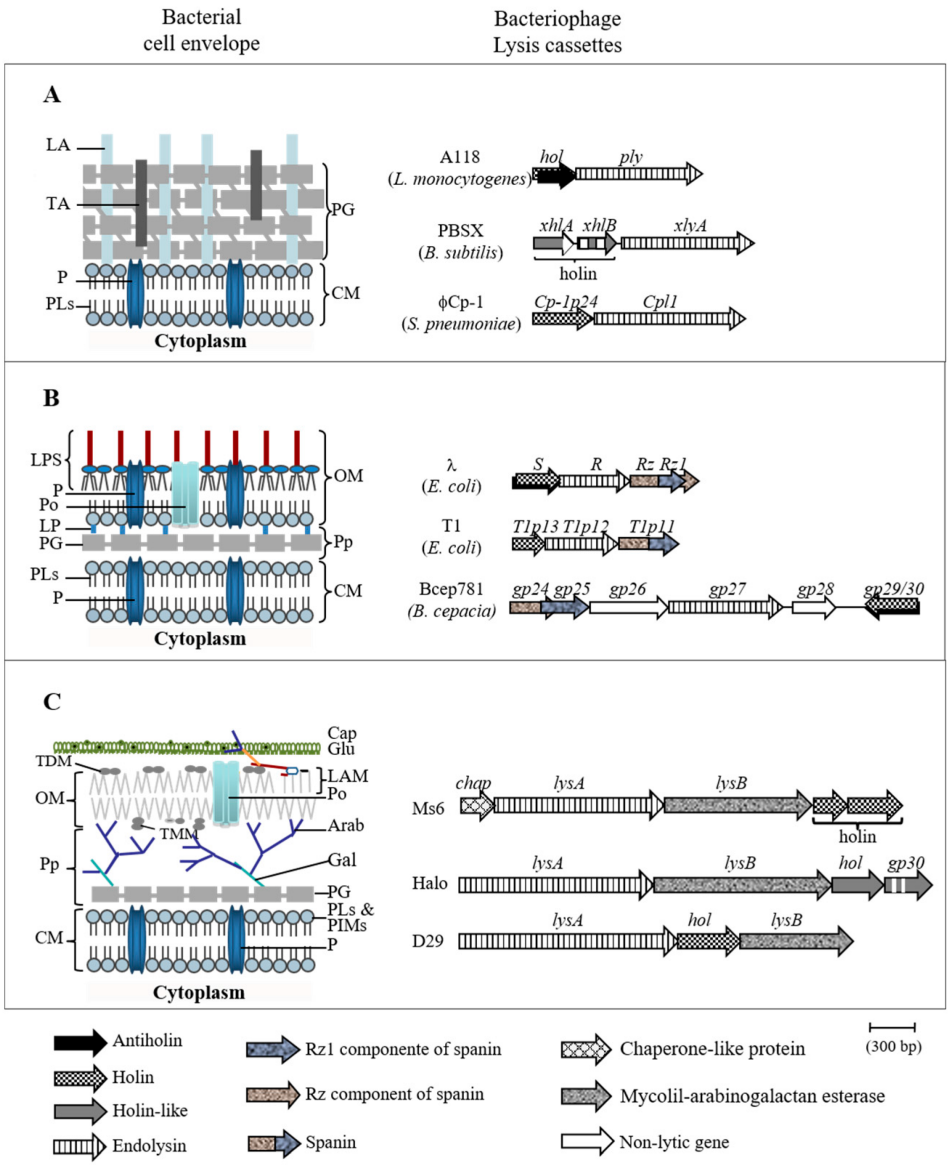
Bacterial
cell envelope
Bacteriophage
Lysis cassettes
A
LA
TA
PG
P
PLs
CM
Cytoplasm
A118
(L. monocytogenes)
hol
ply
PBSX
(B. subtilis)
xhlA
xhlB
xlyA
holin
ϕCp-1
(S. pneumoniae)
Cp-1p24
Cpl1
B
LPS
P
Po
LP
PG
PLs
P
OM
Pp
CM
Cytoplasm
λ
(E. coli)
S
R
Rz
Rz1
T1
(E. coli)
T1p13
T1p12
T1p11
Bcep781
(B. cepacia)
gp24
gp25
gp26
gp27
gp28
gp29/30
C
Cap
Glu
TDM
OM
LAM
Po
TMM
Arab
Pp
Gal
PG
PLs &
PIMs
CM
P
Cytoplasm
Ms6
chap
lysA
lysB
holin
Halo
lysA
lysB
hol
gp30
D29
lysA
hol
lysB
Antiholin
Holin
Holin-like
Endolysin
Rz1 componente of spanin
Rz component of spanin
Spanin
Chaperone-like protein
Mycolil-arabinogalactan esterase
Non-lytic gene
(300 bp)

Figure 2

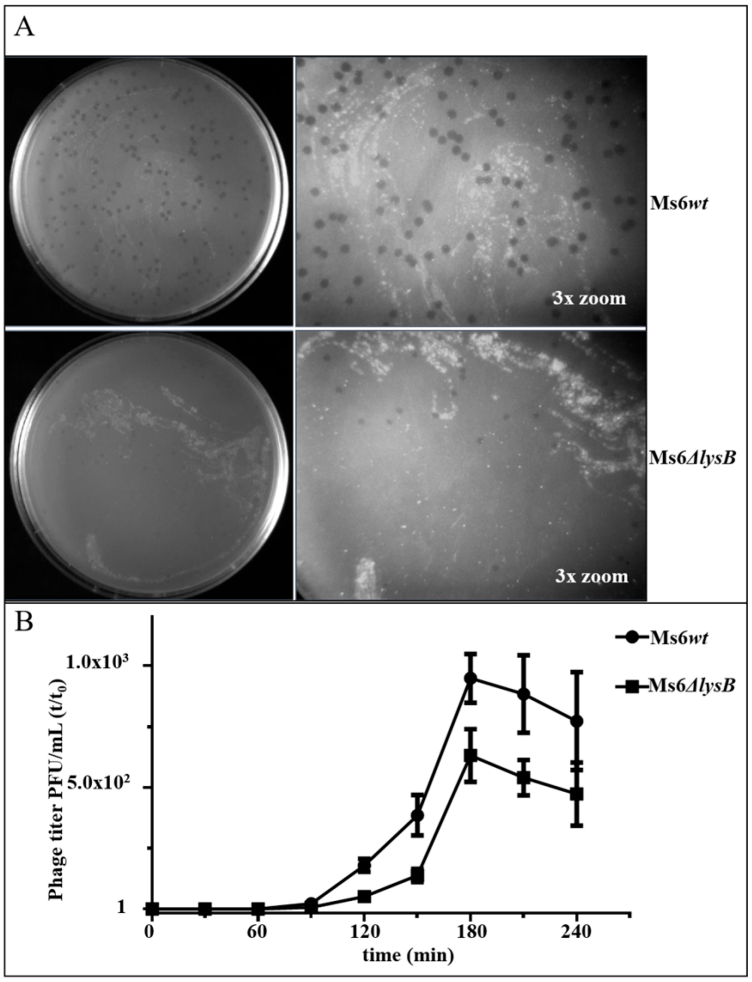
A
Ms6*wt*
3x zoom
Ms6*ΔlysB*
3x zoom
B
Ms6*wt*
Ms6*ΔlysB*
Phage titer PFU/mL (t/t0)
1.0x10³
5.0x10²
1
0
60
120
180
240
time (min)

Figure 3

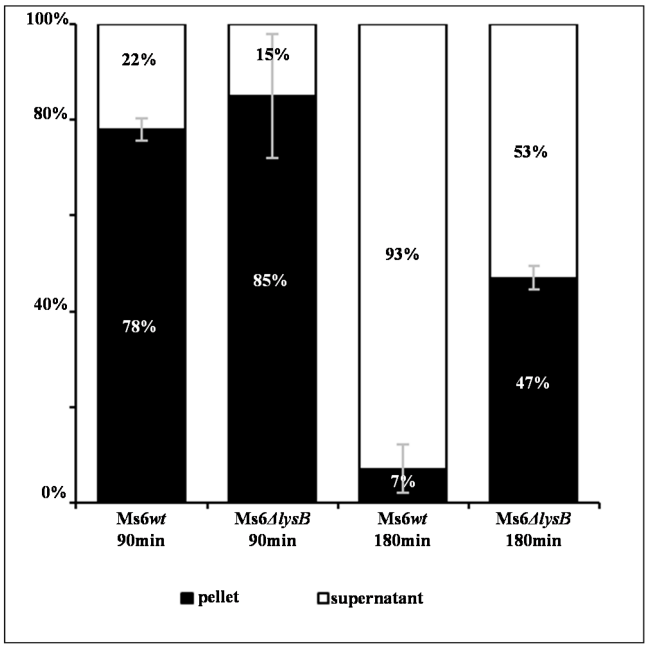
100%
80%
40%
0%
22%
78%
15%
85%
93%
7%
53%
47%
Ms6wt 90min
Ms6ΔlysB 90min
Ms6wt 180min
Ms6ΔlysB 180min
pellet
supernatant

Figure 4

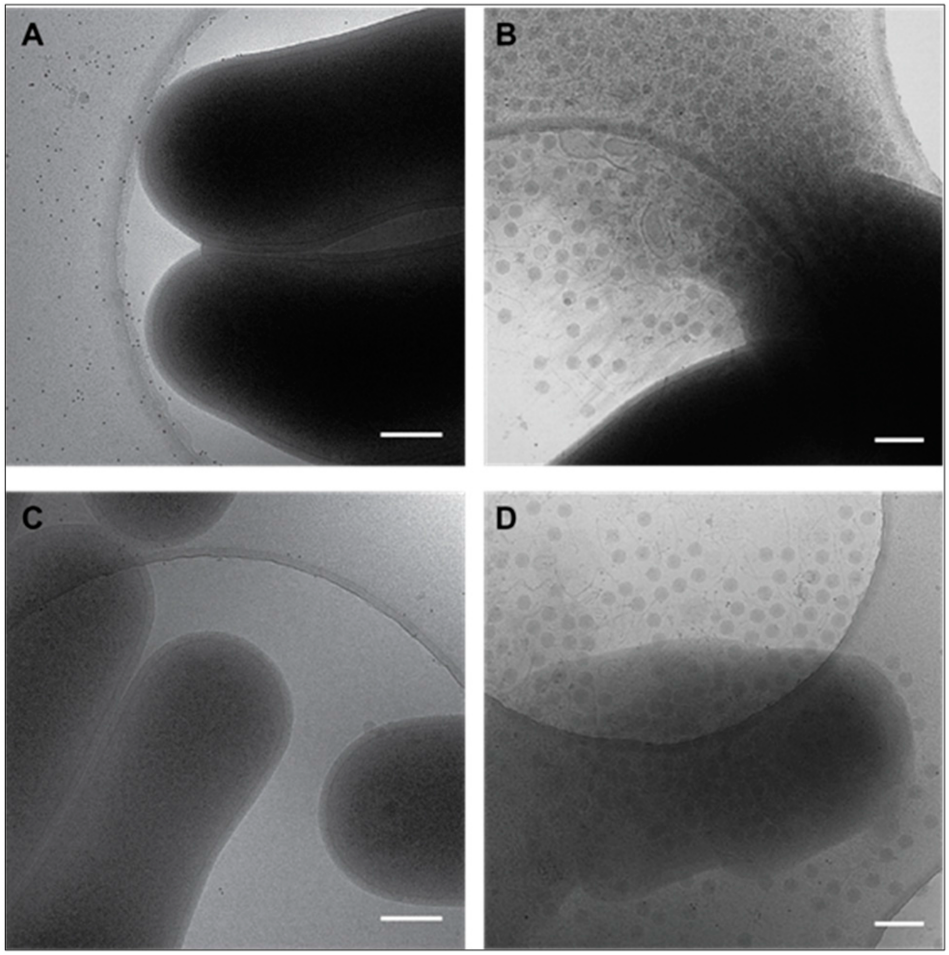

Figure 5

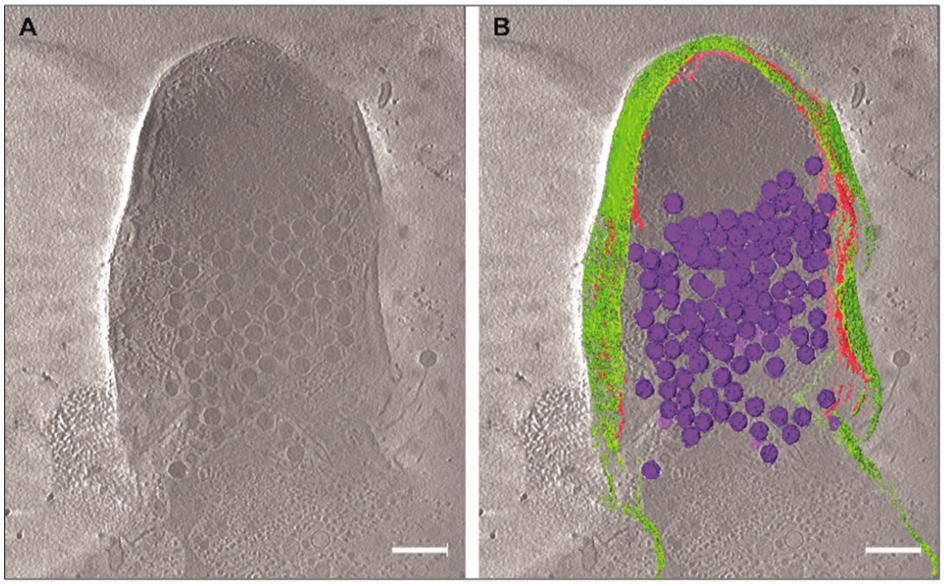

Supplementary Figure 1

A

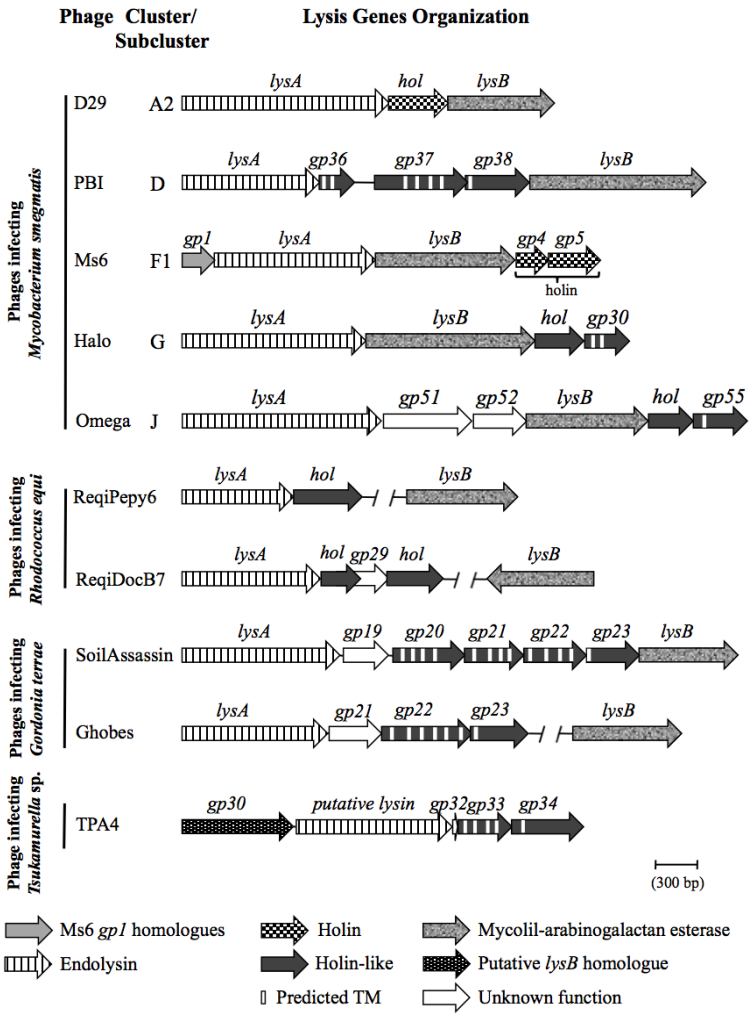

B

```
D29           70 ...ADPYADFAMAGYSQGAIVVGQVLKH...  95
PBI1         168 ...KDPDVEFWFSGYSQKADGLEDALEI... 193
Ms6          156 ...RIETHGTALAGYSQGAVVLSELWMN... 181
Halo         175 ...VNPKIRVVIGGYSAGAIAAAMF-RA... 199
Omega         85 ...RTTPGKIVLSAYSQSAVAFAYVWRD... 110
ReqiPepy6     76 ...SNPGKQFILLAYSGGNRVIHEW-ME... 100
ReqiDocB7     53 ...-FTRQAIFVAGYSQGGTVVTKAIKH...  77
SoilAssassin  71 ...ERSQFDVVVAGYSQGAAVAVHY-AL...  95
Ghobes        77 ...AHPDDRFVVLGYSLGALVGTKF-LE... 101
TPA4          73 ...AAARGRFVGLGYSQGGSLLTEWLNR...  98
```

Table 1. Bacterial strains, phages, plasmids, and oligonucleotides used in this study

Name	Description	Source or Reference
Bacteria		
Mycobacterium smegmatis mc^2155	High-transformation-efficiency mutant of *M. smegmatis* ATCC 607	[26]
Bacteriophages		
Ms6*wt*	Temperate bacteriophage from *M. smegmatis*	[27]
Ms6Δ*lysB*	996 bp in-frame deletion of the Ms6 *lysB* gene	This study
Plasmids		
pJV53	Derivative of pLAM12 with Che9c 60 and 61 under control of the acetamidase promoter; Kan^r	[28]
pAG1	*lysB* gene cloned into pVVAP	This study
pVVAP	Mycobacteria shuttle vector carrying the acetamidase promoter; Kan^r	[29]
Oligonucleotides	**Sequence 5'-3'** [a]	
PrΔlysB	CTCGGCGGAAAAACCCTCCTCGTGGACGCGGTAG CAGAACTGTTGGGCCACTGATAGGAGGCACCCAT GCTGACACGTTCATTCTGGATCGACGCCGCCGAGC G	Ms6ΔlysB
PrExtΔlysBFw	CGAGATCCTGCGGCAACTGCGCGGATACAACCTCA CTGGCTGGCCGCAGCTCGGCGGAAAAACCCTCGT GGACG	Extend PrΔ*lysB*
PrExtΔlysBRv	CCCCGGCGCCGAGGGTGGCGATCGCGGTTTGGGC GAATGTGCGTATGGCACGCTCGGCGGCGTCGATC CAGAATG	Extend PrΔ*lysB*
PrlysBFw	GCGGATCCATGAGCAGAACTGTTGGGCC	Includes BamHI site to clone in pVVAP
PrlysBRv	GGAAGCTTTGTGCGTAGGTAGTCGATG	Includes HindIII site to clone in pVVAP
DADA Δ*lysB* PCRFw	GCGCTAGCAGAACTGTTGGGCCACTGATAG	Ms6Δ*lysB*
DADA Ms6-PCRRv	CGTCTCGTACTGCACGTACCGGTTCTTC	Ms6Δ*lysB*